Understanding of Interaction and Dynamics in Multi-component Chemical Systems

Thesis Submitted for the Degree of

Doctor of Philosophy (Science)

of

Jadavpur University

By

Sandipa Indra

Department of Chemical, Biological and Macromolecular Sciences,

S. N. Bose National Centre for Basic Sciences,

Block-JD, Sector-III, Salt Lake

Kolkata-700098, India

To my

Father Prasanta Indra

And

Mother Sabita Indra

CERTIFICATE FROM THE SUPERVISOR(S)

This is to certify that the thesis entitled **"Understanding of Interaction and Dynamics in Multi-component Chemical Systems"** submitted by **Smt. Sandipa Indra** (Index no. 20/12/Chem./21), who got her name registered on 18/04/12 for the award of Ph. D. (Science) degree of Jadavpur University, is absolutely based upon her own work under the supervision of **Prof. Ranjit Biswas** and that neither this thesis nor any part of it has been submitted for either any degree/diploma or any other academic award anywhere before.

Ranjit Biswas
21/12/15

Dr. Ranjit Biswas

Professor,

Department of Chemical, Biological and Macromolecular Sciences

S. N. Bose National Centre for Basic Sciences

Block – JD, Sector – III, Salt Lake, Kolkata – 700098, West Bengal, India

DR. RANJIT BISWAS
Professor
Dept. of Chemical, Biological & Macromolecular Sciences
S. N. Bose National Centre for Basic Sciences
Block - JD, Sector - III, Salt Lake, Kolkata - 700 098, India

Acknowledgements

Abstract

In this thesis, our main focus was to understand the structure and dynamics of aqueous binary mixtures, complex sugar solutions and electrolyte solutions. It is well known that reactions are substantially modified by environmental polarity and dynamics. Therefore, tailoring reactions for obtaining desired products requires a thorough knowledge of the reactant-medium interaction and environment dynamics. Alcohols and their aqueous binary mixtures are frequently used reaction media where association via hydrophobic and hydrogen bonding interactions lead to substantial change in solution structure and dynamics. Such molecules, which are known as amphiphiles by virtue of possessing both hydrophilic and hydrophobic moieties were our primary interest to study as components for binary mixture with water. Examples of the amphiphiles, which have been studied in this thesis, with brief introduction in the parenthesis are: 2-butoxyethanol (BE) [industrially very useful surfactant], tetramethylurea (TMU) [strong protein denaturant], trimethylamine-N-oxide (TMAO) [protein stabilizer], tetrahydrofuran (THF) and 1,4-dioxane (Diox) [cycloethers and frequently used reaction media].

We explored via combined study of fluorescence measurements (steady-state and time-resolved) and computer simulations the chemistry of aqueous environments in presence of these amphiphiles and qualitatively understand the perturbation of the tetrahedral three-dimensional hydrogen bond (H-bond) network of water in these aqueous binary mixtures. Furthermore, in the area of complex sugar solutions, we have studied cryoprotectant mixtures: trehalose [alpha-linked disaccharide] and glycerol [polyalcohol]. Together they act to enhance the preservation times of biological cells and tissues. We have observed that the structure breaking ability of trehalose plays important role in determining the response of the solvent molecules. Different mechanisms have also been found to control the dynamics of the medium at different temperature regimes in this high-viscous system. Contribution of the formation of ion-pairs in the electrolyte solutions of triflate salts was also examined by monitoring solute–solvent interaction and solvents' dynamical response to the excited solute molecules.

List of Publications

1. "*Heterogeneity in (2-butoxyethanol + water) mixtures: Hydrophobicity-induced aggregation or criticality-driven concentration fluctuations?*" by **Sandipa Indra** and Ranjit Biswas, J. Chem. Phys. **142**, 204501 (2015).

2. "*Hydrogen-bond dynamics of water in presence of an amphiphile, tetramethylurea: signature of confinement-induced effects*" by **Sandipa Indra** and Ranjit Biswas, Mol. Sim. **41**, 471 (2015).

3. "*Are N-methyl Groups of Tetramethylurea (TMU) Hydrophobic? A Composition and Temperature Dependent Fluorescence Spectroscopic Investigation of TMU/Water Binary Mixtures*" by **Sandipa Indra** and Ranjit Biswas, J. Chem. Sci. (2015) (under review).

4. "*Structural Anomaly in Cycloether/Water Binary Mixtures: Signatures from Composition Dependent Dynamic Fluorescence Measurements and Computer Simulations*" by **Sandipa Indra**, Biswajit Guchhait and Ranjit Biswas, J. Chem. Phys. (2015) (under review).

5. "*Is Dynamic Heterogeneity of Water in Presence of a Protein Denaturing Agent Different from that in Presence of a Protein Stabilizer? A Molecular Dynamics Simulation Study*" by **Sandipa Indra** and Ranjit Biswas, Chem. Phys. Lett. (2015) (submitted).

6. "*Effects of Trehalose on the Dynamics of Glycerol: A Combined Fluorescence and Computer Simulation Study*" by **Sandipa Indra** and Ranjit Biswas (Manuscript in preparation).

7. "*Fluorescence Spectroscopic Study of Electrolyte Solutions of Triflate Salts in Polar Aprotic Solvents*" by **Sandipa Indra** and Ranjit Biswas (Manuscript in preparation).

Contents

Chapter 4: Structural Anomaly in Cycloether/Water Binary Mixtures: Signatures from Composition Dependent Dynamic Fluorescence Measurements and Computer Simulations……………………………….....70

Chapter 6: Hydrogen-bond Dynamics of Water in Presence of An Amphiphile, Tetramethylurea: Signature of Confinement-induced Effects..155

Chapter 7: Is Dynamic Heterogeneity of Water in Presence of A Protein Denaturing Agent Different from that in Presence of A Protein Stabilizer? A Molecular Dynamics Simulation Study……………………………………….189

Chapter 8: Fluorescence Spectroscopic Study of Electrolyte Solutions of Triflate Salts in Polar Aprotic Solvents………………………………….227

Chapter 1

Introduction

Understanding interaction and dynamics in condensed phases is of fundamental importance because industrially important reactions are often carried out in solutions or compressed gaseous environments. Some very familiar examples of solvent controlled reactions are proton transfer reaction,[1-7] charge transfer reaction,[8-15] radical recombination reaction,[16-20] isomerisation,[21-25] tautomerization[26-29] and so on. A solvent medium can affect the reaction rate in various ways, such as, modification of the activation energy, frictional and collisional effects etc. For an instance, a change of only 2 kcal of activation energy can modify the room temperature rate by a factor of 30.[30] The role of reaction medium can further be enhanced by addition of the suitable cosolvent. When there exists a prominent polarity difference between reactant and activated state, addition of solvent mixtures of different polarity rather than single solvent can substantially modify the reaction rate by preferential solvation. Moreover, polarity of the reaction medium can also be tuned simply by varying the concentration of the cosolvent. Therefore, binary mixture is a promising reaction medium for tailoring a particular reaction. Since reactions are substantially modified by environmental polarity and dynamics, tailoring reactions for obtaining desired products requires a thorough knowledge of the reactant–medium interaction and environment dynamics.

Apart from the wide-spread use of binary mixtures from biological arena, such as, protein folding, formation lipid bilayers[31-38] to pharmaceuticals, such as, activity of the drugs,[39-41] recent studies have explored newer applications of the binary mixtures in the material science and device development. Solvent mixtures have been found to improve the performances of the device by modifying the solar cell morphology.[42-47] Among all the solvents available, the "universal solvent" water is the mostly used one because of its unique properties[48] (often termed as anomalous properties). Despite being apparently simple but essential in almost everywhere of

our life, understanding of its anomalous behaviour has turned out to be extremely difficult even after carrying out extensive research on this molecule.[49-65]

Aqueous binary mixtures of amphiphiles are of great importance in chemistry and biology. Amphiphiles are those which possesses a combination of hydrophilic (water-attracting) and hydrophobic (water-repelling) moieties. This property of amphiphiles makes the aqueous solution accessible for interaction to a large number of molecules with nonpolar groups and biopolymers. Examples of amphiphilic molecules are methanol (MeOH), ethanol (EtOH), tertiary butanol (TBA), dimethyl sulphoxide (DMSO), tetramethylurea (TMU), 1,4-dioxane (Diox) etc. On addition of amphiphiles aqueous solution exhibits anomalous change in several thermodynamic properties due to inhomogeneous mixing at the molecular level.[66-86] In aqueous solutions of amphiphiles, there is interplay of enthalpy (energy) and entropy in the free energy expression to determine the equilibrium configuration. Water forms extensive hydrogen bonded network which is highly directional. When amphiphiles are added into water, some hydrogen bonds (H-bonds) get disrupted which is energetically unfavourable. But the gain of configurational entropy compensates the energy cost. As a result, these molecules become soluble in water. Again, amphiphiles involve in H-bond interaction with water via the hydrophilic sites, which is energetically favourable, thus helps to retain its solubility into water. Sometimes, they form aggregates in water via hydrophobic hydration. By this way, they create heterogeneous surface in macroscopically homogeneous environment. This surface may catalyze a host of reactions. Formation of aggregates often leads to the macroscopic phase segregation in the aqueous binary mixtures.[75,76,87] However, no study has been performed yet regarding how and to what extent solution micro-heterogeneity have affected simple events including a chemical reaction. All the fascinating properties of the aqueous binary mixtures highly motivated us for a detailed study in this exciting area of research.

We have extended our research to aqueous and non-aqueous electrolyte solutions and biologically important cryoprotectant mixtures. Depending upon the nature, cryoprotectants[88-90]

prevent cell damage during dehydration and ice formation at extremely low temperature. Glycerol, DMSO, polyethyleneglycol (PEG), trehalose, dextrose are among several compounds that can act as cryopreservatives. Researchers have found that mixtures of cryoprotectants increases the cryopreservative efficiency.[89,91] However, the existing limited study in this area has not been able to shed light on the chemistry of this unique medium in terms of interactions and dynamics. We took this opportunity to explore the structural and dynamical aspects of a representative bioprotectant mixture with a hope to extend the study in future for other such systems. Both experiments and simulations have been performed to build a molecular level understanding of the observed phenomena.

Experimental work has been carried out by performing mainly the steady state and time-resolved fluorescence measurements.[92] UV-VIS absorption measurements have also been carried out wherever necessary. Fluorescence Spectroscopy provides a unique opportunity to acquire knowledge of the environment surrounding a photo-excited fluorescent probe. Note steady-state measurements provide information about the average environment surrounding a dissolved probe solute whereas time-resolved measurements monitor the evolution of this environment by recording individual frames at various time slices. Through time-resolved measurements, two different phenomena have been examined: (i) solvation dynamics which is the time-dependent response of the solvent molecules (solvent reorganization) in response to an instantaneous change of solute's charge distribution through laser excitation, and (ii) rotational anisotropy, which determines the extent a fluorophore rotates during the excited-state lifetime. Therefore, the main focus of this Thesis has been to probe the structure and dynamics of a variety of a system via monitoring the solute-centred non-reactive dynamics where spectral signatures carried the required medium information. For example, average solution structural aspect is reflected in the energy position of the recorded fluorescence/absorption spectrum of a dissolved solute whereas the measured dynamic anisotropy profile of the same solute bears the signature of the medium frictional response. Therefore, various solution aspects, such as, association, micro-heterogeneity, anomalous mole fraction dependence etc. have been extensively studied via the spectroscopic measurements and complemented with necessary simulation studies.[93,94] Needless

to mention that computer simulations provide a microscopic view of the environment surrounding a molecule undergoing reactive or non-reactive dynamics. Also, simulated solute and solvent relaxation dynamics, when compared to experiments, provide molecular level understanding of the frictional resistance (and its nature) experienced by the solute in a given complex medium.

This Thesis consists of 9 chapters with the first chapter being the Introduction. In chapter 2, micro-heterogeneity in aqueous solutions of 2-butoxyethanol (BE), a system with closed loop miscibility gap, has been explored via absorption and time-resolved fluorescence measurements of a dissolved dipolar solute, coumarin 153 (C153), in the water-rich region at various BE mole fractions $(0 \leq X_{BE} \leq 0.25)$ in the temperature range, $278 \leq T/K \leq 320$. Evidences for both alcohol-induced H-bond strengthening and subsequent structural transition of H-bond network have been observed. Analyses of steady-state and time-resolved spectroscopic data for these aqueous mixtures and comparisons with the results for aqueous solutions of ethanol and tertiary butanol[82] indicate that alcohol aggregation in BE/water mixtures is driven by hydrophobic interaction with no or insignificant role for criticality-driven concentration fluctuations preceding phase separation. Excitation energy dependence of fluorescence emission of C153 confirms formation of aggregated structures at very low BE mole fractions. No asymptotic critical power law dependence for relaxation rates of the type, $k \propto \left(|T - T_C|/T_C\right)^{\gamma}$, with γ denoting universal critical constant, has been observed for both solute's rotational relaxation and population relaxation rates in these mixtures upon either approaching to critical concentration or critical temperature. Estimated activation energies for rotational relaxation rate of C153 and solution viscosity have been found to follow each other with no abrupt changes in either of them at any mixture composition. In addition, measured C153 rotation times at various compositions and temperatures reflect near-hydrodynamic viscosity coupling through the dependence, $\langle \tau_r \rangle \propto \left(\eta/T\right)^p$, with $p = 0.8 - 1.0$, suggesting solute's orientational relaxation dynamics being, on an average, temporally homogeneous.

Results from temperature and composition dependent fluorescence experiments using a dipolar probe, C153, in TMU/water binary mixtures are presented in chapter 3. Both steady-state and time-resolved measurements indicate, much like in water/alcohol mixtures,[81,82,95] TMU concentration-induced structural transition of the tetrahedral H-bond network of water. A comparison to the results obtained for aqueous alcohol solutions[82] suggests that the cosolvent concentration at which such transition occurs depends both on the polarity of the cosolvent and the size of the cosolvent molecules. UV-Visible absorption measurements reveal aggregation at lower TMU concentration which shows a temperature maximum. In addition, red edge excitation effects have also been observed at very dilute TMU concentration. All these results suggest hydrophobic interaction-induced aggregation of TMU in aqueous solutions and corroborate well with the existing simulation observation.[96] Results presented in this chapter therefore provide a resolution to the ongoing debate whether the methyl groups of TMU are hydrophobic enough.

In chapter 4, we have presented the results from time-resolved fluorescence measurements and computer simulations on structural and dynamical aspects of aqueous binary mixtures of 1,4-dioxane (Diox) and tetrahydrofuran (THF). These binary mixtures are unique in the sense that although both these cosolvents (Diox and THF) are cyclic compounds, dioxane is a quadrupolar solvent whereas tetrahydrofuran a dipolar one. The principal question that has been investigated is whether these cycloethers can induce stiffening and transition of water H-bond network structure, and if they can, whether such structural modification differentiates the chemical nature (dipolar or quadrupolar) of the cosolvent molecules. Composition dependent measured fluorescence lifetimes and rotation times of a dissolved dipolar solute (coumarin 153, C153) suggest mole fraction induced structural transition for both these aqueous binary mixtures in the $0.1 \le X_{THF/Diox} \le 0.2$ regime with no specific dependence on the chemical nature. Interestingly, absorption spectroscopic measurements reveal stiffening of water H-bond structure in presence of both the cycloethers at a nearly equal mole-fraction, $X_{THF/Diox}$ ~0.05. In addition, measurements near the critical solution temperature or concentration indicates no role for the solution criticality on the anomalous structural changes. Evidences for cycloether aggregation at

very dilute concentrations have also been found. These spectroscopic results are qualitatively similar to those obtained earlier for aqueous alcohol solutions,[81,82,95] and indicate dominant role for hydrophobic interaction. Simulated radial distribution functions (RDFs) reflect abrupt changes in respective peak heights at those mixture compositions around which fluorescence measurements revealed structural transition. Simulated water coordination numbers (for a dissolved C153) and number of H-bonds also exhibit minima around these cosolvent concentrations. These simulations therefore provide molecular-level insight to the anomalous solution structure revealed by collective spectroscopic measurements.

The strong preservative efficiency of trehalose[97-99] to proteins, antibodies, tissues, drugs and foods among all other sugar formulations generates immense interest to investigate the nature of interaction of trehalose with other molecules having biological activity. It is proven that protein stability is enhanced by making the preservative formulation a stronger glass-forming liquid. Addition of 20 wt % trehalose into glycerol increases the glass transition temperature of about 13K.[91] In chapter 5, we have employed both fluorescence spectroscopic measurements and molecular dynamics simulations to investigate the influence of trehalose on the structure and dynamics of glycerol. Steady-state fluorescence study reveals red-shift in emission with temperature suggesting emission from solutes with un-relaxed solvent environments. Dynamical response of solvent molecules suggested that the two different dynamical modes are operative in governing the solvation dynamics. At higher temperature the diffusive motion of the solvent governs the dynamics and the solvation dynamics becomes faster with temperature, whereas at lower temperature the diffusive part vanishes allowing the collective solvent modes to dictate the solvation rate. Mean squared displacements of glycerol calculated from simulation trajectories in this medium supported the above fact. Evidence of highly heterogeneous environment has been obtained at lower temperatures. The extent of heterogeneity is reduced at higher temperature but does not vanish completely. Rotational dynamics of the probe C153 follows the slip hydrodynamic prediction although the medium is highly viscous. One should investigate here whether this validity of the slip prediction is merely a coincidence because of rotational jump of the solute induced by the large medium viscosity.

Effects of amphiphile TMU on the hydrogen bond dynamics of water has been investigated varying the concentration of the amphiphile in chapter 6. Various experimental and simulation studies have suggested that the presence of amphiphilic molecules in aqueous solutions substantially perturbs the tetrahedral H-bond network of neat liquid water. Such structural perturbation is expected to impact H-bond lifetime of liquid water. Molecular dynamics simulations of (water + TMU) binary mixtures at various compositions have been performed in order to investigate the microscopic mechanism through which the amphiphiles influence the H-bond dynamics of liquid water at room temperature. Present simulations indicate lengthening of both water–water H-bond lifetime and H-bond structural relaxation time upon addition of TMU in aqueous solution. At the highest TMU mole fraction studied, H-bond lifetime and structural relaxation time are, respectively, ~4 and ~8 times longer than those in neat water. This is comparable with the slowing down of H-bond dynamics for water molecules confined in cyclodextrin cavities.[100] Simulated relaxation profiles are multi-exponential in character at all mixture compositions, and simulated radial distribution functions suggest enhanced water–water and water–TMU interactions upon addition of TMU. No evidence for complete encapsulation of TMU by water H-bond network has been found.

In chapter 7, the dynamic heterogeneity (DH) of aqueous solutions of trimethylamine-N-oxide (TMAO) and tetramethylurea (TMU) at several solute concentrations has been investigated via molecular dynamics simulations. TMAO and TMU are amphiphiles of comparable sizes but TMAO possesses zwitterionic structure and is a protein stabilizer whereas TMU is a regular molecule and a strong protein denaturant. The impact of the above contrasting amphiphilic properties on DH of water in aqueous solutions of these solutes has been the theme of the work presented in this chapter. Results suggest, respectively, weak and strong dependence of DH on solute's identity at low and high solute concentration regimes, and no dramatic slow-down of interfacial diffusive dynamics. Solvation structure shows stronger interaction of water and hydrophilic oxygen of TMAO compared to TMU. Consequently, larger slowing down of H-bond fluctuation dynamics has been found in TMAO solutions.

Modification of solution properties upon addition of sodium triflate $(NaCF_3SO_3)$ into polar aprotic solvents such as N,N-dimethylformamide (DMF), acetonitrile (AcCN) has been monitored by fluorescence spectroscopic study using fluorescent probe coumarin 153 (C153) in chapter 8. Steady-state absorption and emission spectral behaviour showed that DMF complexes with Na^+ ions resulting weak ion–solute(C153) interaction whereas in AcCN larger amount of such interaction exists. Due to strong interaction with DMF, $NaCF_3SO_3$ does not form ion-pairs efficiently in this electrolyte solution. For this behaviour of DMF, replacement of monovalent $NaCF_3SO_3$ by bivalent magnesium triflate $[Mg(CF_3SO_3)_2]$ does not bring any significant change in polarity of the surrounding environment of photo-excited probe C153. Solvation dynamics study of concentrated DMF solution of $NaCF_3SO_3$ indicated the fast solvent mode mainly governs the dynamics. Exponential rotational anisotropy decay of C153 was observed for all the compositions in this electrolyte solution.

Chapter 9 then ends the Thesis with a brief concluding remarks and a list of a few relevant and motivating problems that can be studied in future. These representative problems though do not reflect the vastness of the related area amply reflect the direction the basic physical chemistry of multi-component mixtures is heading to.

References

1.   K. Ando, A. Staib and J. T. Hynes, in *Femtochemistry II*, edited by M. Chergui (World Scientific, Singapore, 1996), pp. 534.

2.   W. H. Thompson and J. T. Hynes, J. Phys. Chem. A **105**, 2582 (2001).

3.   P. M. Kiefer and J. T. Hynes, J. Phys. Chem. A **106**, 1834 (2002).

4.   E. Pines and G. R. Fleming, J. Phys. Chem. **95**, 10448 (1991).

5.   E. Pines, B.-Z. Magnes, M. J. Lang and G. R. Fleming, Chem. Phys. Lett. **281**, 413 (1997).

6.   A. Warshel, J. Chem. Phys. **86**, 2218 (1982).

7.   D. J. Cram, B. Rickborn, C. A. Kingsbury and P. Haberfield, J. Am. Chem. Soc. **83**, 3678 (1961).

8.   M. Maroncelli, J. Macinnis and G. R. Fleming, Science **243**, 1674 (1989).

9.   Y. Wang and K. B. Eisenthal, J. Chem. Phys. **77**, 6076 (1982).

10.   B. Bagchi, Ann. Rev. Phys. Chem. **40**, 115 (1989).

11.   K. Dahl, R. Biswas, N. Ito and M. Maroncelli, J. Phys. Chem. B **109**, 1563 (2005).

12.   T. Pradhan and R. Biswas, J. Phys. Chem. A **111**, 11514 (2007).

13.   T. Pradhan and R. Biswas, J. Phys. Chem. A **111**, 11524 (2007).

14.   A. Das and R. Biswas, J. Phys. Chem. B **119**, 10102 (2015).

15.   R. Biswas, N. Rohman, T. Pradhan and R. Buchner, J. Phys. Chem. B **112**, 9379 (2008).

16.   A. G. Zawadzki and J. T. Hynes, J. Phys. Chem. **93**, 7031 (1989).

17.   Z. Schulten and K. Schulten, J. Chem. Phys. **66**, 4616 (1977).

18.   R. M. Noyes, Prog. React. Kinet. **1**, 129 (1961).

19.   J. P. Lorand, Prog. Inorg. Chem. **17**, 207 (1972).

20.   T. J. Chuang, G. W. Hoffman and K. B. EisenthaI, Chem. Phys. Lett. **25**, 201 (1974).

21.   P. F. Barbara and W. Jarzeba, Acc. Chem. Res. **21**, 195 (1988).

22.   A. A. Heikal, S. H. Chong, J. S. Baskin and A. H. Zewail, Chem. Phys. Lett. **242**, 380 (1995).

23.   J. M. Jean, D. C. Todd, S. Rosenthal, A. J. Ruggiero and G. R. Fleming, in *Ultrafast Phenomena VII*, edited by E. P. (Springer, 1990), pp. 441.

24.   R. Biswas, K. Dahl and M. Maroncelli, J. Phys. Chem. B **106**, 11593 (2002).

25.   Y. Onganer, M. Yin, D. R. Bessire and E. L. Quitevis, J. Phys. Chem. **97**, 2344 (1993).

26.   D. McMorrow and T. J. Aartsma, Chem. Phys. Lett. **125**, 581 (1986).

27.   T. Ishida, F. Hirata and S. Kato, J. Chem. Phys. **110**, 3938 (1999).

28.   J. Powling and H. J. Bernstein, J. Am. Chem. Soc. **73**, 4353 (1951).

29.   A. Douhal, S. K. Kim and A. H. Zewail, Nature **378**, 260 (1995).

30.   J. T. Hynes, Ann. Rev. Phys. Chem. **36**, 573 (1985).

31.   D. R. Canchi and A. E. García, Ann. Rev. Phys. Chem. **64**, 273 (2013).

32.   S. Shimizu and D. J. Smith, J. Chem. Phys. **121**, 1148 (2004).

33.   S. N. Timasheff, Ann. Rev. Biophys. Biomol. Struct. **22**, 67 (1993).

34.   K. W. Plaxco and D. Baker, Proc. Natl. Acad. Sci. U.S.A. **95**, 13591 (1998).

35.   D. W. Bolen and G. D. Rose, Ann. Rev. Biochem. **77**, 339 (2008).

36.   S. N. Timasheff, Adv. Protein Chem. **51**, 355 (1998).

37.   M. T. Record, Jr., W. T. Zhang and C. F. Anderson, Adv. Prot. Chem. **51**, 281 (1998).

38.   J. A. Schellman, Biophys. J. **85**, 108 (2003).

39.   M. A. A. Fakhree, D. R. Delgado, F. Martínez and A. Jouyban, AAPS PharmSciTech. **11**, 1726 (2010).

40.   A. Jouyban, J. Pharm. Pharm. Sci. **11**, 32 (2008).

41.   P. Bustamante, S. Romero, A. Pena, B. Escalera and A. Reillo, J. Pharm. Sci. **87**, 1590 (1998).

42.   F. Zhang, K. G. Jespersen, C. Bjorstrom, M. Svensson, M. R. Andersson, V. Sundstrom, K. Magnusson, E. Moons, A. Yartsev and O. Inganas, Adv. Funct. Mater. **16**, 667 (2006).

43.   J. Peet, C. Soci, R. C. Coffin, T. Q. Nguyen, A. Mikhailovsky, D. Moses and G. C. Bazan, Appl. Phys. Lett. **89**, 252105 (2006).

44.   J. Peet, J. Y. Kim, N. E. Coates, W. L. Ma, D. Moses, A. J. Heeger and G. C. Bazan, Nat. Mater. **6**, 497 (2007).

45.   Y. Yao, J. Hou, Z. Xu, G. Li and Y. Yang, Adv. Funct. Mater. **18**, 1783 (2008).

46.   C. N. Hoth, S. A. Choulis, P. Schilinsky and C. Brabec, J. Adv. Mater. (Weinheim, Ger.) **19**, 3973 (2007).

47.   F. Chen, H. Tseng and C. Ko, Appl. Phys. Lett. **92**, 103316 (2008).

48.   B. Bagchi, *Water in Biological and Chemical Processes*. (Cambridge University Press, London, 2013).

49.   F. H. Stillinger, Adv. Chem. Phys. **31**, 1 (1975).

50.   A. Rahman and F. H. Stillinger, J. Am. Chem. Soc. **95**, 7943 (1973).

51.   C. A. Angell, J. Shuppert and J. C. Tucker, J. Phys. Chem. **77**, 3092 (1973).

52.   H. J. C. Berendsen, J. R. Grigera and T. P. Straatsma, J. Phys. Chem. **91**, 6269 (1987).

53.   R. Jimenez, G. R. Fleming, P. V. Kumar and M. Maroncelli, Nature **369**, 471 (1994).

54.   A. Luzar and D. Chandler, Nature **379**, 55 (1996).

55.   J. R. Errington and P. G. Debenedetti, Nature **409**, 318 (2001).

56.   P. G. Debenedetti and H. E. Stanley, Phys. Today **56**, 40 (2003).

57.   M. Matsumoto, S. Saito and I. Ohmine, Nature **416**, 409 (2002).

58.   D. Laage and J. T. Hynes, Science **311**, 832 (2006).

59.   D. E. Moilanen, E. E. Fenn, Y. Lin, J. L. Skinner, B. Bagchi and M. D. Fayer, Proc. Natl. Acad. Sci. U.S.A. **105**, 5295 (2008).

60.   A. Chandra, Phys. Rev. Lett. **85**, 768 (2000).

61.   S. Balasubramanian, S. Pal and B. Bagchi, Phys. Rev. Lett. **89**, 115501 (2002).

62.   P. L. Geissler, C. Dellago, D. Chandler, J. Hutter and M. Parrinello, Science **291**, 2121 (2001).

63.   S. K. Pal, J. Peon, B. Bagchi and A. H. Zewail, J. Phys. Chem. B **106**, 12376 (2002).

64.   N. Nandi, K. Bhattacharyya and B. Bagchi, Chem. rev. **100**, 2013 (2002).

65.   S. Das, A. Datta and K. Bhattacharyya, J. Phys. Chem. A **101**, 3299 (1997).

66.   S. Dixit, J. Crain, W. C. K. Poon, J. L. Finney and A. K. Soper, Nature **416**, 829 (2002).

67.   A. K. Soper and F. J. L., Phys. Rev. Lett. **71**, 4346 (1993).

68.   M. Brai and U. Kaatze, J. Phys. Chem. **90**, 8946 (1992).

69.   G. B. Dutt, S. Doraiswamy and N. Periasamy, J. Chem. Phys. **94**, 5360 (1991).

70.   K. Yoshida and T. Yamaguchi, Z. Naturforsch. **56A**, 529 (2001).

71.   T. Sato and R. Buchner, J. Chem. Phys. **119**, 10789 (2003).

72.   P. G. Kusalik, A. P. Lyubertsev, D. L. Bergman and A. Laaksonen, J. Phys. Chem. B **104**, 9533 (2000).

73.   K. Yoshida, T. Yamaguchi, A. Kovalenko and F. Hirata, J. Phys. Chem. B **106**, 5042 (2002).

74.   D. T. Bowron and J. L. Finney, J. Phys. Chem. B **111**, 9838 (2007).

75.   G. W. Euliss and C. M. Sorensen, J. Chem. Phys. **80**, 4767 (1984).

76.   T. M. Bender and R. Pecora, J. Phys. Chem. **92**, 1675 (1988).

77.   K. Yoshikata, J. Phys. Chem. **100**, 5172 (1996).

78.   Y. L. A. Rezus and H. J. Bakker, J. Phys. Chem. A **112**, 2355 (2008).

79.   D. Laage, G. Stirnemann and J. T. Hynes, J. Phys. Chem. B **113**, 2428 (2009).

80.   G. Stirnemann, F. Sterpone and D. Laage, J. Phys. Chem. B **115**, 3254 (2011).

81.   T. Pradhan, P. Ghoshal and R. Biswas, J. Phys. Chem. A **112**, 915 (2008).

82.   T. Pradhan, P. Ghoshal and R. Biswas, J. Chem. Sci. **120**, 275 (2008).

83.   H. A. R. Gazi and R. Biswas, J. Phys. Chem. A **115**, 2447 (2011).

84.   K. Tielrooij, J. Hunger, R. Buchner, M. Bonn and H. J. Bakker, J. Am. Chem. Soc. **132**, 15671 (2010).

85.   S. Roy, S. Banerjee, N. Biyani, B. Jana and B. Bagchi, J. Phys. Chem. B **115**, 685 (2011).

86.   S. Banerjee and B. Bagchi, J. Chem. Phys. **139**, 164301 (2013).

87.   C. M. Sorensen, J. Phys. Chem. **92**, 2367 (1988).

88.   F. d. L. Janz, A. d. A. Debes, R. d. C. Cavaglieri, S. A. Duarte, C. M. Romão, A. F. Morón, M. Zugaib and S. P. Bydlowski, J. Biomed. Biotech. (2012).

89.   C. J. Hunt, Transfus Med Hemother **38**, 107 (2011).

90.   D. Averett, M. T. Cicerone, J. F. Douglas and J. J. de Pablo, Soft Matter **8**, 4936 (2012).

91.   R. Busselez, R. Lefort, M. Guendouz, B. Frick, O. Merdrignac-Conanec and D. Morineau, J. Chem. Phys. **130**, 214502 (2009).

92.   J. R. Lakowicz, *Principles of Fluorescence Spectroscopy*. (Kluwer Academic, New York, 1999).

93.   M. P. Allen and D. J. Tildesley, *Computer simulations of liquids*. (Oxford University Press, New York, 1987).

94.   D. Frenkel and B. Smit, *Understanding Molecular Simulation: From Algorithm to Applications*. (Academic Press, San Diego, 1996).

95.   S. Indra and R. Biswas, J. Chem. Phys. **142**, 204501 (2015).

96.   S. Indra and R. Biswas, Mol. Sim. **41**, 471 (2015).

97.   F. Sussich, R. Urbani, F. Princivalle and A. Cesaro, J. Am. Chem. Soc. **120**, 7893 (1998).

98.   D. P. Miller and J. J. de Pablo, J. Phys. Chem. B **104**, 8876 (2000).

99.   J. L. Green and C. A. Angell, J. Phys. Chem. B **93**, 2880 (1989).

100.   M. Jana and S. Bandyapadhyay, J. Phys. Chem. B **115**, 6347 (2011).

Chapter 2

Heterogeneity in (2-Butoxyethanol + Water) Mixtures: Hydrophobicity-induced Aggregation or Criticality-driven Concentration Fluctuations?

2.1 Introduction

Presence of closed loop miscibility gap for aqueous mixtures of 2-butoxyethanol (BE) with the lower critical solution temperature (LCST)[1,2] $T_c(K) \sim 322.5$ and concentration $X_c^{BE}\left(\text{mole fraction}\right) \sim 0.06$ offers a unique opportunity to study the relative roles played by hydrophobicity-induced alcohol aggregation and critical concentration fluctuation in a near room-temperature critical binary mixture. BE, being an amphiphile, can participate in hydrogen bonding (H-bonding) through its hydroxyl (–OH) group and ether-oxygen with surrounding water molecules in aqueous solution while simultaneously undergoing intra-species association through alkyl group interaction. This can lead to aggregation extended over length-scales larger than several molecular diameters, rendering micro-heterogeneity in solution structure. Indeed, formation of micelle-like structures in aqueous mixtures of BE in the water-rich region has been evidenced in small angle neutron scattering (SANS) studies. Accordingly, aqueous mixtures of BE have been termed as disordered systems with amphiphilicity factor $f_a > 1$ placing these room-temperature critical binary mixtures on the positive side of the Lifshitz line.[3,4] What drives the formation of micellar structure – hydrophobic hydration or critical concentration fluctuations – in these aqueous solutions has been a recurrent theme in many early investigations that involve neutron[2-6] and dynamic light scattering (DLS)[1,7-10] experiments; diffusion[11, 12] and viscosity[13] measurements; dielectric,[14] ultrasonic,[15] and thermodynamic studies;[16-20] computer simulations;[21] and other studies.[22-25]

Although these studies attempted to characterize the aggregation phenomenon in water-rich mixtures via relating correlation lengths to concentration fluctuations, length-scales estimated

by different measurements differ widely. For example, SANS[2] and neutron spin echo (NSE)[5] measurements in the temperature range $278 \leq T/K \leq 316$ reported correlation lengths in ~10-100 Å range. In contrast, quasi-elastic light scattering (QELS) measurements below 293 K[2] and ultrasonic relaxation studies at ~298 K[15] suggested presence of much larger aggregated structures of radius ~1000 Å. Subsequent DLS measurements in the temperature range $283 \leq T/K \leq 313$ indicated that contamination in BE samples might have led to formation of such large diffusers, and for contamination-free samples, the estimated correlation lengths were in general agreement with those from neutron[2-6] and light scattering measurements.[23] The scenario becomes even more complex with SANS measurements[5,6] reporting rapid growth of the correlation length with the solution temperature approaching T_c. In addition, scaling laws related to critical phenomena appeared to explain the considerable slowing down of diffusivities in these mixtures as critical concentration $\left(X_c^{BE}\right)$ and temperature $\left(T_c\right)$ were approached.[1,22] Interestingly, aggregation was found to be most pronounced at a BE concentration far from X_c^{BE}, and the typical critical divergence was found to be absent.[2] These contradictory results motivate the present study where we investigate whether (i) longer-lived larger clusters/aggregates indeed form in BE/water mixtures, (ii) critical fluctuations preceding phase transition govern the formation of aggregates, (iii) relaxation dynamics shows any signature of critical slowing down, and (iv) spatial heterogeneity imparts any bearing on diffusion-viscosity coupling in these mixtures.

In order to address the above issues, we have carried out steady state and time-resolved fluorescence spectroscopic measurements of a dissolved dye, coumarin 153 (C153), at different BE concentrations and temperatures. Scheme 2.1 provides chemical structures of BE and C153. Since solute-solvent interactions determine the spectral energy and width, steady-state absorption and fluorescence measurements of a dissolved probe can reveal the alcohol-induced modifications in the structure of these aqueous solutions. Time-resolved fluorescence measurements, on the other hand, track the relaxation dynamics of the medium and provide critical information regarding dynamic solute-environment coupling. These two measurements (steady-state and time-resolved), therefore, provide complementary information and suit well for exploring mixture composition dependent changes in structure

and dynamics of these aqueous alcohol solutions. Formation of stable aggregates at various BE mole fractions has been examined via performing excitation energy dependence of fluorescence emission of C153. Mole fraction and temperature dependent steady state spectroscopic measurements provide a clue regarding the relative importance for critical fluctuations in promoting the aggregate formation while the corresponding lifetime and dynamic anisotropy measurements investigate the effects of critical slowing down, if any, on the relaxation dynamics in these mixtures. A master curve showing the dependence of average solute rotation time measured at various mixture compositions and temperatures on temperature-reduced viscosity (η/T) then explores the coupling between viscosity and solute rotation. This assumes importance if one considers that scattering data have been routinely analyzed in terms of Brownian diffusion of non-interacting spherical particles dispersed at a low concentration in a liquid medium.[2,5-7,10]

[A]   [B]
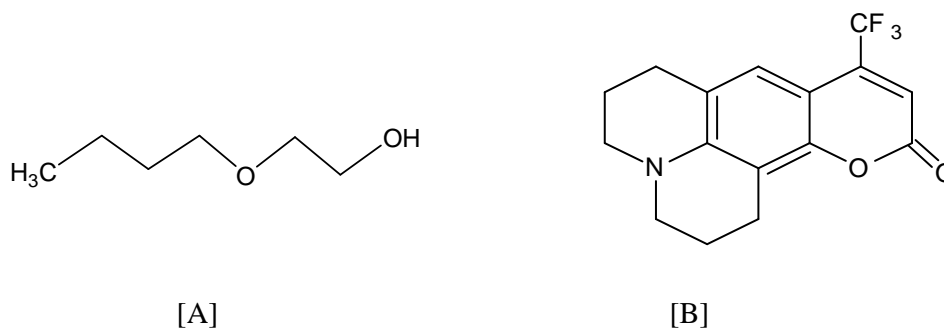
Scheme 2.1: Structure of 2-butoxyethanol (BE) [A] and coumarin 153 (C153) [B].

2.2 Experimental Details

2.2.1 Sample Preparation

Laser grade C153 (Exciton) and BE (Alfa-Aesar) were used as received. Deionized (Millipore) water was used for preparing the aqueous BE solutions at various mole fractions. Measured amounts of BE were dissolved in separate volumetric flasks containing required amounts of water, shaken gently for a few minutes. For measurements at each composition,

~3–4 ml of these stock solutions was then poured, one-by-one, into an optically clean quartz cuvette (1 cm path length) impregnated with C153 (using heptane as a career solvent followed by evaporation via gently blowing mildly hot dry air) and the solution was stirred for some time to ensure complete dissolution. Note that the concentration of C153 was maintained at $\leq 10^{-5}$ M in all BE mole fractions studied here. To ensure thermal equilibration before measurements, sufficient time was allowed after loading the sample containing cuvette in the preheated sample chamber at each desired temperature (with uncertainty $\pm 0.5\,K$).

Densities and viscosity coefficients of these samples were measured as before[26-28] by using, respectively, automated temperature controlled density-cum-sound analyzer (Anton Paar, DSA5000), micro viscometer (AMVn, Anton Paar).

2.2.2 Data Collection and Analysis for Steady-state Fluorescence Spectroscopy

Absorption spectra were recorded using UV-visible spectrophotometer (Model UV-2450, Shimadzu) for different BE-water solutions. The emission spectra were recorded (SPEX Fluoromax-3, Jobin-Yvon, Horiba) after adjusting the absorbance of the solutions ~0.1 with the excitation wavelength fixed at 409 nm. Both absorption and emission spectra of C153 in different BE mole fractions were also recorded at controlled temperature. A temperature equilibration time of ~15 minutes was given after loading the sample cuvette into the temperature controlled sample chamber of both the spectrometers before data collection.

Solvent blanks were subtracted every time from both absorption and emission spectra prior to analysis and converted to frequency representation after properly weighting the intensity with λ^2. Absorption and emission peak frequencies were calculated by simply averaging the numbers obtained from fitting the upper half of the spectrum with an inverted parabola, first moment and the arithmetic mean of the frequencies at half intensities on both blue and red ends of each of the spectrum.[29-34] The consistency of the above method was further checked

by fitting the absorption and emission spectra to a log-normal function by broadening and shifting the absorption and emission spectrum of C153 in a nonpolar solvent.[31,33] This was necessary particularly when the spectra were noisy. The resolution of the instrument for peak frequency determination was ~250 cm^{-1}.

2.2.3 Data Collection and Analysis for Time-resolved Fluorescence Anisotropy

As described earlier,[35-39] fluorescence emission intensity decays were collected via time-correlated single-photon counting (TCSPC) technique based on a laser system (Lifespec-ps, Edinburgh, U.K.). A light-emitting diode (LED) producing 409 nm light was used as the excitation source. Full-width-at-half-maxima (FWHM) of the instrument response function (IRF) was ~90 ps. The fluorescence emission decay was collected using an emission band pass of 0.5 nm at the wave-length of peak maximum of steady-state fluorescence emission to minimize the effect of fast decay or rise due to solvent reorganization.[40-45] The sample cuvette was placed into a temperature controlled chamber. Emission decay was collected at three different positions of emission polarizer, magic angle (54.7^0), parallel $[I_\parallel(t)]$ and perpendicular $[I_\perp(t)]$ with respect to the polarization of the excitation light.

At first the magic angle emission decay was de-convoluted from IRF and fitted to appropriate exponential function using an iterative re-convolution algorithm.[41,42] Bi-exponential function was fitted well to the emission decay. Subsequently, the same procedure was followed for fitting parallel and perpendicular emission decay. The time-resolved fluorescence anisotropy $[r(t)]$ was constructed from the values of $[I_\parallel(t)]$ and $[I_\perp(t)]$ by the following formula,[40]

$$r(t) = \frac{I_\parallel(t) - GI_\perp(t)}{I_\parallel(t) + 2GI_\perp(t)}, \qquad (2.1)$$

where the geometric factor G accounts for the differential sensitivity to the two polarizations which was obtained by tail matching the intensity decays $I_\parallel(t)$ and $I_\perp(t)$. Constructed $r(t)$

decays were then fit to multi-exponential functions of time after de-convoluting from the IRF using an iterative reconvolution fitting program,[40]

$$r(t) = r(0)\sum_i a_i \exp[-t/\tau_i],\qquad (2.2)$$

where $a_1 + a_2 = 1$ and $r(0)$ is the initial anisotropy in the absence of any orientational diffusion of the excited solute. a_i and τ_i represent the decay amplitudes and the associated time constant. We have used $r(0) = 0.376$.[40] While single-exponentials were found to adequately describe the $r(t)$ decays at very low BE concentrations, bi-exponentials were required at higher alcohol concentrations. Stretched exponentials were found to provide worse description than bi-exponentials. Subsequently, average solute rotation times $(\langle \tau_r \rangle)$ were obtained as follows:

$$\langle \tau_r \rangle = \int_0^\infty dt \left[\frac{r(t)}{r(0)} \right] = \int_0^\infty dt \sum_i a_i \exp[-t/\tau_i] = \sum_i a_i \tau_i . \qquad (2.3)$$

2.3 Results and Discussion

2.3.1 Steady-state Studies: Spectral Signatures for Association

Steady-state UV-VIS absorption and fluorescence emission spectra of C153 at 298 K in these aqueous mixtures with X_{BE} = 0.005, 0.01, 0.015, 0.02, 0.1, and 0.2 are shown in Figure 2.A.1 (Appendix 2.A).[46] A careful inspection of these spectra reveals that absorption spectrum successively shifts toward lower energy (red-shift) upon addition of BE in the mixture up to $X_{BE} = 0.015$ and then turns around to register blue-shift upon further increasing BE concentration in the aqueous mixture. Interestingly, emission spectrum does not show any such turn around and shifts continuously to higher energy (blue-shift) upon increasing BE concentration. This continuous blue-shift for emission at all BE mole fractions and the same for absorption at $X_{BE} > 0.015$ are only expected if one examines the mixture composition dependence of solution density, static dielectric constant (ε_0),[47,48] and reaction field factor[49,50] provided in Figure 2.A.2 (Appendix 2.A).[46]

Spectral features summarized in Figure 2.1 show the mixture composition dependence of absorption and emission frequencies and widths at T = 298 and 318 K. Clearly, a red-shift of ~400-500 cm^{-1} in the absorption spectrum can be seen at these temperatures when BE concentration is increased to ~0.02 mole fraction which follows approximately an equal amount of blue-shift for increasing the alcohol mole fraction up to 0.2. This red-shift up to $X_{BE} \leq 0.02$ suggests enhancement of solution structure at a very local level and indicates, as in the case for aqueous mixtures of tertiary butanol (TBA),[51-54] alcohol association and strengthening of H-bonding network. Interestingly, anomalous increase in sound velocity[2] and thermodynamic quantities[16,18,30] has been observed around this BE mole fraction $\left(X_{BE} \sim 0.02 \right)$ with photon correlation spectroscopic measurements[15] suggesting most pronounced aggregation (hydrodynamic radius, r_h, of the cluster ~2100 Å)[15] at this mixture composition. The observation here that the absorption red-shift at 318 K, a temperature ~4 K below the T_c, very similar to those at 298 K and 278 K (~400 cm^{-1}, not shown here to avoid clutter) probably indicates an insignificant role for the critical fluctuations in rendering microheterogeneity in BE/water mixtures. Note temperature dependent absorption and fluorescence emission frequencies at a few low BE mole fractions shown in Figure 2.A.3 (Appendix 2.A) do not indicate any abrupt changes as T approaches T_c. The present results therefore support the conjecture[2,21] that formation of large micellar aggregates rather than criticality that governs the solution structure in these aqueous solutions at low alcohol concentrations.
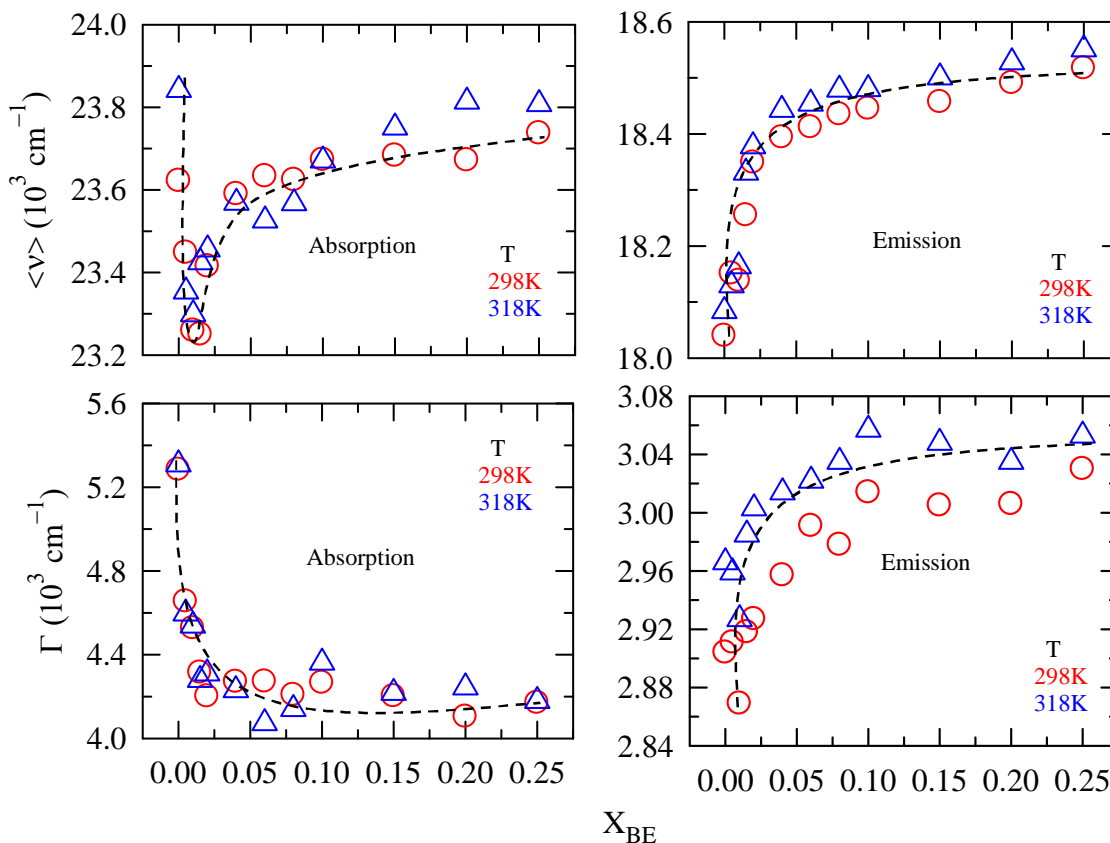
Figure 2.1: Mixture composition dependence of absorption and fluorescence emission spectral characteristics for C153 at ~298 K (red circles) and ~318 K (blue triangles). While spectral frequencies are represented by $\langle v \rangle$, spectral full-widths- at-half maxima are denoted by Γ. X_{BE} represents concentration of BE in mole fraction present in BE/water mixtures. Dashed lines are guides to bare eyes. Uncertainties (largest) associated with $\langle v \rangle$ and Γ are ± 200 cm^{-1} and ± 100 cm^{-1} (based on 3-4 separate measurements at a few representative mixture compositions).

It is interesting to note emission frequencies of C153 in these microheterogeneous solutions (right upper panel of Figure 2.1) do not exhibit any anomalous composition dependence and merely follow the average solution polarity. This suggests that the solvation environment surrounding the excited solute experiences rapid fluctuations during the average lifetime $\left(\left\langle \tau_{life} \right\rangle \right)$ of the solute in its excited state, and as a result, fluorescence emission frequencies report fluctuation-averaged polarity of the local environment. NSE measurements indeed

suggest lifetime of alcohol aggregates in the sub-nanosecond to nanosecond regime,[5] and therefore, information regarding inhomogeneous solvation shells is likely to be lost in a study that uses C153 whose $\langle \tau_{life} \rangle$ ranges, depending upon medium, between a few and several nanoseconds.[55] Another interesting aspect is the initial narrowing and broadening of spectral widths, respectively, for absorption and emission upon addition of BE in the solution at both these representative temperatures (lower panels, Figure 2.1). For single component molecular liquids, polarity-induced absorption red-shift accompanies concomitant spectral broadening and fluorescence emission narrowing.[55] The reverse seen here with C153 for both absorption and fluorescence emission in BE/water mixtures is similar to earlier observation with the same solute in ethanol (EtOH)/water and TBA/water mixtures,[33] indicating complex medium effects on the underlying vibronic structure of the solute in these aqueous solutions.

The microheterogeneity aspect of BE/water mixtures is further investigated via monitoring the excitation wavelength $(\lambda_{exc.})$ dependence of fluorescence emission of C153 at ~298 K. This is because NSE measurements[5] report cluster lifetimes approximately a nanosecond in the limit of very low wavenumber ($q < 0.05$ Å) in solutions with $X_{BE} < 0.1$, and monitoring $\lambda_{exc.}$ dependence may help in revealing the presence of those longer-lived clusters. Figure 2.2 summarizes the results of such a study where $\lambda_{exc.}$ dependence of fluorescence emission frequencies $(\nu_{em.})$ of C153 at a few low BE mole fractions and the corresponding widths are shown. These BE concentrations are chosen because absorption red-shift is observed in this range of X_{BE}, and a fixed excitation at 409 nm did not reveal any anomalous X_{BE} dependence of fluorescence emission (see Figure 2.1, upper-right panel). Interestingly, $\lambda_{exc.}$ dependence of $\nu_{em.}$ is the most pronounced at $X_{BE} = 0.005$ which indicates existence of aggregated structures in these solutions that may have lifetime in nanoseconds. If the total magnitude of $\lambda_{exc.}$-induced emission shift, $\Delta \nu_{em.}(\lambda_{exc.}) = \nu_{em.}(380\,nm) - \nu_{em.}(480\,nm)$, is proportional to the extent of association, then we may infer that the solution at $X_{BE} = 0.005$ is spatially the most heterogeneous $\left(\Delta \nu_{em.} \sim 500\,cm^{-1} \right)$ among the compositions investigated here. Note $\lambda_{exc.}$ dependence of emission width, $\Delta \Gamma_{em.}$, is also the strongest at this BE mole
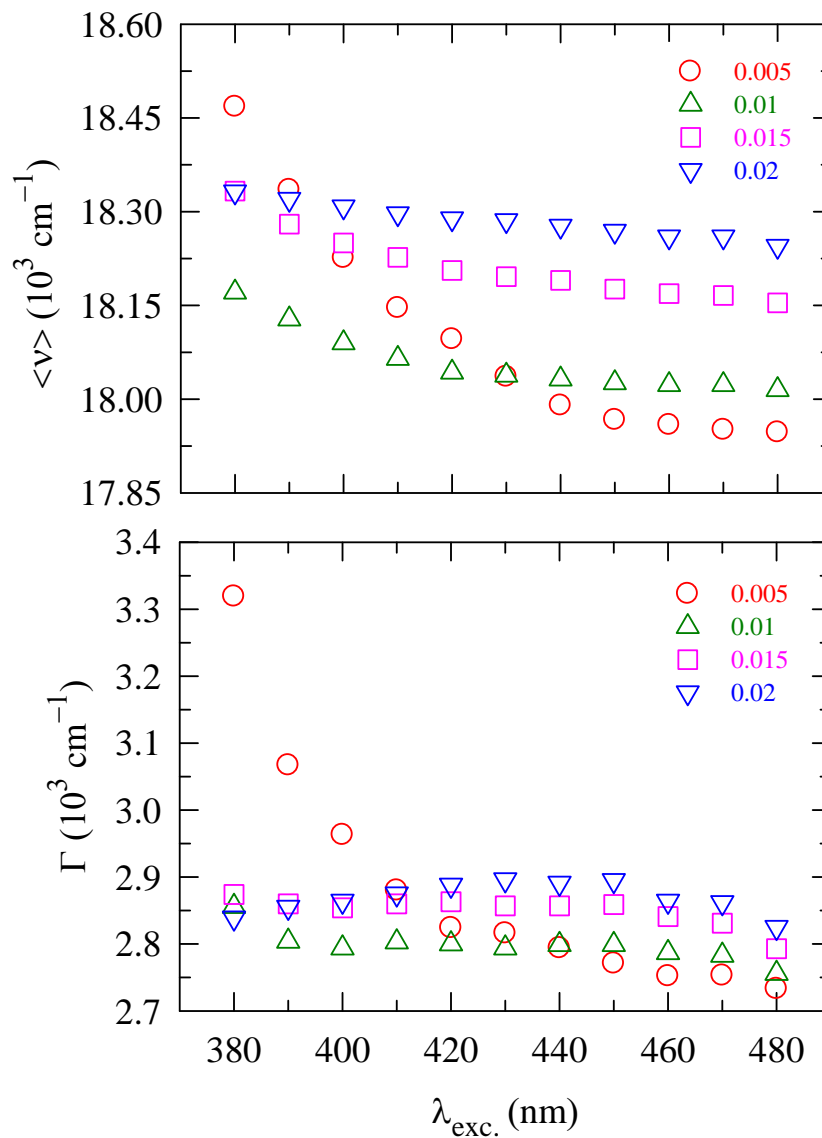
Figure 2.2: Excitation wavelength $\left(\lambda_{exc.}\right)$ dependence of fluorescence emission frequencies $\left(\langle v \rangle\right)$ and widths $\left(\Gamma\right)$ of C153 at four different BE mole fractions and ~298 K. Data representations are colour-coded. Uncertainties in $\langle v \rangle$ and Γ are as those reported in Figure 2.1.

fraction ($\sim$500 cm^{-1} compared to $\sim$100 cm^{-1} at other X_{BE}). This variation in both $\nu_{em.}$ and $\Gamma_{em.}$ with $\lambda_{exc.}$ indicates presence of relatively longer-lived aggregates in aqueous BE mixtures at very low alcohol concentrations and provides an independent support to conclusions from earlier NSE[5] measurements. These data, however, do not indicate that aqueous BE mixtures at other compositions are spatially homogeneous because observation of $\lambda_{exc.}$. Dependence (of $\nu_{em.}$ and $\Gamma_{em.}$) depends on $\langle \tau_{life} \rangle$ of the solute used.[26,38] This may also be the reason for the observed $\lambda_{exc.}$. Dependence not being the most pronounced at $X_{BE} \sim 0.02$ (where absorption frequency shift is the maximum). In addition, the presence of a third component (C153 in the present study) may realign the interactions that lead to alcohol aggregations in aqueous binary mixtures, altering the qualitative and quantitative features of aggregations occurring in otherwise pure binary mixtures.[56]

2.3.2 Measurements of Relaxation Rates: Search for the Criticality Effects

Figure 2.3 depicts the composition dependence of average fluorescence lifetime, $\langle \tau_{life} \rangle$, measured using C153 in BE/water mixtures (upper panel) and compares with the same in EtOH/ water and TBA/water mixtures[33] at $\sim$298 K (lower panel). Temperature effects on the composition dependence of $\langle \tau_{life} \rangle$ in BE/water mixtures are also shown in the same figure. Bi-exponential fit parameters required for adequately describing the relevant magic angle intensity decays are summarized in Table 2.1. Note in Table 2.1 that none of the intensity decays require more than two exponentials. In addition, fit parameters do not suggest, through any anomalous change of amplitudes $(a_i \ s)$ and time constants $(\tau_i \ s)$, partitioning of the dye solute into alcohol-rich and water-rich domains. Moreover, upper panel of Figure 2.3 shows that the abrupt change in the slope for composition dependence of $\langle \tau_{life} \rangle$ occurs at $X_{BE} \approx 0.04$ at 298 K, and this location remains nearly unchanged at 278 K and 318 K (see inset). The fact that the slope changes at a mole fraction significantly lower than the critical concentration $\left(X_{BE}^c \sim 0.06 \right)$ at 298 K, and the location of this change remains nearly insensitive even when the critical temperature is approached $\left(T_c \sim 322.5 \ K \right)$ strongly suggests domination
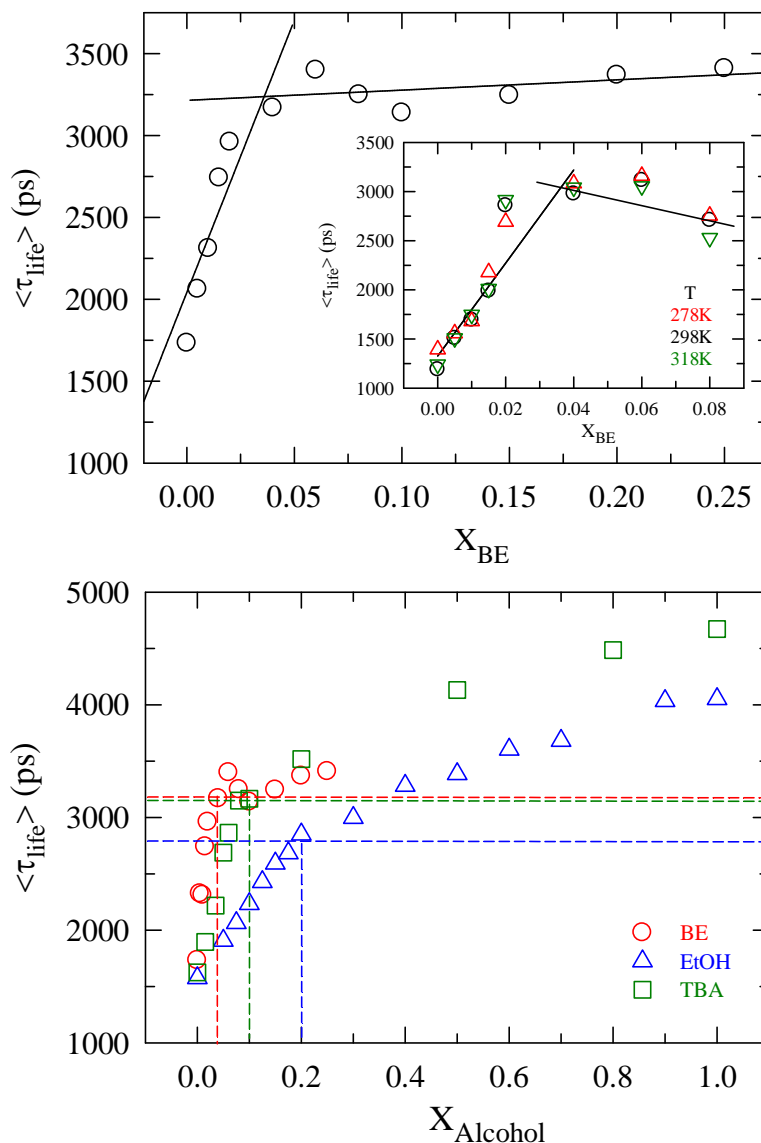
Figure 2.3: BE mole fraction dependence of average excited state lifetime $\left(\left\langle \tau_{life} \right\rangle\right)$ of C153 in BE/water mixtures at ~298 K (upper panel) and a comparison for the same among aqueous solutions of BE, TBA, and EtOH (lower panel). Inset of the upper panel shows variation of composition dependent $\left\langle \tau_{life} \right\rangle$ with temperature on an expanded composition axis to facilitate location of the slope-change. Data representations in both the panels are, as before, colour-coded. Solid lines in the upper panel and in the inset represent fit through data at ~298 K only. Dashed lines in the lower panel are shown to indicate the alcohol mole fraction at which slope changes due to structural transition. Largest uncertainty in $\left\langle \tau_{life} \right\rangle$ is $\pm 5\%$ of the values reported in both the panels (determined from 3 to 4 independent measurements at a few representative alcohol mole fractions).

Table 2.1: Bi-exponential fit parameters for magic angle fluorescence emission decays and average fluorescence lifetimes ($\langle \tau_{life} \rangle = \sum_{i=1}^{n} a_i \tau_i$, with $\sum_{i=1}^{n} a_i = 1$)[a] of C153 at various BE mole fractions at ~298 K.

X_{BE}	a_1	τ_1 (ps)	a_2	τ_2 (ps)	$\langle \tau_{life} \rangle$ (ps)[b]
0.00	0.19	943	0.81	1923	1737
0.005	0.06	166	0.94	2184	2063
0.01	0.05	91	0.95	2435	2318
0.015	0.07	516	0.93	2918	2750
0.02	0.12	325	0.88	3324	2964
0.04	0.12	516	0.88	3517	3157
0.06	0.08	627	0.92	3641	3400
0.08	0.13	443	0.87	3668	3250
0.10	0.14	305	0.86	3609	3146
0.15	0.13	342	0.87	3661	3229
0.20	0.08	421	0.92	3630	3373
0.25	0.09	341	0.91	3726	3421

a. At $X_{BE} = 1$ and ~298 K, $\langle \tau_{life} \rangle \approx 4330 \ ps$ with $a_1 = 0.15$, $\tau_1 = 186 \ ps$, $a_2 = 0.85$, and

   $\tau_2 = 5061 \ ps$.

b. Error (maximum) associated with $\langle \tau_{life} \rangle$ is $\pm 5\%$ of the reported values (based on a limited set of measurements).

of alcohol-water interaction in guiding the solution structure and a very minor role for the criticality effects. Note critical density fluctuations have also been found to play an insignificant role in controlling local solvent density augmentation around a dissolved solute in supercritical media.[29,30,57]

A comparison among the mixture composition dependent $\langle \tau_{life} \rangle$ for C153 in BE/water, TBA/water,[33] and EtOH/water[33] mixtures, shown in the lower panel of Figure 2.3, further suggests that it is the alcohol-size rather than the criticality-driven density fluctuations which sets the steepness of the initial slope for the composition dependence and determines the

location of the slope-change on the composition axis. Consequently, the slope-change is the sharpest for BE/water mixtures among these three alcohol/water systems and occurs at alcohol mole fractions, ~0.04 for BE, ~0.1 for TBA, and ~0.2 for EtOH. Since these alcohol mole fractions for TBA and EtOH correspond to mixture compositions at which structural transition (from three-dimensional water-type H-bonding network to zigzag alcohol-like H-bonding structure) occurs[53] and are different from concentrations at which thermodynamic anomalies are the strongest,[58-61] it is likely that similar structural transition also takes place for aqueous mixtures of BE at X_{BE}~0.04. For BE/water mixtures, thermodynamic anomalies occur at X_{BE}~0.02 [16,17] around which we have observed largest red-shift in the absorption spectrum. Note the present study is probably the first report which successfully identifies, through spectroscopic measurements, BE mole fractions, at which effects of H-bond strengthening (via spectral red-shift) and structural transition (via dependence of lifetime) can be observed distinctly and separately.

Figure 2.4 presents the composition dependence of the average rotation times, $\langle \tau_r \rangle$, measured for BE/water mixtures, and compares with earlier results[33] for TBA/water and EtOH/water mixtures.[33] As observed for the composition dependence of $\langle \tau_{life} \rangle$ in Figure 2.3, $\langle \tau_r \rangle$ also experiences a sudden change in slope at X_{BE}~0.04, where aqueous solution may have undergone a structural transition. Temperature effects (inset, upper panel), however, are relatively stronger for $\langle \tau_r \rangle$ with initial slopes becoming steeper and structural transition occurring at lower X_{BE} upon decreasing temperature. Fit parameters for composition dependent $r(t)$ decays at ~298 K summarized in Table 2.B.1 (Appendix 2.B)[46] again indicate no anomalous change in amplitudes and time constants as the critical composition is approached. A representative fit is provided in Figure 2.A.5[46] to show the typical quality of fits achieved here regardless of solution composition and temperature. Fit parameters describing temperature dependent $r(t)$ decays also do not suggest any effects typical of critical fluctuations preceding phase transition as T_c is approached. Since $r(t)$ decay traces the time-dependent friction exerted by the surround environment on the rotating dye molecule, any signature of the mixture separating into alcohol and water phases would have
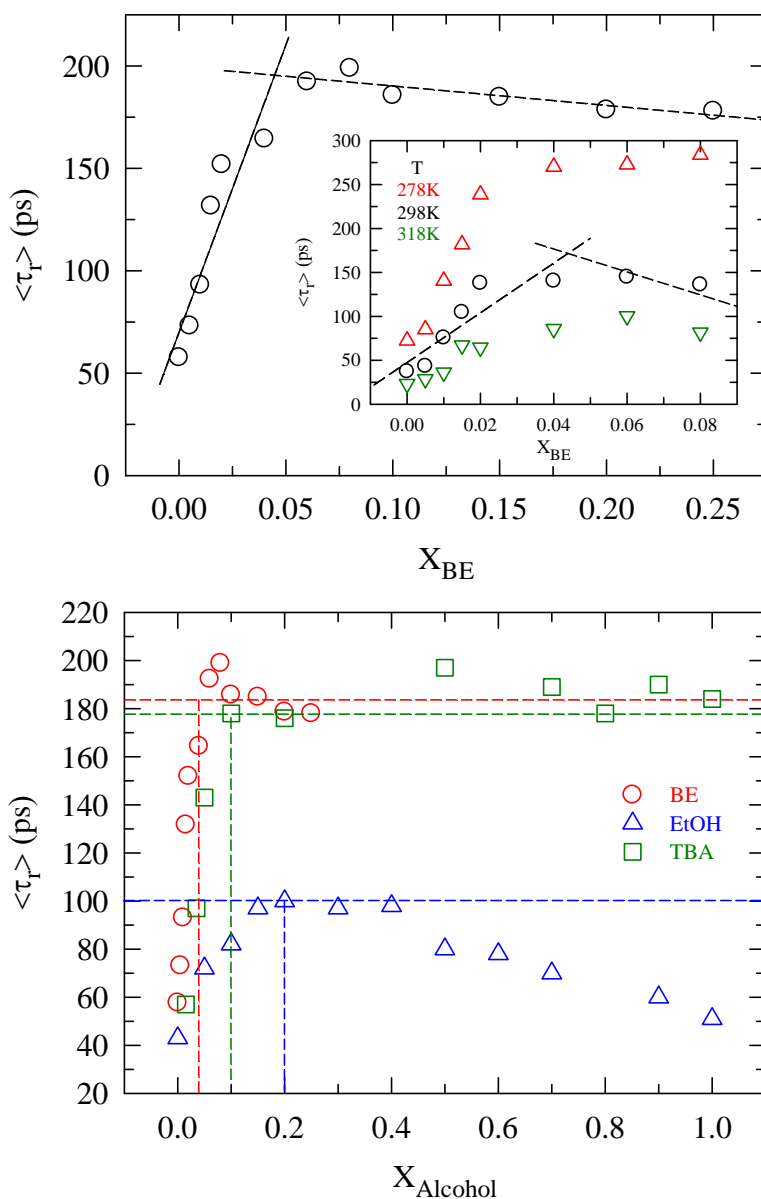
Figure 2.4: BE mole fraction dependence of average rotational time, $\langle \tau_r \rangle$, of C153 in BE/water mixtures at ~298 K (upper panel) and a comparison with the same among BE/water, TBA/water, and EtOH/water solutions (lower panel). Inset presents data at three different temperatures using expanded composition axis as in Figure 2.3. Representations are colour coded. Solid lines going through the data in the upper panel and inset are fits through data at ~298 K only. Dashed lines in the lower panel are guides for locating the alcohol mole fractions at which the slopes change suddenly. For C153 in neat BE at ~298 K, $r(t)$ has been found to be single-exponential, producing $\langle \tau_r \rangle \sim 291\,ps$. Largest uncertainty in $\langle \tau_r \rangle$ is $\pm 5\%$ of the values reported (based on a limited set of measurements).

been reflected in the fit parameters either via abrupt changes in the fit parameters or via the emergence of a completely new decay component. A comparison of the composition dependence of $\langle \tau_r \rangle$ among aqueous solutions of three alcohols (BE, TBA, and EtOH), shown in the lower panel, again reveals the dominating effects of alcohol size in determining the slope for the composition dependence at low alcohol concentration and the mole fractions at which slopes change for these alcohol/water mixtures. Note earlier dynamic anisotropy,[62] transient absorption,[63] and vibrational lifetime[64] measurements in supercritical solvents have also reported insignificant criticality effects and interpreted experimental results in terms of inter-species interactions.

A search for the impact of critical slowing down on relaxation rate has been further conducted in Figure 2.5 where the dependence of solute's rotational relaxation rate $\left(\langle \tau_r \rangle^{-1} \right)$ in these mixtures on the reduced temperature, $(T_c - T)/T_c$, is shown in a double-logarithmic plot. This is motivated by an earlier report[12] of asymptotic critical power-law dependence for the mutual diffusion coefficient along the liquid-liquid coexistence curve in BE/water mixtures, $D \propto \left(|T - T_c|/T_c \right)^{\gamma}$, with $\gamma \sim 0.8$ (theoretical value for γ is ~ 0.67). Interestingly, measured temperature dependent anisotropy relaxation rates at seven different BE mole fractions shown in Figure 2.5 do not exhibit any linear dependence on reduced temperature in this log-log plot. This suggests that criticality effects are probably overwhelmed by the temperature dependence of the solute-medium interaction, allowing solution viscosity to dictate the frictional resistance on the dissolved rotating solute. Figure 2.A.6 (Appendix 2.A)[46] demonstrates that the temperature dependence of the measured rotation rates and viscosities (data provided, respectively, in Tables 2.B.2 and 2.B.3)[46] at these compositions of BE/water mixtures is Arrhenius-type.
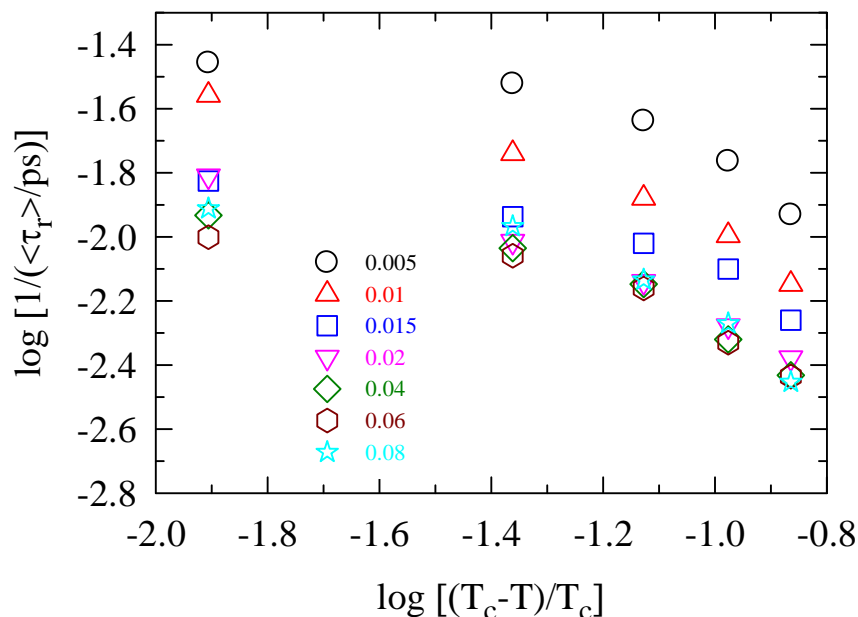
Figure 2.5: Search for the effects of critical slowing down on measured temperature dependent $\langle \tau_r \rangle$ at various compositions of BE/water mixtures in the water-rich region. Note the non-linearity in the dependence of $\langle \tau_r \rangle$ on reduced temperature at all BE mole fractions.

Activation energies, $E_a(\langle \tau_r \rangle)$ and $E_a(\langle \eta \rangle)$, estimated from the above temperature dependent study are in the range ~7-11 kJ/mol (see Table 2.B.4)[46] for both solute rotation and solution viscosity. This similarity in E_a range as well as absence of any drastic variation among the individual values strongly indicate the dominance of solute-solvent coupling via viscosity in regulating the mixture composition dependent relaxation rates with no or very minor roles for solution criticality. The correlation between $E_a(\langle \tau_r \rangle)$ and $E_a(\langle \eta \rangle)$ is depicted in Figure 2.6. Linear dependence between these two activation energies here indicates solute rotation in these mixtures, as in normal media and in the absence of any specific interactions, is guided by the structural relaxation of the surrounding environment. Interestingly, activation energy range found in the present study is very close to that (~10 kJ/mol) reported earlier[1] for centre-of-mass diffusion process in BE/water mixtures along the liquid-liquid coexistence curve at $T(K) = T_c + 25$, but ~3 times less than the estimate (~23 kJ/mol) from NSE measurements.[5]

Such a difference can, however, be explained reminding that NSE measurements can probe much slower dynamics (timescales ~0.1 – 100 ns)[65,66] than fluorescence measurement because $\langle \tau_{life} \rangle$ of a dye in the later strongly limits confident detection of slow timescales unless special techniques[67] are employed.

Correlation Between Activation Energies in
(2-Butoxethanol + Water) Mixtures

$$E_a\left[\langle \tau_r \rangle\right] = 4.480 + 0.567 E_a[\eta]$$
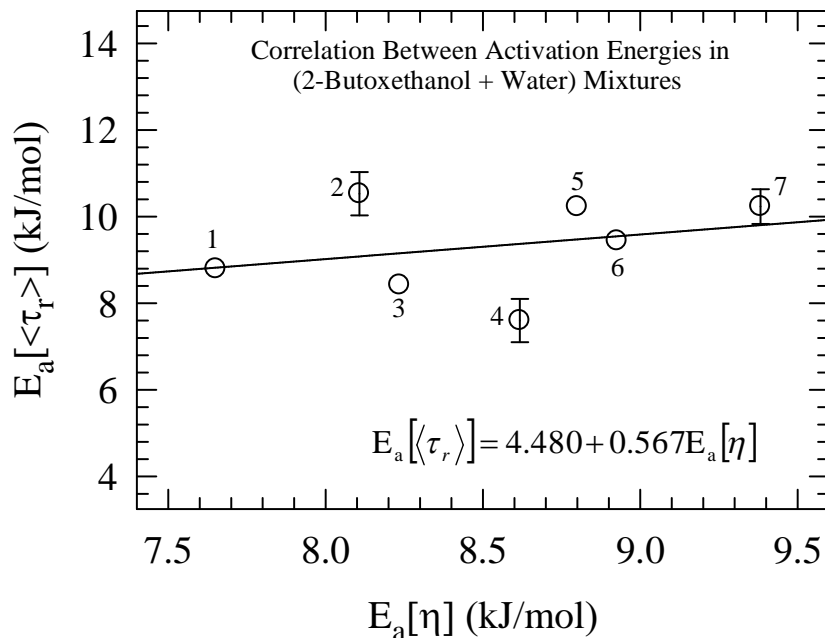
Figure 2.6: Correlation between activation energies for solute rotation $\left(E_a\left(\langle \tau_r \rangle\right)\right)$ and solution viscosity $\left(E_a\left(\langle \eta \rangle\right)\right)$ estimated from our temperature dependent measurements of $\langle \tau_r \rangle$ and η. Line through the data represents the fit, and the fit expression is provided inside the panel. Error bars (based on limited numbers of sets) are found to be ~1 kJ/mole and are shown for some representative BE concentrations. Numbers attached to each data point represents BE mole fractions, and their identities are 1 → 0.005, 2 → 0.01, 3 → 0.06, 4 → 0.015, 5 → 0.02, 6 → 0.04, and 7 → 0.08. Only compositions with low BE mole fractions were investigated to capture anomaly, if any, around the critical concentration which is ~0.06.

Finally, diffusion-viscosity coupling in these BE/water mixtures is investigated in Figure 2.7 where temperature dependent average rotation times $\left(\langle \tau_r \rangle\right)$ of the solute measured at various mixture compositions are shown as a function of temperature-reduced solution viscosity (η/T) in a double-logarithmic fashion. The line going through the data represents a fit to the expression, $\langle \tau_r \rangle \propto A(\eta/T)^p$, with $p \approx 0.95$. Such an average value for p indicates rotational relaxation of the solute taking place, like in a homogeneous system with large solute-solvent size ratio, through stochastic Brownian angular moves. This probably justifies the use of
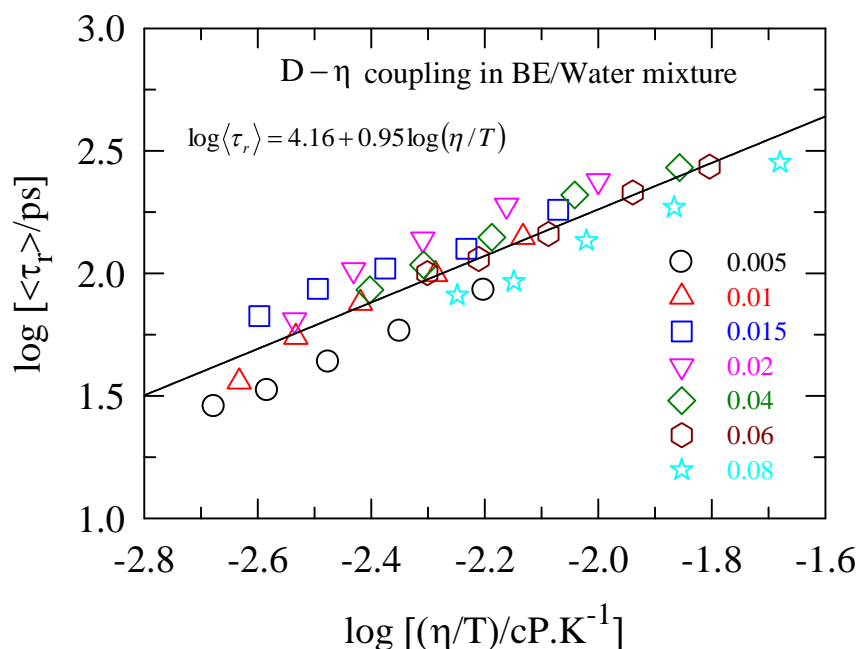
Figure 2.7: Coupling between C153 rotation and viscosity in BE/water mixtures. Measured C153 rotation times, $\langle \tau_r \rangle$, at various BE mole fractions and temperatures are shown as a function of temperature-reduced viscosity, η/T, on a log-log scale. As indicated, different geometrical symbols denote data at different BE mole fractions. Fit through all the data presented here is shown by the solid line. Fit expression is also shown inside the figure panel.

hydrodynamics in scattering measurements[2,5-7,10] for estimating size of the aggregated structures in BE/water mixtures. Note, however, that the appearance of these mixtures as being dynamically homogeneous is strongly conditioned to the excitation energy employed $\left(\lambda_{exc.} = 409 \ nm\right)$ in the present measurements, and studies using different $\lambda_{exc.}$ may reveal different heterogeneity aspect. In addition, detection of dynamical heterogeneity via fractional viscosity dependence as attempted here depends significantly on the size of the probe solute[68,69] (diameter of C153 is 7.8 Å)[55] in the relevant measurements and its lifetime.[38]

2.4 Concluding Remarks

In conclusion, the present study indicates overwhelming domination of alcohol-water interactions for the micro-heterogeneous solution structure in BE/water mixtures and finds no role for the critical fluctuations preceding phase separation. Excitation wavelength dependence of steady state fluorescence emission (of a dissolved solute) confirms formation of aggregated structures at very low BE mole fractions with stability times in the nanosecond domain. Strengthening of H-bonds upon addition of BE at the water-rich regime is suggested by the initial red-shift of the absorption spectrum, while the structural transition of H-bond network is marked by the abrupt changes in the slopes for composition dependent fluorescence lifetimes and rotation times. Comparison with the corresponding results for EtOH/water and TBA/water mixtures confirms specific role for the alcohol size to determine the location on composition axis for these two solution events and underlines the importance of hydrophobic interaction to the aggregation process in aqueous alcohol solutions.[32,33,51,70-73] No asymptotic critical power law dependence has been found for the temperature dependent average rotation times, negating any effective contributions from criticality on relaxation dynamics probed. Activation energy for solute rotation at each BE mole fraction follows that of solution viscosity, implying no partitioning of solute in domains made primarily of individual components while the critical concentration or temperature was approached. The coupling between solute's rotational diffusion and solution viscosity has been found to be nearly hydrodynamic, justifying use of Brownian diffusion model in estimating hydrodynamic size of the aggregated structures from scattering measurements of BE/water mixtures. This study provides thorough spectroscopic measurements at the water-rich region

from very dilute BE concentration to a regime of alcohol with moderate presence and reveals for the first time evidences for both strengthening of H-bonds and solution structural transition.

Appendix 2.A
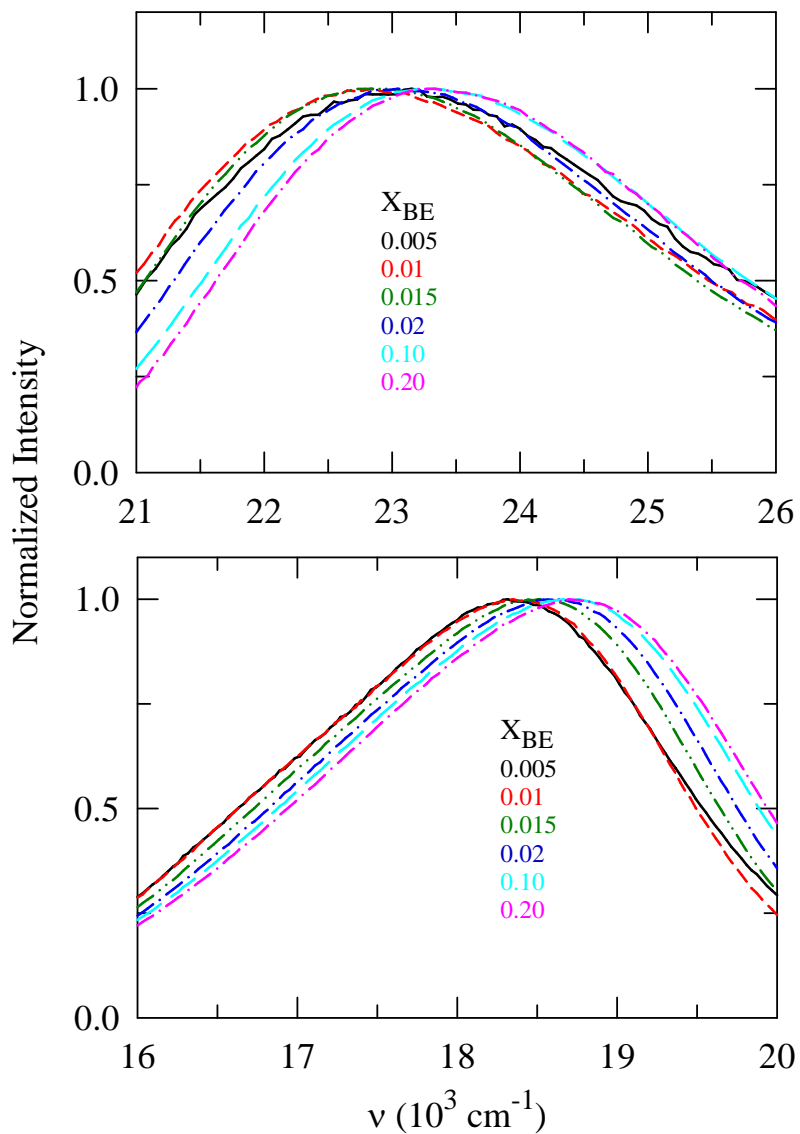
Figure 2.A.1: Absorption and emission spectra of coumarin 153 (C153) at different mole fractions of 2-butoxy ethanol (BE) in BE-water mixture at ~298 K. Upper panel shows the absorption spectra and lower panel shows the emission spectra. Representations are colour-coded and indicated.
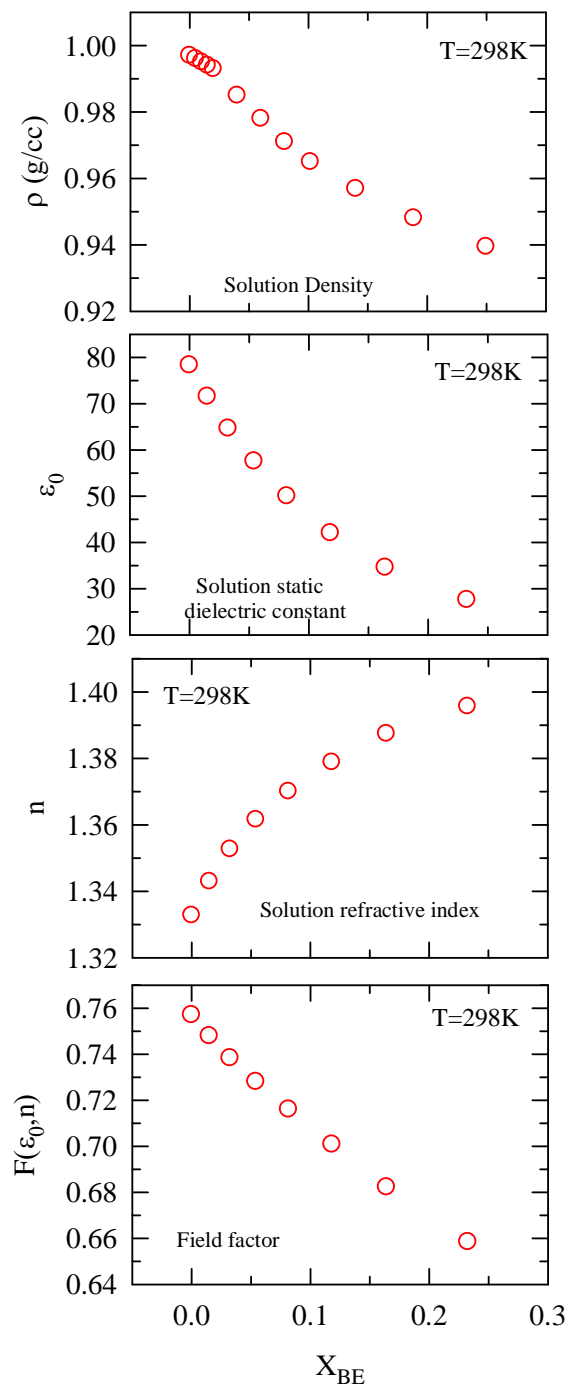
Figure 2.A.2: BE mole fraction dependent density (ρ), static dielectric constant (ε_0), refractive index (n) and reaction field factor $[F(\varepsilon_0, n)]$ of (BE+Water) mixtures at ~298 K.

$$F(\varepsilon_0, n) = \frac{\varepsilon_0 - 1}{\varepsilon_0 + 2} - \frac{n^2 - 1}{n^2 + 2}.$$
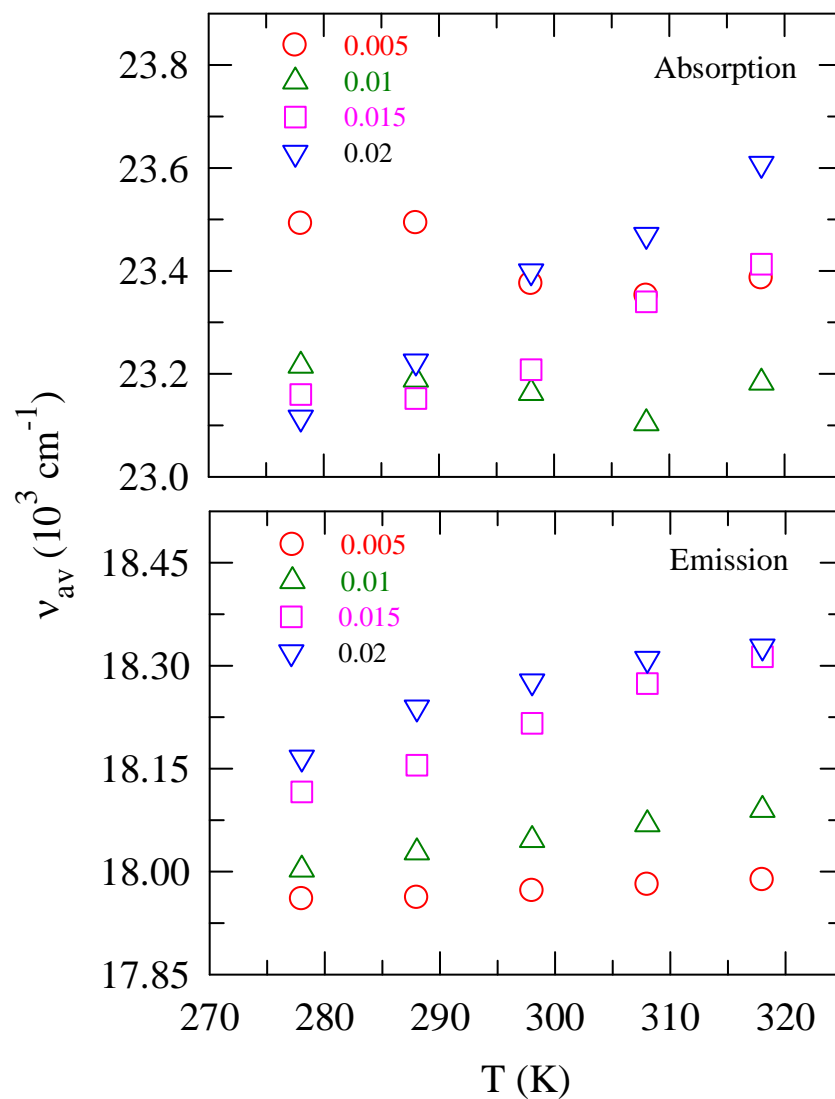
Figure 2.A.3: Temperature dependence of absorption and emission spectral frequencies at a few representative BE mole fractions in the dilute limit. Error (maximum) associated with $\langle v \rangle$ is ± 200 cm^{-1} (based on a limited data set).

$X_{BE} = 0.04$ $\underline{T=298K}$

$a_1 = 0.50, \tau_1 = 260.9 \text{ ps}$

$a_2 = 0.50, \tau_2 = 18.46 \text{ ps}$

$\chi^2 = 1.13$
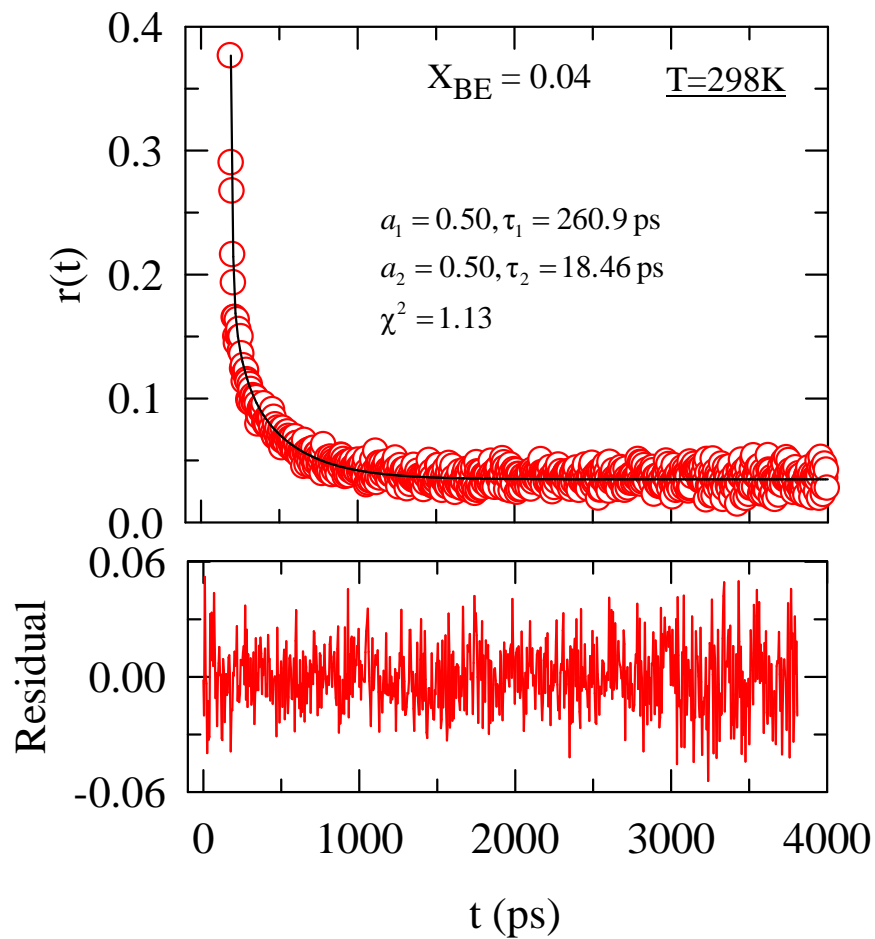
Figure 2.A.4: Representative fit to collected fluorescence anisotropy decay for C153 in BE/water mixture at 0.04 BE mole fraction. Open circles represent the measured data, the solid line shows the fit through the data. Fit parameters are listed in the upper panel. The *goodness of fit parameter* $\left(\chi^2\right)$ is also shown. Residuals are shown in the bottom panel.
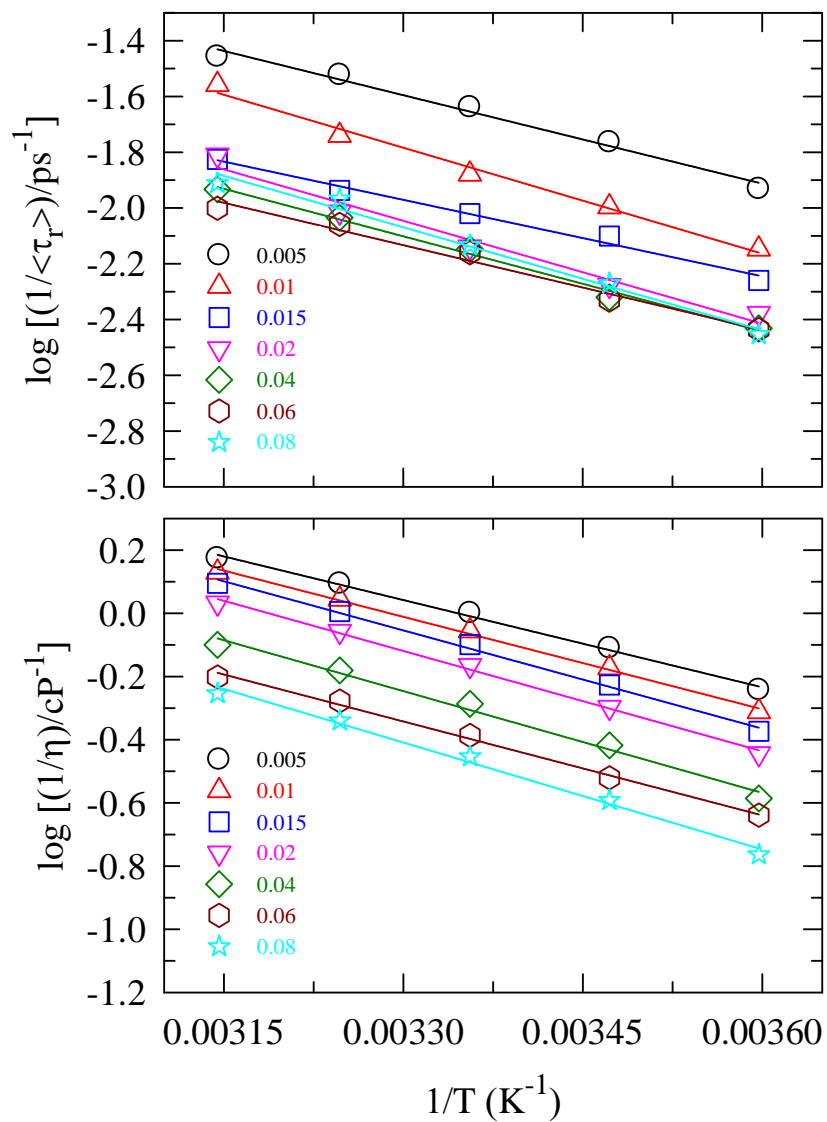
Figure 2.A.5: Arrhenius-type plots for temperature dependent C153 average rotation times and solution viscosity in BE/water mixtures at low alcohol mole fraction range.

Appendix 2.B

Table 2.B.1: Fit parameters for rotational anisotropy decay of C153 at various BE mole fractions in (BE+Water) mixtures at ~298 K.

X_{BE}	a_1	τ_1 (ps)	a_2	τ_2 (ps)	$\langle \tau_r \rangle$ (ps)[a]
0.00	1.00	58			58
0.005	1.00	73			73
0.01	1.00	93			93
0.015	0.55	24	0.45	266	133
0.02	0.69	46	0.31	386	151
0.04	0.53	15	0.47	329	163
0.06	0.48	44	0.52	330	193
0.08	0.56	15	0.44	434	200
0.10	0.55	27	0.45	380	186
0.15	0.57	30	0.43	391	186
0.20	0.54	40	0.46	340	178
0.25	0.48	19	0.52	322	177

a) Error (maximum) associated with $\langle \tau_r \rangle$ is $\pm 5\%$ of the reported values (based on a limited set of measurements).

Table 2.B.2: Fit parameters for the collected temperature dependent C153 anisotropy decays, and average rotational times.

X_{BE}	T (K)	a_1	τ_1 (ps)	a_2	τ_2 (ps)	$\langle \tau_r \rangle$ (ps)
0.005	278	1.00	85.32			85.32
	288	1.00	58.06			58.06
	298	1.00	43.45			43.45
	308	1.00	33.26			33.26
	318	1.00	28.62			28.62
0.01	278	0.52	228.6	0.48	43.86	140.5
	288	0.46	171.4	0.54	38.12	99.03
	298	0.29	169.8	0.71	36.82	75.66
	308	0.23	127.9	0.77	33.12	54.91
	318	1.00	36.10			36.10
0.015	278	0.72	242.3	0.28	29.38	181.9
	288	0.67	180.2	0.33	17.90	126.0
	298	0.54	173.3	0.46	24.57	104.7
	308	0.48	153.3	0.52	24.46	86.46
	318	1.00	57.84			57.84
0.02	278	0.54	409.2	0.46	42.23	238.7
	288	0.53	333.2	0.47	28.20	189.5
	298	0.48	261.9	0.52	24.64	137.8
	308	0.48	194.9	0.52	20.23	103.3
	318	1.00	64.55			64.55
0.04	278	0.51	499.7	0.49	28.97	270.2
	288	0.49	393.8	0.51	29.36	209.0
	298	0.50	260.9	0.50	18.46	140.4
	308	0.45	220.6	0.55	16.00	108.4
	318	0.49	145.0	0.51	28.49	85.62
0.06	278	0.52	499.0	0.48	24.58	272.8
	288	0.49	401.5	0.51	32.20	214.0
	298	0.51	262.0	0.49	21.95	144.8
	308	0.46	218.5	0.54	26.42	114.5
	318	0.33	199.4	0.67	50.84	100.2
0.08	278	0.48	551.4	0.52	34.11	283.8
	288	0.48	358.5	0.52	29.21	186.3
	298	0.47	258.2	0.53	28.12	136.1
	308	0.42	178.9	0.58	31.42	92.69
	318	1.00	81.59			81.59

Table 2.B.3: Temperature dependent viscosity the BE/water mixtures at various BE mole fractions.

X_{BE}	T (K)	η (cP)[a]
0.005	278	1.747
	288	1.287
	298	0.997
	308	0.804
	318	0.669
0.01	278	2.048
	288	1.488
	298	1.136
	308	0.903
	318	0.741
0.015	278	2.362
	288	1.686
	298	1.256
	308	0.987
	318	0.804
0.02	278	2.785
	288	1.984
	298	1.462
	308	1.141
	318	0.927
0.04	278	3.854
	288	2.617
	298	1.935
	308	1.516
	318	1.259
0.06	278	4.353
	288	3.317
	298	2.435
	308	1.896
	318	1.590
0.08	278	5.802
	288	3.906
	298	2.840
	308	2.187
	318	1.795

a) Error (maximum) associated with η values is $\pm 3\%$ of the reported values

Table 2.B.4: BE mole fraction dependence of activation energies for solution viscosity and C153 rotation in (BE+Water) mixtures.

X_{BE}	$E_a[\eta]$ (kJ/mol)	$E_a[\langle\tau_r\rangle]$ (kJ/mol)
0.005	7.6509	8.7964
0.01	8.1074	10.5286
0.015	8.6169	7.6005
0.02	8.7996	10.2287
0.04	8.9262	9.4426
0.06	8.2347	8.4218
0.08	9.3820	10.2320

References

1. J. Schmitz, L. Belkoura and D. Woermann, J. Chem. Phys. **101**, 476 (1994).

2. G. D'Arrigo, F. Mallamace, N. Micali, A. Paparelli, J. Teixeira and C. Vasi, Prog. Colloid Polym. Sci. **84**, 177 (1991).

3. G. D'Arrigo, R. Giordano and J. Teixeira, Eur. Phys. J. E **10**, 135 (2003).

4. R. D. Koehler, K. V. Schubert, R. Strey and E. W. Kaler, The Journal of chemical physics **101**, 10843 (1994).

5. K. Yoshida, T. Yamaguchi, T. Otomo, M. Nagao, H. Seto and T. Takeda, J. Mol. Liq. **119**, 125 (2005).

6. G. D'Arrigo and J. Teixeira, J. Chem. Soc. Faraday Trans. **86(9)**, 1503 (1990).

7. G. W. Euliss and C. M. Sorensen, J. Chem. Phys. **80**, 4767 (1984).

8. N. Ito, T. Fujiyama and Y. Udagawa, Bull. Chem. Soc. Jpn. **56**, 379 (1983).

9. N. Ito, K. Saito, T. Kato and T. Fujiyama, Bull. Chem. Soc. Jpn. **54**, 991 (1981).

10. T. M. Bender and R. Pecora, J. Phys. Chem. **92**, 1675 (1988).

11. R. C. Castillo, H. C. Domínguez and M. Costas, J. Phys. Chem. **94**, 8731 (1990).

12. C. Ikier, H. Klein and D. Woermann, J. Chem. Phys. **96**, 859 (1992).

13. F. Mallamace, N. Micali and G. D'Arrigo, Phys. Rev. A **44**, 6652 (1991).

14. U. Kaatze, R. Pottel and A. Schumacher, J. Phys. Chem. **96**, 6107 (1992).

15. S. Kato, D. Jobe, N. P. Rao, C. H. Ho and R. E. Verrall, J. Phys. Chem. **90**, 4167 (1986).

16. Y. Koga, W. W. Y. Siu and T. Y. H. Wong, J. Phys. Chem. **94**, 3879 (1990).

17. Y. Koga, J. Phys. Chem. **96**, 10466 (1992).

18. Y. Koga, J. Phys. Chem. **100**, 5172 (1996).

19. Y. Koga, P. Westh, Y. Moriya, K. Kawasaki and T. Atake, J. Phys. Chem. B **113**, 5885 (2009).

20. K. Yoshida, S. Baluja, A. Inaba and Y. Koga, J. Chem. Phys. **134**, 214502 (2011).

21. R. Gupta and G. N. Patey, J. Phys. Chem. B **115**, 15323 (2011).

22. R. Bennes, J. M. Douillard, M. Privat and L. Tenebre, J. Phys. Chem. **89**, 1822 (1985).

23. T. Kato, J. Phys. Chem. **88**, 1248 (1984).

24. D. Subramanian, C. T. Boughter, J. B. Klauda, B. Hammouda and M. A. Anisimov, Faraday Discuss. **167**, 217 (2013).

25. A. Perera, R. Mazighi and B. Kežić, J. Chem. Phys. **136**, 174516 (2012).

26. B. Guchhait, S. Das, S. Daschakraborty and R. Biswas, J. Chem. Phys. **140**, 104514 (2014).

27. B. Guchhait, S. Daschakraborty and R. Biswas, The Journal of chemical physics **136**, 174503 (2012).

28. A. Das, S. Das and R. Biswas, J. Chem. Phys. **142**, 034505 (2015).

29. R. Biswas, J. E. Lewis and M. Maroncelli, Chem. Phys. Lett. **310**, 485 (1999).

30. J. E. Lewis, R. Biswas, A. G. Robinson and M. Maroncelli, J. Phys. Chem. B **105**, 3306 (2001).

31. T. Pradhan and R. Biswas, J. Phys. Chem. A **111**, 11514 (2007).

32. T. Pradhan, P. Ghoshal and R. Biswas, J. Phys. Chem. A **112**, 915 (2008).

33. T. Pradhan, P. Ghoshal and R. Biswas, J. Chem. Sci. **120**, 275 (2008).

34. T. Pradhan, H. A. R. Gazi and R. Biswas, The Journal of chemical physics **131**, 054507 (2009).

35. T. Pradhan and R. Biswas, J. Phys. Chem. A **111**, 11524 (2007).

36. B. Guchhait, H. A. R. Gazi, H. K. Kashyap and R. Biswas, J. Phys. Chem. B **114**, 5066 (2010).

37. B. Guchhait, R. Biswas and P. K. Ghorai, J. Phys. Chem. B **117**, 3345 (2013).

38. A. Das, S. Das and R. Biswas, Chem. Phys. Lett. **581**, 47 (2013).

39. H. A. R. Gazi, B. Guchhait, S. Daschakraborty and R. Biswas, Chem. Phys. Lett. **501**, 358 (2011).

40. M. L. Horng, J. A. Gardecki and M. Maroncelli, J. Phys. Chem. A **101**, 1030 (1997).

41. K. Dahl, R. Biswas, N. Ito and M. Maroncelli, J. Phys. Chem. B **109**, 1563 (2005).

42. J. E. Lewis and M. Maroncelli, Chem. Phys. Lett. **282**, 197 (1998).

43. H. A. R. Gazi, H. K. Kashyap and R. Biswas, J. Chem. Sci. **127**, 61 (2015).

44. R. Biswas, A. R. Das, T. Pradhan, D. Tauraud, W. Kunz and S. Mahiuddin, J. Phys. Chem. B **112**, 6620 (2008).

45. N. Sarma, J. M. Borah, S. Mahiuddin, H. A. R. Gazi, B. Guchhait and R. Biswas, J. Phys. Chem. B **115**, 9040 (2011).

46.   See Appendix 2.A and 2.B for steady-state absorption and emission spectra of C153 at ~298 K in these mixtures at various X(BE), composition dependent densities, static dielectric constant, refractive index, and reaction field factor, temperature (T) dependence of absorption and emission frequencies at a few representative X(BE), fit parameters for composition dependent r(t) decay at ~298 K, representative fit of r(t) decay at a given composition at ~298 K, T-dependent rotation times, viscosity values and their corresponding Arrhenius-type plots, and composition dependent activation energies for C153 rotation and solution viscosity.

47.   G. Douhéret and A. Pal, J. Chem. Eng. Data **33**, 40 (1988).

48.   Y. Shindo and K. Kusano, J. Chem. Eng. Data **24**, 106 (1979).

49.   J. A. Gardecki and M. Maroncelli, Chem. Phys. Lett. **301**, 571 (1999).

50.   H. A. R. Gazi and R. Biswas, J. Chem. Sci. **123**, 265 (2011).

51.   H. A. R. Gazi and R. Biswas, J. Phys. Chem. A **115**, 2447 (2011).

52.   D. T. Bowron and J. L. Finney, J. Phys. Chem. B **111**, 9838 (2007).

53.   I. Omelyan, A. Kovalenko and F. Hirata, J. Theor. Comput. Chem. **2**, 193 (2003).

54.   I. M. Svishchev and P. G. Kusalik, J. Chem. Phys. **99**, 3049 (1993).

55.   M. L. Horng, J. A. Gardecki, A. Papazyan and M. Maroncelli, J. Phys. Chem. B **99**, 17311 (1995).

56.   D. T. Bowron and S. D. Moreno, J. Phys. Chem. B **109**, 16210 (2005).

57.   W. Song, R. Biswas and M. Maroncelli, J. Phys. Chem. A **104**, 6924 (2001).

58.   K. Yoshida and T. Yamaguchi, Z. Naturforsch. **56A**, 529 (2001).

59.   F. Franks and D. J. G. Ives, Q. Rev. Chem. Soc. **20**, 1 (1966).

60.   M. D. Zeidler, in *Water, a Comprehensive Treatise*, edited by F. Franks (Plenum, New York, 1966), Vol. 2, pp. 529.

61.   E. M. Arnett and D. R. Mcklevey, J. Am. Chem. Soc. **88**, 5031 (1966).

62.   R. Biswas, K. Dahl and M. Maroncelli, J. Phys. Chem. B **106**, 11593 (2002).

63.   Y. Kimura and N. Hirota, J. Mol. Liq. **65-66**, 425 (1995).

64.   D. J. Myers, R. S. Urdahl, B. J. Cherayil and M. D. Fayer, J. Chem. Phys. **107**, 9741 (1997).

65.   H. Seto, T. Kato, M. Monkenbusch, T. Takeda, Y. Kawabata, M. Nagao, D. Okuhara, M. Imai and S. Komura, J. Phys. Chem. Solids **60**, 1371 (1991).

66.   T. Takeda, Y. Kawabata, H. Seto, S. Komura, S. K. Ghosh, M. Nagao and D. Okuhara, J. Phys. Chem. Solids **60**, 1375 (1991).

67.   A. M. Funston, T. A. Fadeeva, J. F. Wishart and E. W. Castner Jr., J. Phys. Chem. B **111**, 4963 (2007).

68.   W. Huang and R. Richert, Philos. Mag. **87**, 371 (2007).

69.   M. D. Ediger, Annu. Rev. Phys. Chem. **51**, 99 (2000).

70.   H. Shirota and E. W. Castner Jr., J. Chem. Phys. **112**, 2367 (2000).

71.   S. Banerjee, R. Ghosh and B. Bagchi, J. Phys. Chem. B **116**, 3713 (2012).

72.   S. Banerjee and B. Bagchi, J. Chem. Phys. **139**, 164301 (2013).

73.   S. Banerjee, J. Furtado and B. Bagchi, J. Chem. Phys. **140**, 194502 (2014).

Chapter 3

Are N-methyl Groups of Tetramethylurea (TMU) Hydrophobic? A Composition and Temperature Dependent Fluorescence Spectroscopic Investigation of TMU/Water Binary Mixtures

3.1 Introduction

Recent study[1] of thermodynamic properties of aqueous solutions of amphiphiles suggested that methyl group, which is known to be hydrophobic in nature, may not always show hydrophobic character. The hydrophobic nature of methyl group depends on the atom to which it is attached. The study also indicated that methyl groups attached to electronegative nitrogen atoms show hydrophilicity rather than hydrophobicity. Tetramethylurea (TMU) is an example of such type of molecule which possesses amphiphilic character as well as –N methyl groups. Another important characteristic of TMU is the strong protein denaturing ability.[2,3] But computer simulation studies[4-6] have shown that TMU aggregates by the hydrophobic interactions among methyl groups in aqueous solutions at very low concentrations. Disagreement among different studies stimulates further research in this area.

Study of binary mixtures of water with other co-solvents, specially, those which can interact with water via both hydrogen bond donor and acceptor sites such as alcohols, has long been a matter of discussion.[7-27] Researchers have found that the tetrahedral hydrogen bonding network of water becomes stronger in presence of small amount of alcohols due to their accommodation into the tetrahedral cavity. This three dimensional tetrahedral structure of water gets disrupted to chain structure at comparatively larger alcohol concentrations where tetrahedral network of water can no longer accommodate alcohol molecules.[17,18,20] This effect is more pronounced while moving from small alcohols like ethanol (EtOH) to larger alcohols like tertiary butanol (TBA) because hydrophobic interaction plays a crucial role in determining the structural arrangement of both the specie in a given binary mixture.[18]

Consequently, dynamical properties of aqueous solutions exhibit significant changes in presence of co-solvents.

Several experimental studies such as dielectric relaxation,[28] femtosecond IR,[29,30] and ultrafast optical Kerr effect[31] measurements revealed that in aqueous solutions of TMU, the reorientational dynamics of water in hydrophobic hydration shell undergoes substantial retardation than that of bulk water. Subsequent computer simulation studies[32-34] have suggested that slower H-bond exchange near the hydrophobic groups is the key factor for retarded reorientational dynamics of water. We have also observed the slowing down of water–water H-bond persistence time in presence of TMU into water.[6] At concentrated TMU solutions, the elongation of H-bond dynamical timescales due to solute–induced confinement of water is reminiscent of water in explicit confined environment.[35,36]

Here, we are interested to see whether the hydrophobic part containing four N–methyl groups of TMU acts in the similar manner in aqueous solution as we found before in aqueous solution of alcohols.[17-20] In this chapter, we have investigated various compositions of TMU in water at different temperatures by fluorescence spectroscopic technique. Absorption and steady-state emission of a nonreactive probe coumarin 153 (C153) in TMU–Water binary mixture have provided important information regarding the structural change of H-bonding network of water upon addition of TMU. As we know the structure of the solution is intimately related to its dynamics, structural modification of water upon addition of TMU will also affect the solution dynamics. Therefore, time-resolved fluorescence anisotropy measurements have been carried out to correlate solute–solvent coupling in this macroscopically homogeneous but microscopically heterogeneous system. Chemical structure of TMU is shown in Scheme 3.1 along with three other co-solvents considered in the present study.
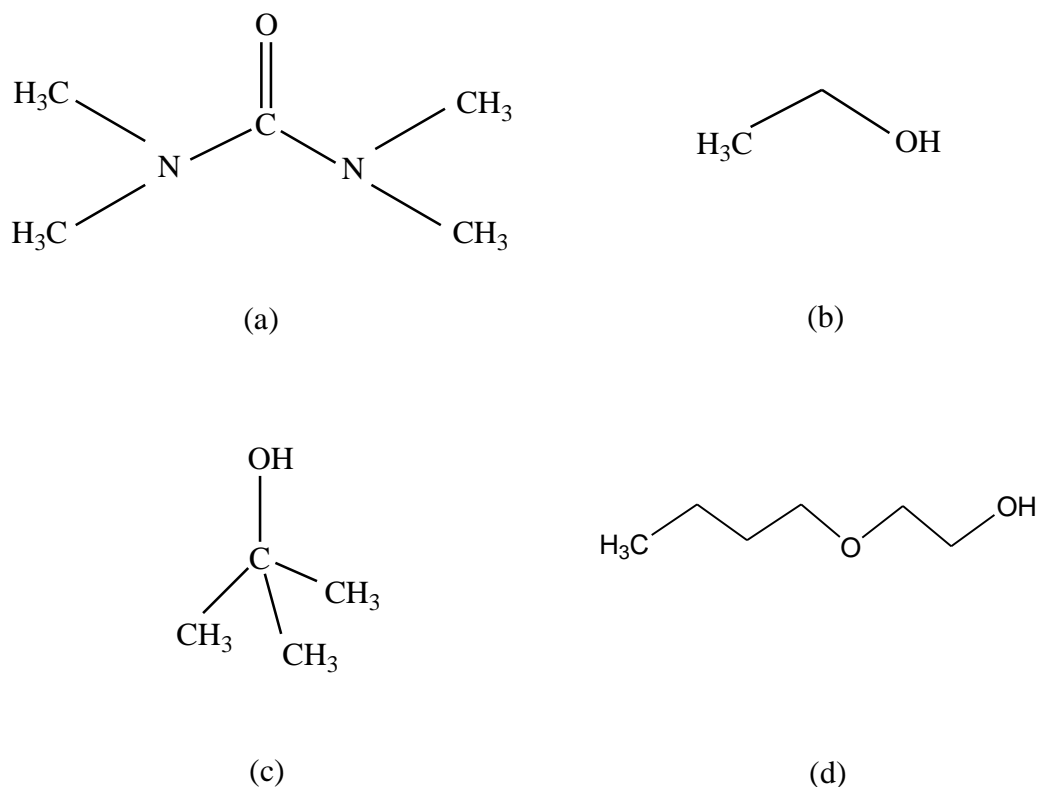
Scheme 3.1: Chemical Structures of (a) Tetramethylurea (TMU), (b) Ethanol (EtOH), (c) Tertiary butanol (TBA), (d) 2-butoxyethanol (BE).

The main results of this study are as follows: absorption spectrum of C153 in TMU–Water binary mixture shows red-shift at low TMU mole fraction and after reaching the minima at $X_{TMU} = 0.07$, it blue-shifts up continuously to the highest TMU mole fraction $X_{TMU} = 1$. Interestingly, emission spectrum does not exhibit such minima and show only the effects of average polarity of the medium. C153 shows excitation wavelength dependent emission at very low TMU mole fraction ($X_{TMU} = 0.005$). Increase of TMU concentration reduces the excitation wavelength dependence. Temperature dependent steady-state study reveals maximum red shift of absorption spectrum occurs at T ~ 293 K. The average excited-state lifetime of C153 $\langle \tau_{life} \rangle$ in these binary mixtures exhibits mixture composition dependence with an abrupt change of slope at $X_{TMU} \sim 0.20$. Time dependent fluorescence anisotropy decay of C153 has been found to be single-exponential at low TMU mole fractions (using an

instrument response function of ~90 ps) and bi-exponential at higher TMU mole fractions with well-separated timescales. The average rotational time, $\langle \tau_r \rangle$ of C153 shows rapid slowing down up to $X_{TMU} = 0.20$, indicating stronger solute-medium interaction, followed by gradual shortening of timescale upon further increase of TMU concentration in the water/TMU mixture. Behaviour of TMU in aqueous solutions resembles with those observed in aqueous aqueous EtOH solutions.

3.2 Experimental Section

3.2.1 Sample Preparation

Laser grade C153 and TMU, purchased from Exciton and Sigma–Aldrich respectively, were used as received. Deionized (Millipore) water was used for preparing different compositions of (TMU+Water) mixtures. The solutions were prepared by adding a measured amount of TMU into a measured amount of water in a volumetric flask followed by a gentle shaking of the solution for a few minutes. Proper caution was exercised to ensure the accuracy of mole fractions. Subsequently, few μL freshly prepared solution of C153 in heptane was poured into a quartz cuvette of optical path length 1 cm. The nonpolar solvent was then evaporated off by gently blowing hot air around outer surface of the cuvette. Subsequenly, 3–4 ml of aliquot was added to the cuvette and stirred the solution for sometimes to ensure complete dissolution of the C153 grains. Note that the concentration of C153 was maintained at ≤ 10^{-5} M in all TMU mole fractions studied here.

3.2.2 Data Collection and Analysis for Steady-state and Time-resolved Fluorescence Measurements

Absorption and fluorescence emission spectra were recorded using UV–Visible spectrophotometer (Model UV–2450, Shimadzu) and Fluorolog (Jobin–Yvon, Horiba) at controlled temperature for different TMU–Water solutions. Fluorescence emission was collected after adjusting the absorbance of the solutions ~0.1 with the excitation wavelength

fixed at 409 nm. Spectra were then processed by following the standard procedure[18,37-40] to obtain the spectral frequencies and widths [full-width-at-half-maxima (FWHM)].

The time-correlated single photon counting (TCSPC) technique based on a laser system (Lifespec–ps, Edinburgh, U.K.) with a light-emitting diode (LED) producing excitation at 409 nm was employed to collect the necessary sets of fluorescence emission intensity decays. The FWHM of the instrument response function (IRF) (measured by using water) was found to be ~90 ps. The sample cuvette was placed into a temperature controlled chamber. For dynamic anisotropy measurements, emission decays were collected at three different positions of emission polarizer, magic angle (54.7^0), parallel (0^0, $I_{\parallel}(t)$) and perpendicular (90^0, $I_{\perp}(t)$) with respect to the polarization of excitation. Further proceedings of the collected decays to obtain the rotational anisotropy decay, $r(t)$ of the solute C153 in the binary mixtures have already been described in chapter 2 with references.[41,42]

3.3 Results and Discussion

3.3.1 Steady State Spectroscopic Studies: Unusual Spectral Behaviour

Absorption and steady-state emission of C153 have been measured at various TMU mole fractions, X_{TMU} over the temperature range, T ~ 278 – 353 K. We have observed anomalous behaviour in absorption spectral shift of C153 at low X_{TMU}. Figure 3.1 represents the absorption and emission spectra of C153 at a few TMU solutions at T ~ 293K, showing the un-expected composition dependence of the spectral shift. Upper panel of this figure indicates that similar to (alcohol+water) binary mixtures,[17,18,20] aqueous TMU solutions also exhibit initial absorption spectral red-shift (up to X_{TMU} ~ 0.07). Then the absorption spectrum shifts to higher frequency (blue-shift) with further increase of X_{TMU} (middle panel). Lower panel shows the steady blue-shift of emission spectrum with increase of TMU concentration in the binary mixture. Both the absorption and emission spectral characteristics have been represented in Figure 3.2 in terms of spectral frequency, ν and width (FWHM), Γ
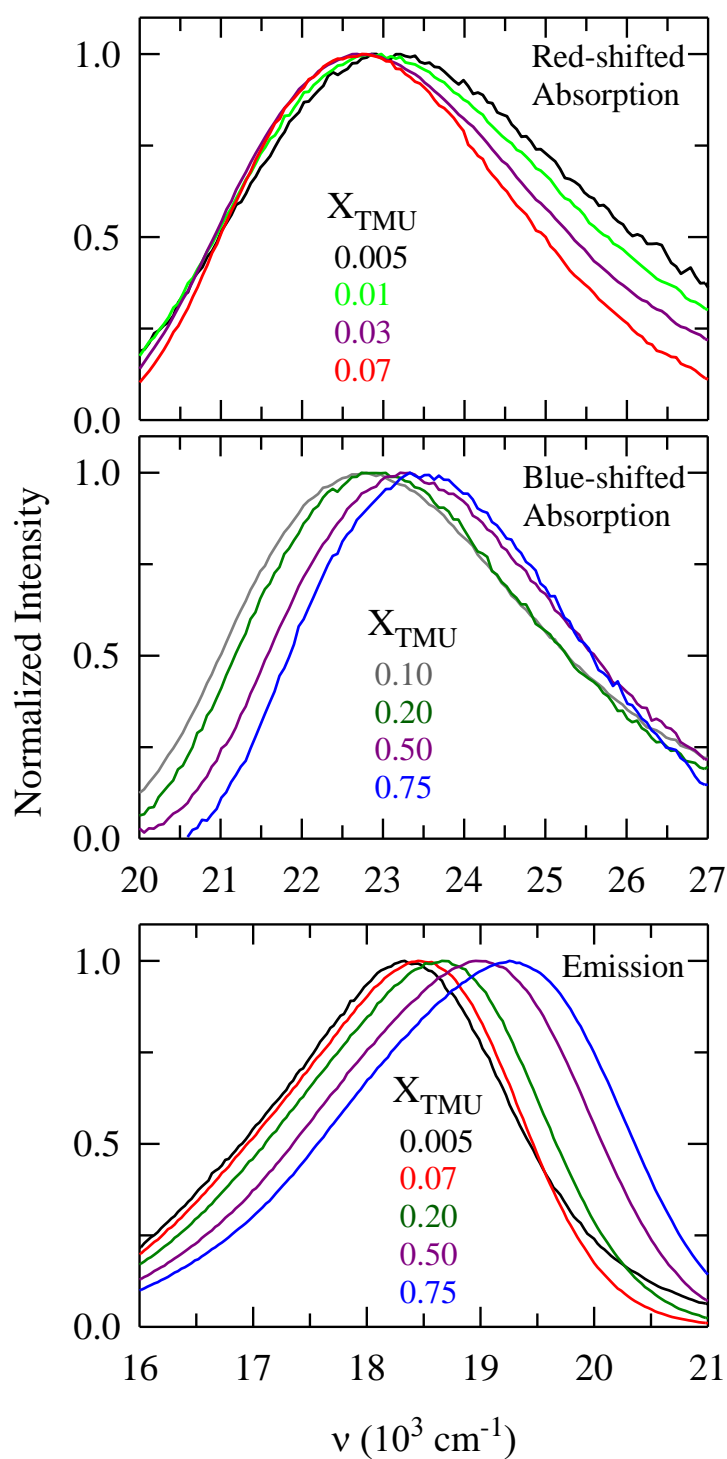
Figure 3.1: Absorption (upper and middle panels) and emission (lower) spectra of C153 at different TMU mole fractions, X_{TMU} into water at T = 293K. Each X_{TMU} is colour-coded and represented in the figure.
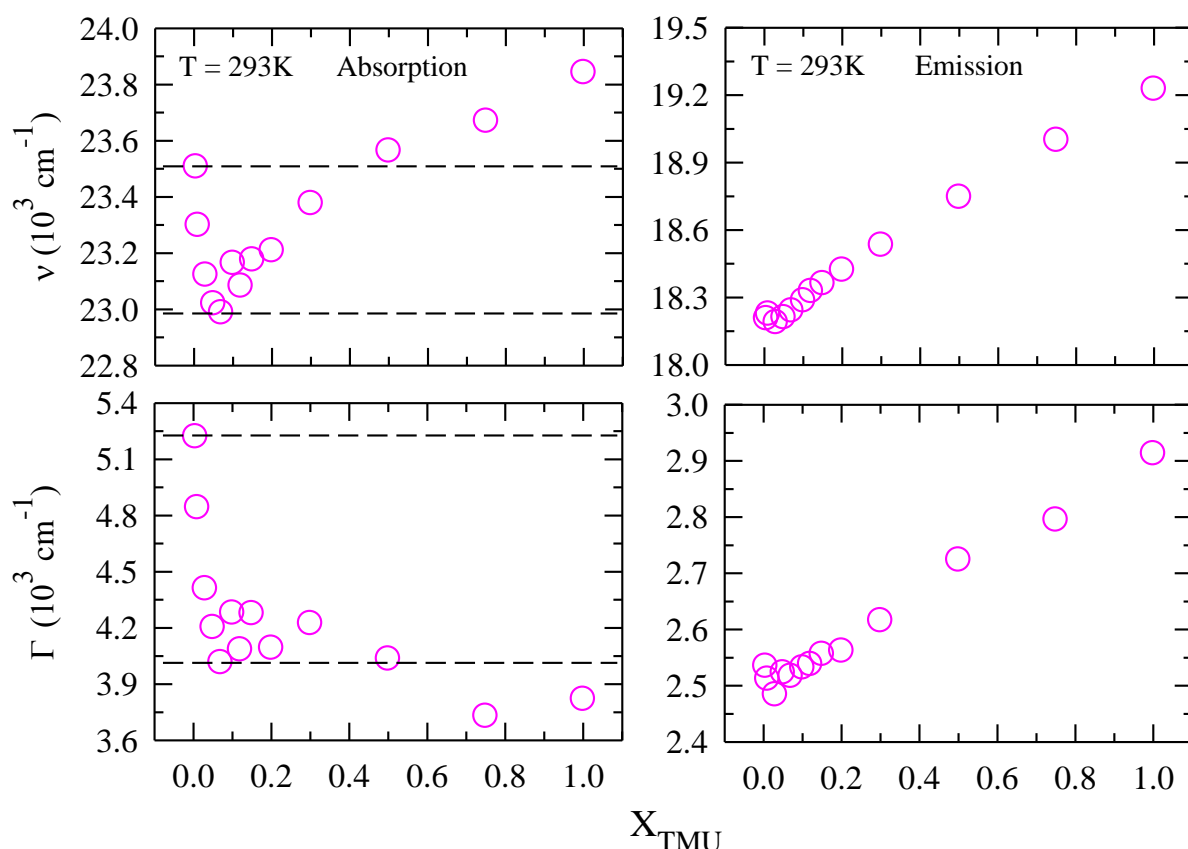
Figure 3.2: Variation of absorption and emission spectral frequency, ν (upper panels) and width, FWHM, Γ (lower panels) of C153 with increase of X_{TMU} into water at T = 293K. Dashed lines represent red-shift of absorption spectral ν and Γ at lower X_{TMU}. Here, ν is obtained by averaging over first moment frequency, peak frequency and half average frequency.

over the entire composition range. Note the total red-shift with respect to pure water is ~500 cm^{-1} (shown by the horizontal dashed lines).

We mentioned the absorption spectral red-shift as anomalous because the extra stabilization of energy levels of fluorophore C153 at low X_{TMU} for showing red-shift does not come from the average polarity of the medium as addition of TMU (static dielectric constant, $\varepsilon_0 \approx 23$)[43] into water ($\varepsilon_0 \approx 80$) reduces the same. Note here that computer simulation study of TMU–Water binary mixtures[6] suggests enhancement of solution structure. The H-bonding

interaction of water–water and water–TMU has been found to be increased upon addition of TMU in water. This stiffening of solution structure has been reflected by the lowering of frequency at low TMU concentrations. But solute's emission frequency did not sense this solution structural enhancement because of the longer excited-state lifetime of C153 which is 2–4 ns for this binary mixture. We have shown in our simulation study[6] that the average H-bond persistence time between two H-bonding specie in this system is in the order of sub-hundred picoseconds. Therefore, during the excited state lifetime of C153, surrounding environment undergoes many fluctuations, forcing the emission frequency to report only the averaged-out environmental effects. We have also noticed by comparing the present results with our previous studies of (alcohol+water) binary mixtures[18,20] that the extent of red-shift in absorption spectrum is highly dependent on the bulkiness of the hydrophobic moiety present in the molecule. The observed red-shift for TBA–H_2O binary mixture was ~1000 cm^{-1}, while it is ~500 cm^{-1} for EtOH–H_2O and 2-butoxyethanol (BE)–H_2O mixtures. Absorption and emission spectral widths which have been shown in the lower panels of Figure 3.2 behave in a manner similar to that observed in aqueous solutions of alcohols.[17,18,20] The initial narrowing (~1200 cm^{-1}) and broadening of spectral widths, respectively, for absorption and emission spectra with increasing X_{TMU} are characteristics of the binary mixtures due to complex medium effects, although reverse is seen in neat liquids.[37]

In Figure 3.3, excitation wavelength $\left(\lambda_{ex.}\right)$ dependence of emission of C153 in this binary mixture has been monitored at low TMU concentrations where abnormality was found in absorption spectral behaviour. Excitation wavelength dependent emission study is very informative for the systems where microscopic inhomogeneous domains are formed even at ambient condition due to competing interactions in a variety of systems, for example, deep eutectic solvents, ionic liquids etc.[44-47] In viscous media, emission spectrum shifts to lower frequency on moving towards longer excitation wavelengths. This phenomenon is known as red-edge-effect (REE).[48-50] Although, here the viscosity of the medium is very low,[51] the most dilute TMU solution, $X_{TMU} = 0.005$ exhibits the maximum $\lambda_{ex.}$-dependent ν_{em}, $\Delta\nu_{em}\left(\lambda_{ex.}\right) = \nu_{em}(380nm) - \nu_{em}(480nm) \sim 400\, cm^{-1}$, whereas, neat TMU shows $\Delta\nu_{em}\left(\lambda_{ex.}\right) = 40\, cm^{-1}$ (upper panel). Further increase of X_{TMU} reduces the $\Delta\nu_{em}\left(\lambda_{ex.}\right)$. Lower
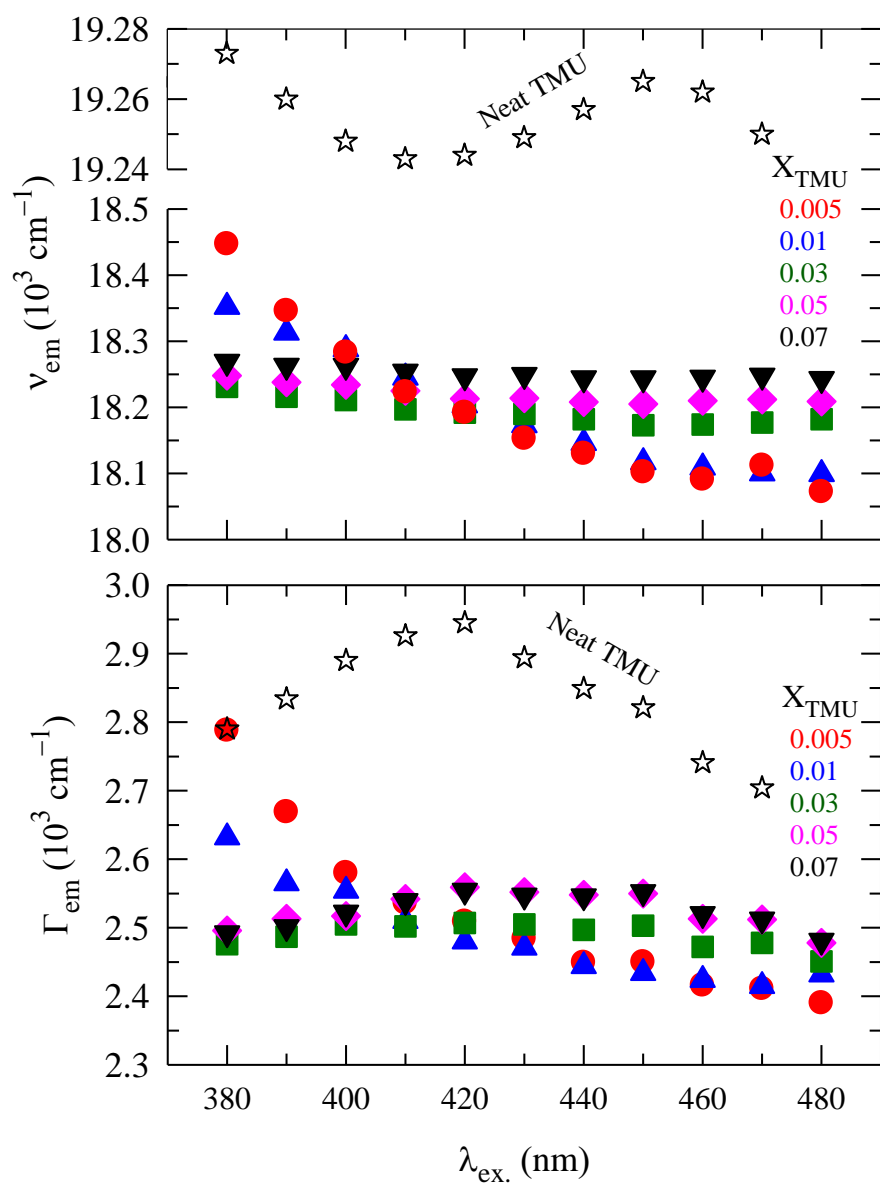
Figure 3.3: Excitation wavelength $(\lambda_{ex.})$ dependent emission spectral frequency, ν_{em} (upper panel) and Γ_{em} (lower panel) of C153 at various TMU mole fractions at T = 293K. Representation of each TMU mole fraction is colour-coded.

panel shows the similar $\lambda_{ex.}$-dependence on Γ_{em}. This suggests that solution with $X_{TMU} \sim 0.005$ is the most spatially heterogeneous among the TMU mole fractions studied here. Support such a view can be accessed from simulation studies which suggest that aggregation of TMU molecules in aqueous mixtures takes place at low TMU concentrations.[4-6] It also suggests that at $X_{TMU} = 0.005$ the aggregated domains are sufficiently longer-lived to be detected via the excitation wavelength dependent study.

3.3.2 Search for Temperature Maximum of Absorption Red-shift

Next we have investigated the temperature effects on the absorption and emission spectra. In Figure 3.4, temperature dependent absorption spectral red-shift is shown. The red-shift grows upon increasing temperature from 278K. It reaches maximum at T = 293K. Then red-shift decreases gradually with further increase of temperature.
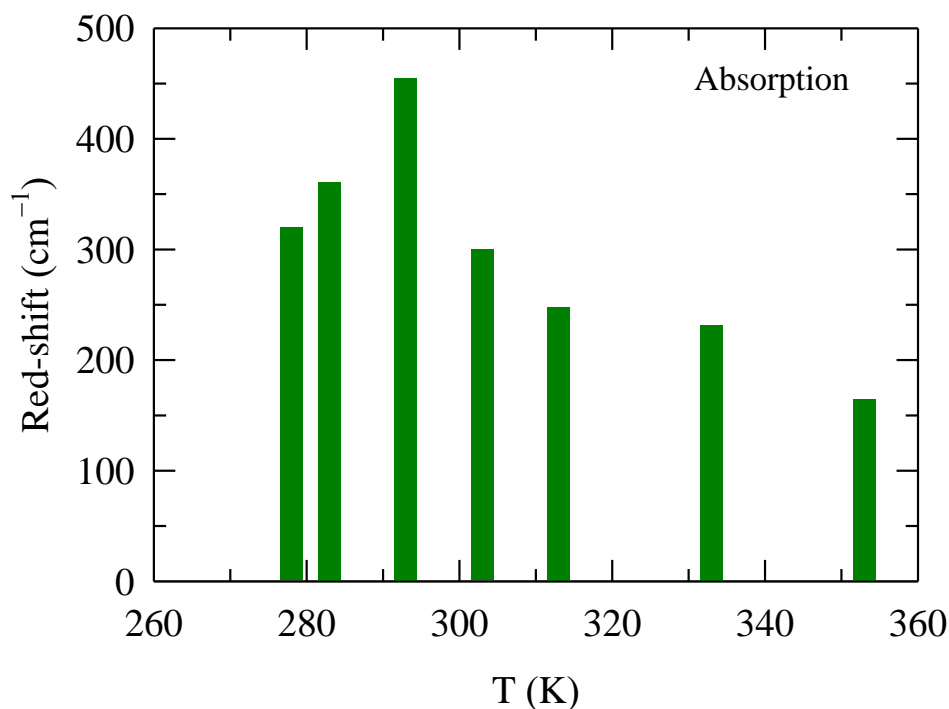
Figure 3.4: Temperature dependent absorption spectral red-shift of C153 at low TMU concentrations.

Previous studies also found that the temperature-assisted aggregation due to hydrophobic interaction of small nonpolar solutes and amphiphilic molecules in dilute aqueous solutions.[19,52-56] Here the growth of absorption spectral red-shift up to 293K may suggest an enhancement of the hydrophobic interaction among the –N methyl groups of TMU leading to the aggregation of TMU molecules in aqueous solutions at low concentrations.[4-6] Largest extent of red-shift at T = 293K may therefore indicate maximization of hydrophobic interaction among methyl groups at this temperature. In aqueous solution of TBA, small-angle neutron scattering (SANS) study showed that TBA clustering reaches the maximum for $X_{TBA} = 0.04$ at ~353K.[16] But the fluorescence spectroscopic study of TBA–Water system[19] could not capture the temperature maximum probably due to the presence of the third component C153 for reasons suggested for the ternary system of cyclohexene–TBA–water[57]. In Figure 3.5, the change of emission frequency of C153 in dilute TMU solutions with temperature displays only blue-shift, suggesting nothing but the lowering of average polarity of the medium with temperature[19].
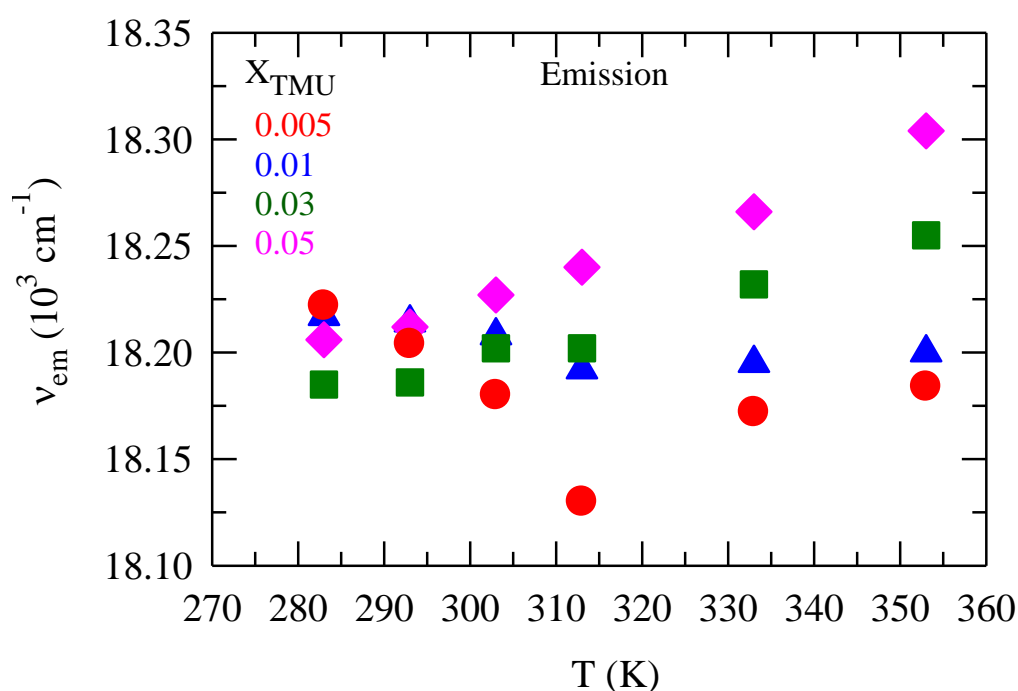
Figure 3.5: Temperature dependence of emission spectral frequencies at a few representatives TMU mole fractions in the dilute limit.

3.3.3 Time-resolved Fluorescence Emission Studies

The average excited-state lifetime $\left\langle \tau_{life} \right\rangle$ of C153 at different compositions of TMU into water has been obtained by fitting the magic angle (54.7^0) fluorescence emission decay with bi-exponential functions (best numerical representation) at all the TMU concentrations studied here. The fitting parameters are summarized in Table 3.1. A careful observation of these time constants reveals that the long time constant τ_1 represents the excited-state lifetime of C153 whereas the short time constant τ_2 associates with solvent reorganization. The upper and middle panels of Figure 3.6 represent, respectively, the distribution of long and short time constants multiplied by the weightage of the corresponding amplitudes. Both the amplitude-weighted long $\left(a_1 \tau_1 \right)$ and short $\left(a_2 \tau_2 \right)$ time constants describe different slopes (represented by the dashed lines) depending upon the TMU mole fractions. The intersection of two slopes for $a_1 \tau_1$ takes place at $X_{TMU} \sim 0.20$ while that for $a_2 \tau_2$ occurs at $X_{TMU} \sim 0.10$. These two different mole fractions may represent H-bond stiffening of the local solvation structure at the lower mole fraction (picked up by the faster of the two decay components) and over-all structural change at the higher mole fraction where, much like in alcohol-water systems, three dimensional H-bond network of water gives way for the two dimensional solution structure after a certain mixture composition. Note also that the slope change for $a_2 \tau_2$ occurs at a TMU mole fraction very close to that ($X_{TMU} \sim 0.07$) where the largest absorption red-shift has been recorded.

Table 3.1: Bi-exponential fit parameters for magic angle fluorescence emission decays and average fluorescence lifetimes $\left(\langle \tau_{life} \rangle = [a_1\tau_1 + a_2\tau_2]/[a_1 + a_2]; a_1 + a_2 = 1 \right)$ of C153 at various TMU mole fractions at T = 293K.

X_{TMU}	a_1	τ_1/ns	a_2	τ_2/ps	$\langle \tau_{life} \rangle$/ns
0.005	0.70	2.124	0.30	181	1.541
0.01	0.91	2.230	0.09	707	2.093
0.03	0.87	2.540	0.13	345	2.255
0.05	0.78	2.743	0.22	95	2.160
0.07	0.86	2.897	0.14	115	2.508
0.10	0.83	3.070	0.17	106	2.566
0.12	0.83	3.182	0.17	92	2.657
0.15	0.85	3.344	0.15	313	2.889
0.20	0.89	3.593	0.11	455	3.248
0.30	0.79	3.994	0.21	197	3.197
0.50	0.77	4.617	0.23	192	3.599
0.75	0.66	5.076	0.34	79	3.377
1.00	0.84	5.312	0.16	116	4.481

In the lower panel of the figure we show the composition dependent $\langle \tau_{life} \rangle$ of C153 in TMU– water solutions and compared with those measured for the other three different aqueous alcohol (EtOH, TBA, BE) solutions.[18,20] We observed very similar behaviour of the (TMU+Water) and (EtOH+Water) binary mixtures. Both the binary mixtures encounter the over-all solution structural transition at $X_{TMU,EtOH} = 0.20$, whereas, the transition occurs for TBA–Water and BE–Water solutions at $X_{TBA} = 0.10$ and $X_{BE} = 0.04$ respectively. We can see from Scheme 3.1 and Table 3.2[43,58-62] that size of TMU is greater than EtOH as the former contains larger hydrophobic moieties, although they possess nearly equal solvent polarity. Table 3.2 also indicates that presence of cosolvent with relatively less polarity (as represented by ε_0) shifts the transition mole fraction to lower cosolvent concentration. This suggests that besides the size of the hydrophobic groups, polarity of the cosolvent also plays an important role in determining the transition composition.
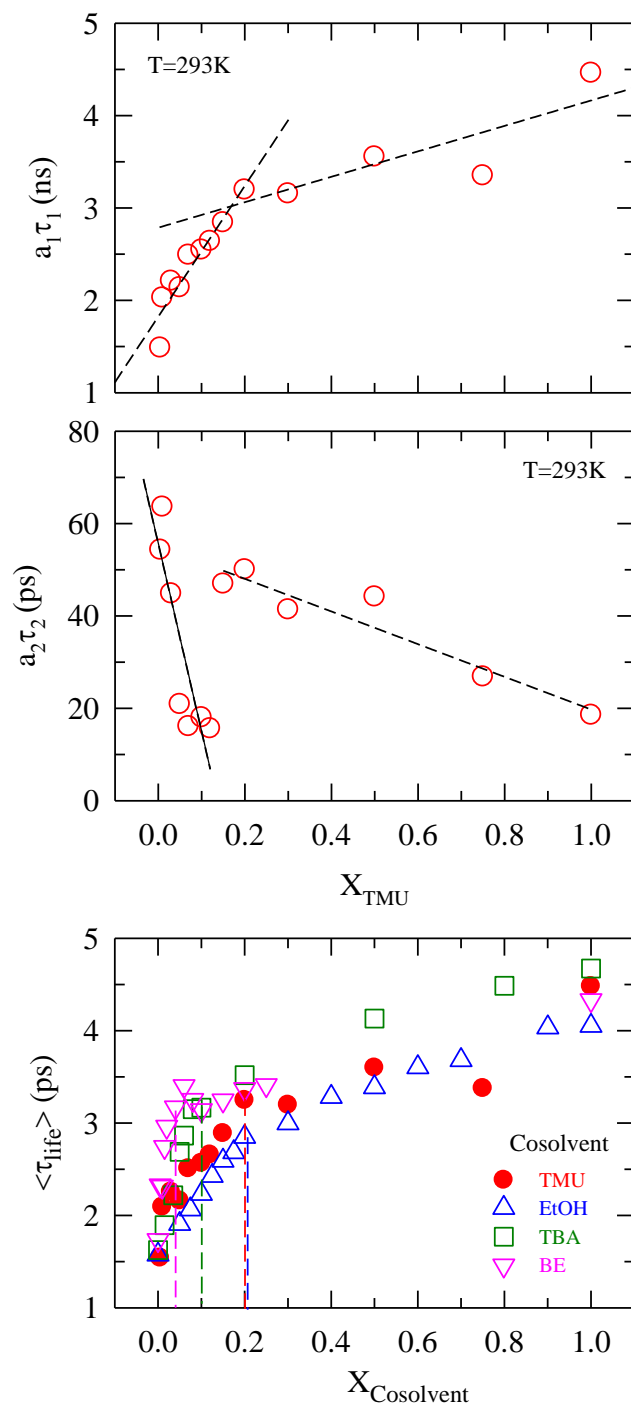
Figure 3.6: X_{TMU} -dependence of the time constants (amplitude weighted) for bi-exponential fit of excited-state fluorescence lifetime decay (upper and middle panels) and average life $\langle \tau_{life} \rangle$ of C153 (lower panel) at T = 293K. For comparison $\langle \tau_{life} \rangle$ of C153 in EtOH+Water, TBA+Water and BE+Water binary mixtures are also plotted in lower panel. Dashed lines in the lower panel are shown to indicate the cosolvent mole fraction at which slope changes due to structural transition.

Table 3.2: Static dielectric constant $\left(\varepsilon_0\right)$ and radius (r) of four different cosolvents of water.

Cosolvent	ε_0	r (Å)
EtOH	24	2.33
TMU	23	3.50
TBA	12	2.76
BE	9	3.15

Table 3.3: Fit parameters for $r(t)$ decays and average rotational time, $\langle \tau_r \rangle$ of C153 at various concentrations of TMU in water at ~293K.

X_{TMU}	a_1	τ_1/ps	a_2	τ_2/ps	$\langle \tau_r \rangle$/ps
0.005	1.00	53			53
0.01	1.00	69			69
0.03	1.00	98			98
0.05	0.52	227	0.48	33	133
0.07	0.51	279	0.49	37	159
0.10	0.58	315	0.42	29	194
0.12	0.58	368	0.42	33	229
0.15	0.65	346	0.35	26	234
0.20	0.64	399	0.36	19	263
0.30	0.54	389	0.46	32	223
0.50	0.53	248	0.47	24	143
0.75	0.38	173	0.62	28	83
1.00	1.00	59			59

We have further explored how the rotation of the solute C153 gets affected in this binary mixture. Dynamic fluorescence anisotropy $r(t)$ has been constructed by equation 1. Single exponential function of time was required for adequate fitting of $r(t)$ decays at very low TMU concentrations and pure components, whereas, $r(t)$ decays at other higher TMU concentrations were fitted by double exponential function. All the fitting parameters along with the average rotational time $\langle \tau_r \rangle$ are provided in Table 3.3. Note that these well separated two time constants arise due to the inherent nature of the underlying time-

dependent friction.[41] Representative $r(t)$ decay and corresponding residual of C153 in $X_{TMU} = 0.05$ at T = 293K are shown in Figure 3.7. Here, the residual reflects the goodness of bi-exponential fitting.
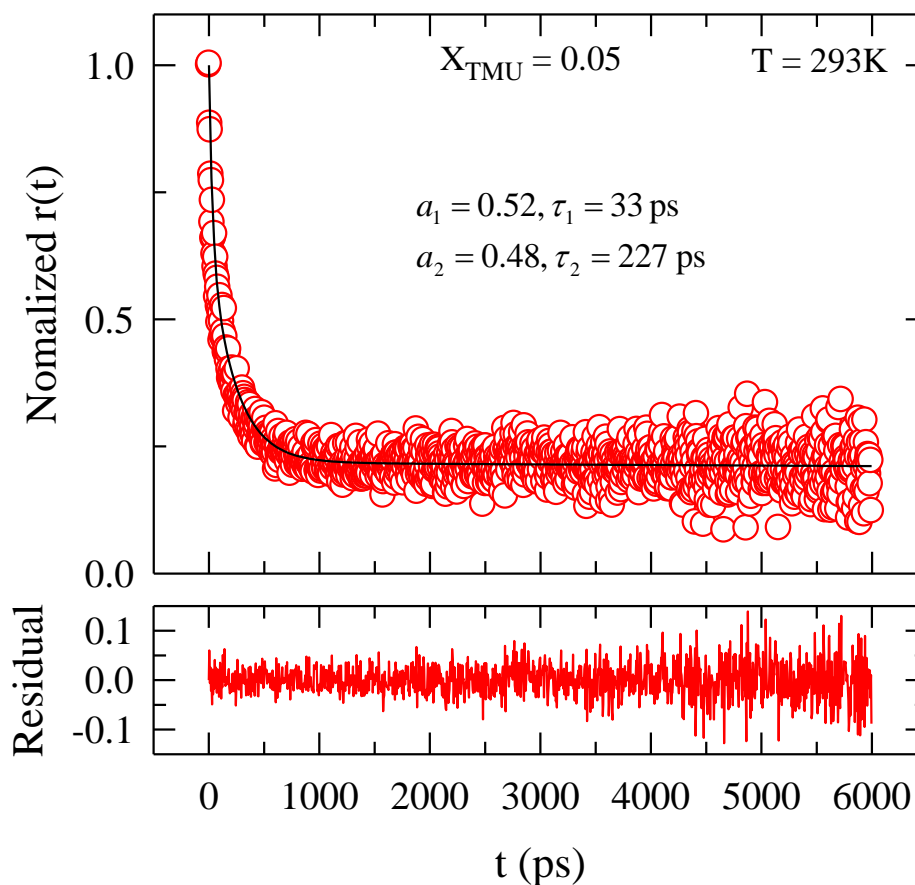
Figure 3.7: Normalized fluorescence rotational anisotropy decay, $r(t)$ (red circles, upper panel) of C153 with bi-exponential fitting (solid black line, upper panel) in $X_{TMU} = 0.05$ at ~293K and corresponding residual of the fit (lower panel). Fitting parameters are also summarized in the inset of upper panel.

Figure 3.8 depicts composition dependence of $\langle \tau_r \rangle$ in TMU-water mixtures, and compares with the data obtained for C153 in aqueous solutions of EtOH[18] , TBA[18] and BE.[20] The interesting aspect of this figure is that $\langle \tau_r \rangle$ increases gradually with increase of X_{TMU} up to

$X_{TMU} = 0.20$. Then $\langle\tau_r\rangle$ suddenly changes its slope and decreases continuously up to $X_{TMU} = 1.00$. Here also the slope change of $\langle\tau_r\rangle$ takes place at the same concentration $(X_{TMU} = 0.20)$ where $\langle\tau_{life}\rangle$ altered the slope.
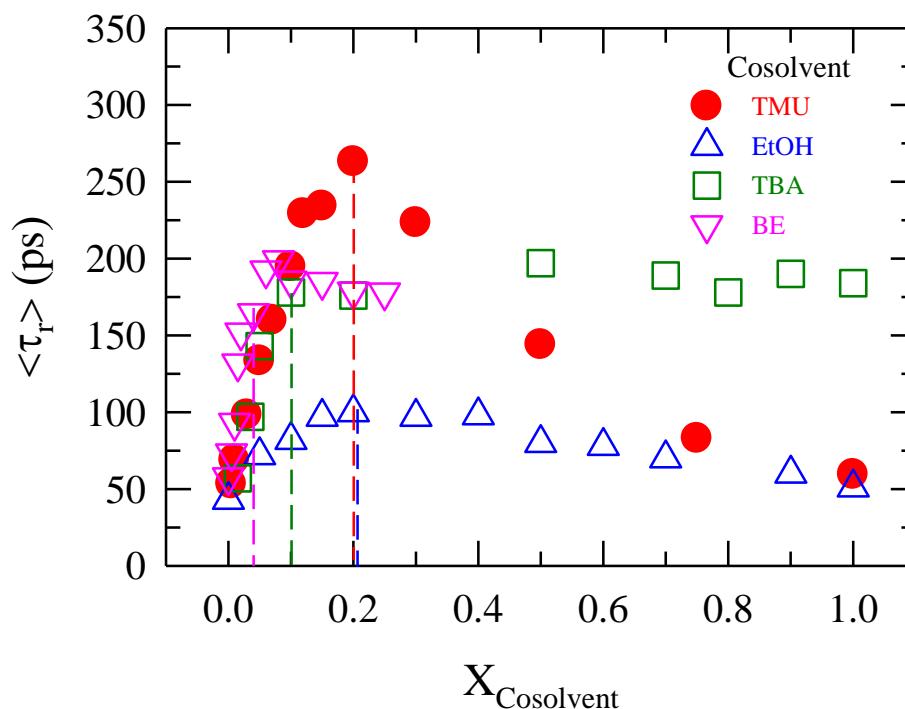
Figure 3.8: Variation of average rotational time, $\langle\tau_r\rangle$ of C153 with increase of cosolvent concentration into water, $X_{Cosolvent}$. Dashed lines are shown to indicate the $X_{Cosolvent}$ where solution structural transition takes place. Symbolic representations of cosolvents are given in the figure.

The rotational behaviour of C153 at various X_{TMU} correlates well with the viscosity of the aqueous TMU solutions.[51] Including viscosity other physicochemical properties of this binary mixture, such as, density, ultrasonic absorption, sound velocity have been also found to attain the maximum at $X_{TMU} = 0.20$. Although the concept of formation of "tetramethylurea tetrahydrate" at $X_{TMU} = 0.20$ prevailed for sometimes,[63] subsequent computer simulation

study ruled out that possibility[64]. By comparing the $\langle \tau_r \rangle$ values of C153 at various compositions of other cosolvents (TMU, EtOH, TBA, BE) in water, we found that in presence of either of the cosolvent TMU or EtOH, aqueous solutions undergo solution structural transition at equivalent composition of the cosolvent $\left(X_{TMU,EtOH} = 0.20 \right)$. The decreasing order of $X_{Cosolvent}$, at which the transition occurs, is $X_{TMU} \approx X_{EtOH} > X_{TBA} > X_{BE}$. The maximum slowing down at lower mole fractions of the cosolvents has been observed for (TMU+Water) binary mixture. This indicates that TMU induces comparatively more ordering in the structure of the aqueous solutions. Hence, these four N–methyl groups of TMU acts in the similar way as methyl groups of alcohol molecules do.

We have also explored the temperature effect on the $\langle \tau_r \rangle$ of C153 for different TMU solutions in Figure 3.9, but did not observe any irregularity for any particular TMU concentration. $\langle \tau_r \rangle$ becomes faster with increase of temperature for all the compositions studied here suggesting only the lowering of viscosity of the medium with rise of temperature solely dictates the solute rotation at a given composition of this binary mixture.
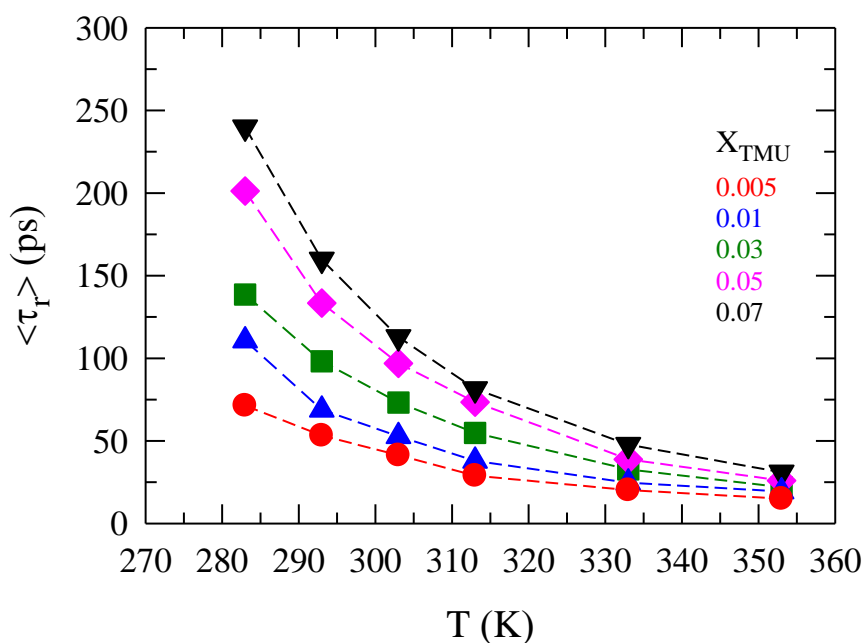
Figure 3.9: Temperature dependence of $\langle \tau_r \rangle$ of C153 at various TMU mole fractions, X_{TMU}.

3.4 Conclusion

In summary, our present experimental results indicate the hydrophobic nature of N–methyl groups of TMU,[1] and suggest effects on structure of aqueous solution as those observed for several water-alcohol binary mixtures. Strengthening of H-bond structure of water found in simulation study has been reflected here by the observed red-shift of the absorption spectrum of C153 at the lower concentration of TMU. Excitation wavelength dependence of the emission of C153 at very low TMU mole fraction also confirms the aggregation of TMU molecules at very dilute condition.[4-6] Interestingly, we have seen the presence of temperature maximum for hydrophobic interaction induced aggregation in TMU-water binary mixtures, which was observed before via SANS measurements for aqueous solutions of TBA[16]. By analogy to water-alcohol mixtures, we propose that TMU also induces transition from tetrahedral H-bond network to chain-like H-bond structure upon successive addition of TMU in water. A comparison to observation made earlier for aqueous alcohol mixtures reveals that this transition point depends upon both the size of the hydrophobic (here alkyl groups) moiety attached to the cosolvent molecules and the cosolvent polarity.

References

1. Y. Koga, P. Westh, K. Nishikawa and S. Subramanian, J. Phys. Chem. B **115**, 2995 (2011).

2. C. N. Pace and H. F. Marshall, Arch. Biochem. Biophys. **199**, 270 (1980).

3. G. Barone, P. del Vecchio, C. Giancola and G. G. Graziano, Thermochim. Acta, **227**, 67 (1993).

4. Y. Marcus, Phys. Chem. Chem. Phys. **4**, 4462 (2002).

5. L. Almásy, A. Len, N. K. Székely and J. Pleštil, Fluid Phase Equilib. **257**, 114 (2007).

6. S. Indra and R. Biswas, Mol. Sim. **41**, 471 (2015).

7. F. Franks and D. J. G. Ives, Q. Rev. Chem. Soc. **20**, 1 (1966).

8. G. S. Beddard, D. T. and J. Hudales, Nature **294**, 145 (1981).

9. M. Brai and U. Kaatze, J. Phys. Chem. **90**, 8946 (1992).

10. A. K. Soper and F. J. L., Phys. Rev. Lett. **71**, 4346 (1993).

11. K. Yoshida and T. Yamaguchi, Z. Naturforsch. **56A**, 529 (2001).

12. S. Dixit, J. Crain, W. C. K. Poon, J. L. Finney and A. K. Soper, Nature **416**, 829 (2002).

13. S. S. N. Murthy, J. Phys. Chem. A **103**, 7927 (1999).

14. D. Wojtkow and M. Czarnecki, J. Phys. Chem. A **109**, 8218 (2005).

15. P. G. Kusalik, A. P. Lyubertsev, D. L. Bergman and A. Laaksonen, J. Phys. Chem. B **104**, 9533 (2000).

16. D. T. Bowron and J. L. Finney, J. Phys. Chem. B **111**, 9838 (2007).

17. T. Pradhan, P. Ghoshal and R. Biswas, J. Phys. Chem. A **112**, 915 (2008).

18. T. Pradhan, P. Ghoshal and R. Biswas, J. Chem. Sci. **120**, 275 (2008).

19. H. A. R. Gazi and R. Biswas, J. Phys. Chem. A **115**, 2447 (2011).

20. S. Indra and R. Biswas, J. Chem. Phys. **142**, 204501 (2015).

21. Y. Koga, J. Phys. Chem. **100**, 5172 (1996).

22. R. Gupta and G. N. Patey, J. Phys. Chem. B **115**, 15323 (2011).

23. T. A. Pascal and W. A. Goddard, J. Phys. Chem. B **116(47)** (13905) (2012).

24. V. Matvejev, M. Zizi and J. Stiens, J. Phys. Chem. B **116(48)**, 14071 (2012).

25. Y. Koga, K. Nishikawa and P. Westh, J. Phys. Chem. A **108**, 3873 (2004).

26. Y. Marcus, J. Mol. Liq. **158**, 23 (2011).

27.   S. Roy, S. Banerjee, N. Biyani, B. Jana and B. Bagchi, J. Phys. Chem. B **115**, 685 (2011).

28.   K. Tielrooij, J. Hunger, R. Buchner, M. Bonn and H. J. Bakker, J. Am. Chem. Soc. **132**, 15671 (2010).

29.   Y. L. A. Rezus and H. J. Bakker, J. Phys. Chem. A **112**, 2355 (2008).

30.   Y. L. A. Rezus and H. J. Bakker, Phys. Rev. Lett. **99**, 148301 (2007).

31.   K. Mazur, I. A. Heisler and S. R. Meech, J. Phys. Chem. B **115**, 2563 (2011).

32.   D. Laage, G. Stirnemann and J. T. Hynes, J. Phys. Chem. B **113**, 2428 (2009).

33.   G. Stirnemann, F. Sterpone and D. Laage, J. Phys. Chem. B **115**, 3254 (2011).

34.   W. H. Brandeburgo, S. T. van der Post, E. J. Meijerab and B. Ensing, Phys. Chem. Chem. Phys. **17**, 24968 (2015).

35.   G. Hummer, J. C. Rasaiah and J. P. Noworyta, Nature **414**, 188 (2001).

36.   Y. Xu, R. Gnanasekaran and D. M. Leitner, J. Atom. Mol. Opt. Phys., 125071 (2012).

37.   M. L. Horng, J. A. Gardecki, A. Papazyan and M. Maroncelli, J. Phys. Chem. B **99**, 17311 (1995).

38.   R. Biswas, J. E. Lewis and M. Maroncelli, Chem. Phys. Lett. **310**, 485 (1999).

39.   J. E. Lewis, R. Biswas, A. G. Robinson and M. Maroncelli, J. Phys. Chem. B **105**, 3306 (2001).

40.   T. Pradhan and R. Biswas, J. Phys. Chem. A **111**, 11514 (2007).

41.   M. L. Horng, J. A. Gardecki and M. Maroncelli, J. Phys. Chem. A **101**, 1030 (1997).

42.   K. Dahl, R. Biswas, N. Ito and M. Maroncelli, J. Phys. Chem. B **109**, 1563 (2005).

43.   A. Fratiello, R. E. Lee, D. P. Miller and V. M. Nishida, Mol. Phys. **13**, 349 (1967).

44.   B. Guchhait, H. A. R. Gazi, H. K. Kashyap and R. Biswas, J. Phys. Chem. B **114**, 5066 (2010).

45.   A. Das and R. Biswas, J. Phys. Chem. B **119**, 10102 (2015).

46.   H. Jin, X. Li and M. Maroncelli, J. Phys. Chem. B Lett. **111**, 13473 (2007).

47.   P. K. Mandal, M. Sarkar and A. Samanta, J. Phys. Chem. A **108**, 9048 (2004).

48.   J. R. Lakowicz, *Principles of Fluorescence Spectroscopy*. (Kluwer Academic, New York, 1999).

49.   W. C. Galley and R. M. Purkey, Proc. Natl. Acad. Sci. U.S.A. **67**, 1116 (1970).

50.   A. P. Demchenko, Luminescence **17**, 19 (2002).

51.   E. P. G. Arêas, J. A. G. Arêas, J. Hamburger, W. L. Peticolas and P. S. Santos, J. Colloid Interface Sci. **180**, 578 (1996).

52.   G. W. Euliss and C. M. Sorensen, J. Chem. Phys. **80**, 4767 (1984).

53.   T. M. Bender and R. Pecora, J. Phys. Chem. **92**, 1675 (1988).

54.   T. M. Raschke, J. Tsai and M. Levitt, Proc. Natl. Acad. Sci. U.S.A. **98**, 5965 (2001).

55.   D. Paschek, J. Chem. Phys. **120**, 6674 (2004).

56.   N. Ito, T. Kato and T. Fujiyama, Bull. Chem. Soc. Jpn. **54**, 2573 (1981).

57.   D. T. Bowron and S. D. Moreno, J. Phys. Chem. B **109**, 16210 (2005).

58.   G. B. Dutt and S. Doraiswamy, J. Chem. Phys. **96**, 2475 (1992).

59.   G. B. Dutt, S. Doraiswamy and N. Periasamy, J. Chem. Phys. **94**, 5360 (1991).

60.   G. Douhéret and A. Pal, J. Chem. Eng. Data **33**, 40 (1988).

61.   R. Biswas, Ph.D thesis, IISc. Bangalore, 1998.

62.   in *www.chemicalize.org*.

63.   K. Sasaki and K. Arakawa, Bull. Chem. Soc. Jpn. **46**, 2738 (1973).

64.   P. Belletato, L. C. G. Freitas, E. P. G. Arêas and P. S. Santos, Phys. Chem. Chem. Phys. **1**, 4769 (1999).

Chapter 4

Structural Anomaly in Cycloether/Water Binary Mixtures: Signatures from Composition Dependent Dynamic Fluorescence Measurements and Computer Simulations

4.1 Introduction

Due to nearly zero dipole moment $(\mu = 0.45\,D)$,[1] continuum dielectric theory fails to predict the nuclear reorganization energy of nondipolar solvent 1,4-dioxane (Diox) in response to an altered charge distribution of a dissolved dipolar solute. Diox produces comparable fluorescence Stokes shift for solvatochromic probe coumarin 153 (C153) to that in tetrahydrofuran (THF), a moderately dipolar solvent possessing a dipole moment of 1.75 D.[1] This unexpected observed shift for C153 in Diox was correlated[1] with the solute–solvent dipole–quadrupole and higher order multipole interactions. The chemical structures of these two solvents, THF and Diox (shown in Scheme 4.1), are similar and contain polar CH_2–O–CH_2 group/groups. But the molecular symmetry results negligible μ value for Diox. Another striking feature associated with these molecules is that aqueous solution of THF exhibits a closed immiscibility loop with a lower consolute temperature (LCST) of $T_L^C = 344K$ (superheated regime, boiling point of THF = 339K) with critical concentration $X_{THF}^C = 0.225$ and an upper consolute temperature (UCST) of about $T_U^C = 410K$,[2] whereas Diox is completely miscible in water at all temperatures[3] (boiling point of Diox = 374K[4]). Despite the non-existence of a critical point for Diox/water system, aqueous solutions of both THF and Diox show anomalous behaviour in thermodynamic properties,[5-9] ultrasonic velocity[10] and absorption,[11] and explained in terms of concentration fluctuations.[5-11]
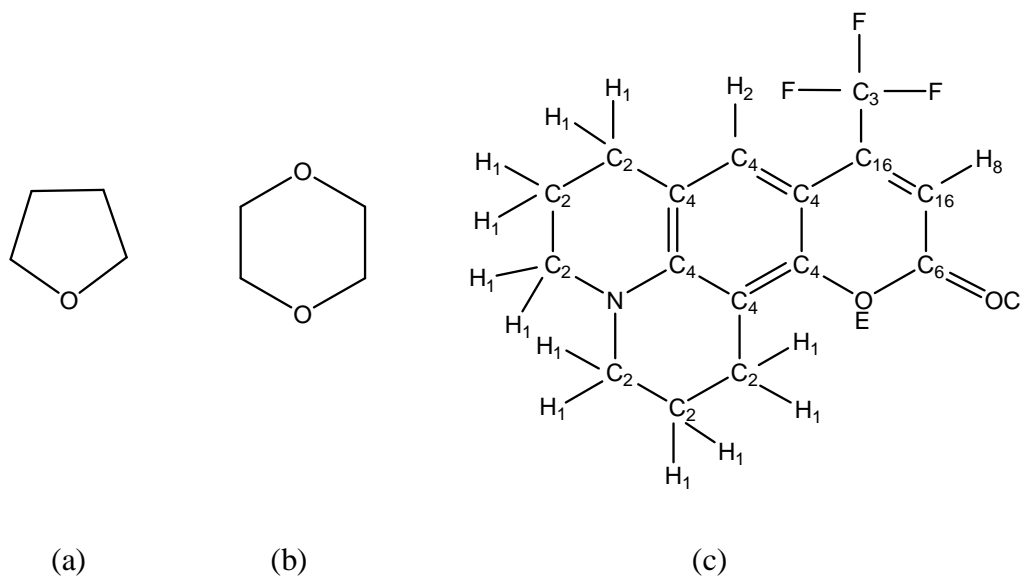
Scheme 4.1: Chemical structures of (a) Tetrahydrofuran (THF), (b) 1,4-dioxane (Diox) and (c) Coumarin 153 (C153). Representation of different atomic sites of C153 is shown here as used in the simulations of radial distribution function (RDF).

Correlation lengths associated with concentration fluctuations in these aqueous binary mixtures revealed by various experimental techniques differs significantly from one another. For example, laser light scattering[12] showed the existence of dynamic correlation length of ~200–600 nm, whereas small angle neutron scattering (SANS)[13,14] suggested the largest length of ~2 nm. Several other measurements such as Rayleigh light scattering,[15] low frequency Raman scattering,[16,17] nuclear magnetic resonance (NMR),[18,19] X-ray diffraction,[18] Mass spectroscopy,[18,20] X-ray scattering,[13,21] dielectric relaxation[22-24] further reported on this aspect and observed different mixing schemes depending on concentration of these cycloethers in water. Raman scattering[16,17] study showed that the tetrahedral H-bonding network of water collapses at $X_{ether} \sim 0.2 - 0.3$. While the effects of hydrophobic moieties on retaining the characteristic water structure were explored by mass spectroscopy,[20] NMR[19] measurements suggested hydrophobic moiety does not play any role in inducing anomalous polarization of water molecules; H-bonding basicity of the polar group is the determining factor here. Later, solvation dynamics study of different solvatochromic probes in Diox+Water binary mixtures correlated the slower rotational diffusion of the Diox–water

oligomeric species as the origin of the longer timescale.[25,26] Interestingly, dynamic light scattering (DLS)[27] study in THF/water mixtures reported growth of concentration fluctuation correlation length while approaching liquid–liquid lower critical solution point with a critical point exponent[28] value of 0.65 and the effect was prominent at room temperature which is far from the LCST. Similar kind of growth of the correlation length was also found in 2-butoxyethanol (BE)/water binary mixtures with a closed-loop miscibility gap,[29] but we observed no role for the critical fluctuations preceding phase separation from time-resolved fluorescence spectroscopic measurements.[30]

In aqueous solution, THF and Diox molecules do not involve in hydrogen bonding (H-bonding) interaction among themselves due to lack of donor hydrogen atoms, but they can form H-bond with water by the acceptor oxygen atoms. Therefore, the study of aqueous solutions of these cycloethers provides an avenue to investigate how they affect the tetrahedral H-bond network structure of water. In steady-state absorption and fluorescence spectroscopic measurements, the added solute (usually present at $\leq 10^{-5}\,\mathrm{M}$) reports about modification in the solute–medium interaction upon variation of concentration of the cosolvent in the binary mixture via changes in the spectral frequencies and widths. These spectral changes are reflection of the cosolvent-induced changes in the equilibrium structure of the binary mixture. Time-resolved fluorescence measurements, on the other hand, inform on alteration of relaxation dynamics due to the structural changes in the solution. We would, however, like to mention here that although the composition dependent absorption and fluorescence spectroscopic changes are often interpreted in terms of solute-solvent direct interaction (a sort of nearest-neighbour events), these collective measurements sense modifications over large lengthscale where participation of many molecules takes place. In such a situation, computer simulations provide an effective tool for detail understanding of the interactions at the microscopic level. However, presence of only a few such studies[31-36] with the primary focus of most of them[34-36] being on the molecular mechanism of phase separation has not served the purpose. This has been the principal motivation for us to perform molecular dynamics (MD) simulation study along with spectroscopic (steady state and time-resolved) measurements of THF/water and Diox/water binary mixtures employing coumarin 153 (C153) as a solute probe (Scheme 4.1). In this study, the following solution

aspects have been addressed: (i) whether presence of critical point affects the structure of the solution differently, (ii) how the structural changes of the solution alters the dynamics (as reported by the probe solute) of these media, and (iii) whether the modifications in solution structural and dynamical aspects bear any signature of cycloether identity.

4.2 Experimental and Simulation Details

4.2.1 Sample Preparation

Laser grade C153 were purchased from Exciton and was used as received. Dioxane and THF (spectroscopic grade) were obtained from Sigma–Aldrich. Deionized (Millipore) water was used for preparing aqueous solutions of THF and dioxane. Same method was followed to prepare composition dependent THF/water and Diox/water solutions as described in literature.[30]

4.2.2 Steady-state and Time-resolved Spectroscopic Measurements

Absorption spectra of temperature equilibrated (Julabo) aqueous THF solutions were recorded using UV–Visible spectrophotometer (Model UV–2450, Shimadzu). The emission spectra were recorded (SPEX Fluoromax–3, Jobin–Yvon, Horiba) after adjusting the absorbance of the solutions ~0.1 with excitation wavelength fixed at 409 nm. The spectra were then analysed by the standard procedure[37-41] to obtain the spectral frequencies and full widths at half maxima (FWHMs).

Time-resolved fluorescence anisotropy decays were collected using time-correlated single photon counting (TCSPC) technique based on a laser system (Lifespec–ps, Edinburgh, UK) with 409 nm light as excitation. The full width at half maximum of the instrument response function (IRF) with the above excitation was approximately 90 ps. Following the standard method,[42-45] the emission intensity decays of C153 at different THF and Diox concentrations corresponding to emission polarizer orientation at magic angle (54.7^0), parallel (0^0) $I_{\parallel}(t)$ and

perpendicular (90^0) $I_{\perp}(t)$ were collected and constructed the fluorescence rotational anisotropy decay $r(t)$ as described in chapter 2.

4.2.3 Model and Force Field

The present simulation study employed SPC/E model of water.[46] For THF, total potential energy function used was of the following form:[47]

$$U = \left[\sum_{bonds} k_r^{ab}\left(r_{ij} - r_0^{ab}\right)^2\right] + \left[\sum_{angles}\left\{k_\theta^{abc}\left(\theta_{ijk} - \theta_0^{abc}\right)^2 - k_r^{ac}\left(r_{ik} - r_0^{ac}\right)^2\right\}\right]$$
$$+ \left[\sum_{torsions}\sum_n k_{\tau,n}^{abcd}\left[1 + \cos\left(n\tau_{ijkl} - \tau_0^{abcd}\right)\right]\right] + \left[\sum_{i<j}\left\{4\varepsilon^{ab}\left[\left(\frac{\sigma^{ab}}{r_{ij}}\right)^{12} - \left(\frac{\sigma^{ab}}{r_{ij}}\right)^6\right] + \frac{q^a q^b}{4\pi\varepsilon_0 r_{ij}}\right\}\right] \quad (4.1)$$

Here, the intramolecular bonded interactions consist of harmonic terms for bond stretching (bond length, r_{ij}; equilibrium bond length, r_0 and bond force constant, k_r), angle bending (bond angle, θ_{ijk}; equilibrium bond angle, θ_0 and angle force constant, k_θ) and torsional potential defined over cosines of the dihedral angle τ_{ijkl} (multiplicity, n; phase, τ_0 and torsional parameter, $k_{\tau,n}$). The two-body Urey–Bradley 1–3 interaction term is also included here which comprises a harmonic potential along the distance between first and third atoms of a bond angle. The nonbonded interactions were included by Lennard–Jones (LJ) and Coulomb interactions. Potential well depth, van der Waals radius, distance between atoms in the above equation are symbolized by ε, σ and r respectively. The parameter q represents the partial charge of the atom and ε_0 represents the static dielectric constant. LJ interactions between unlike atoms were calculated via Lorentz–Berthelot combining rule.[48] The force field parameters for THF were taken from CHARMM[47] force field using DL_FIELD[49].

For Diox, the following form for the potential energy function was considered:[50]

$$U = \left[\sum_{bonds} k_r^{ab} \left(r_{ij} - r_0^{ab} \right)^2 \right] + \left[\sum_{angles} k_\theta^{abc} \left(\theta_{ijk} - \theta_0^{abc} \right)^2 \right]$$

$$+ \left[\sum_{torsions} \left\{ \frac{V_1}{2} \left(1 + \cos\varphi \right) + \frac{V_2}{2} \left(1 - \cos 2\varphi \right) + \frac{V_3}{2} \left(1 + \cos 3\varphi \right) \right\} \right]$$

$$+ \left[\sum_{i<j} \left\{ 4\varepsilon^{ab} \left[\left(\frac{\sigma^{ab}}{r_{ij}} \right)^{12} - \left(\frac{\sigma^{ab}}{r_{ij}} \right)^6 \right] + \frac{q^a q^b}{4\pi\varepsilon_0 r_{ij}} \right\} \right] \quad (4.2)$$

Except V_1, V_2, V_3 which are the coefficients of the Fourier series and φ (the torsion angle), all other parameters have usual meaning as described above. The force field parameters and initial coordinates for Diox and C153 were adopted from the relevant literatures.[50,51] Note that all the bond lengths of Diox molecules were kept constrained and rigid model[51] of C153 was used in our study. Partial charges for all the atomic sites of C153 were taken from literature.[51]

4.2.4 Simulation Protocols

Simulations at various compositions were carried out with a total number of 512 (cycloether+water) molecules using DL_POLY_Classic suite,[52] employing cubic box with periodic boundary condition[48]. Additionally, one C153 molecule was added into the binary mixtures to maintain a very low solute concentration in the solution. Equations of motions were solved by Verlet–Leapfrog algorithm[48] with time step of 1 fs. Trajectory was obtained running the simulation in canonical (NVT) ensemble using Nosé–Hoover thermostat[53,54] with relaxation time of 0.5 ps at 300K after reproducing the experimental density in simulation (within ±2% of experimental density) employing NPT ensemble. For analysis, 4 ns trajectory was saved after 1 ns equilibration. Ewald summation technique[48] and SHAKE algorithm[55] were respectively used to handle electrostatic interactions and constrained all bonds involving hydrogen atoms.

4.3 Results and Discussion

4.3.1 Steady-state Studies: Change in Spectral Behaviour

The change with X_{THF} of steady-state absorption and emission frequency, ν and width, Γ (full width at half maximum) of C153 at two different temperatures, 298K and 333K (closer to T_L^C), are shown in Figure 4.1. Representative steady-state absorption and emission spectra of C153 at 298K are shown in Figure 4.A.1 of Appendix 4.A[56]. Note that absorption frequency undergoes an initial decrease and records a red-shift of ~550 cm^{-1} at $X_{THF} = 0.05$, and then further addition of THF reverses the slope producing the expected blue-shift of ~750 cm^{-1} at 298K as the mixture composition reaches to $X_{THF} = 0.40$. As observed before in aqueous binary mixtures of tertiary butanol (TBA) and 2-butoxyethanol (BE) (TBA/water[40,41] and BE/water[30] systems), this initial red-shift contradicts the composition dependent solution density,[57] polarity,[58,59] and refractive index[58] depicted in Figure 4.A.2 (Appendix 4.A)[56]. Furthermore, this concentration is far from critical concentration of THF/water mixture,[2] $X_{THF}^C = 0.225$. The initial red-shift therefore suggests enhancement of the local solvation structure around C153 which may occur, as in the cases for alcohol-water mixtures,[30,40,41] due to the cosolvent-induced stiffening of the H-bond network of water rather than from the solution criticality effects. Almost comparable amount of red-shift followed by blue-shift is also observed in Diox/water binary mixtures which does not show any solution criticality[3] around room temperature. Absorption spectral widths also report anomalous composition dependence at low mole fraction as they report significant narrowing while undergoing red-shift. However, emission spectral widths follow the ambient neat liquid behaviour.[60] Widths at 344K show the same trend. All these observation may therefore suggest that the solution criticality does not play any role in producing the anomalous absorption spectral characteristics at low cosolvent concentrations in these aqueous binary mixtures; it is the cosolvent-induced modification in the water structure that provides an unique local solvation shell, producing the absorption red-shift with concomitant narrowing at the low mole fraction regime.
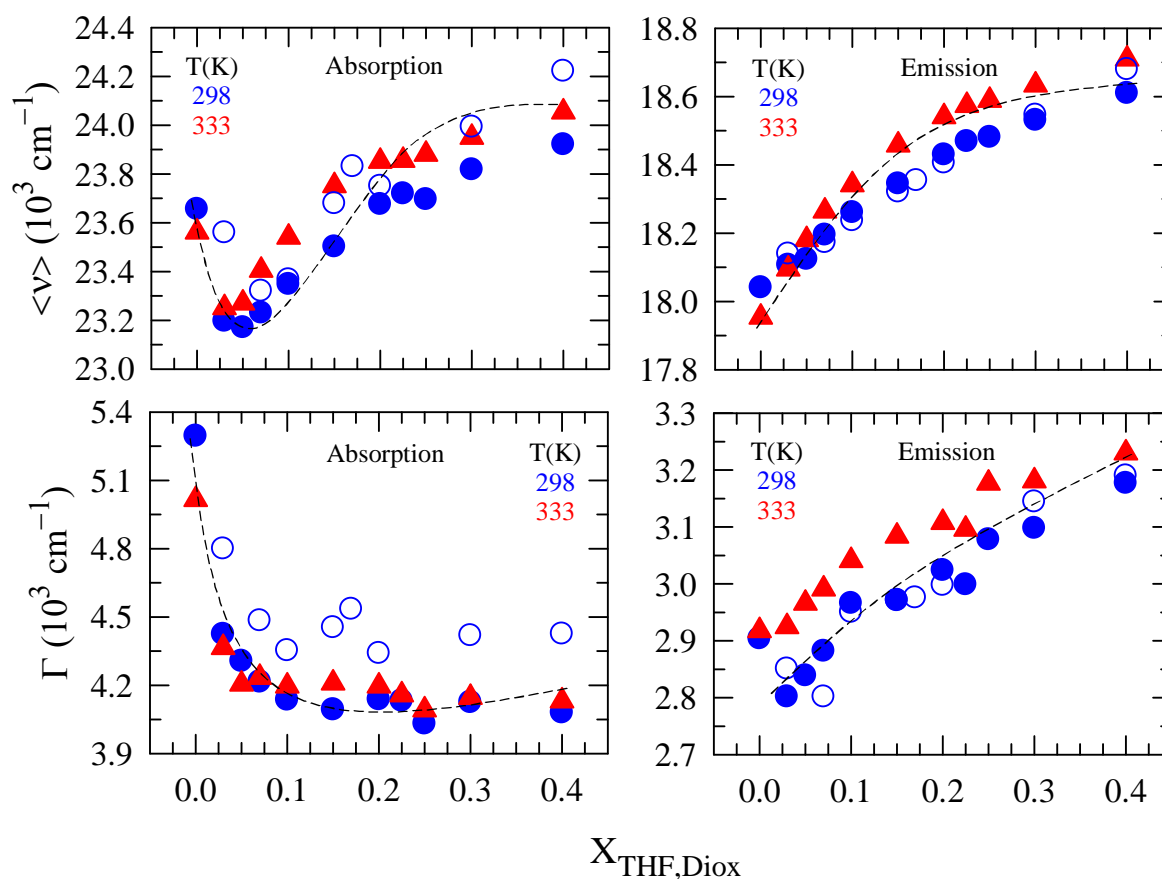
Figure 4.1: Cycloether mole fraction $\left(X_{ether}\right)$ dependence of absorption (left panels) and emission (right panels) spectral frequencies $\left(\nu\right)$ and widths $\left(\Gamma\right)$ of C153 at temperatures ~298K (blue circles) and ~333K (red triangles). Filled and open symbols represent data in THF/water and Diox/water binary mixtures, respectively. Here, ν is the mean of first moment, peak and half average frequencies, Γ the full width at half maxima (FWHM). Dashed lines are guides to the bare eyes.

The above is further supported by the fact that the total absorption red-shift at 333K is less (~300 cm^{-1}) than that at 298K (see Figure 4.1) although this temperature (333K) is closer to the critical temperature ($T_L^C = 344K$). This reflects softening of the cosolvent-water H-bond interaction and randomization of solution structure at higher temperature. Interestingly, corresponding emission frequencies of C153 do not exhibit any cosolvent concentration dependent anomaly, reporting only the change expected based on solution polarity or field factor.[1] This we interpret, as in the cases for alcohol/water mixtures, in terms of excited

solute sensing only the averaged-out solvation environment due to a large number of rapid fluctuations during its excited-state lifetime (~2–5 ns).

In Figure 4.2, we have further investigated excitation wavelength ($\lambda_{ex.}$) dependent emission of C153 at $X_{THF} = 0.05$ where the maximum red-shift in absorption frequency has been observed and at $X_{THF} = 0.10$ where absorption frequency started to register usual spectral behaviour. If there exists some aggregated structures with sufficiently longer timescales, emission frequency will show $\lambda_{ex.}$ dependence as was observed before for BE/water mixtures at low BE concentrations.[30] Here, we found $\lambda_{ex.}$ dependent emission frequency shift $\Delta \nu_{em}(\lambda_{ex.}) = \nu_{em}(\lambda = 375\,\text{nm}) - \nu_{em}(\lambda = 490\,\text{nm}) = 340\,\text{cm}^{-1}$ at $X_{THF} = 0.05$ and 280 cm^{-1} at $X_{THF} = 0.10$. Such values of $\lambda_{ex.}$ dependent emission shifts indicate aggregation of cycloethers in aqueous medium at very low concentrations. These aggregates are longer-lived as well because they are detectable in the fluorescence measurements.
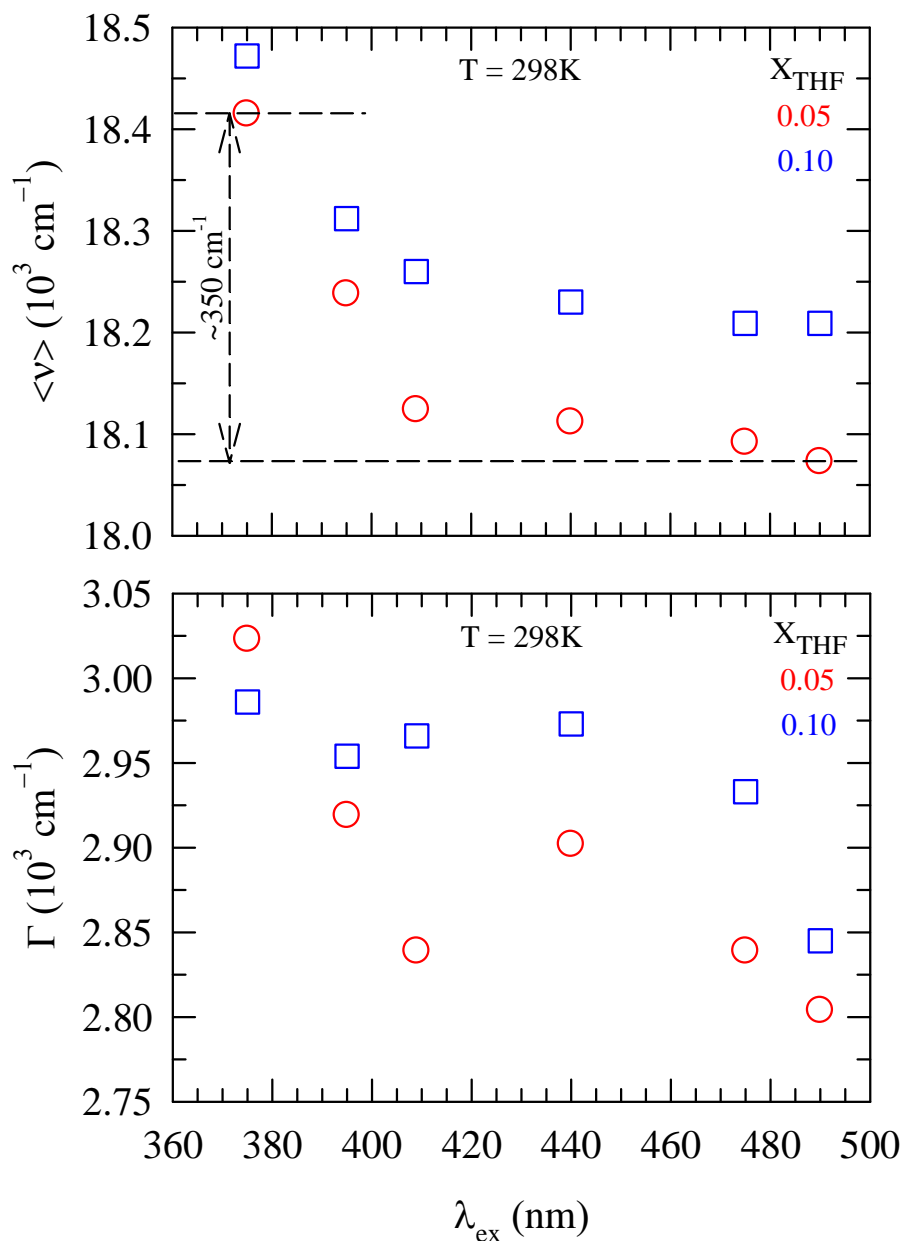
Figure 4.2: $\lambda_{ex.}$-dependent emission frequency, ν and FWHM, Γ of C153 in THF concentrations, $X_{THF} = 0.05$ and $X_{THF} = 0.10$ at ~298K. Note that the largest total absorption red-shift was observed at $X_{THF} = 0.05$. Moderate $\lambda_{ex.}$-dependent emission shift (~350 cm^{-1} at $X_{THF} = 0.05$ and ~300 cm^{-1} at $X_{THF} = 0.10$) signifies aggregation in aqueous solutions at low cycloether concentrations.

We would like to mention here that dynamic light scattering measurements[27] of THF/water binary mixtures have revealed that the concentration fluctuation correlation length at critical concentration $X_{THF}^{C} = 0.225$ grows as one approaches the LCST (344K). Therefore, it is important to check whether the temperature-dependent absorption spectral response at X_{THF}^{C} reflect any signature of the concentration fluctuations. We have shown in Figure 4.A.3 (Appendix 4.A)[56] the change of absorption frequency and width of C153 with temperature at $X_{THF}^{C} = 0.225$ which reports blue-shift with temperature (because of the consequent decrease in solution polarity) accompanied by spectral broadening. Such behaviour with temperature for absorption spectrum of C153 is normal.[60]

4.3.2 Time-resolved Studies: Fluorescence Lifetime of C153 in the Binary Mixtures

Average fluorescence lifetime, $\langle \tau_{life} \rangle$ of C153 has been obtained from bi-exponential and single-exponential fitting of the magic angle fluorescence emission decays in THF/water and Diox/water, respectively. The fit parameters are summarized in Tables 4.B.1 and 4.B.2 of Appendix 4.B[56]. Figure 4.3 shows the composition dependence of $\langle \tau_{life} \rangle$ for both THF/water and Diox/water binary mixtures. The X_{ether}-dependent variation of $\langle \tau_{life} \rangle$ produces two distinctly different slopes which intersect respectively at $X_{THF} \sim 0.10$ and $X_{Diox} \sim 0.15$. This strongly suggests that solution structures in these binary mixtures undergo transitions at these respective compositions. Note these cycloether concentrations are higher than the compositions at which the maximum absorption red-shift $(X_{ether} \sim 0.05)$ occurred due to cosolvent-induced stiffening of water H-bond network structure.
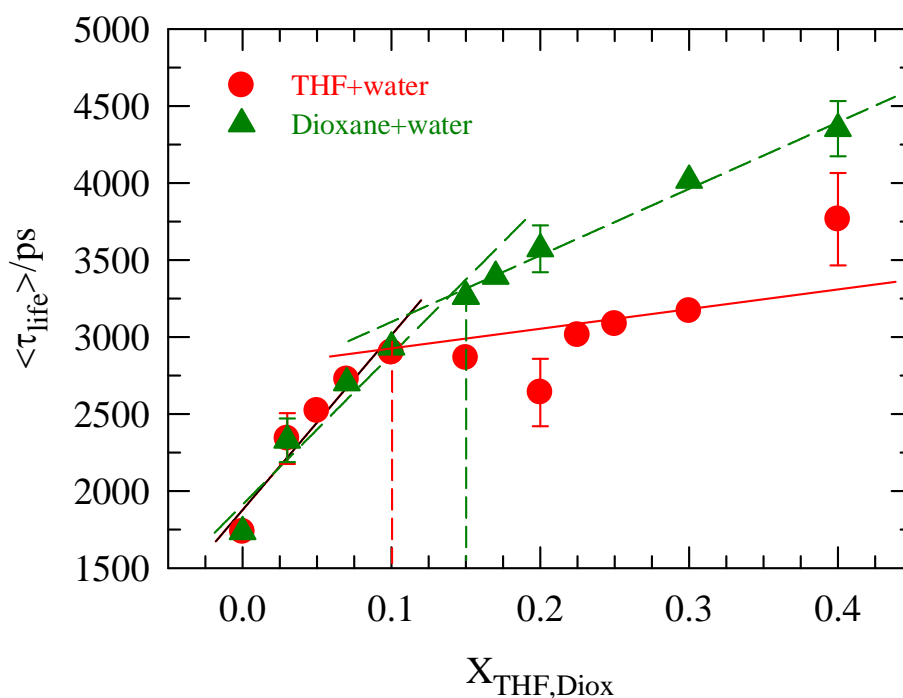
Figure 4.3: Variation of the measured average excited-state lifetime, $\langle \tau_{life} \rangle$ of C153 dissolved in aqueous solutions of THF (red circles) and dioxane (green triangles). Solid lines through the data show two different slopes. Vertical dashed lines indicate the cycloether concentrations where changes in the respective slopes have taken place.

Rotational anisotropy, $r(t)$, of C153 in these binary mixtures have been constructed from fluorescence emission decays using equation 2.1 (chapter 2). Representative $r(t)$ decay and exponential fit to the experimental data for $X_{THF} = 0.07$ is shown in Figure 4.A.4 (Appendix 4.A)[56]. Fit parameters at the THF and Diox concentrations are tabulated in Table 4.B.3 and 4.B.4 of Appendix 4.B[56]. Single exponential function was required for adequate fitting at lower X_{THF} and pure components whereas bi-exponential function was required for all other X_{ether}. Average rotational time, $\langle \tau_r \rangle$ of C153 is shown as a function of X_{ether} in the upper panel of Figure 4.4. τ_r values predicted via Stokes–Einstein–Debye (SED) relation[42] for both stick and slip boundary conditions at different cycloether concentrations are also shown in the same figure. Experimental composition dependent viscosity coefficients (η) for both THF/water[61] and Diox/water[57] binary mixtures are also provided in the same figure (lower
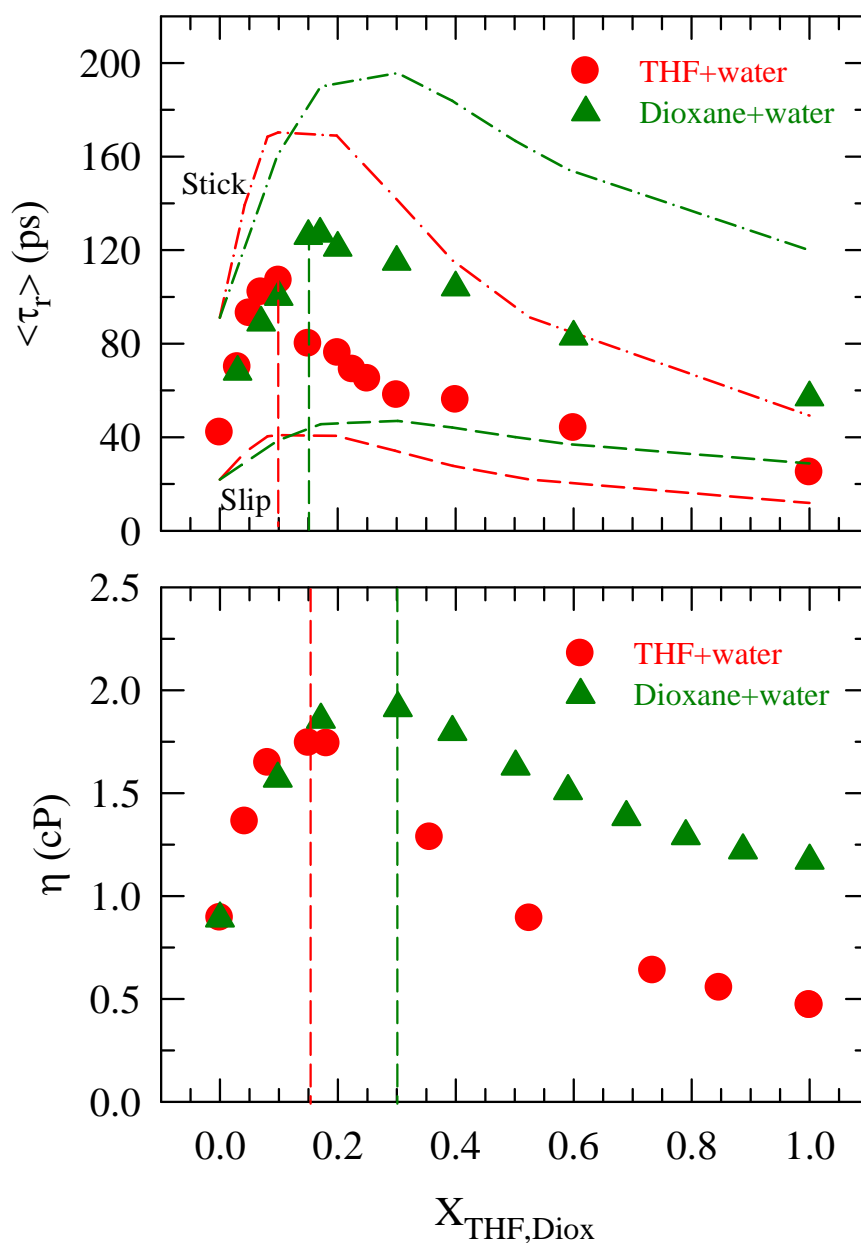
Figure 4.4: X_{ether}-dependence of the measured average rotational time, $\langle \tau_r \rangle$ of C153 (upper panel) and viscosity ceofficient, η (lower panel) in THF/water (red circles) and dioxane/water (green triangles) mixtures at ~298K. Predicted $\langle \tau_r \rangle$ of C153 from the SED relation using stick (dash-dot lines) and slip (dashed lines) boundary conditions are shown in the upper panel. Vertical dashed lines represent the composition of cycloethers where structural transition is believed to have taken place.

panel). Clearly, $\langle \tau_r \rangle$ slows down at the lower cycloether concentrations in these aqueous mixtures. There are maxima for $\langle \tau_r \rangle$ at $X_{THF} = 0.10$ and $X_{Diox} = 0.15$ for THF/water and Diox/water binary mixtures, respectively. After the maxima, $\langle \tau_r \rangle$ gradually decrease with further increase of cycloether concentrations in water. Viscosity in these media also passes through a maximum, which appears at $X_{THF} = 0.15$ and $X_{Diox} = 0.30$ for THF/water and Diox/water binary mixtures, respectively. Slope change in $\langle \tau_r \rangle$ at composition lower than the composition of viscosity-maximum therefore suggests a critical role played by solution structure in regulating the rotational motion of a dissolved solute. Note also these solution compositions are different from those where the maxima in absorption red-shift were observed. However, these are the same cosolvent (cycloether) concentrations where slope changes in $\langle \tau_{life} \rangle$ also occurred. In case of alcohol/water binary mixtures[30,41] we have seen that there were two different alcohol concentration regimes where H-bond strengthening/stiffening (relatively lower concentration) and structural transition (relatively higher concentration) took place. In the present scenario, the increase of $\langle \tau_r \rangle$ at low cycloether concentrations reflects increased friction due to a stiffening of water structure. This agrees well with the observation from other studies[12-15] such as light scattering, SANS, NMR that water–cycloether interaction enhances in the intermediate cycloether concentration regime $0.10 \leq X_{Cyet} \leq 0.20$. Further addition of cosolvent beyond this composition leads to structural loosening due to disruption of three-dimensional H-bond network of water, allowing the solute to rotate relatively freely. As a result, solute rotation time becomes faster with further increase of cycloether in the mixture. Note also in this figure that measured $\langle \tau_r \rangle$ in both these binary mixtures lie in between the SED slip and stick predictions. This further indicates an important role for the solution structure on the rotation of a dissolved solute.

4.3.3 Solution Structure: Insight from Simulated Radial Distribution Functions (RDFs)

Cycloether-water interaction: Site–site radial distribution functions, $g(r)$, between different atomic pairs of water and cycloethers (in the absence of C153) are shown as a function of distance, r in Figure 4.5. Note the wide difference in the intensity scale between the water-water RDF and the other RDFs presented here. Clearly, the first peak intensity of the RDF between the oxygen atoms of water, O(W)–O(W) (upper panels), increases with the increase of cycloether concentration for both THF/water and Diox/water binary mixtures. Interestingly, this growth at low concentrations is nearly independent of the cycloether identity (see Figure 4.A.5, Appendix 4.A)[56]. However, at higher concentrations, O(W)-O(W) RDF senses the cycloether identity and, at 0.8 mole fraction, the first peak of $g(r)$ for Diox/water system becomes nearly double than that for THF/water system. All these features of O(W)–O(W) indicates cycloether-induced stronger (relative to neat water) water-water interaction in these binary mixtures. Interestingly, O(W)-O(ether) RDF shows complex concentration dependence: for THF/water mixtures, the first peak intensity increases with increasing THF mole fraction whereas the O(W)–O(Diox) RDF shows initial decrease up to $X_{Diox} = 0.20$ and then increases with X_{Diox}.

Lower panel shows the RDF between cycloether O atoms, O(ether)–O(ether). Note that there was no peak at the distance of collision diameter of the oxygen atom. This suggests the nonexistence of the first solvation shell around the cycloether O atoms in both these binary mixtures. This is probably due to the closed loop structure of the cycloethers which prevents packing of cycloether molecules at the distance of collision diameter of the oxygen atom. RDF peak intensity of the second solvation shell shows non-monotonic composition dependence for both the binary mixtures. It grows up to $X_{ether} = 0.10$, then decreases with the increase of X_{ether}. Interestingly, this is the mixture composition around which abrupt change in slopes for the measured composition dependent $\langle \tau_{life} \rangle$ and $\langle \tau_r \rangle$ has been observed. Similar composition dependence can also be found for the carbon-carbon RDF among the cycloether molecules in these aqueous mixtures (see Figure 4.A.6, Appendix 4.A)[56].
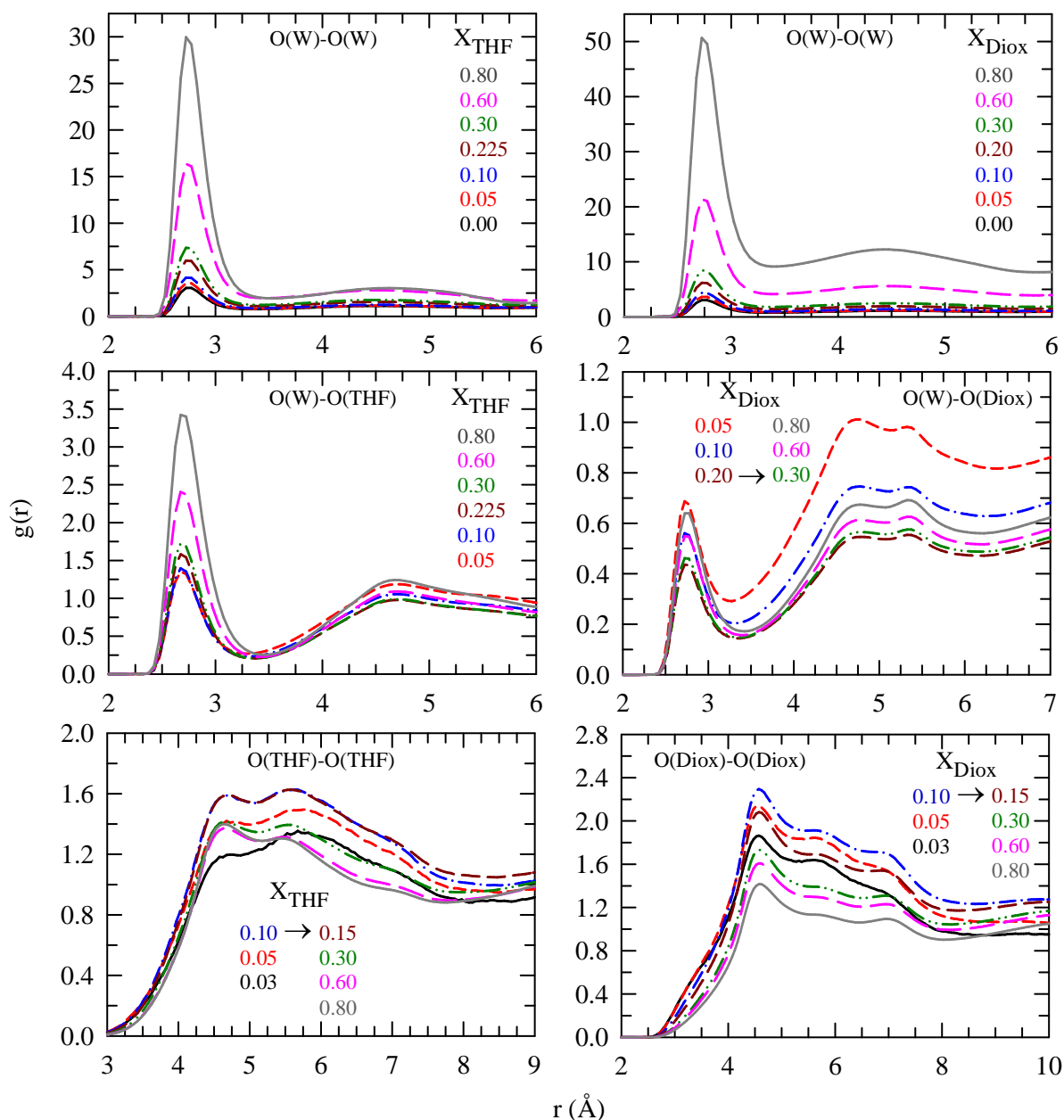
Figure 4.5: Simulated radial distribution function (RDF), $g(r)$ between several atomic pairs as a function of distance r for binary mixtures of THF/water (left panels) and dioxane/water (right panels). Atomic pairs are indicated in the inset of every panel. Cycloether compositions are colour-coded. Colour codes are as following: neat water/0.03: black solid line, 0.05: red short-dash, 0.10: blue dash-dot, 0.15/ 0.225/0.20: dark red medium-dash, 0.30: green dash-dot-dot, 0.60: pink large-dash, 0.80: gray solid line. Arrow in each panel indicates the concentration at which RDF changes its peak intensity.

Interaction of C153 with cycloether and water in binary mixtures: We have chosen carbonyl oxygen (OC, polar moiety) of C153 (shown in Scheme 4.1) in order to follow how polar interaction between C153 and oxygen atoms of water and cycloether molecules drives the solvation structure around C153. The role of non-polar interaction between C153 and cycloether is then investigated via following the interaction of the ring carbon atoms C2 and C4 of C153 with carbon atoms of cycloethers. Interaction of polar moieties of C153 with the binary solvents is shown in Figure 4.6 which suggests preferential interaction with water than cycloether, although C153 contains a large non-polar (hydrophobic) moiety. Here again reversal of simulated water-C153 RDF intensities occurs around the cycloether concentrations (see upper panel) at which the measured timescales suggested structural modification via slope-changes. After this composition, g(r) peak intensity of O(W)–OC(C153) increases with increase of X_{ether} (upper panel). In contrast, the O(ether)–OC(C153) RDF peak intensity (shown in the lower panel) decreases with the increase of X_{ether}. Identical behaviour is also observed for C(ether)–C2(C153) and C(ether)–C4(C153) RDFs shown in Figure 4.A.7 (Appendix 4.A)[56].
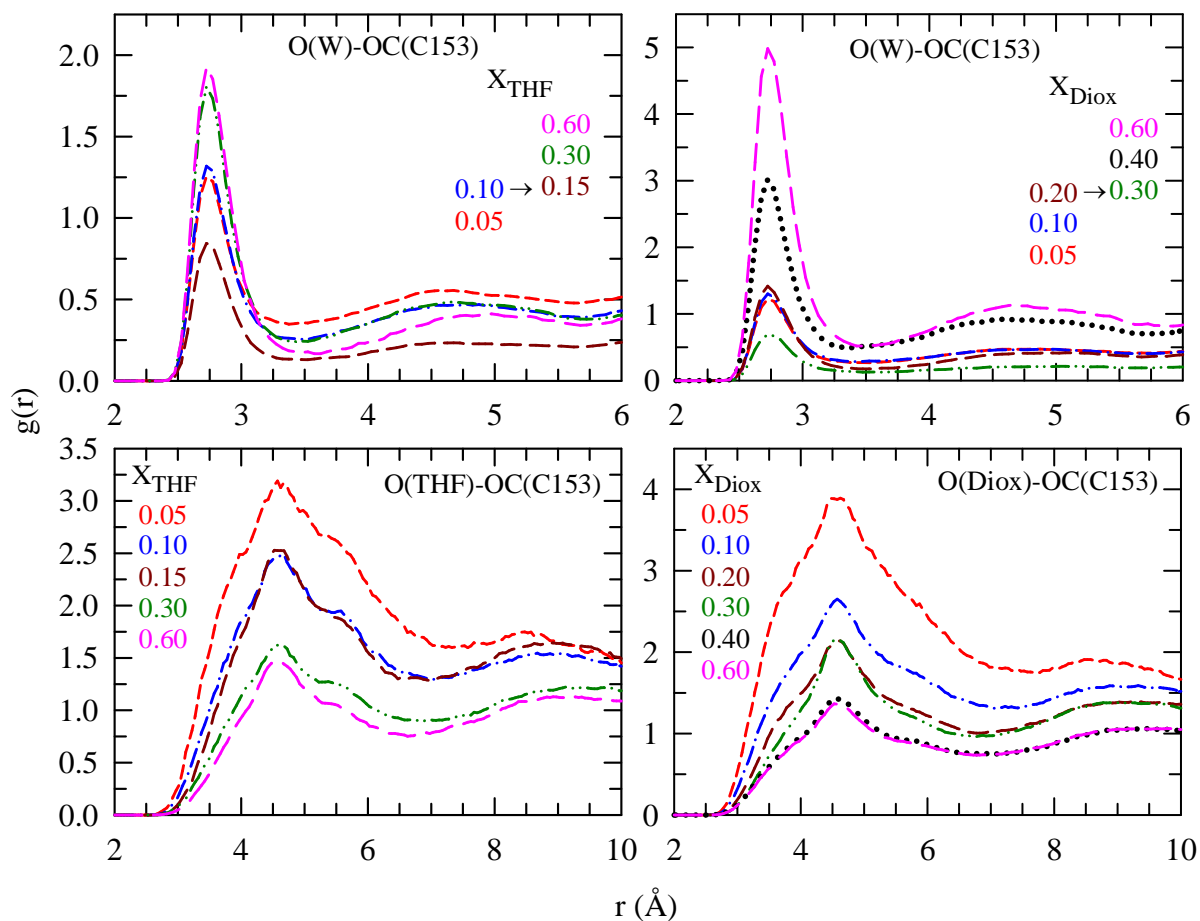
Figure 4.6: Plot of simulated RDF, $g(r)$ as a function of distance, r corresponding to the interaction of C153 with the hydrophilic moieties of water and cycloethers in THF/water (left panels) and dioxane/water (right panels) systems. Cycloether compositions are colour-coded and indicated in each panel. Atomic pairs are shown in the inset of the panels.

As C153 interacts preferentially with water in these binary mixtures, we have further calculated the number of water molecules in the first solvation shell of OC site of C153 by using the formula[62]

$$CN = \int_{0}^{R} \rho_{\beta}\, g_{\alpha-\beta}(r)\, 4\pi r^{2}\, dr \,, \qquad (4.3)$$

where CN denotes the coordination number of water molecules and R the first minimum distance of the $g(r)$ which is 3.5 Å in the present case. ρ_β is the number density of water. CN calculated thus are shown in the upper panel of Figure 4.7. Note CN of water decreases
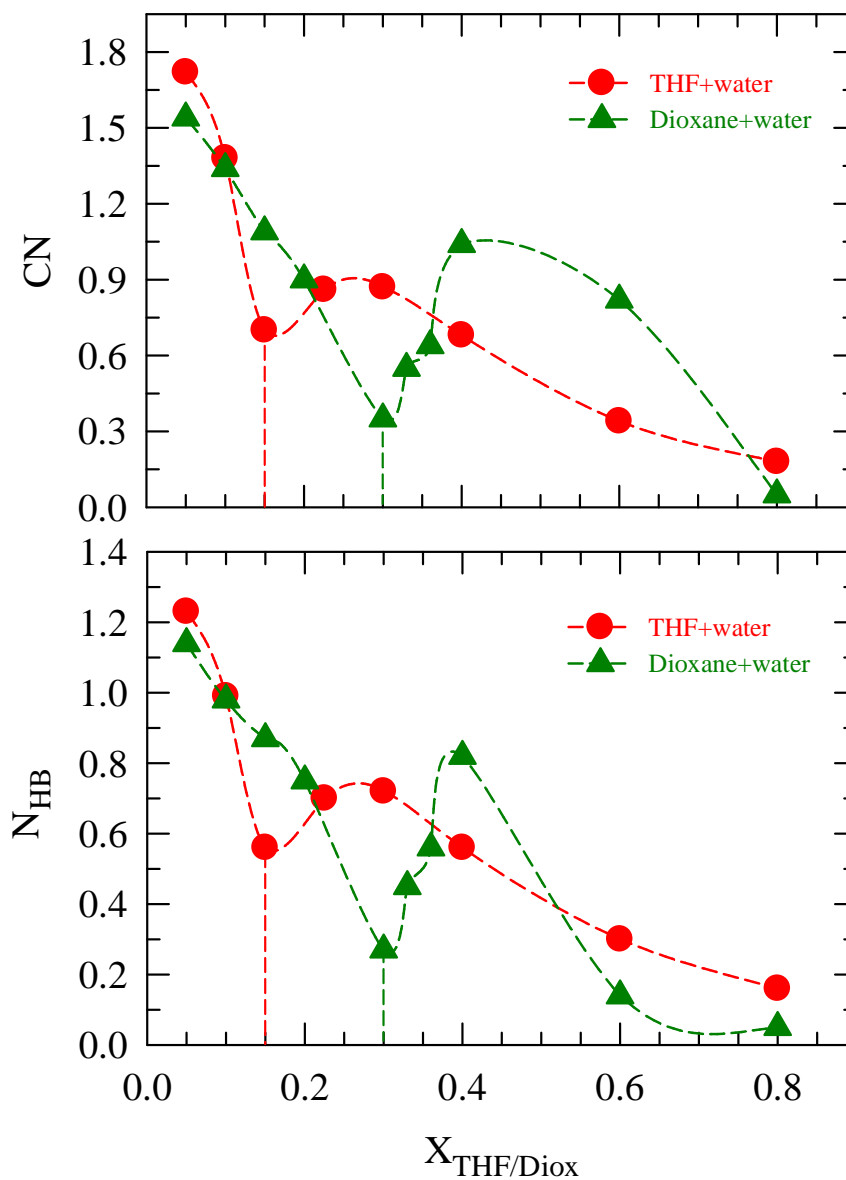
Figure 4.7: Simulated number of water molecules (CN) in the first solvation shell of OC group of C153 [Scheme 4.1] (upper panel) and number of H-bonds (N_{HB}) between OC group and water molecules (lower panel) as a function of X_{ether} in THF/water (red circles) and dioxane/water (green triangles) systems.

with increasing cycloether concentration at this water-rich regime for both the binary mixtures. This means release of water molecules to the bulk during the process of structural transition which is supported by the increase in solution entropy. Interestingly, CN shows minima at $X_{THF} = 0.15$ and $X_{Diox} = 0.30$ around which measured $\langle \tau_{\text{life}} \rangle$ and $\langle \tau_r \rangle$ also exhibit abrupt changes in slope. After this, CN continues to increase up to $X_{THF} = 0.30$ and $X_{Diox} = 0.40$ because the solution structure supports increased interaction between water and C153 in these aqueous solutions. Increase of cycloether concentration beyond these mole fractions leads the solutions to the water-depleted regime where CN (of water) naturally decreases. We have further calculated the number of H-bonds (N_{HB}) OC can form with water molecules using the following geometric conditions between the donor and the acceptor:[63,64] (i) the donor-acceptor O–O distance must be less than 3.5Å, (ii) the angle between O–O bond vector and O–H bond vector must be less than 30^0, and (iii) the O–H distance of donor-acceptor must be less than 2.45Å. The distance criteria correspond to the first minimum of the respective RDFs. The results are shown in the lower panel of Figure 4.7. Distribution of N_{HB} with cycloether concentration also produces the similar pattern as observed for the composition dependent CN. These two simulated parameters, CN and N_{HB}, therefore provide a microscopic view of the solution structural transition suggested by the dynamic fluorescence anisotropy and lifetime measurements.

4.4 Conclusion

In summary, THF/water and Diox/water binary mixtures show both stiffening and transition of the three-dimensional H-bond network structure of water with stiffening occurring at cosolvent (THF or Diox) mole fractions lower than those for transitions. Evidences for cycloether aggregation at very dilute concentrations have been found. Moreover, these structural modifications derive no contributions from the solution criticality, suggesting hydrophobic interaction driven structural transition and aggregation in aqueous media. Quite interestingly, no dependence on the chemical nature of these cosolvent molecules (dipolar or quadrupolar) of the anomalous composition dependence of the solution structure has been found. Such an observation provides support to the view that water structure in these binary mixtures, as previously interpreted for aqueous alcohol solutions, is overwhelmingly

influenced   by the hydrophobic interaction between the cosolvent and water molecules with no role for the solution criticality.   Simulated radial distribution functions reflect abrupt changes in distribution intensities at those compositions around which experiments report structural transition. Minima in simulated water coordination number for the dissolved dipolar solute and number of H-bonds at these solution compositions strongly support the view of structural transition and provide microscopic insight to the anomalous composition dependence of the spectral data. Further study exploring the dependence of solution dynamic heterogeneity[65-68] on the chemical nature of cosolvent would contribute to a better understanding of aqueous dynamics in diverse environments.

Appendix 4.A
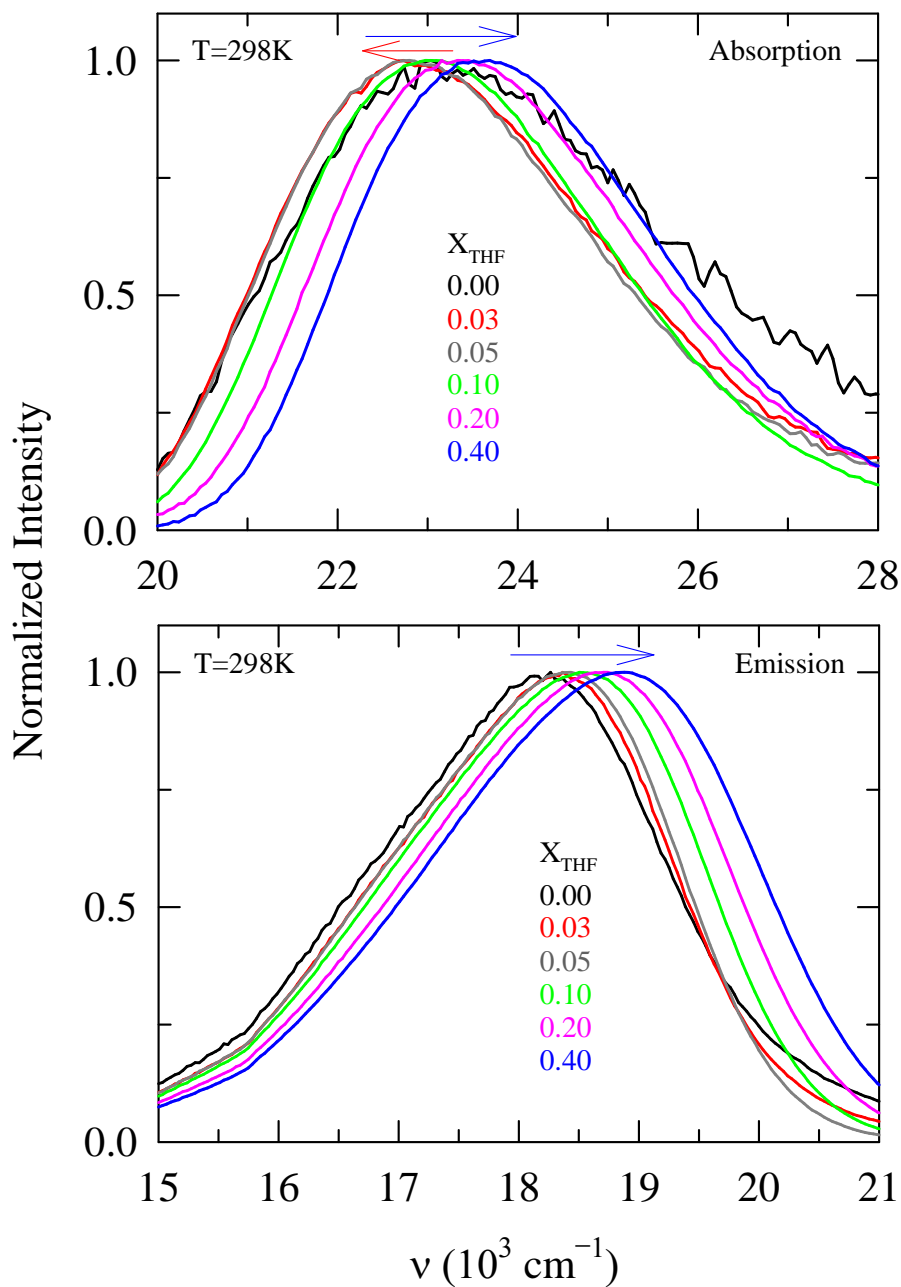
Figure 4.A.1: Normalized absorption (upper panel) and emission (lower panel) spectra of C153 at different mole fractions of THF in water (X_{THF}) at ~298K. Spectral shift with increase of X_{THF} is represented by arrows. THF concentrations are colour-coded in each panel.
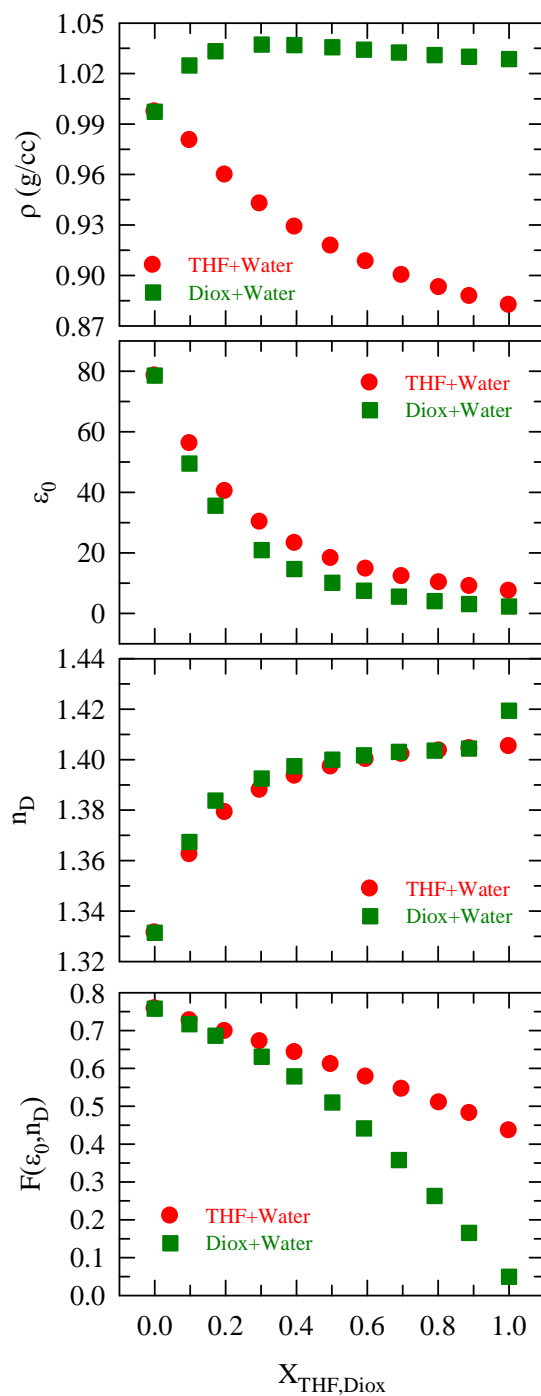
Figure 4.A.2: Mole fraction dependence (X_{ether}) of density (ρ), static dielectric constant (ε_0), refractive index (n_D) and reaction field factor $[F(\varepsilon_0, n_D)]$ of THF/water and dioxane/water at 298K. Here, $F(\varepsilon_0, n_D) = \dfrac{\varepsilon_0 - 1}{\varepsilon_0 + 2} - \dfrac{n_D{}^2 - 1}{n_D{}^2 + 2}$.
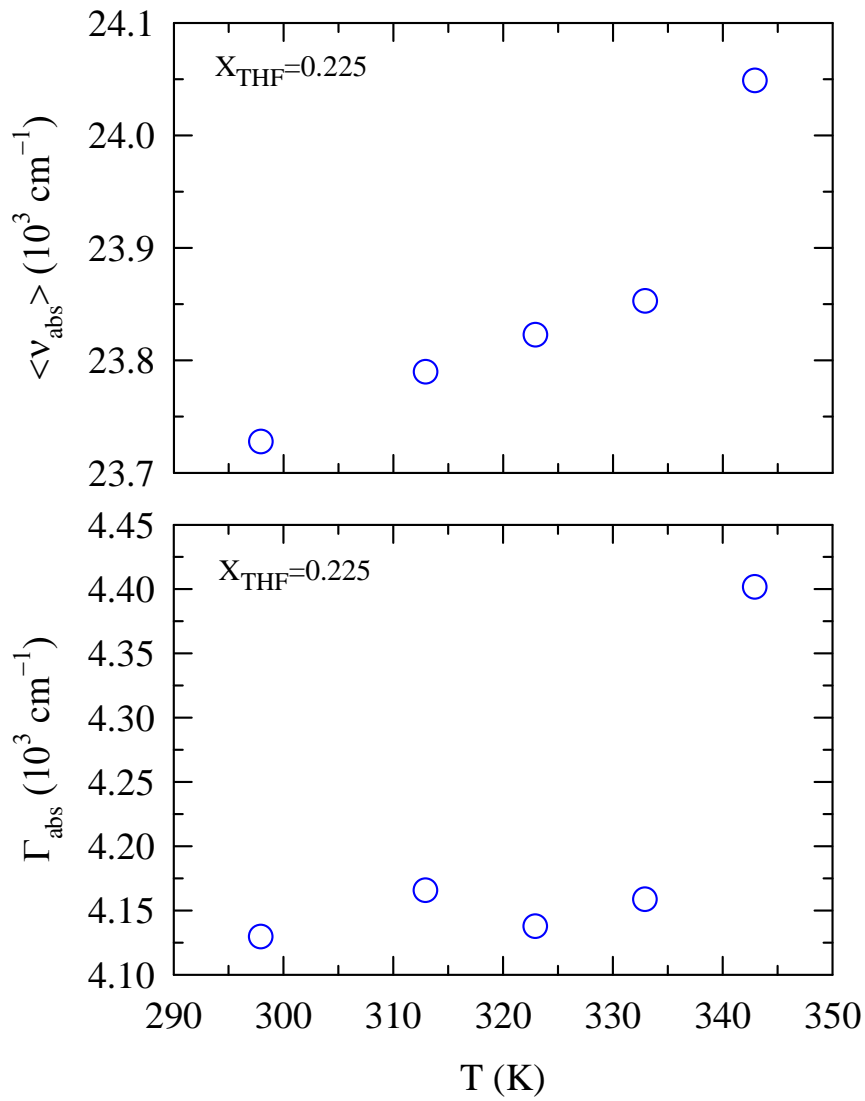
Figure 4.A.3: Temperature dependence of average absorption spectral frequency $\langle v_{abs} \rangle$ and width Γ_{abs} of C153 at the lower critical concentration of THF/water binary mixture, $X_{THF}^{C} = 0.225$.
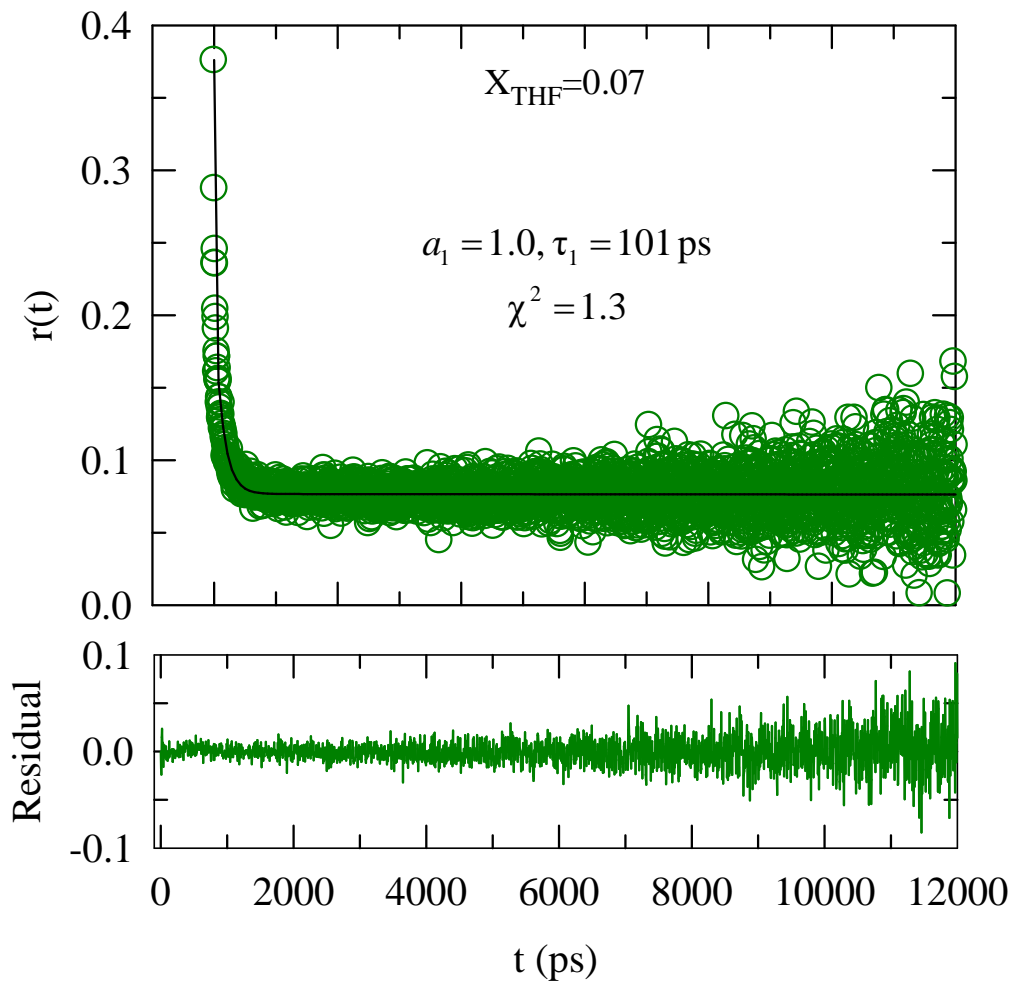
Figure 4.A.4: Representative fluorescence rotational anisotropy $r(t)$ decay of C153 at $X_{THF} = 0.07$ (upper panel) and the residual of exponential fit (lower panel). Solid line in the upper panel represents the exponential fit. Fit parameters are also summarized.
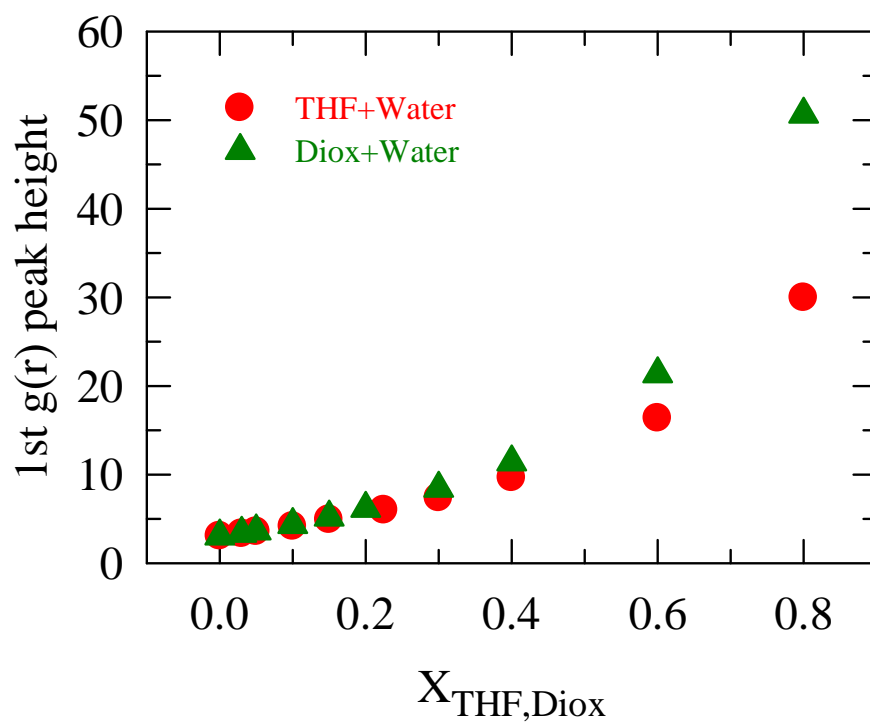
Figure 4.A.5: First O(W)–O(W) RDF peak height as a function of cycloether concentrations in THF/water (red circles) and dioxane/water (green triangles) binary mixtures.
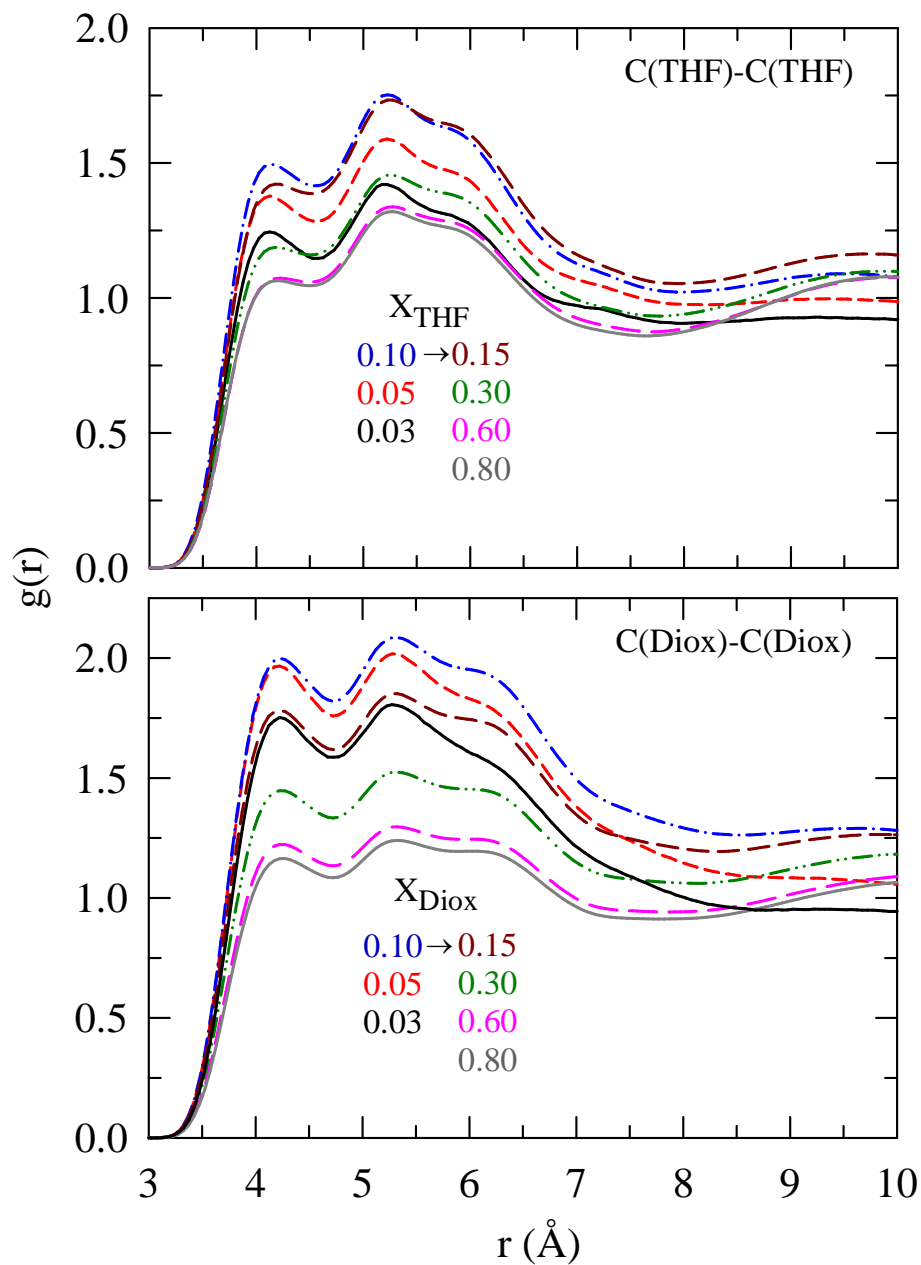
Figure 4.A.6: RDF, $g(r)$ for C(ether)–C(ether) interactions in aqueous solutions of THF (upper panel) and dioxane (lower panel) as a function of distance r. Cycloether compositions are colour-coded in each panel.
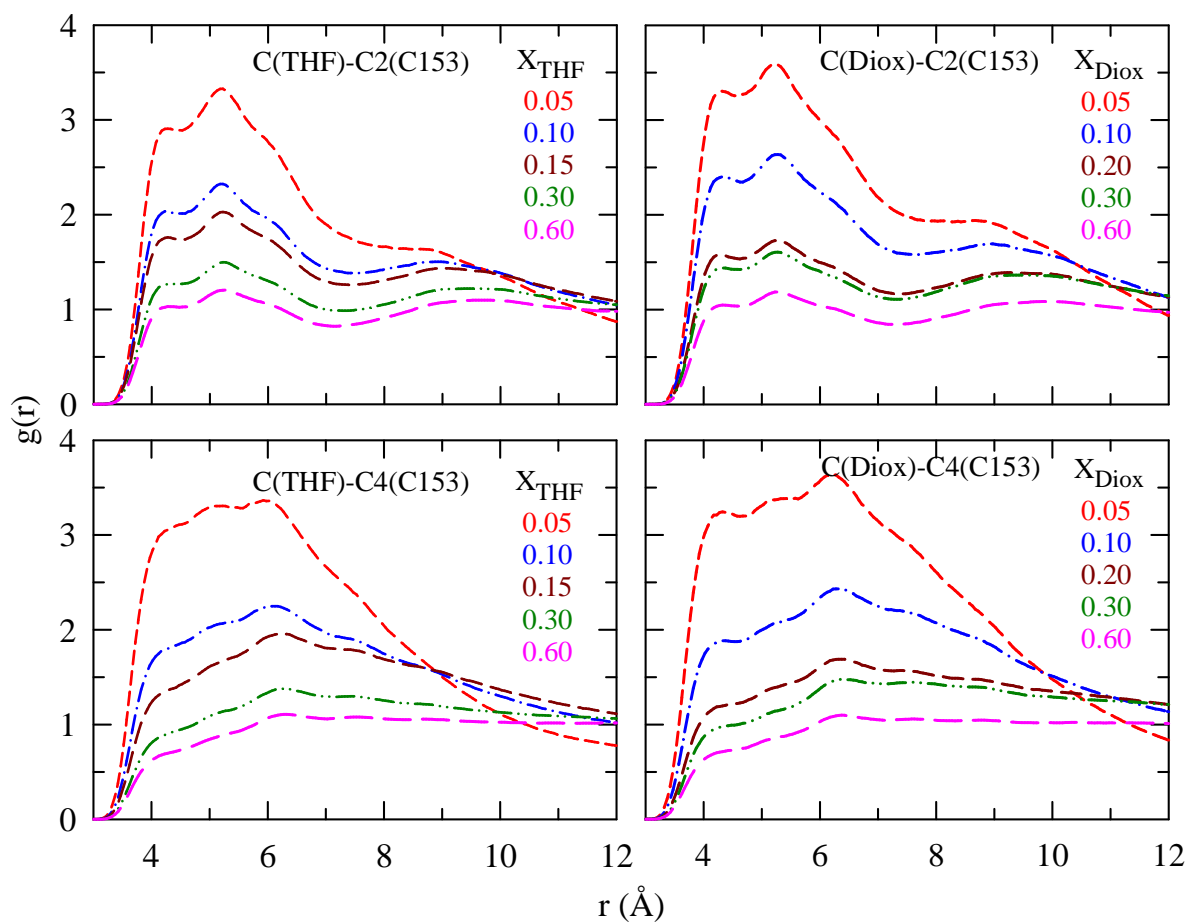
Figure 4.A.7: Plot of RDF, $g(r)$ as a function of distance, r corresponding to the interaction of C153 with the hydrophobic moieties of cycloethers in THF/water (left panels) and dioxane/water (right panels). Cycloether compositions are colour-coded and indicated in each panel. Atomic pairs are shown in the inset of the panels.

Appendix 4.B

Table 4.B.1: Bi-exponential fit parameters for magic angle emission decay and average excited-state lifetime, $\langle \tau_{life} \rangle$ of C153 at various THF mole fractions in water at ~298K.

X_{THF}	a_1	τ_1 /ps	a_2	τ_2 /ps	$\langle \tau_{life} \rangle$ /ps
0.00	0.81	1923	0.19	943	1737
0.03	0.82	2824	0.18	140	2341
0.05	0.83	3005	0.17	157	2521
0.07	0.89	3044	0.11	145	2725
0.10	0.85	3412	0.15	135	2900
0.15	0.82	3459	0.18	158	2865
0.20	0.72	3622	0.28	115	2640
0.225	0.80	3723	0.20	171	3013
0.25	0.81	3765	0.19	185	3085
0.30	0.80	3918	0.20	173	3169
0.40	0.91	4117	0.09	209	3765
1.00	1.00	5273			5273

Table 4.B.2: Single-exponential fit parameters for magic angle emission decay and $\langle \tau_{life} \rangle$ of C153 in different dioxane mole fractions in water (X_{Diox}) at ~298K.

X_{Diox}	a	τ /ps	$\langle \tau_{life} \rangle$ /ps
0.03	1.00	2330	2330
0.07	1.00	2703	2703
0.10	1.00	2935	2935
0.15	1.00	3264	3264
0.17	1.00	3394	3394
0.20	1.00	3573	3573
0.30	1.00	4018	4018
0.40	1.00	4353	4353
1.00	1.00	5258	5258

Table 4.B.3: Fit parameters for rotational anisotropy, $r(t)$ at various mole fractions of THF into water, X_{THF} at T ~298K.

X_{THF}	a_1	τ_1/ps	a_2	τ_2/ps	$\langle \tau \rangle$/ps
0.00	1.00	42			42
0.03	1.00	70			70
0.05	1.00	93			93
0.07	1.00	102			102
0.10	0.66	149	0.34	27	107
0.15	0.45	158	0.55	15	80
0.20	0.36	164	0.64	26	76
0.225	0.39	138	0.61	24	69
0.25	0.45	126	0.55	15	65
0.30	0.40	122	0.60	15	58
0.40	0.32	141	0.68	15	56
1.00	1.00	25			25

Table 4.B.4: Fit parameters for rotational anisotropy, $r(t)$ at various mole fractions of dioxane in water, X_{Diox} at T ~298K.

X_{Diox}	a_1	τ_1/ps	a_2	τ_2/ps	$\langle \tau \rangle$/ps
0.03	0.71	111	0.29	24	86
0.07	0.60	136	0.40	18	89
0.10	0.74	131	0.26	11	100
0.15	0.75	160	0.25	25	126
0.17	0.71	168	0.29	26	127
0.20	0.64	173	0.36	29	121
0.30	0.65	165	0.35	22	115
0.40	0.73	131	0.27	32	104
1.00	1.00	57			57

References

1.   L. Reynolds, J. A. Gardecki, S. J. V. Frankland, M. L. Horng and M. Maroncelli, J. Phys. Chem. **100**, 10337 (1996).

2.   A. Oleinikova and H. Weingärtner, Chem. Phys. Lett. **319**, 119 (2000).

3.   T. Kouissi, M. Bouanz and N. Ouerfelli, J. Chem. Eng. Data **54**, 566 (2009).

4.   S. Budvari, in *The Merck Index* (Merck and Co., Rahway, NJ, 1989).

5.   N. G. David and W. Harry, Can. J. Chem. **51**, 1933 (1973).

6.   H. Nakayama and K. Shinoda, J. Chem. Thermodyn. **3**, 401 (1971).

7.   M. Sakurai, J. Chem. Eng. Data **37**, 492 (1992).

8.   G. N. Malcolm and J. S. Rowlinson, Trans. Faraday Soc. **53**, 921 (1957).

9.   P. Lejček, J. Matouš, J. P. Novák and J. Pick, J. Chem. Thermodyn. **7**, 927 (1975).

10.   E. K. Baumgartner and G. Atkinson, J. Phys. Chem. **76**, 2336 (1971).

11.   G. Atkinson, S. Ralagopalan and B. L. Atkinson, J. Phys. Chem. **85**, 733 (1981).

12.   C. Yang, W. Li and C. Wu, J. Phys. Chem. B **108**, 11866 (2004).

13.   T. Takamuku, A. Nakamizo, M. Tabata, K. Yoshida, T. Yamaguchi and T. Otomo, J. Mol. Liq. **103**, 143 (2003).

14.   J. Hao, H. Cheng, P. Butler, L. Zhang and C. C. Han, J. Chem. Phys. **132**, 154902 (2010).

15.   Y. G. Wu, M. Tabata and T. Takamuku, J. Mol. Liq. **94**, 273 (2001).

16.   Y. Tominaga and S. M. Takeuchi, J. Chem. Phys. **104**, 7377 (1996).

17.   T. Fukasawa, Y. Amo and Y. Tominaga, J. Chem. Phys. **118**, 6387 (2003).

18.   T. Takamuku, A. Yamaguchi, M. Tabata, N. Nishi, K. Yoshida, H. Wakita and Y. T., J. Mol. Liq. **83**, 163 (1999).

19.   K. Mizuno, S. Imafuji, T. Fujiwara, T. Ohta and Y. Tamiya, J. Phys. Chem. B **107**, 3972 (2003).

20.   T. Fukasawa, Y. Tominaga and A. Wakisaka, J. phys. Chem. A **108**, 59 (2004).

21.   M. Katayama and K. Ozutsumi, J. Solution Chem. **37**, 841 (2008).

22.   S. Schrödle, B. Fischer, H. Helm and R. Buchner, J. Phys. Chem. A Lett. **111**, 2043 (2007).

23.   S. Schrödle, G. Hefter and R. Buchner, J. Phys. Chem. B **111**, 5946 (2007).

24. S. Mashimo, N. Miura, T. Umehara, S. Yagihara and K. Higasi, J. Chem. Phys. **96**, 6358 (1992).

25. T. Molotsky and D. Huppert, J. Phys. Chem. A **107**, 8449 (2003).

26. S. Mukherjee, K. Sahu, D. Roy, S. K. Mondal and K. Bhattacharyya, Chem. Phys. Lett. **384**, 128 (2004).

27. C. M. Sorensen, J. Phys. Chem. **92**, 2367 (1988).

28. H. E. Stanley, *Introduction to Phase Transitions and Critical Phenomena*. (Oxford University Press, New York, 1971).

29. N. Ito, T. Kato and T. Fujiyama, Bull. Chem. Soc. Jpn. **54**, 2573 (1981).

30. S. Indra and R. Biswas, J. Chem. Phys. **142**, 204501 (2015).

31. K. Remerie, J. B. F. N. Engberts and W. F. V. Gunsteren, Chem. Phys. **101**, 27 (1986).

32. P. I. Nagy, G. Völgyi and K. Takács–Novák, J. Phys. Chem. B **112**, 2085 (2008).

33. L. C. G. Freitas and J. M. M. Cordeiro, J. Mol. Str. (Theochem) **335**, 189 (1995).

34. I. Brovchenko and B. Guillot, Fluid Phase Equilib. **183**, 311 (2001).

35. A. Oleinikova, I. Brovchenko and A. Geiger, J. Chem. Phys. **117**, 3297 (2002).

36. I. Brovchenko, A. Geiger and A. Oleinikova, Phys. Chem. Chem. Phys. **6**, 1982 (2004).

37. R. Biswas, J. E. Lewis and M. Maroncelli, Chem. Phys. Lett. **310**, 485 (1999).

38. J. E. Lewis, R. Biswas, A. G. Robinson and M. Maroncelli, J. Phys. Chem. B **105**, 3306 (2001).

39. T. Pradhan and R. Biswas, J. Phys. Chem. A **111**, 11514 (2007).

40. T. Pradhan, P. Ghoshal and R. Biswas, J. Phys. Chem. A **112**, 915 (2008).

41. T. Pradhan, P. Ghoshal and R. Biswas, J. Chem. Sci. **120**, 275 (2008).

42. M. L. Horng, J. A. Gardecki and M. Maroncelli, J. Phys. Chem. A **101**, 1030 (1997).

43. K. Dahl, R. Biswas, N. Ito and M. Maroncelli, J. Phys. Chem. B **109**, 1563 (2005).

44. J. E. Lewis and M. Maroncelli, Chem. Phys. Lett. **282**, 197 (1998).

45. R. Biswas, A. R. Das, T. Pradhan, D. Tauraud, W. Kunz and S. Mahiuddin, J. Phys. Chem. B **112**, 6620 (2008).

46. H. J. C. Berendsen, J. R. Grigera and T. P. Straatsma, J. Phys. Chem. **91**, 6269 (1987).

47. A. D. MacKerell, Jr. , J. Wiórkiewicz-Kuczera and M. Karplus, J. Am. Chem. Soc. **117**, 11946 (1995).

48.   M. P. Allen and D. J. Tildesley, *Computer simulations of liquids*. (Oxford University Press, New York, 1987).

49.   C. W. Yong, *DL_FIELD – a force field and model development tool for DL_POLY*. (STFC Daresbury Laboratory, Daresbury, 2010).

50.   G. Cinacchi, F. Ingrosso and A. Tani, J. Phys. Chem. B **110**, 13633 (2006).

51.   N. Kometani, S. Arzhantsev and M. Maroncelli, J. Phys. Chem. A **110**, 3405 (2006).

52.   W. Smith, T. R. Forester and I. T. Todorov, *DL_POLY Classic*. (STFC Daresbury Laboratory, Daresbury, 2012).

53.   S. Nose, J. Chem. Phys. **81**, 511 (1984).

54.   W. G. Hoover, Phys. Rev. A **31**, 1695 (1985).

55.   J. P. Ryckaert, G. Ciccotti and H. J. C. Berendsen, J. Comput. Phys. **23**, 327 (1977).

56.   See Appendix 4.A and 4.B for steady-state abosorption and emission spectra of C153 in various concentrations of THF into water, behaviour of density, polarity, refractive index and reaction field factor in the binary mixtures of THF/water and Diox/water, temperature effect on the absorption spectral frequency and width at the critical concentration of THF (0.225 mole fraction) into water, fitting parameters for excited-state lifetime decay and rotational anisotropy decay of C153 in both cycloether/water binary mixtures, representative rotational anisotropy decay of C153 in THF/water mixture, distribution of peak heights of radial distribution functions (RDFs) of water oxygen atoms in cycloether/water mixtures, RDFs between several atomic pairs of these solutions.

57.   T. M. Aminabhavi and B. Gopalakrishna, J. Chem. Eng. Data **40**, 856 (1995).

58.   F. E. Critchfield, J. A. Gibson, Jr. and J. L. Hall, J. Am. Chem. Soc. **75**, 6044 (1953).

59.   J. E. Lind and R. M. Fuoss, J. Phys. Chem. **65**, 999 (1961).

60.   M. L. Horng, J. A. Gardecki, A. Papazyan and M. Maroncelli, J. Phys. Chem. B **99**, 17311 (1995).

61.   W. Hayduk, H. Laudie and O. H. Smith, J. Chem. Eng. Data **18**, 1973 (1973).

62.   J. P. Hansen and I. R. McDonald, *Theory of simple liquids*. (Academic Press, New York, 1986).

63.   A. Luzar and D. Chandler, Nature **379**, 55 (1996).

64.   A. Luzar and D. Chandler, J. Chem. Phys. **98**, 8160 (1993).

65.   S. Indra and R. Biswas, Mol. Sim. **41**, 471 (2015).

66.   T. Pal and R. Biswas, J. Chem. Phys. **141**, 104501 (2014).

67.   T. Pal and R. Biswas, J. Phys. Chem. B (2015) DOI: 10.1021/acs.jpcb.5b08763.

68.   T. Pal and R. Biswas, Theor. Chem. Acc. **132**, 1348 (2013).

Chapter 5

Effects of Trehalose on the Dynamics of Glycerol: A Combined Fluorescence and Computer Simulation Study

5.1 Introduction

To survive at extreme conditions, such as at very low temperature and humidity, live cells and tissues are known to synthesize some sugars and polyalcohols in both their inter and intracellular fluids. These particular sugars and polyalcohols help preventing cell damage due to extreme environmental conditions and keep the integrative cell functions intact. These particular molecules are therefore termed as cryoprotectants and the process is known as cryopreservation. Glycerol, a simple polyol, and trehalose, an alpha-linked disaccharide, are known to function as cryoprotectants. While glycerol acts as intracellular agent, trehalose resides as extracellular compound.[1,2] The effective way to enhance preservative efficiency is antiplasticization[3] that is the slowing-down of large-scale molecular transport. Trehalose has been proven to be the most effective preservative among all other sugar formulations because of its high glass transition temperature $\left(T_g = 390\mathrm{K}\right)$.[4-6] On the other hand, glycerol is stronger glass former $\left(T_g = 190\mathrm{K}\right)$ than trehalose because its smaller size facilitates efficient packing in the glassy state. However, in the "strong-fragile" scheme,[7,8] both glycerol and trehalose are classified as 'intermediate' glass formers. Raman spectroscopy and neutron scattering studies[9-11] suggested that protein preservation time can be enhanced by making the preservative formulation a stronger glass-forming liquid. Researchers have also observed that addition of 20 wt. % trehalose into glycerol increases the T_g of about 13K.[12,13] This extent of reduction of T_g is two times smaller than the predicted value assuming a regular solution model.[13,14]

Glycerol possesses extensive H-bond network[15] and large dipole moment.[16,17] These properties have motivated dielectric relaxation measurements of glycerol at temperatures from normal to supercooled ones.[18-24] Both experimental[25-30] and computer simulation[31-35] studies of aqueous solutions of trehalose have shown that trehalose has a high propensity to form H-bond with water as well as to other trehalose molecules. In this way, trehalose can obstruct the crystallization process by disrupting the tetrahedral H-bond structure of water. Like trehalose, glycerol in aqueous solution also exhibit cryoprotective properties.[36,37] There are several studies of trehalose–glycerol system at the glassy state.[3,38-43] It has been observed that addition of small amount of glycerol (~2.5 %) into trehalose makes the system stronger glass former due to stronger interspecies (trehalose–glycerol) H-bonding. This antiplasticizing effect of glycerol on trehalose can significantly increase the preservation times of proteins.[44-46] Interestingly, despite these biological relevance and important basic scientific aspect, a detailed understanding of this cryoprotectant mixture in terms of interactions is still lacking.

In this work, we have employed both fluorescence spectroscopic measurements and molecular dynamics (MD) simulations to understand how addition of trehalose affects the network structure of glycerol and alters the dynamical signatures of this associating liquid. For studying in solution phase at room temperature, we have chosen two different compositions: 5 wt % and 20 wt % of trehalose into glycerol. Note that the maximum amount of trehalose that can be completely soluble in glycerol is 20 wt %. We would like to mention here that our fluorescence measurements have been performed by using the commercially available trehalose dihydrate, whereas simulations have considered the anhydrous compound. Coumarin 153 (C153) has been used as solute probe in the relevant spectroscopic measurements. The chemical structures of these molecules are shown in Scheme 5.1.

Dynamic fluorescence Stokes shift and anisotropy relaxation of C153 in these trehalose/glycerol mixtures have been measured over a temperature range of 298K–353K. Measured dynamic Stokes shift data suggest disruption of H-bond network of glycerol by trehalose. Measured solvation and rotation times reflect fractional viscosity dependence[47-54]

and sort of partial decoupling between rotation and translation. Simulated radial distribution functions (between several atomic pairs) and mean squared displacements indicate glass-like structure of the system at room temperature. We have also found that the dynamics of the system is controlled by different mechanisms at two different temperature ends. At low temperature region due to glassy nature of the system the inertial motion of the molecules govern the dynamics whereas the diffusion controlled mechanism operates at higher temperature region.

(a)   (b)
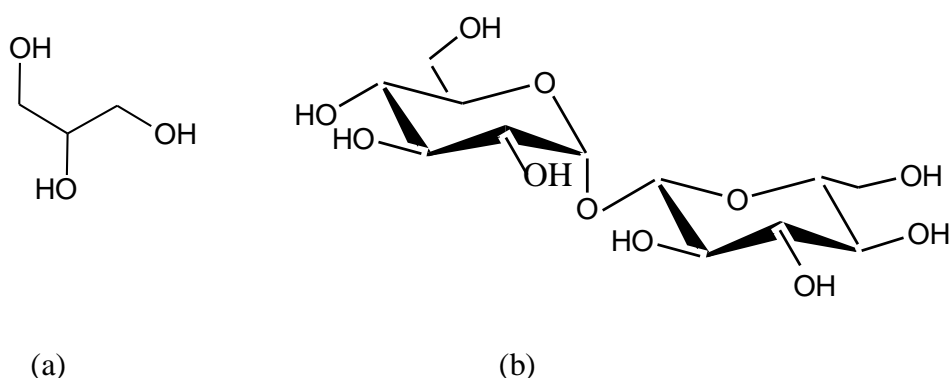
Scheme 5.1: Schematic representations of the bioprotectants (a) Glycerol, and (b) α, α - Trehalose.

5.2 Experimental and Simulation Procedures

5.2.1 Sample Preparation

Laser grade C153 was purchased from Exciton and used as fluorescent probe. Glycerol ($\geq 99.5\%$) and D-(+)-trehalose dihydrate ($\geq 99\%$) were obtained from Sigma–Aldrich and used without further purification. A measured amount of trehalose was added to a measured volume of glycerol in an airtight glass vessel. The clear solution was prepared by heating at 333K and stirring the solution by magnetic stirrer for 3 hours. After getting the clear solution, it was cooled to room temperature. A few µL freshly prepared solution of C153 in heptane was poured into a quartz cuvette of optical path length 1 cm. The nonpolar solvent was then

evaporated by blowing hot air around outer surface of the cuvette. Then 3–4 ml of sample solution was added to the cuvette. The solution was heated at 333K and stirred for some time to ensure complete dissolution of the probe molecules into the solution. Next, the solution was cooled to room temperature and required measurements were performed. Note that the concentration of C153 was maintained at $\leq 10^{-5}$ M in all the trehalose–glycerol compositions studied here.

5.2.2 Data Collection and Analysis for Absorption and Steady-state Fluorescence Emission Spectra

UV–Visible spectrophotometer (UV–2450, Shimadzu) and fluorimeter (Fluorolog–3, Jobin-Yvon, Horiba) were used to record, respectively, absorption and emission spectra of C153 at different solution compositions and temperatures. Temperature was controlled via using Julabo and Peltier temperature-controller respectively. The resolution of the instrument for peak frequency determination was ~250 cm^{-1}. Spectral analysis procedure[55-59] was the same as discussed in chapter 2.

5.2.3 Data Collection and Analysis for Time-resolved Fluorescence Emission Spectra

The time-correlated single photon counting (TCSPC) technique based on a laser system (Lifespec–ps, Edinburgh, U.K.) with a light-emitting diode (LED) was used to collect fluorescence emission intensity decays. The laser of 409 nm wavelength was used as excitation source. The full width at half maximum (FWHM) of the instrument response function (IRF) (measured at the magic angle (54.7^0) using distilled water and 409 nm excitation light) was ~90 ps. The fluorescence emission decay was collected using an emission band pass of $\leq$ 2.0 nm. All the measurements were recorded using a Peltier temperature controller with an accuracy in the temperature measurements of $\pm$ 1K.

5.2.4 Data Collection and Analysis for Solvation Dynamics

For solvation dynamics studies, typically 17–18 emission intensity decays were collected at the magic angle (54.7^0) at equally spaced wavelengths across the steady state emission spectrum of C153 in the solution. The collected emission decays were first deconvoluted from the IRF to remove the instrumental broadening and then fitted with multi-exponential functions using an iterative reconvolution algorithm.[55,60] Such a fitting procedure is known to sharpen the effective time resolution by a factor of ~4–5,[55,59-62] and therefore, time scales in the ~20–25 ps range generated from decay fits in the present study may indicate the presence of such dynamics or much faster ones in these solutions. Time-resolved emission spectra (TRES) were then reconstructed from the decay fit parameters in conjunction with normalized intensities at each of these wavelengths of the steady state emission spectrum.[63] The time dependent solvation of the laser excited probe was then followed by constructing the normalized spectral or solvation response function[55]

$$S(t) = \frac{\nu(t) - \nu(\infty)}{\nu(0) - \nu(\infty)}, \qquad (5.1)$$

where, $\nu(t)$ denotes some measure of the time dependent frequency (first moment frequency was considered in present study) of the fluorescence emission spectrum of the laser excited dye dissolved in that medium. $\nu(0)$ is the emission frequency of the time zero spectrum (at a time when the vibrational relaxation in the excited probe molecule is complete but the solvent relaxation has not begun yet) and $\nu(\infty)$ represents the emission frequency after the solvent relaxation is complete.[64] It is therefore expected that the fluorescence emission spectrum at $t = \infty$ obtained from the time-resolved experiments should be the same as that obtained from the steady state experiments.[55] Determination of the proper time-zero emission spectrum for solvation studies is very difficult because the position of time-zero spectrum strongly depends on the resolution of the instrument. In our instrumental resolution, it is not possible to obtain proper time zero emission spectrum. So we have estimated the time zero emission spectrum from the method described in the literature.[65] One thing is to note here that $S(t)$ is normalized such that it decays from unity at $t = 0$ to zero at $t = \infty$, and a time integration of $S(t)$ produces the average solvation time, $\langle \tau_s \rangle$. This is represented by the following equation:

$$\langle \tau_s \rangle = \int_0^\infty dt S(t) = \int_0^\infty dt \sum_i [a_i \exp(-t/\tau_i)] = \sum_i a_i \tau_i \left(\sum_i a_i = 1 \right), \qquad (5.2)$$

a_i and τ_i are the amplitude and time constant obtained from exponential fit to the measured $S(t)$ decay.

5.2.5 Data Collection and Analysis for Rotational Anisotropy

For the measurements of rotational anisotropy decay, $r(t)$, emission intensity decay was collected at the wavelength of peak maximum of steady-state fluorescence emission to minimize the effect of fast decay or rise due to solvent reorganization.[66,67] Emission decays were collected at three different positions of emission polarizer, magic angle (54.7^0), parallel $[I_{\parallel}(t)]$ and perpendicular $[I_{\perp}(t)]$ with respect to the polarization of the excitation light. Detailed analysis procedure[61,64,66,68] for $r(t)$ decays has been given in the experimental section of chapter 2.

5.2.6 Viscosity and Density Measurements

The density and ultrasonic velocity of the solutions were measured by using automated density cum sound analyzer (DSA 5000, Anton Paar). Viscosity coefficients of the solutions were then measured by an automated micro viscometer (AMVn, Anton Paar).

5.2.7 Force Field

We have performed simulation studies using GLYCAM06[69] force field for trehalose and OPLS-AA[70] force field for glycerol. Note that the modified partial charges for various atomic sites of glycerol are used here.[71] The total potential energy expression for trehalose is as follows:

$$U = \left[\sum_{bonds} k_{r_{ij}} \left(r_{ij} - r_{ij}^0 \right)^2 \right] + \left[\sum_{angles} k_{\theta_{ijk}} \left(\theta_{ijk} - \theta_{ijk}^0 \right)^2 \right] + \left[\sum_{torsions} k_{\phi_{ijkl}} \left[1 + \cos\left(n\phi_{ijkl} - \delta \right) \right] \right]$$

$$+ \left[\sum_{i<j} \left\{ 4\varepsilon_{ij} \left[\left(\frac{\sigma_{ij}}{r_{ij}} \right)^{12} - \left(\frac{\sigma_{ij}}{r_{ij}} \right)^6 \right] + \frac{q_i q_j}{4\pi\varepsilon_0 r_{ij}} \right\} \right] \quad (5.3)$$

For glycerol, the relevant expression is given by

$$U = \left[\sum_{bonds} k_{r_{ij}} \left(r_{ij} - r_{ij}^0 \right)^2 \right] + \left[\sum_{angles} k_{\theta_{ijk}} \left(\theta_{ijk} - \theta_{ijk}^0 \right)^2 \right]$$

$$+ \left[\sum_{torsions} \left\{ \frac{V_1}{2} (1 + \cos\varphi) + \frac{V_2}{2} (1 - \cos2\varphi) + \frac{V_3}{2} (1 + \cos3\varphi) \right\} \right]$$

$$+ \left[\sum_{i<j} \left\{ 4\varepsilon_{ij} \left[\left(\frac{\sigma_{ij}}{r_{ij}} \right)^{12} - \left(\frac{\sigma_{ij}}{r_{ij}} \right)^6 \right] + \frac{q_i q_j}{4\pi\varepsilon_0 r_{ij}} \right\} \right] \quad (5.4)$$

Here, the intramolecular bonded interactions consist of harmonic terms for bond stretching (bond length, r_{ij}; equilibrium bond length, r_{ij}^0 and bond force constant, $k_{r_{ij}}$), angle bending (bond angle, θ_{ijk}; equilibrium bond angle, θ_{ijk}^0 and angle force constant, $k_{\theta_{ijk}}$) and torsional potential defined over cosines of the dihedral angle ϕ_{ijkl} (multiplicity, n; phase shift angle, δ and torsional force constant, $k_{\phi_{ijkl}}$). In OPLS-AA potential, V_1, V_2, V_3 denote the coefficients of the Fourier series and φ is the torsional angle.

The nonbonded interactions are included via Lennard–Jones (LJ) and Coulomb interactions. Potential well depth, van der Waals radius, distance between atoms are symbolized by ε_{ij}, σ_{ij} and r_{ij} respectively. The parameter q represents the partial charge of the atom and ε_0 represents the static dielectric constant. LJ interactions between unlike atoms are calculated via Lorentz–Berthelot combining rules.[72]

5.2.8 Simulation Details

All the necessary simulations were carried out with a total 512 number of molecules in cubic box with periodic boundary condition employing DL_Classic_1.9[73] MD simulation package. As the system was highly viscous, the following method was adopted to reach the properly equilibrated configuration. First, the system was heated up to 500K via step-up process with a step of 100K in NVT ensemble. Subsequently, the system was cooled down to the desired temperature via step-down process with the same temperature gap. Next, the system was equilibrated in NPT ensemble for 2ns to achieve the experimental density. Furthermore, 2 ns equilibration run followed by 50 ns production run was performed in NVT ensemble using Nosé–Hoover thermostat[74,75] with relaxation time of 0.5 ps for calculating different structural and dynamical properties. Equations of motions were solved by Verlet–Leapfrog algorithm[72] with time step of 1 fs. Ewald summation technique[72] and SHAKE algorithm[76] were used to respectively handle electrostatic interactions and constrain all bonds involving hydrogen atoms.

5.3 Required Statistical Mechanical Relations for Data Analysis

The translational self-diffusion coefficient (D) of a particle moving in a fluid can be calculated from the mean squared displacements (MSDs) of centre-of-mass position vectors $\mathbf{r}_i(t)$ as follows:

$$\left\langle \left|\Delta\mathbf{r}(t)\right|^2 \right\rangle = \frac{1}{N}\left\langle \sum \left|\mathbf{r}_i(t) - \mathbf{r}_i(0)\right|^2 \right\rangle, \qquad (5.5)$$

with $\left\langle \left|\Delta\mathbf{r}(t)\right|^2 \right\rangle$ denoting the MSD. Subsequently, D has been calculated from the simulated $\left\langle \left|\Delta\mathbf{r}(t)\right|^2 \right\rangle$ at long time as follows[77]:

$$D = \left[\frac{1}{6t}\left(\left\langle \left|\Delta\mathbf{r}(t)\right|^2 \right\rangle\right)\right]_{t\to\infty}. \qquad (5.6)$$

The translational non-Gaussian (NG) parameter $\alpha_2(t)$ can be obtained from the simulated MSD using the following relation[78]:

$$\alpha_2(t) = \frac{3\langle \Delta r^4(t)\rangle}{5\langle \Delta r^2(t)\rangle^2} - 1, \qquad (5.7)$$

where $\langle \Delta r^2(t)\rangle = \left\langle N^{-1}\sum_{i=1}^{N}|\Delta \mathbf{r}(t)|^2\right\rangle$ and $\langle \Delta r^4(t)\rangle = \left\langle N^{-1}\sum_{i=1}^{N}|\Delta \mathbf{r}(t)|^4\right\rangle$ with Δr denoting the single particle displacement. $\Delta \mathbf{r}(t) = \mathbf{r}_i(t) - \mathbf{r}_i(0)$.

Required relation for calculating the translational new non-Gaussian (NNG) parameter $\gamma(t)$ as follows[79]:

$$\gamma(t) = \frac{1}{3}\langle \Delta r^2(t)\rangle\left\langle \frac{1}{\Delta r^2(t)}\right\rangle - 1, \qquad (5.8)$$

with $\left\langle \dfrac{1}{\Delta r^2(t)}\right\rangle = \left\langle \dfrac{1}{N}\sum_{i=1}^{N}\dfrac{1}{|\Delta \mathbf{r}(t)|^2}\right\rangle$.

Four point dynamic susceptibility, $\chi_4(\mathbf{k},t)$ is defined as the variance of the fluctuations of self-intermediate scattering function, $F_s(\mathbf{k},t)$.[80-82]

$$\chi_4(\mathbf{k},t) = N\left[\left\langle F_s(\mathbf{k},t)^2\right\rangle - \left\langle F_s(\mathbf{k},t)\right\rangle^2\right], \qquad (5.9)$$

where,

$$F_s(\mathbf{k},t) = \frac{1}{N}\sum_{i=1}^{N}\langle \cos \mathbf{k}\cdot[\mathbf{r}_i(t) - \mathbf{r}_i(0)]\rangle. \qquad (5.10)$$

The relaxation of H-bond lifetime is calculated by the time-correlation function, $S_{HB}(t)$,[83-85]

$$S_{HB}(t) = \frac{\langle h(0)H(t)\rangle}{\langle h\rangle}, \qquad (5.11)$$

where $H(t) = 1$ if the tagged pair of molecules, for which $h(0)$ is calculated, remains continuously H-bonded till time t, else zero. $S_{HB}(t)$ describes the probability that a tagged pair of molecules remains continuously H-bonded up to time t, and approaches to zero when H-bonding between them breaks down for the first time. The time profile of $S_{HB}(t)$ therefore

represents relaxation of H-bond lifetime, and hence, the average H-bond lifetime, $\left\langle \tau_S^{HB} \right\rangle$, can be obtained via time integration of this normalised time correlation function.

The structural relaxation time of H-bond is calculated by the time-correlation function, $C_{HB}(t)$, defined as[83-85]

$$C_{HB}(t) = \frac{\langle h(0)h(t) \rangle}{\langle h \rangle} , \tag{5.12}$$

where $C_{HB}(t)$ exhibits a much slower decay than $S_{HB}(t)$, as the former is independent of possible breaking of H-bonds between the tagged pair of molecules in the intermediate time and considers the reformation of bond after breakage. $C_{HB}(t)$ is, therefore, associated with H-bond structural relaxation, and thus the time integration of this normalised correlation function provides the average structural relaxation time, $\left\langle \tau_C^{HB} \right\rangle$.

5.4 Results and Discussion

5.4.1 Absorption and Steady-state Emission Spectra: Temperature Effect

First, we have investigated the effects of temperature on the absorption and steady-state emission spectra of C153 in pure glycerol and trehalose/glycerol bioprotectant mixtures. Absorption and emission frequencies (ν) are shown as a function of temperature at three different concentrations of trehalose in Figure 5.1. Temperature dependent absorption and emission spectra of C153 in 20 wt % trehalose are shown in Figure 5.A.1 of Appendix 5.A. Figure 5.1 indicates that the variation of absorption frequency, ν_{abs}, with temperature is small compared to that of emission frequency, ν_{em}. The maximum change in ν_{abs} with temperature in 20 wt % trehalose is ~200 cm^{-1}. This amount of shift does not carry any significant information as it is within our instrumental resolution (250 cm^{-1}). Interestingly, ν_{em} shifts to the lower frequency (red-shift) with rise of temperature. This is viscosity effect as high temperature reduces the medium viscosity which in turn allows the solute emission to come from the relatively better solvent-equilibrated state. The excited-state dipole moment

of C153 increases significantly due to electronic redistribution.[86-90] Therefore, the enhanced interaction with the solvent molecules at more mobile condition leads to the extra stabilization of the energy levels of C153. The red-shift is also found to be larger in trehalose/glycerol solution (~400 cm^{-1}) than in pure glycerol.
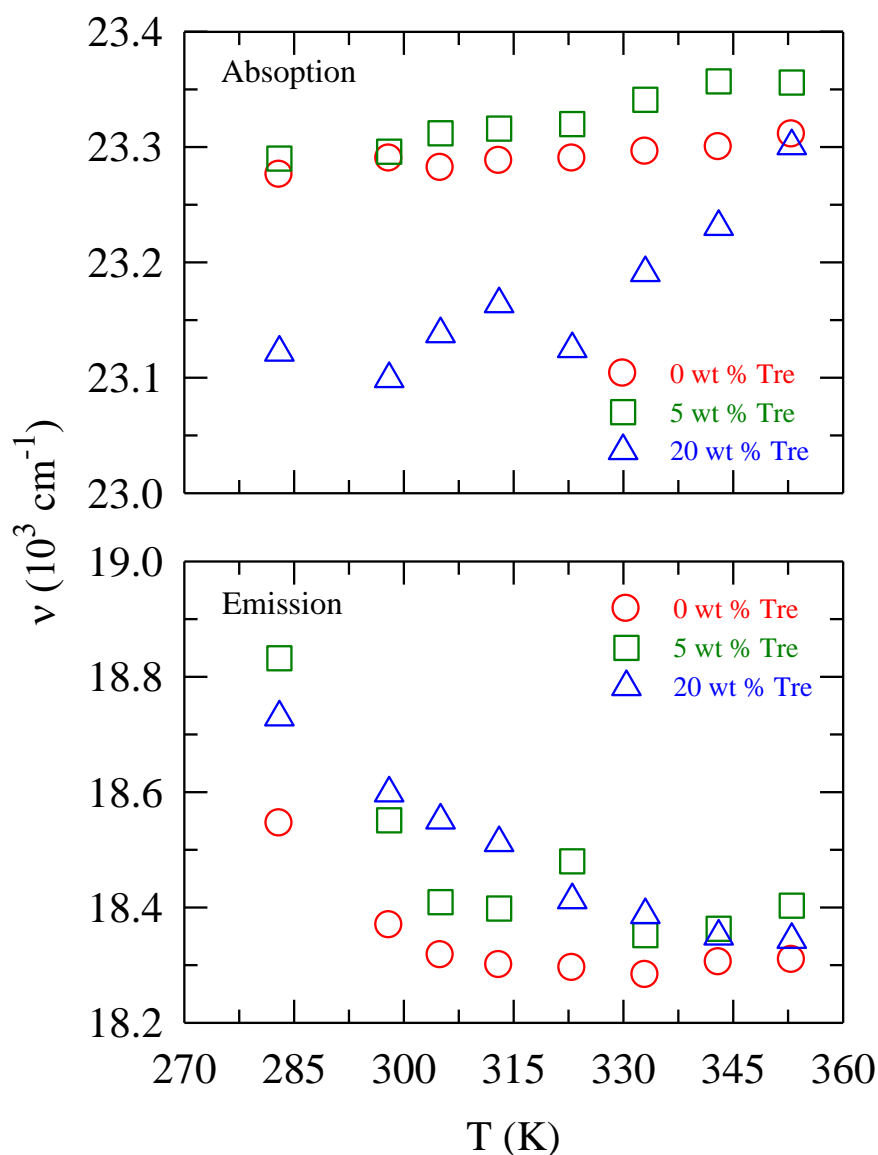
Figure 5.1: Temperature dependence of absorption (upper panel) and emission (lower panel) spectral frequency of C153 in three different compositions of trehalose into glycerol (0 wt %, 5 wt % and 20 wt %). Different colour coded symbols in each panel represent different trehalose concentrations. Average frequencies of first moment frequency, peak frequency and half average frequency are shown here.

Further, we have explored the spatial heterogeneity aspect of the medium monitoring the excitation wavelength (λ_{ex}) dependence on the emission frequency (ν_{em}) and spectral width (Γ_{em}) [FWHM] of the solute C153 in Figure 5.2. λ_{ex}-dependent emission has been recorded
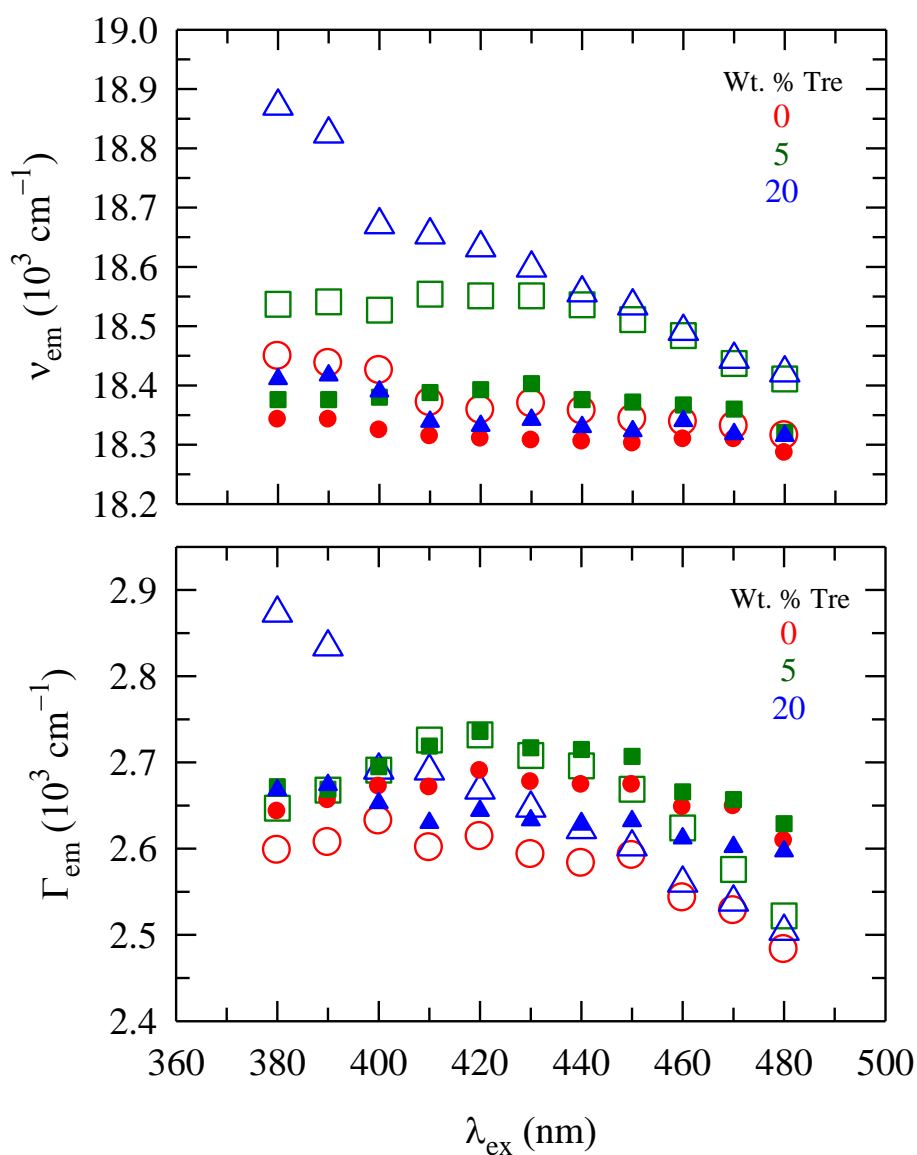
Figure 5.2: Excitation wavelength, λ_{ex} dependent emission frequency, ν_{em} and spectral width Γ_{em} of C153 in different trehalose-glycerol compositions at ~298K (open symbols) and ~353K (filled symbols). Trehalose concentrations are colour-coded in respective panel.

at two different temperatures, 298K and 353K. We observed that ν_{em} and Γ_{em} of C153 show the strongest λ_{ex}-dependence at 20 wt % trehalose at 298 K, suggesting the inhomogeneous nature of the environment around C153 in this medium at this temperature. At 353 K, this dependence disappears because of temperature-induced rapid interconversion among various solvation configurations around the dissolved probe C153.

5.4.2 Solvation Dynamics: Temperature Dependence

Representative time-resolved emission spectra (TRES) of C153 in the solution of 20 wt % trehalose at ~333K are shown in the upper panel of Figure 5.3. The TRES are obtained from fitting the reconstructed data points to a log-normal line shape function.[63] The difference between the first moment frequencies of reconstructed time-zero spectrum and spectrum at $t = \infty$ is found to be ~600 cm^{-1}, which is nearly 30% less than the estimated 'true' dynamic Stokes shift $\left(\nu_{est.}^{SS} = 840\,\mathrm{cm}^{-1}\right)$ for C153 in this solution. The steady-state emission spectrum of C153 in this solution at this temperature is also shown in the same panel. Note that the steady state emission spectrum is blue-shifted ~90 cm^{-1} relative to the time-resolved emission spectrum at $t = \infty$. Although, the blue-shift is very small, this deviation originates probably either from the sluggish movement of solvent molecules, or from the subtle changes in the vibronic structure of the spectrum.[49,91] Representative frequency shift with time, t for this composition and temperature has been plotted in the middle panel of this figure. The overall spectral shape of the time-resolved spectrum obtained at different time slices remains the same with t. But the width, provided in the bottom panel, shows irregular change at the initial times for pure solvent glycerol as well as trehalose/glycerol solution. The use of broader time resolution in the present experiments and consequently poor fitting of the data points for the time-resolved spectrum at the initial times are probably the reasons for the inconsistency of spectral width of time-evolved spectrum. However, $\Gamma(t)$ reaches a plateau as solvation progresses with t. This is also observed for polar solvation energy relaxation in neat solvents[55] and molten mixtures[49,50,91]. All values of $\Gamma(t)$ obtained from both steady-state (shown Figure 5.A.1 of Appendix 5.A) and time-infinity ($t = \infty$) emission spectra agree with each other. For this composition (20 wt % trehalose), steady-state and time-infinity emission spectral widths are 2621 and 2618 cm^{-1} respectively at 333K. Above all, the larger amount of
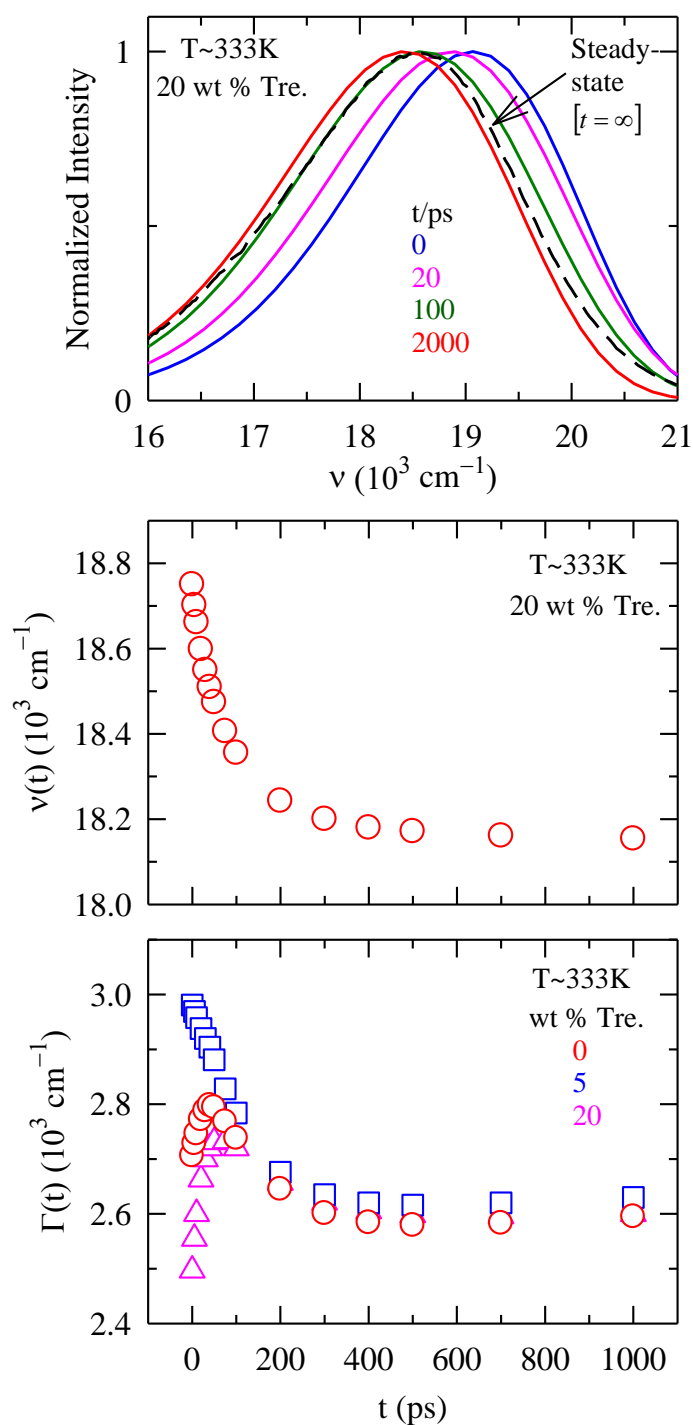
Figure 5.3: Synthesized time resolved emission spectra (TRES) of C153 at different time slices from the experimentally obtained decays in 20 wt % trehalose at 333K. TRES shown (upper panel) are at the following time intervals after solute excitation: 0 ps, 20 ps, 100 ps and 2000 ps. Time evolution of the first moment frequencies, $v(t)$ are shown in the middle panel and the widths $\Gamma(t)$ are shown in the lower panel for the same composition and temperature.

dynamic Stokes shift (middle panel) compared to change of time-resolved spectral width suggests the medium reorganization around the perturbed solute in these solutions.

In Figure 5.4, we have plotted the emission decays of C153 collected at three different wavelengths (480, 550, 630 nm) of emission spectrum in the solution of 20 wt % trehalose at ~353K (upper panel) and ~298K (lower panel). Corresponding IRFs are also shown in both the panels. Inset presents the data on shorter timescale for better resolution. The temperature dependent viscosity (η) of the medium for different trehalose concentrations $(C_{Tre.})$ has been provided in Table 5.1. In such high viscous media, solvation dynamics is expected to possess a significant contribution from slow diffusive solvent modes. This would be reflected by a rise component in the time-resolved emission intensity decay collected at the longer wavelength (red end) of the steady-state emission spectrum. Here we have seen at 353K that decay characteristics involves rise followed by decay at the red end and only decay at the blue end. This clearly indicates the environmental rearrangement in response to the instantaneously altered dipole moment of the solute dissolved in this solution. Interestingly, at 298 K this rise component is completely missing (see the lower panel) although the viscosity of the medium at 298K is much larger than that at 353K (Table 5.1). The probable reason for such an observation could be that in such a high viscous condition (~22P), solvation energy relaxes mainly via the solvent inertial modes, leaving a tiny fraction for the slow diffusive relaxation. This system contains several –OH groups which can support collective solvent intermolecular vibrations and librations. These collective modes are known to participate in polar solvation energy relaxation at the sub-picosecond regime.[92,93] Unfortunately, such a fast response cannot be detected by the present set-up, and as a result, the fast solvation response (which could be the entire response at 298K) is completely missed.
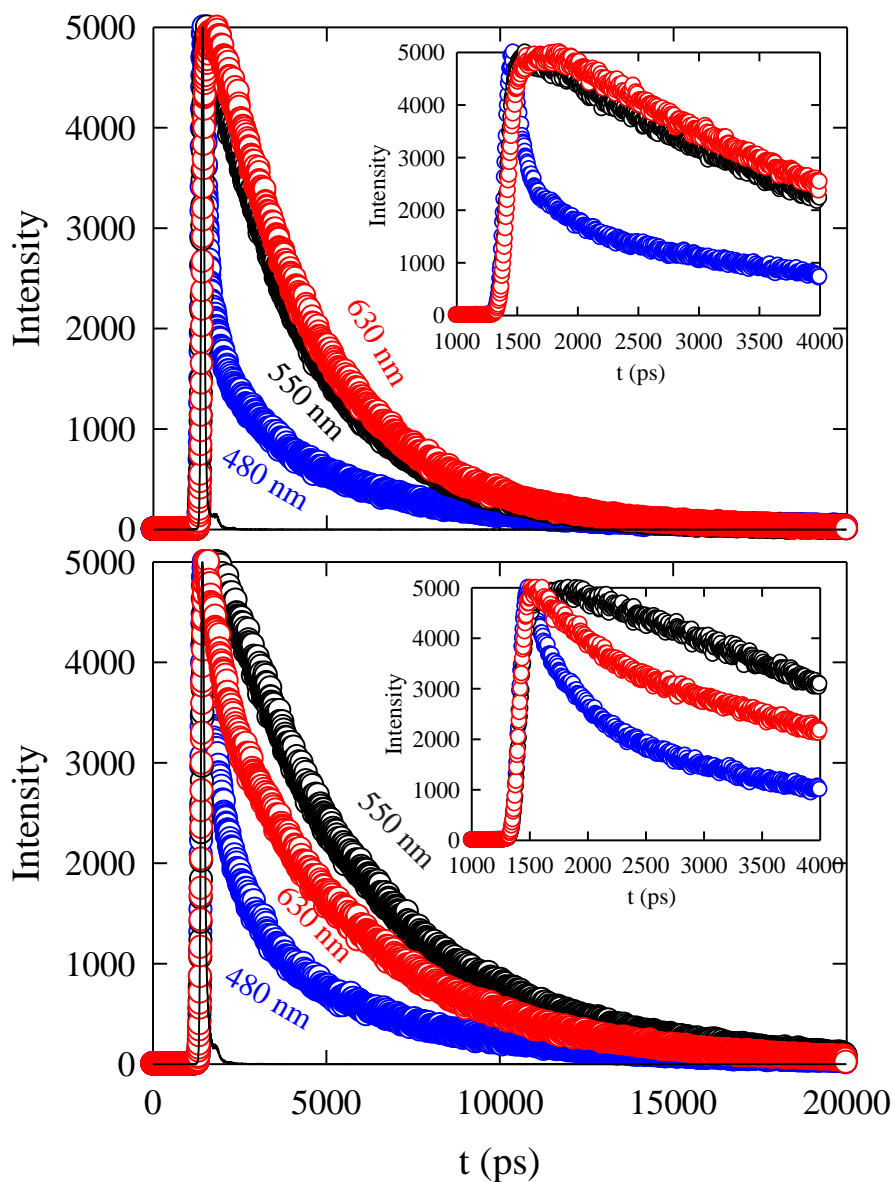
Figure 5.4: Representative fluorescence intensity decay of C153 in 20 wt % trehalose at three different wavelengths of emission spectrum; blue, middle (close to peak maximum) and red at ~353K (upper panel) and ~298K (lower panel). Experimental data are shown by circles. The instrument response function is also shown in the same figure (solid line). Decay at each wavelength is represented by different colours. The same plots are shown at the inset of each panel by narrowing the scaling of the X-axis for better visualization.

Table 5.1: Experimentally measured temperature dependent viscosity (η) of different trehalose concentrations into glycerol $(C_{Tre.})$.

$C_{Tre.}(wt.\%)$	$T(K)$	$\eta(cP)$
0	298	861
	313	273
	333	82
	353	33
5	298	937
	313	298
	333	89
	353	36
20	298	2258
	313	631
	333	167
	353	61

Representative solvation response functions, $S(t)$ of three different compositions of trehalose–glycerol solutions at ~333K are shown in the upper panel of Figure 5.A.2 (Appendix 5.A) whereas lower panel of the plot shows temperature dependent $S(t)$ of 20 wt % trehalose solution. $S(t)$ is constructed by equation 5.1. Note that first moment frequencies of time-resolved spectra were considered for all the cases. Single and Bi-exponential functions were adequate to fit the observed $S(t)$. Fitting parameters of the response functions are summarized in Table 5.2. We observed that average solvation time, $\langle \tau_s \rangle$ becomes slower with addition of trehalose into glycerol as η of the medium (Table 5.1) increases with increase of trehalose concentrations, $C_{Tre.}$. $\langle \tau_s \rangle$ becomes faster with increase of temperature because η decreases with temperature. Interestingly, when the temperature was increased from 333K to 353K for $C_{Tre.} = 20\,wt\,\%$, $\langle \tau_s \rangle$ becomes slower. Following our study of alcohol/water binary mixtures,[62,94-96] it may be assumed that this binary mixture probably undergoes a structural transition at higher temperature, allowing the slow diffusion to participate in solvation by reducing the contributions from the collective solvent vibration and libration modes. Further study is required to confirm what kind of structural transition is involved in these systems.

Table 5.2: Fitting parameters for observed solvation response functions $[S(t)]$ of different $C_{Tre.}$ using C153 at various temperatures.

$C_{Tre.}(wt.\%)$	$T(K)$	a_1	τ_1/ps	a_2	τ_2/ps	$\langle\tau_s\rangle$/ps
0	298	1.00	345			345
	313	0.24	49	0.76	178	147
	333	0.24	34	0.76	100	84
	353	1.00	44			44
5	298					
	313	0.40	67	0.60	227	163
	333	0.84	66	0.16	238	94
	353	0.73	35	0.27	143	64
20	298					
	313	0.48	78	0.52	455	274
	333	0.44	39	0.56	167	111
	353	0.87	68	0.13	909	177

Further, we have calculated dynamic Stokes shift magnitudes and shown in Table 5.3. Note that the total Stokes shift has been estimated via the Fee-Maroncelli method[65] by determining the 'true' time-zero spectrum. Table 5.3 shows that missing percentage is maximum in case of pure glycerol at 298K. Glycerol is known to form extensive H-bond network at room temperature.[97-99] At 298K, the high viscosity (861 cP) of glycerol ensures sluggish solvent relaxation. As a result, fast libration (sub-hundred fs) of H-bond network predominantly contributes to the solvation energy relaxation. Consequently, the current measurements employing limited time resolution failed to capture the dominant portion of the total solvation response. Interestingly, the missing percentage decreases with the increase of temperature. Increase of temperature leads to disruption of H-bond network since H-bond energy (< 200 cm^{-1}) is comparable to thermal energy (~ 200 cm^{-1}), reducing the contribution of the collective solvent intermolecular modes to the total relaxation. This in turn increases the participation of the slow solvent diffusive modes. Consequently, missing percentage decreases with increase of temperature. Another important observation from this table is that addition of trehalose also decreases the missing percentage. Here, H-bond structure breaking ability[100,101] of trehalose comes into play. This leads to the reduction of missing percentage with increase of trehalose concentration.

Table 5.3: Temperature dependent dynamic Stokes shift and missing % at different $C_{Tre.}$.

$C_{Tre.}(wt.\%)$	$T(K)$	$\Delta\nu_{Est.}(cm^{-1})$	$\Delta\nu_{Obs.}(cm^{-1})$	Missing $(\%)$
0	298	1175	352	70
	313	1192	599	50
	333	1109	604	46
	353	1022	539	47
5	298			
	313	1093	594	46
	333	1072	637	41
	353	990	618	38
20	298			
	313	727	482	34
	333	840	603	28
	353	1053	452	57

5.4.3 Rotational Dynamics: Effect of Temperature

Rotational dynamics of C153 has been measured at different $C_{Tre.}$ varying solution temperature from 298K to 353K to explore the extent of solute–solvent coupling in these bioprotectant mixtures. Representative $r(t)$ decay of C153 in $C_{Tre.} = 20\,wt\%$ at 313K constructed by using equation 2.1 (shown in chapter 2) is shown in Figure 5.A.3 of Appendix 5.A. Bi-exponential fitting parameters are also given in the upper panel of the plot. Residual of the fit is shown in the bottom panel. Fitting parameters for single and bi-exponential functions required for adequate fitting of observed $r(t)$ decays of C153 in different trehalose-glycerol solutions at various temperatures are given in the Table 5.4.

Table 5.4: Fitting parameters for rotational anisotropy, $r(t)$ decays of C153 in various $C_{Tre.}$ at different temperatures.

$C_{Tre.}(wt.\%)$	$T(K)$	a_1	τ_1 /ns	a_2	τ_2 /ps	$\langle\tau_r\rangle$/ns
0	298	1.00	82.18			82.18
	313	0.69	8.09	0.31	20	5.55
	333	0.80	2.65	0.20	20	2.12
	353	0.79	0.96	0.21	20	0.76
5	298	1.00	96.95			96.95
	313	0.51	8.99	0.49	20	4.60
	333	0.77	2.96	0.23	20	2.29
	353	0.79	1.01	0.21	20	0.80
20	298	1.00	229.5			229.5
	313	0.67	23.15	0.33	20	15.45
	333	0.71	5.34	0.29	41	3.82
	353	0.63	1.53	0.37	26	0.98

The experimentally observed values of average rotational times, $\langle\tau_r\rangle$ of C153 were compared with the predicted values of $\langle\tau_r\rangle$ from *modified* Debye-Stokes-Einstein (SED) relation: $\tau_{rot} = V\eta f C/k_B T$, where, V (= 248 Å^3 for C153) is the volume of C153, η is the viscosity of the medium and $k_B T$ is the Boltzmann's constant times the temperature. f (=1.71 for C153) is the shape factor of C153 and C is the coupling parameter. For stick and slip boundary conditions,[66] the values of C were taken 1 and 0.24 respectively. The observed and predicted $\langle\tau_r\rangle$ values of C153 in glycerol and glycerol–trehalose solutions are plotted as a function of temperature reduced viscosity, η/T in Figure 5.5. All the $\langle\tau_r\rangle$ values are summarized in Table 5.B.1 of Appendix 5.B. From the table we can see that the observed $\langle\tau_r\rangle$ of C153 at ~298K is extremely slow (in the order of hundreds of ns). It increases with increase of trehalose concentration as η also increases. Note that there always remains uncertainties in determining such high values of rotational times of the probe C153 which has an excited-state lifetime ~4–6 ns. However, researchers have found the presence of very slow rotational time component of C153 in case of ionic liquids possessing very high viscosity.[102] We also found that solute rotation becomes faster with rise of temperature. This essentially
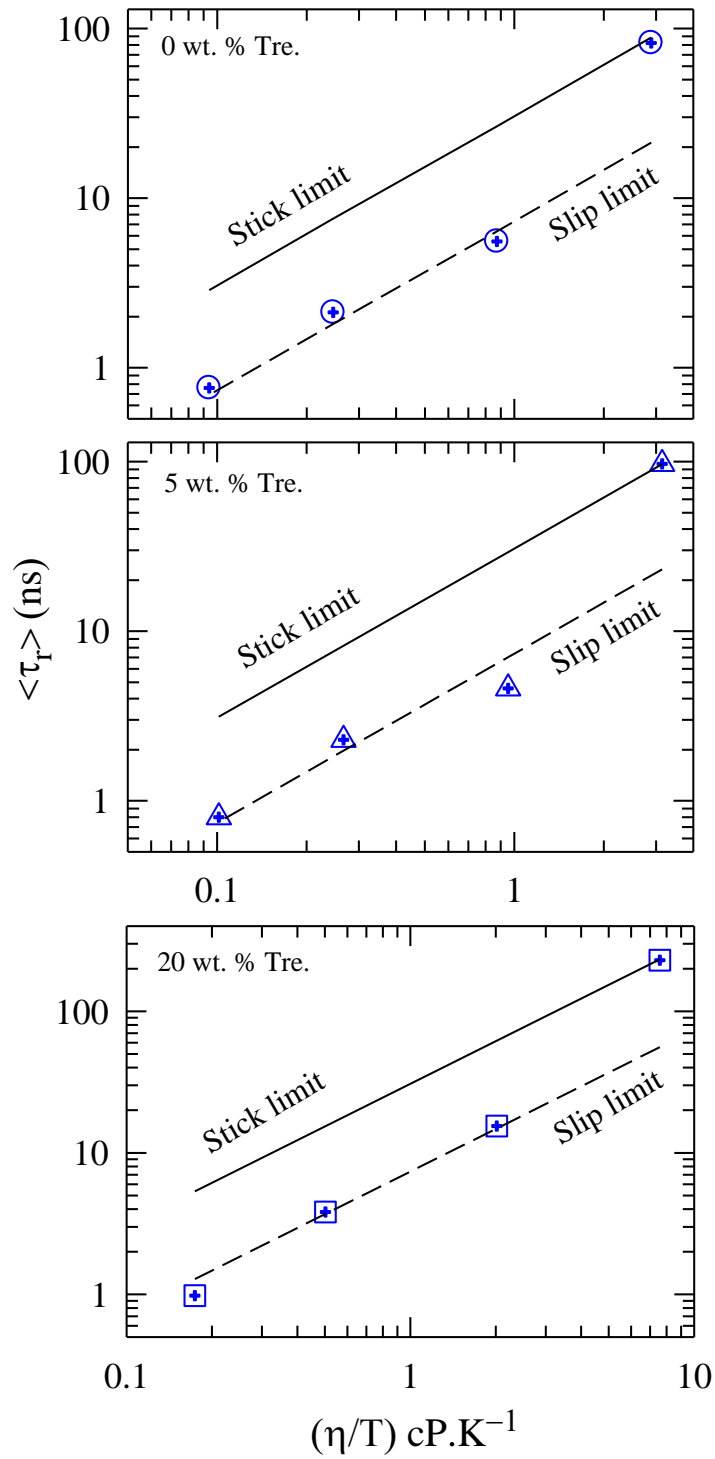
Figure 5.5: Variation of observed average rotational time, $\langle \tau_r \rangle$ of C153 in different $C_{Tre.}$ (symbols) with temperature reduced viscosity, η/T. The predicted values of $\langle \tau_r \rangle$ for stick (solid line) and slip (dashed line) boundary conditions of SED relation for each case are shown in the corresponding panel.

suggests that viscosity of the medium mainly governs the solute's rotational dynamics. Another interesting aspect is that the observed $\langle \tau_r \rangle$ follows the stick boundary condition of SED relation at 298K where viscosity is excessively high and it follows slip boundary condition at higher temperature. Therefore, the measured $\langle \tau_r \rangle$ values reside within the two limits of the hydrodynamic prediction.

We illustrate the coupling of both $\langle \tau_r \rangle$ of C153 and $\langle \tau_s \rangle$ of the solvent molecules with the viscosity of the medium in Figure 5.6, where, in a log-log plot, the composition dependent $\langle \tau_r \rangle$ and $\langle \tau_s \rangle$ measured at different $C_{Tre.}$ varying the temperature of the solution are shown as a function of η/T. $\langle \tau_s \rangle$ exhibits a fractional viscosity dependence, $\langle \tau_s \rangle \propto (\eta/T)^p$ with $p = 0.5$, whereas, $\langle \tau_r \rangle$ shows p value larger than unity $(p = 1.3)$. $p > 1$ for $\langle \tau_r \rangle$ was also found in case of highly viscous medium of ionic liquids.[103-105] Such scaling with η suggests coupling of solute rotational time to structural reorganization in the solvent. The fractional η-dependence of $\langle \tau_s \rangle$ and subsequent departure from the conventional Stokes-Einstein (SE) predictions for these sugar solutions are reminiscent of environmental decoupling observed in deeply supercooled liquids[49,91,106,107].
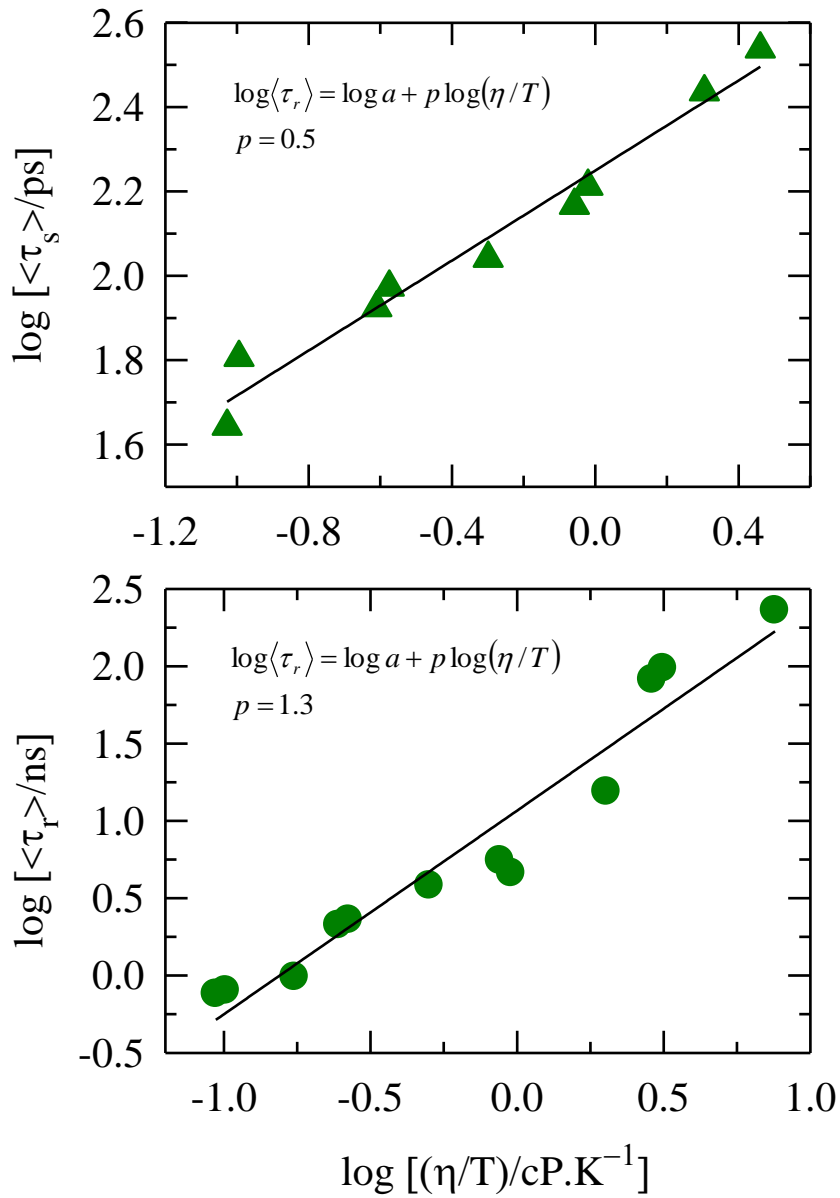
Figure 5.6: Log-log plot of $\langle \tau_s \rangle$ (upper panel) and $\langle \tau_r \rangle$ of C153 (lower panel) versus η/T in various trehalose–glycerol compositions. The solid lines represent the best fit of the experimentally measured data to the relation: $\log\langle\tau\rangle = \log a + p\log(\eta/T)$, the p values are given in each panel.

We have further investigated the system by carrying out MD simulation. Validity of the force field used for glycerol has been checked by comparing the simulated density with our experimental value (Table 5.B.2 of Appendix 5.B).

5.4.4 Solvation Structures: Radial Distribution Functions

Distribution of the oxygen atoms of glycerol, O(G), is shown in Figure 5.7 via the simulated radial distribution function (RDF), $g(r)$, at three different compositions of trehalose/glycerol mixtures at ~298K and ~353K. We found that addition of trehalose does not alter the solvation structure of glycerol molecules. The peak positions and intensities of O(G)–O(G) RDF remain nearly unaltered at all the three compositions. The first peak intensity of O(G)–O(G) RDF at 298K is larger than that at 353K in all the cases. Increase of temperature randomizes the solution structure and hence the peak intensity decreases on going from 298K to 353K.

In Figure 5.8, we have shown the RDFs between trehalose oxygen atoms O(T)–O(T) in the left panels and trehalose oxygen and glycerol oxygen atoms O(T)–O(G) in the right panels. In the RDF of O(T)–O(T), large number of peaks have appeared because of the presence of various –OH groups at different positions of the trehalose molecules. In 5 wt % trehalose, intensity of the peaks of O(T)–O(T) RDF is ~3 times greater than in 20 wt % trehalose, which indicates the aggregation among trehalose molecules at low concentration. With the increase of $C_{Tre.}$, the trehalose molecules disperse into glycerol. However, O(T)–O(G) RDFs remain almost invariant with change of trehalose concentration.
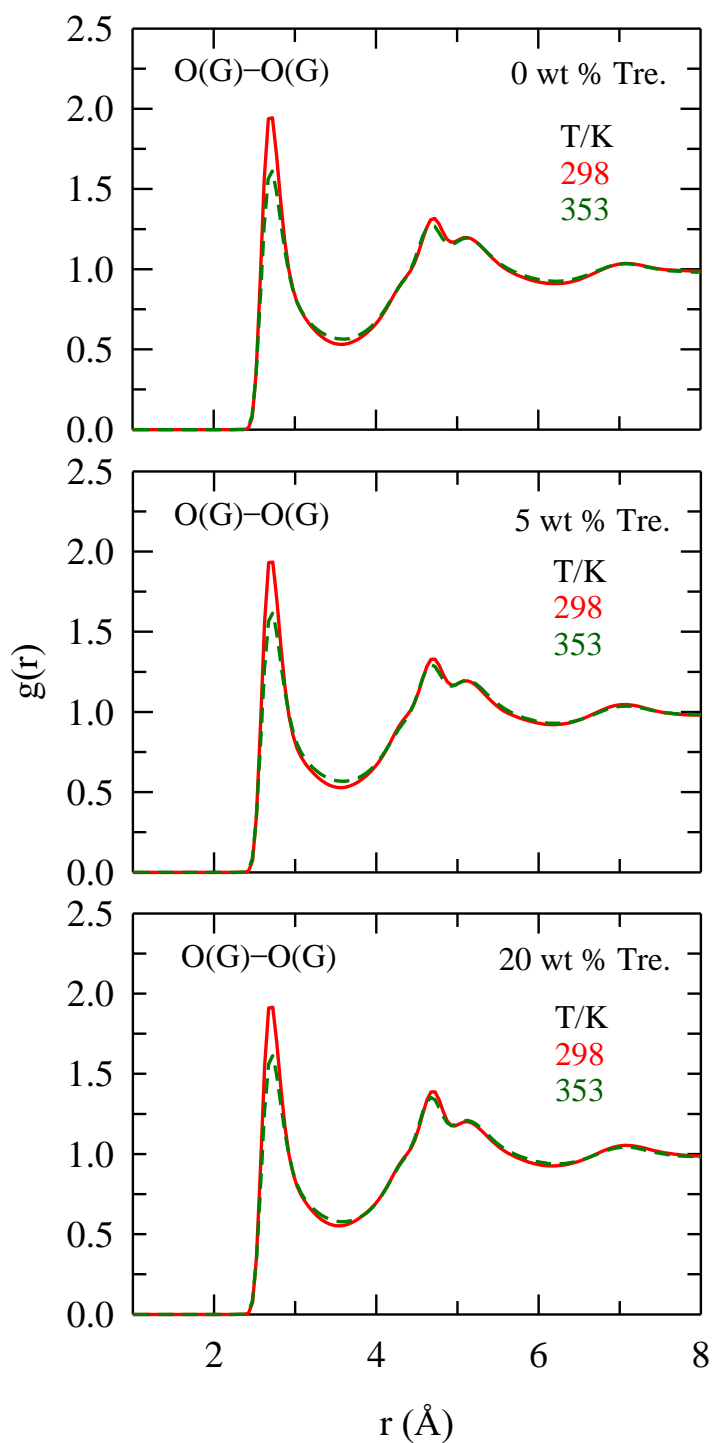
Figure 5.7: Site-site radial distribution function, $g(r)$ between oxygen atoms of glycerol, O(G)–O(G) at three different concentrations of trehalose into glycerol (three panels) as a function of distance r at temperatures ~298K (red) and ~353K (green).
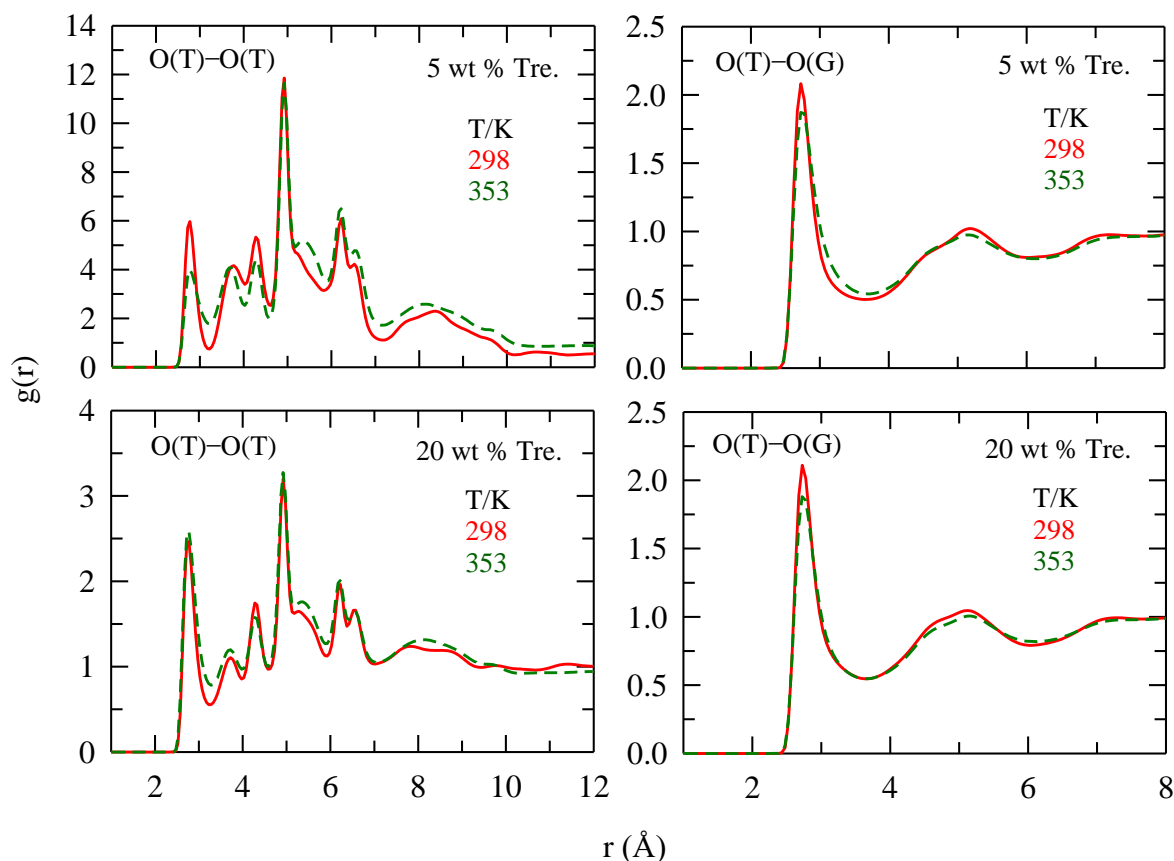
Figure 5.8: Site-site radial distribution function, $g(r)$ between oxygen atoms of trehalose, O(T)–O(T) (left panels) and oxygen atoms of glycerol and trehalose O(T)–O(G) (right panels) for 5 wt % trehalose and 20 wt % trehalose as a function of distance r at temperatures ~298K (red) and ~353K (green).

5.4.5 Dynamical Properties: Mean Squared Displacement

To understand the dynamical behaviour of the molecules in these highly viscous systems, self diffusion coefficient (D) of glycerol has been calculated from the slope of mean squared displacement, MSD (equation 5.5) using Einstein's relation (equation 5.6). For glycerol, we calculated D considering the centre-of-mass (cm) of the molecule and compared with D-value obtained from oxygen atom of –OH group of glycerol. In Figure 5.9, we have plotted the trajectories of the cm and oxygen atom of terminal –OH group of glycerol along the X and Y axes to compare the difference of their motions. At 298K, cm and oxygen atom of glycerol show well separated trajectories whereas their separation decreases at 353K. Thus,

motion of cm and oxygen atom of glycerol is highly decoupled at 298K. In glassy state, it is very likely that resistance on cm motion will be much larger than on the terminal –OH group's motion. With rise of temperature the mobility of the system increases. As a result, both the motions start to couple to each other. The corresponding D values are shown in Table 5.B.3 (Appendix 5.B). We obtained ~3 times slower D for cm than the oxygen atom of –OH group of glycerol. Our simulated D agrees well with the experimental value[108] when we calculated D considering the terminal –OH at smaller array length. Since the motion of different parts of the molecules in glassy state is largely different, careful selection of experimental techniques is necessary in determination of diffusion constant in this type of system.

Mean squared displacement, $\left\langle \left| \Delta r(t) \right|^2 \right\rangle$ of cm of glycerol in different compositions of trehalose–glycerol mixture has been plotted as a function of time, t in Figure 5.10. Here, MSDs exhibit three different time dependent regimes: (i) inertial regime: t^2-dependence at initial time, (ii) sub-diffusive regime at intermediate time where the power of t is less than 1 and (iii) diffusive regime: t^1-dependence at long time. This is characteristic feature of supercooled liquids, ionic glasses and ionic liquids.[109-111] As expected, the upper level of sub-diffusive region gets shortened from ~100 ps to ~50 ps with increase of temperature from 298K to 353K. Interestingly, a subtle dynamical change takes place with addition of 5 wt % trehalose into glycerol at 298K. MSD of glycerol becomes faster in 5 wt % trehalose than in pure glycerol, although, the viscosity of the medium increases after addition of this amount of trehalose into glycerol from 861 to 937 cP (Table 5.1). This is probably due to the disruption of H-bond network of glycerol in addition of trehalose. This signature was also found in dynamic Stokes shift study. Hence, in presence of small amount of trehalose glycerol diffuse at a faster rate. But, further addition of trehalose (20 wt %) reduces the MSD of glycerol. Besides the H-bond breaking-ability of trehalose, addition of 20 wt % of this large molecule enhances the steric crowding of the system. This results the reduction of diffusion of glycerol molecules in this highly congested medium. At 353K, MSD was found to follow the normal trend. It shows gradual slowing-down with increase of $C_{Tre.}$.
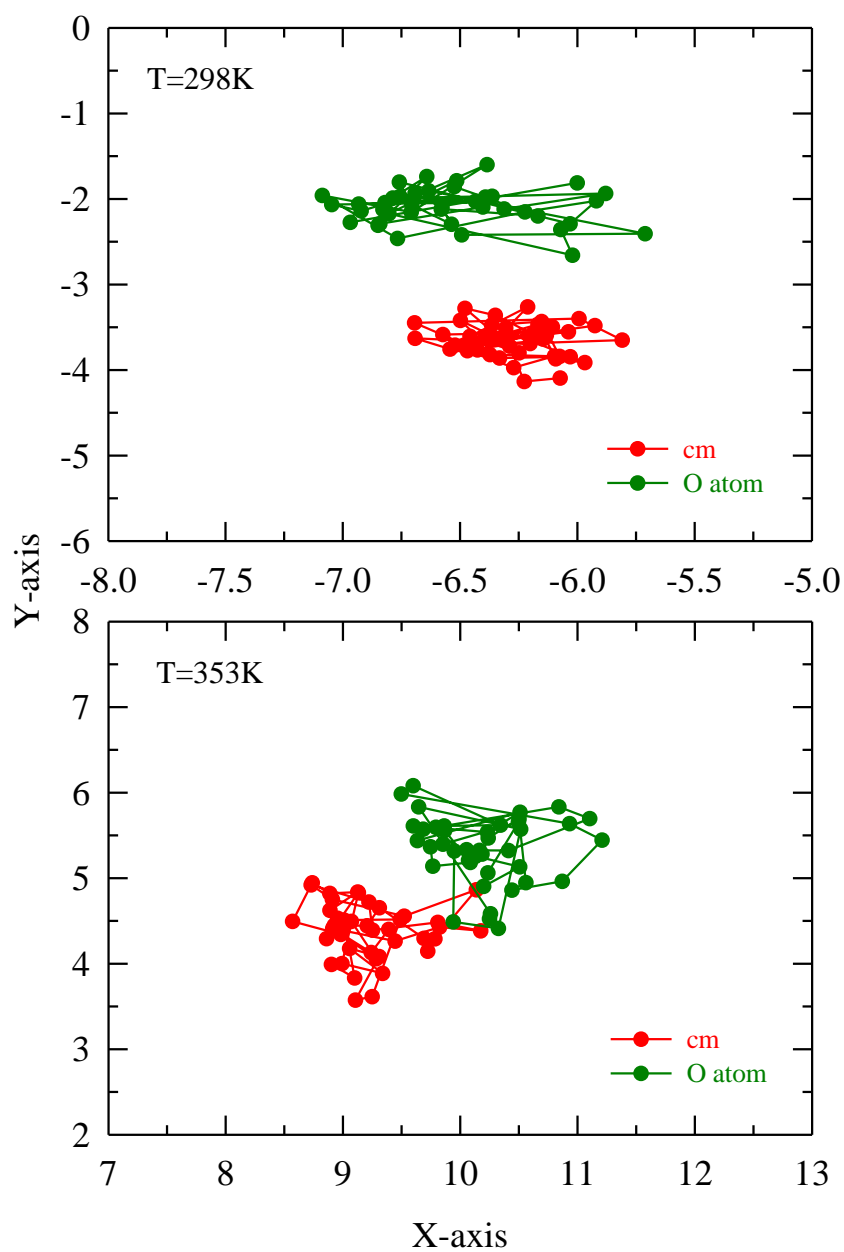
Figure 5.9: Comparison of trajectories between the motions of centre-of-mass (cm) and terminal oxygen of –OH group of glycerol along X and Y axes at ~298K (upper panel) and ~353K (lower panel).
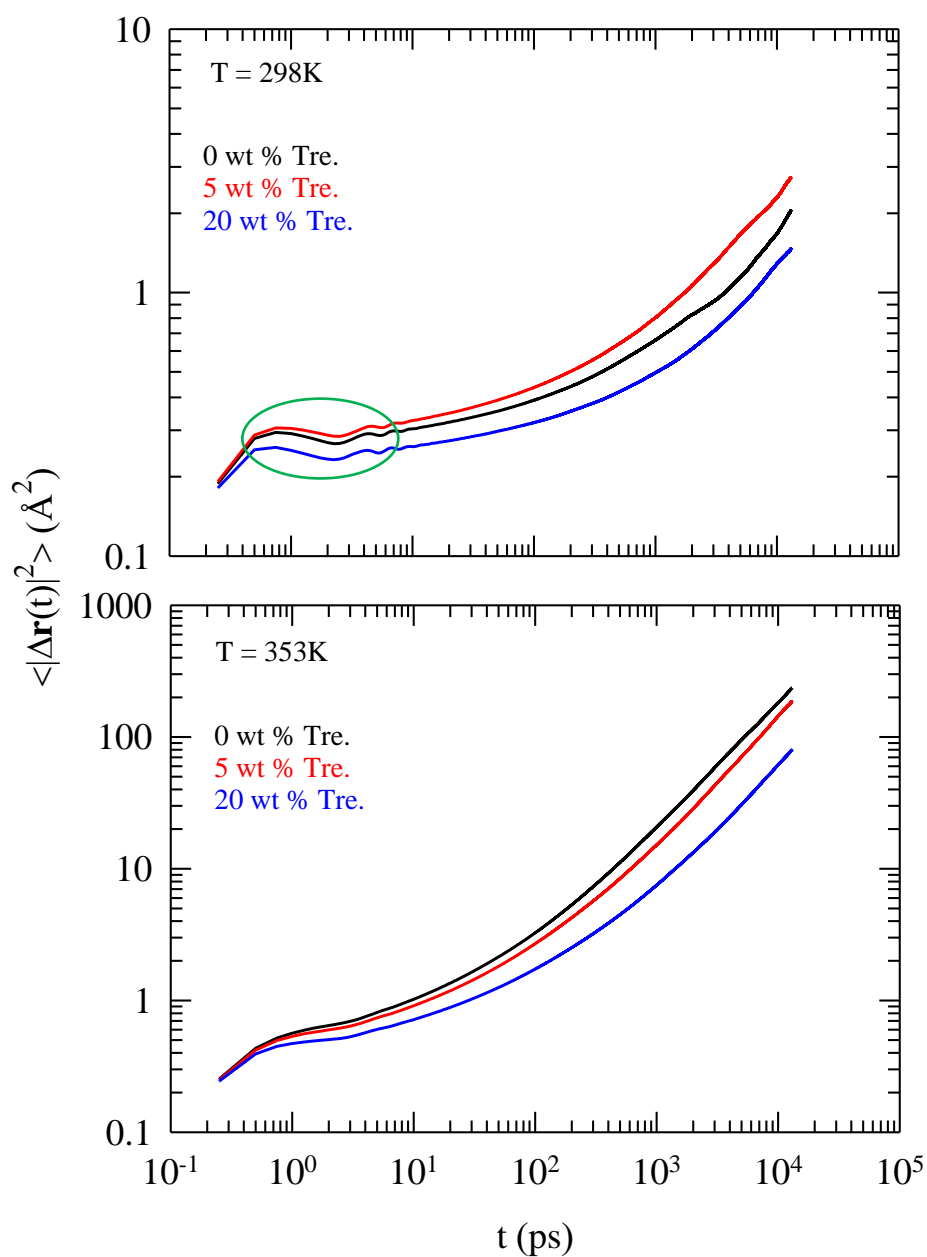
Figure 5.10: Mean squared displacement, $\left\langle |\Delta \mathbf{r}(t)|^2 \right\rangle$ of cm of glycerol as a function of time, t in pure glycerol, 5 wt % trehalose and 20 wt % trehalose into glycerol at ~298K (upper panel) and ~353K (lower panel).

5.4.6 Temporal (Dynamic) Heterogeneity

The λ_{ex}-dependent spectral emission of C153 in trehalose/glycerol mixture and fractional η-dependence of $\langle \tau_s \rangle$ of solvent molecules suggest spatio-temporal heterogeneity in the medium. To explore further information about the dynamic heterogeneity (DH) we have calculated non-Gaussian (NG) parameter $\alpha_2(t)$, which can be quantified by the deviation from Gaussian behaviour of time-dependent van Hove self-correlation function. Equation 5.7 was used to calculate $\alpha_2(t)$. We have shown the distribution of $\alpha_2(t)$ of glycerol in pure state and in presence of trehalose as a function of t in Figure 5.11. Systems possessing DH show a non-monotonous time-dependence of $\alpha_2(t)$ with peak value greater than 0.2.[78] Appearance of the peak value of $\alpha_2(t)$ at greater than 0.2 for all the three different $C_{Tre.}$ clearly indicates presence of DH which is more prominent at 298K. The timescales corresponding to the peak position of $\alpha_2(t)$, τ_{NG} are shown in Table 5.5. At 298K, peak value of $\alpha_2(t)$ shows maximum for pure glycerol with time $\tau_{NG} \approx 2400$ ps suggesting that pure glycerol is the most heterogeneous at room temperature. Intriguingly, addition of trehalose decreases the peak intensity of $\alpha_2(t)$, although, λ_{ex}-dependence on emission spectral frequency was most prominent at 20 wt % trehalose. This indicates that trehalose reduces DH of the medium. Note the system remains heterogeneous even at 353K with peak value of $\alpha_2(t)$ greater than 0.2. At this temperature, peak of $\alpha_2(t)$ shifts to the larger value with longer τ_{NG} with increase of trehalose content.

Existence of another slower DH timescales has also been revealed via calculating the new non-Gaussian (NNG) parameter (equation 5.8). The distribution of $\gamma(t)$ with t has been shown in Figure 5.A.4 (Appendix 5.A). We observed that peak time for $\gamma(t)$, τ_{NNG}, appears at much longer time than τ_{NG} (Table 5.5). We could not get the full distribution of $\gamma(t)$ in glycerol and 20 wt % trehalose at 298K within 13 ns time-window. As displacement of glycerol becomes accelerated in 5 wt % trehalose, so τ_{NNG} was found to appear at 6 ns. As observed for $\alpha_2(t)$, similar behaviour of $\gamma(t)$ was observed at 353K.
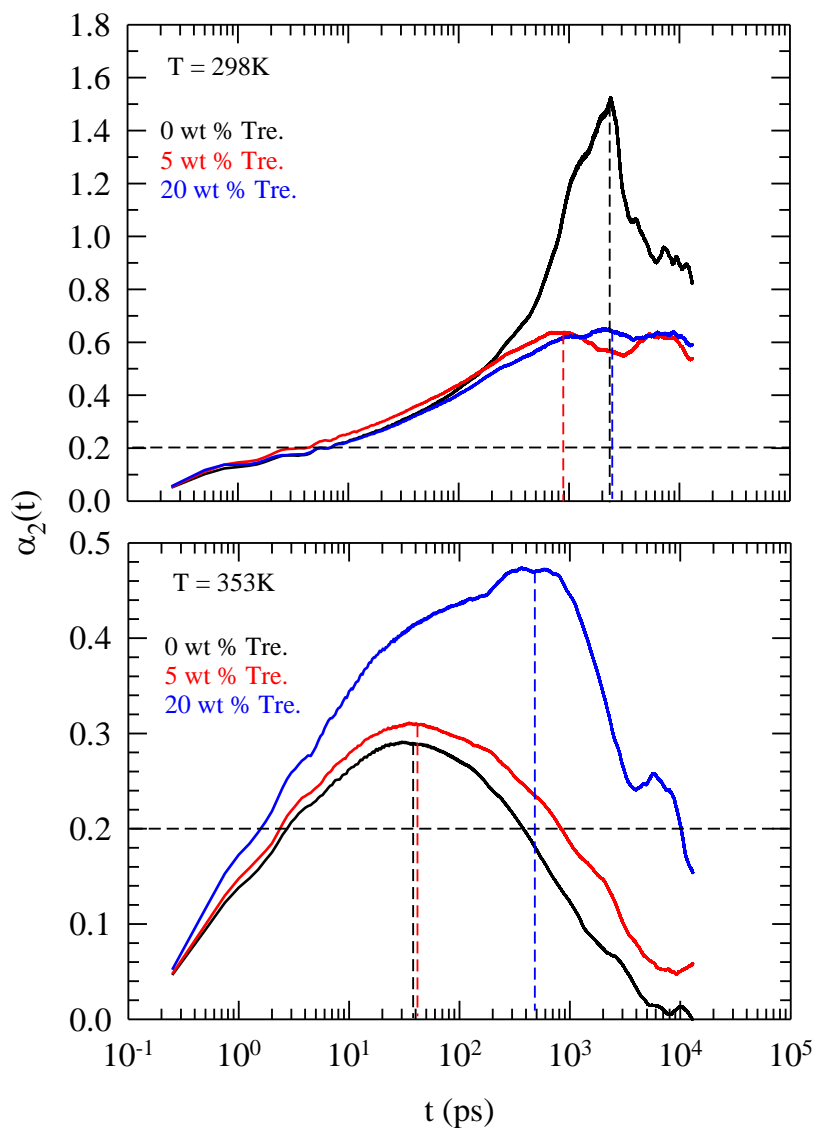
Figure 5.11: Distribution of non-Gaussian parameter, $\alpha_2(t)$ with time t in glycerol and trehalose–glycerol mixture at ~298K and ~353K. Vertical dashed lines are drawn to show the time corresponding to the peak maximum of $\alpha_2(t)$, τ_{NG}.

Table 5.5: $C_{Tre.}$ dependent τ_{NG}, τ_{NNG}, τ_{α} and τ_4 values at ~298K and ~353K. Definitions of these timescales are given in the text.

$C_{Tre.}(wt.\%)$	τ_{NG} /ps		τ_{NNG} /ps	τ_{α} /ps	τ_4 /ps	
	$T = 298\,\mathrm{K}$	$T = 353\,\mathrm{K}$	$T = 353\,\mathrm{K}$	$T = 353\,\mathrm{K}$	$T = 298\,\mathrm{K}$	$T = 353\,\mathrm{K}$
0	2400	35	70	178	9000	175
5	900	40	130	239	6000	250
20	2500	500	1600	596		1500

5.4.7 Self-dynamic Structure Factor and Four Point Dynamic Susceptibility

Self-dynamic structure factor, $F_s(\mathbf{k},t)$ of glycerol in both presence and absence of trehalose has been calculated using equation 5.10 in the limit of nearest neighbour wave number ($\mathbf{k}\sigma \rightarrow 2\pi$, σ being the diameter) and are shown in the upper panel of Figure 5.12. The α-relaxation time (τ_{α}) (shown by bullets in the figure), when a tagged molecule escapes from the cage, is defined as $F_s(\mathbf{k},\tau_{\alpha}) = e^{-1}$. The figure shows very slow relaxation of $F_s(\mathbf{k},t)$ in the glassy state at 298K. We could observe maximum 40 % of the total decay at 298K within 13 ns time. Here also we have seen that in presence of 5 wt % trehalose decay of $F_s(\mathbf{k},t)$ becomes faster. The full relaxation decay which was found at 353K, followed normal trend as expected from medium viscosity. The corresponding τ_{α} values (Table 5.5) shifted to larger values with increase of $C_{Tre.}$. Bi-exponential function was used to fit the simulated $F_s(\mathbf{k},t)$ in glycerol and 5 wt. % trehalose whereas stretched exponential function was required 20 wt % trehalose. The fitting parameters are provided in Table 5.B.4 (Appendix 5.B). From the comparison between two slower timescales τ_{NNG} and τ_{α} at 353K, structural relaxation, τ_{α} provided the slowest one in case of glycerol and 5 wt % trehalose, but in 20 wt % trehalose, glycerol molecules executing smaller displacements, τ_{NNG} is larger than τ_{α}.
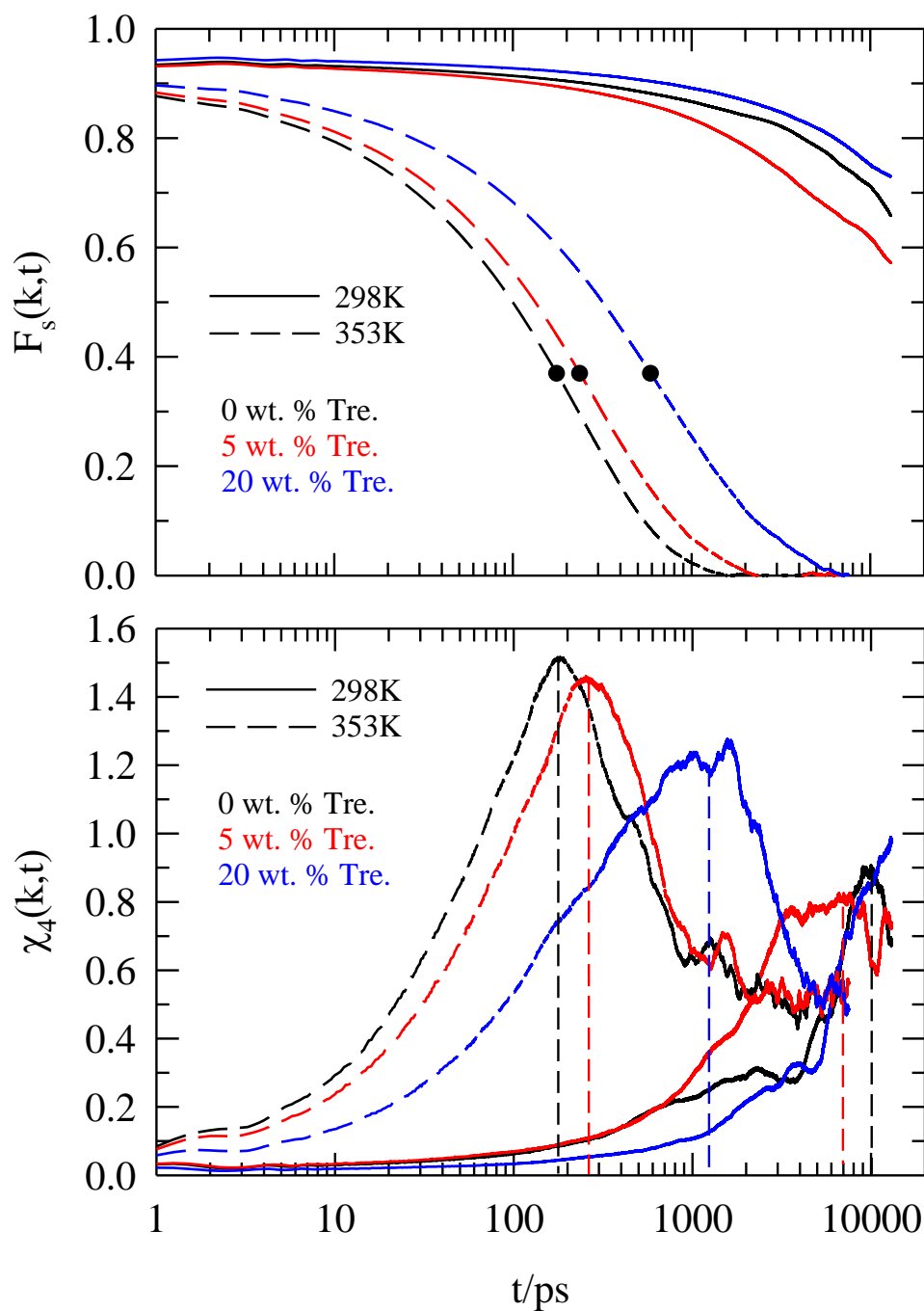
Figure 5.12: Time dependent behaviour of normalized decays of self-dynamic structure factor $F_s(\mathbf{k},t)$ (upper panel) and four point dynamic susceptibility $\chi_4(\mathbf{k},t)$ (lower panel) at the nearest neighbour wavenumber $\left(F_s(k\sigma \to 2\pi,t)\right)$ for different concentrations of trehalose into glycerol at two different temperatures, 298K and 353K.

Four point dynamic susceptibility, $\chi_4(\mathbf{k},t)$ which accounts how molecular motions are correlated between time 0 and t from the correlation of the fluctuations of two-point correlation function, $F_s(\mathbf{k},t)$ (equation 5.9). Simulated $\chi_4(\mathbf{k},t)$ presented in the lower panel of Figure 5.12 shows non-monotonous t-dependence with a peak time, τ_4 suggesting dynamic heterogeneity in all the three compositions of trehalose at two temperatures. This non-monotonous behaviour of $\chi_4(\mathbf{k},t)$ has already been characterized for different heterogeneous environments such as glass-forming liquids,[112,113] ionic liquids,[114,115] colloidal gels,[116] poly dispersed systems[117,118] etc. Generally, the peak time of $\chi_4(\mathbf{k},t)$, τ_4 appears on a timescale comparable to τ_α. The τ_4 values summarized in Table 5.5 show that upon increasing temperature τ_4 shifts to the lower time. At higher temperature ~353K, τ_4 values well agree with τ_α in pure glycerol and 5 wt % trehalose in glycerol. But in 20 wt % trehalose, τ_4 was found to be elongated to a value close enough of τ_{NNG}. At room temperature ~298K, longer timescales (in the order of few ns) were obtained for τ_4. In fact, the decorrelation of the fluctuations in $F_s(\mathbf{k},t)$ in 20 wt % trehalose at 298K was not started within 13 ns.

5.4.8 H-bond Fluctuation Dynamics

The change in glycerol–glycerol H-bond dynamical timescales in presence of trehalose has been monitored by calculations of two different time-correlation functions; H-bond lifetime relaxation $S_{HB}(t)$ and H-bond structural relaxation $C_{HB}(t)$.[83-85] The definition of these time correlation functions and calculation procedures are provided in section 5.3. Equation 5.11 and 5.12 were used to calculate $S_{HB}(t)$ and $C_{HB}(t)$ respectively. Here we have only considered the intermolecular H-bonds between glycerol molecules. The geometric conditions[99] adopted in present study for defining a proper H-bond between two glycerol molecules were as follows: the distance between two O atoms must be < 3.5 Å which is corresponding to the 1st minimum distance of O(G)–O(G) RDF, angle between O–O bond vector and O–H bond vector must be < 35^0 and the distance between O and H atoms of two

glycerol molecules under consideration must be < 2.55 Å which corresponds to the 1st minimum distance of O(G)–H(G) RDF.
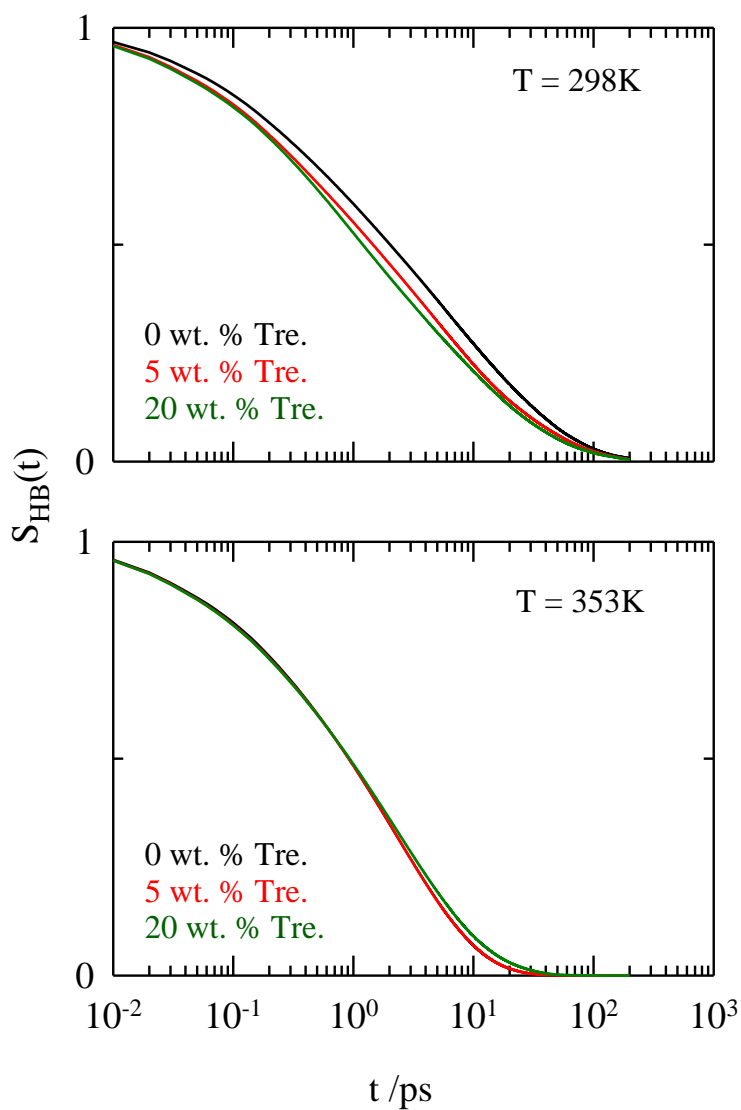
Figure 5.13: Glycerol–glycerol H-bond lifetime relaxation, $S_{HB}(t)$ with time t in 0 wt %, 5 wt % and 20 wt % trehalose into glycerol at ~298K (upper panel) and ~353K (lower panel). The trehalose concentrations are colour-coded in each panel.

The correlation functions $S_{HB}(t)$ and $C_{HB}(t)$ are shown in Figures 5.13 and 5.A.5 of Appendix 5.A at two different temperatures. The stretched and tri-exponential functions were required to fit the $S_{HB}(t)$ and $C_{HB}(t)$ decays respectively. The corresponding fitting parameters are provided in Tables 5.B.5 and 5.B.6 (Appendix 5.B). Data shown here suggest that the correlation function decays at faster rate by addition of 5 wt % trehalose into glycerol at 298K. It has been already proven that the dynamics of $S_{HB}(t)$ is controlled by the structure of the local environment, not by the viscosity of the medium.[119] So here the effect of viscosity is insignificant. Since trehalose acts as a structure breaker, it plays the same role by breaking the H-bonds between glycerol molecules. As a result, the H-bond dynamics becomes faster at lower temperature. This probably explains why using TCSPC we missed the maximum solvation dynamics in presence of trehalose into glycerol at 298K. In our previous study,[120,121] we found that addition of small solutes like tetramethylurea, trimethylamine-N-oxide into water lengthened the H-bond dynamical timescales. Interestingly, here in presence of large solute the opposite effect has been observed. The origin of the stretched exponential timescales can be correlated to the DH of the system as observed from the non-Gaussian movement of the molecules. At 353K, we observed the dynamical slowing down with increase of trehalose concentration. This indicates that the dynamics of these complex media is being controlled by two different motions of the involved specie at two different temperature ends. Both experiment and simulation support the fact that at lower temperature dynamics is mainly governed by the inertial motion of the molecules whereas at higher temperature the dynamics of the system becomes diffusion controlled.

5.5 Conclusion

Several interesting properties of this bioprotectant mixture have been revealed from this combined study of fluorescence spectroscopic measurements and computer simulations. Here, we have done a comparative study of the properties of this system at 298K, and at 353K. Fluorescence emission of C153 was found to depend on the excitation wavelength only in 20 wt % trehalose into glycerol at 298K. This indicates the presence of longer-lived heterogeneous domains compared to excited-state lifetime of C153 in this composition of trehalose/glycerol at room temperature. Solvation dynamics study at room temperature

suggested that libration of H-bonded –OH group mainly governs the solvation response in at lower temperature. Dynamic Stokes shift measurements revealed that temperature and trehalose play the role of solution structure breaker. By disrupting the H-bond network of glycerol, trehalose helps to reduce the contribution of the fast solvation response of this system. Surprisingly, rotation of C153 was found to follow the hydrodynamic relation in this complex medium, although average solvation time exhibits fractional viscosity dependence. Simulated radial distribution functions between different atomic pairs indicated 'glassy' nature of the glycerol and trehalose/glycerol binary mixtures at room temperature. Mean squared displacements of glycerol at 298K showed the characteristic behaviour of supercooled liquids. From simulation study we observed that trehalose acts as the most efficient structure breaker at small concentration, ~5 wt % at room temperature. This signature was found in H-bond fluctuation dynamics of glycerol and all the parameters depicting dynamical heterogeneity. Dynamic heterogeneity timescales also showed complex behaviour at the two temperature regimes in this system. Further experimental and simulation studies are required to fully explore the structural and dynamical aspects of these biologically important systems.

Appendix 5.A
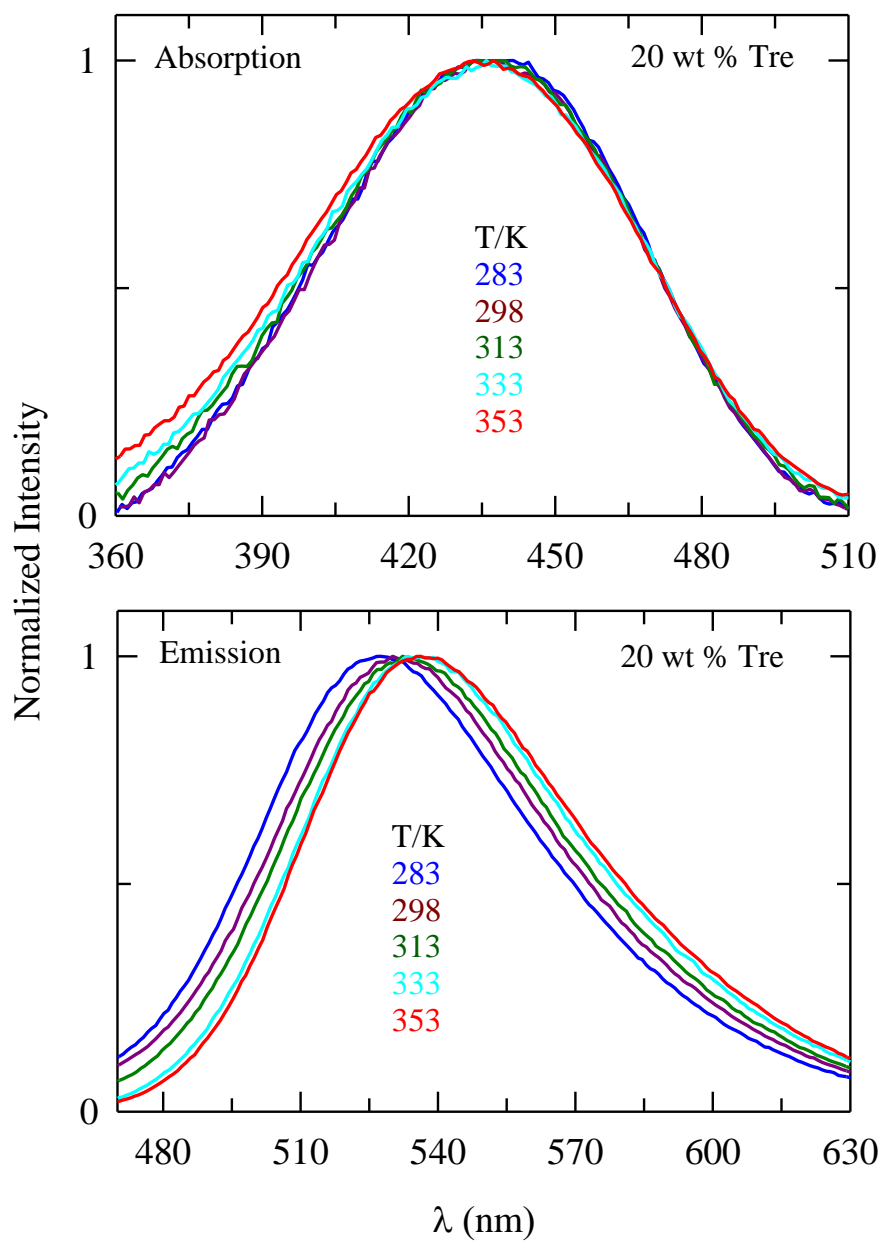
Figure 5.A.1: Temperature dependent absorption (upper panel) and emission (lower panel) spectra of C153 in 20 wt % trehalose into glycerol. Different temperatures are colour-coded and indicated in each panel.
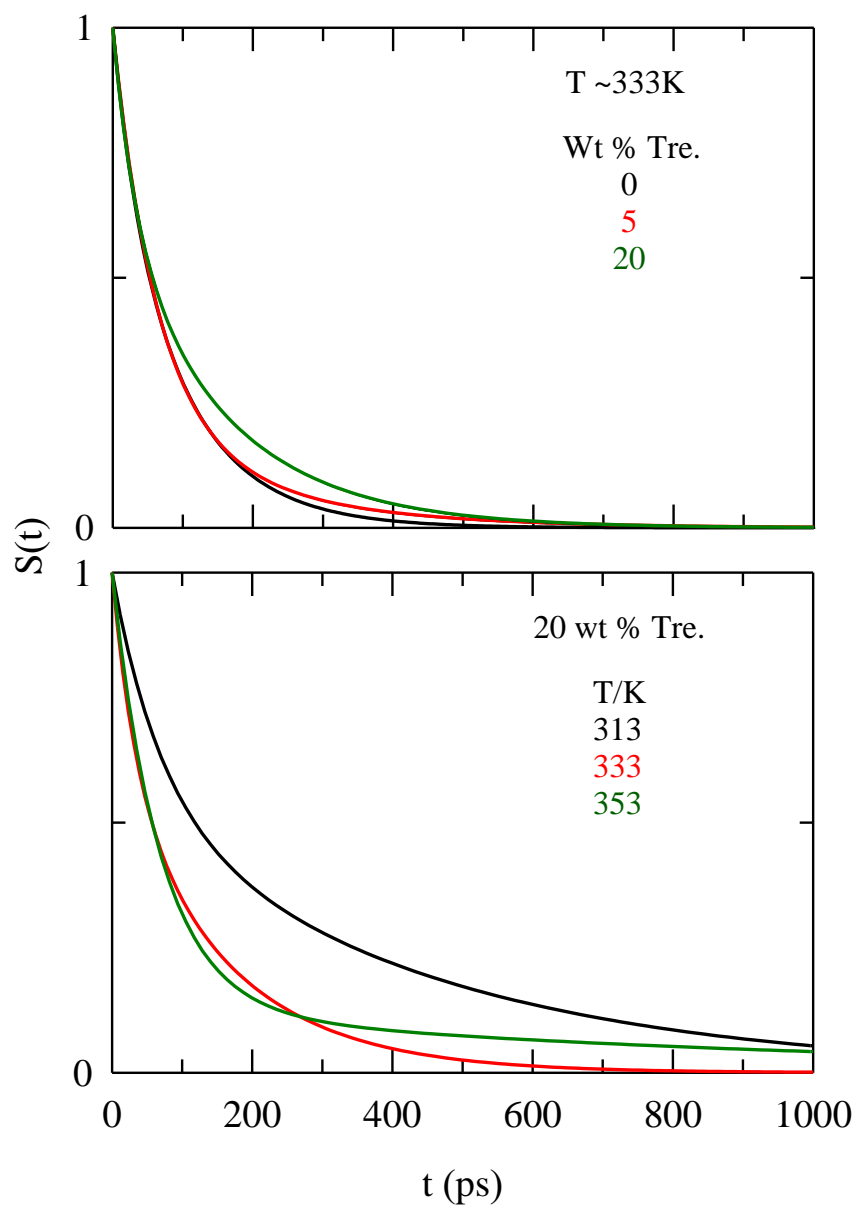
Figure 5.A.2: Representative decays of solvation response function, $S(t)$ with time, t at three different trehalose–glycerol compositions (upper panel) and at three different temperatures (lower panel). The representations are colour-coded.
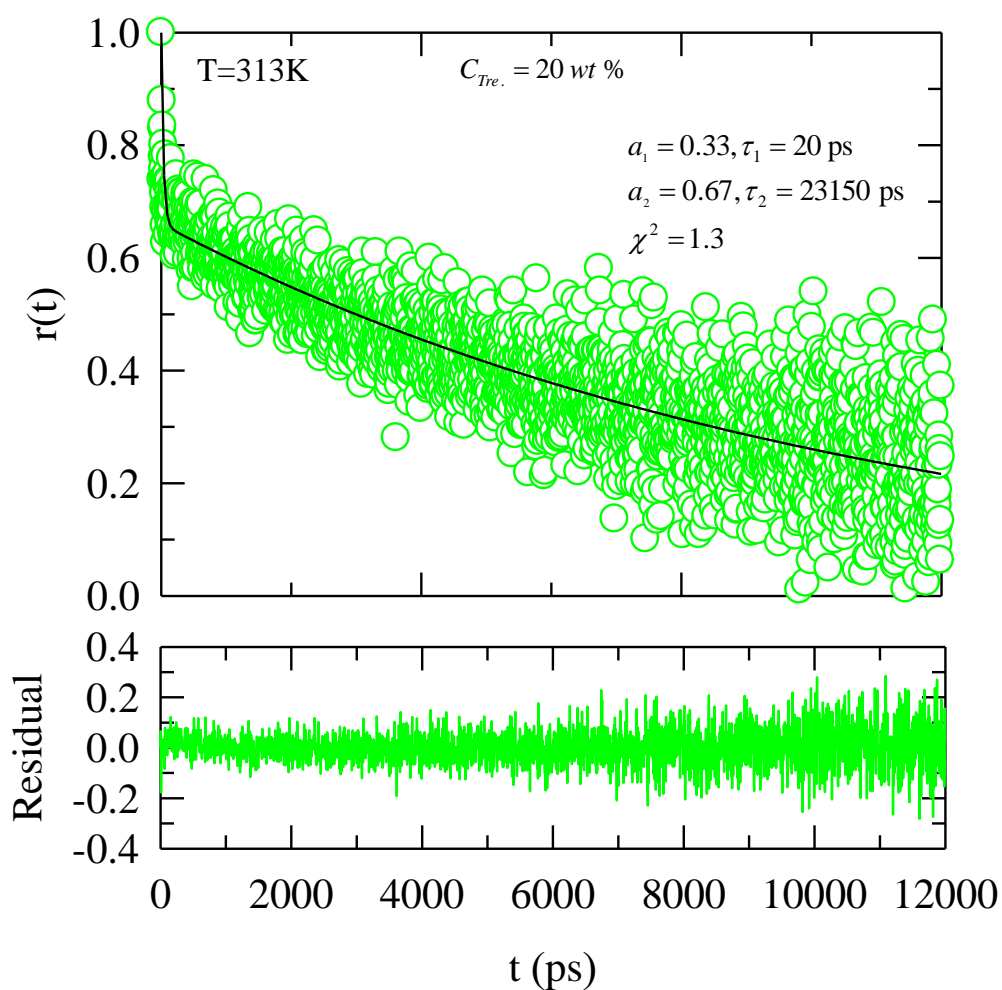
Figure 5.A.3: Representative fluorescence anisotropy decay, $r(t)$ of C153 in 20 wt % trehalose at ~313K (upper panel). While open circles represent the data, the solid line shows the fit through the data. Parameters obtained from the bi-exponential fit to the data are also listed in the upper panel. The *goodness of fit parameter* (reduced χ^2) is also shown. Residual is represented in the bottom panel.
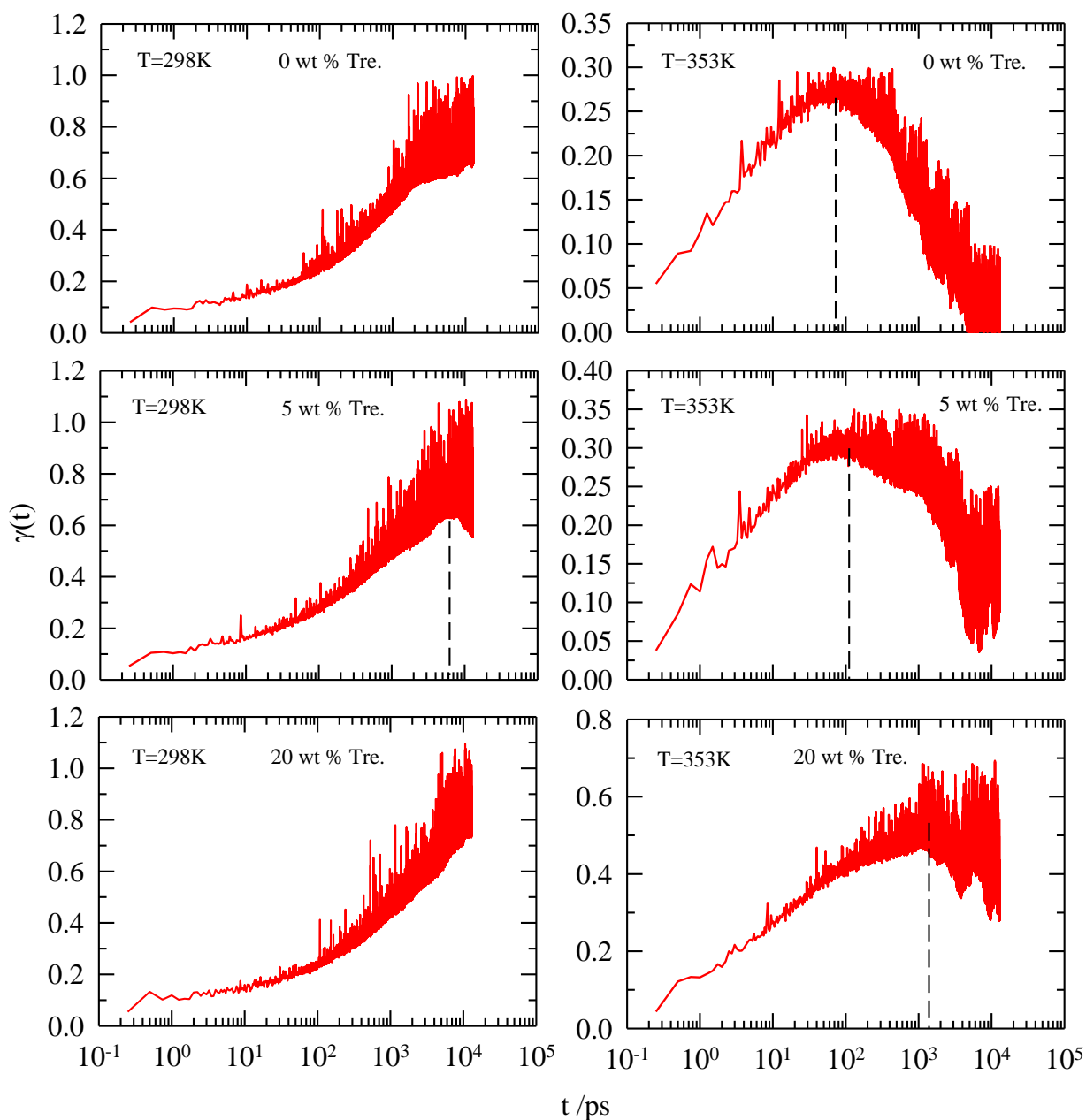
Figure 5.A.4: Simulated new non-Gaussian $\gamma(t)$ parameters for glycerol in three different trehalose–glycerol compositions at ~298K (left panels) and ~353K (right panels). Vertical dashed lines represent peak times τ_{NNG} of $\gamma(t)$.
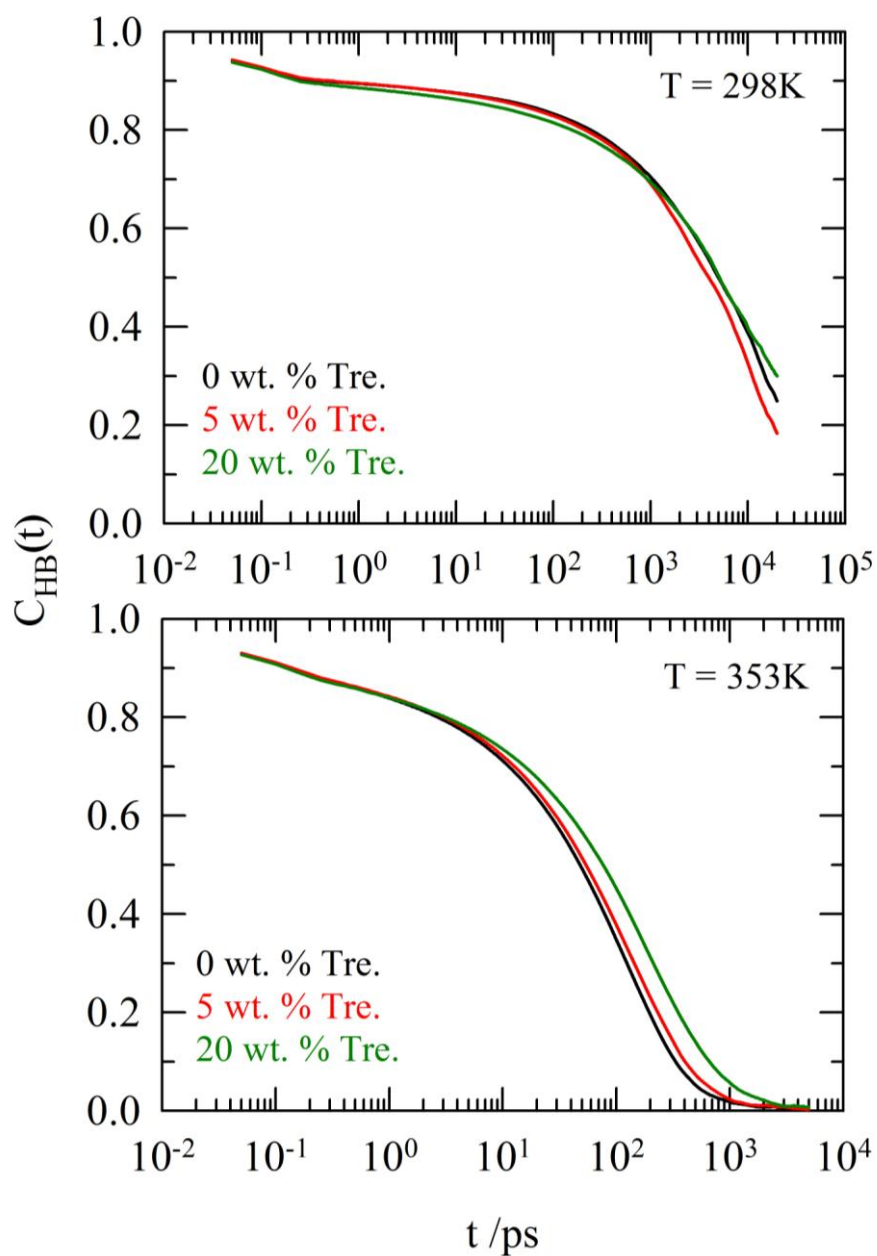
Figure 5.A.5: Glycerol–glycerol H-bond structural relaxation, $C_{HB}(t)$ with time, t in 0 wt %, 5 wt % and 20 wt % trehalose concentrations in glycerol at ~298K (upper panel) and ~353K (lower panel). The trehalose concentrations are colour-coded.

Appendix 5.B

Table 5.B.1: Average rotational time, $\langle \tau_r \rangle$ of C153 obtained from experiment and prediction from stick and slip boundary conditions of SED relation at different $C_{Tre.}$ and temperatures.

$C_{Tre.}(wt.\%)$	$T(K)$	Observed $\langle \tau_r \rangle$/ns	Predicted $\langle \tau_r \rangle$ (SED relation)	
			Slip/ns	Stick/ns
0	298	82.18	21.26	88.68
	313	5.55	6.36	26.51
	333	2.12	1.81	7.57
	353	0.76	0.69	2.87
5	298	96.95	23.17	96.62
	313	4.60	7.01	29.26
	333	2.29	1.97	8.21
	353	0.80	0.75	3.13
20	298	229.5	55.83	232.85
	313	15.45	14.85	61.95
	333	3.82	3.70	15.41
	353	0.98	1.28	5.34

Table 5.B.2: Comparison of simulated density, ρ_{sim} with the experimental value,[a] ρ_{exp} at 298K.

$C_{Tre.}(wt.\%)$	ρ_{sim} (g/cc)	ρ_{exp} (g/cc)
0	1.223	1.257

a. This work.

Table 5.B.3: Self-diffusion coefficient (D) of centre-of-mass (cm) and O-atoms of glycerol at two different temperatures. The time-window considered for calculation of D has been provided in the parenthesis.

T(K)	$D_{cm} \times 10^9$ (m²/s)		$D_O \times 10^9$ (m²/s)	
298	0.0002 (100ps-13ns)	0.0006 (100-500ps)	0.0006 (100ps-13ns)	0.0024 (100-500ps)
353	0.0301 (50ps-13ns)	0.0334 (50-500ps)	0.0312 (50ps-13ns)	0.0547 (50-500ps)

Table 5.B.4: Fit parameters for self-dynamic structure factor, $F_s(\mathbf{k},t)$ for glycerol in different $C_{Tre.}$ at ~353K.

$C_{Tre.}(wt.\%)$	a_1	τ_1/ps	a_2	τ_2/ps	β	$\langle\tau\rangle$/ps
0	0.27	10.64	0.73	269.18		199.37
5	0.34	28.55	0.66	422.46		288.53
20	1.00	577.73			0.60	869.24

Table 5.B.5: Stretched exponential fit parameters for glycerol–glycerol H-bond lifetime relaxation, $S_{HB}(t)$ in different concentrations of trehalose into glycerol at 298K and 353K.

$C_{Tre.}(wt.\%)$	T/K	a	τ /ps	β	$\langle\tau\rangle$ /ps	$\langle h\rangle$
0	298	1.00	5.282	0.42	15.430	0.90
	353	1.00	1.806	0.57	2.915	0.80
5	298	1.00	3.721	0.40	12.366	0.87
	353	1.00	1.800	0.57	2.905	0.77
20	298	1.00	3.167	0.39	11.304	0.87
	353	1.00	1.918	0.53	3.464	0.76

Table 5.B.6: Tri-exponential fit parameters for glycerol–glycerol H-bond structural relaxation, $C_{HB}(t)$ in different concentrations of trehalose into glycerol at 298K and 353K.

$C_{Tre.}(wt.\%)$	T/K	a_1	τ_1 /ps	a_2	τ_2 /ps	a_3	τ_3 /ps	$\langle\tau\rangle$ /ps	$\langle h\rangle$
0	298	0.16	6.89	0.21	1661.59	0.63	21152.6	13676.0	0.78
	353	0.30	4.35	0.65	137.67	0.05	1108.8	146.23	0.67
5	298	0.16	3.34	0.21	1307.99	0.63	15292	9909.17	0.77
	353	0.32	6.25	0.62	164.86	0.06	1199.9	176.21	0.65
20	298	0.20	19.64	0.28	3081.08	0.52	36638.2	19918.5	0.77
	353	0.31	5.51	0.56	203.93	0.13	1153.1	265.81	0.59

References

1.   F. d. L. Janz, A. d. A. Debes, R. d. C. Cavaglieri, S. A. Duarte, C. M. Romão, A. F. Morón, M. Zugaib and S. P. Bydlowski, J. Biomed. Biotech. (2012).

2.   C. J. Hunt, Transfus Med Hemother **38**, 107 (2011).

3.   A. Anopchenko, T. Psurek, D. VanderHart, J. F. Douglas and J. Obrzut, Phys. Rev. E **74**, 031501 (2006).

4.   F. Sussich, R. Urbani, F. Princivalle and A. Cesaro, J. Am. Chem. Soc. **120**, 7893 (1998).

5.   D. P. Miller and J. J. de Pablo, J. Phys. Chem. B **104**, 8876 (2000).

6.   J. L. Green and C. A. Angell, J. Phys. Chem. B **93**, 2880 (1989).

7.   R. Bohmer, K. Ngai, C. A. Angell and D. J. Plazek, J. Chem. Phys. **99**, 4201 (1999).

8.   L. Martinez and C. A. Angell, Nature **410**, 663 (2001).

9.   G. Caliskan, A. Kisliuk, A. M. Tsai, C. L. Soles and A. P. Sokolov, J. Non-Cryst. Solids **307–310**, 887 (2002).

10.   M. T. Cicerone, A. Tellington, L. Trost and A. Sokolov, BioProc. Int. **1**, 36 (2003).

11.   M. T. Cicerone and C. L. Soles, Biophys. J. **86**, 3836 (2004).

12.   R. Busselez, R. Lefort, M. Guendouz, B. Frick, O. Merdrignac-Conanec and D. Morineau, J. Chem. Phys. **130**, 214502 (2009).

13.   R. Busselez, Ph.D thesis, University of Rennes 1, 2008.

14.   J. M. Gordon, G. B. Rouse, J. H. Gibbs and W. M. Risen, Jr., J. Chem. Phys. **66**, 4971 (1977).

15.   J. J. Towey, A. K. Soperb and L. Dougan, Phys. Chem. Chem. Phys. **13**, 9397 (2011).

16.   H. A. Rizk and M. Elanwar, Can. J. Chem. **46**, 507 (1968).

17.   R. J. Sengwa, Madhvi, Abhilasha and S. Sankhla, Ind. J. Pure & Appl. Phys. **44**, 943 (2006).

18.   J. Wong and C. A. Angell, in *Glass: Structure by Spectroscopy* (M. Dekker, New York, 1974), pp. 750.

19.   W. D. Davidson and R. H. Cole, J. Chem. Phys. **18**, 1417 (1950).

20.   U. Schneider, P. Lunkenheimer, R. Brand and A. Loidl, J. Non-Crystalline Solids **235-237**, 173 (1998).

21.   Y. Sun and E. Pickwell-MacPherson, in *Conference Article*.

22.   M. Paluch, S. J. Rzoska, P. Habdas and J. Ziolo, J. Phys. Condens. Matter **8**, 10885 (1996).

23.   R. Behrends, K. Fuchs, U. Kaatze, Y. Hayashi and Y. Feldman, J. Chem. Phys. **124**, 144512 (2006).

24.   P. Lunkenheimer, A. Pimenov, M. Dressel, Y. G. Goncharov, R. Böhmer and A. Loidl, Phys. Rev. Lett. **77**, 318 (1996).

25.   C. Branca, S. Magazù, G. Maisano and P. Migliardo, J. Chem. Phys. **111**, 881 (1999).

26.   C. Branca, S. Magazù, G. Maisano, P. Migliardo, V. Villari and A. P. Sokolov, J. Phys. Condens. Matter **11**, 3823 (1999).

27.   S. Magazù, G. Maisano, F. Migliardo and C. Mondelli, J. Phys. Chem. B **108**, 13580 (2004).

28.   S. Magazù, F. Migliardo and A. J. Ramirez-Cuesta, J. R. Soc. Interface **4**, 167 (2007).

29.   M. Paolantoni, L. Comez, M. E. Gallina, P. Sassi, F. Scarponi, D. Fioretto and A. Morresi, J. Phys. Chem. B **113**, 7874 (2009).

30.   M. Sajadi, Y. Ajaj, I. Ioffe, H. Weingärtner and N. P. Ernsting, Angew. Chem. Int. Ed. **49**, 454 (2010).

31.   P. Bordat, A. Lerbret, J.-P. Demaret, F. Affouard and M. Descamps, Europhys. Lett. **65(1)**, 41 (2004).

32.   L. Sapir and D. Harries, J. Phys. Chem. B **115**, 624 (2011).

33.   S. L. Lee, P. G. Debenedetti and J. R. Errington, J. Chem. Phys. **122**, 204511 (2005).

34.   A. Lerbret, P. Bordat, F. Affouard, M. Descamps and F. Migliardo, J. Phys. Chem. B **109**, 11046 (2005).

35.   G. Bonanno, R. Noto and S. L. Fornili, J. Chem. Soc., Faraday Trans. **94**, 2755 (1998).

36.   M. Paolantoni, P. Sassi, A. Morresi and S. Santini, J. Chem. Phys. **127**, 024504 (2007).

37.   J. L. Dashnau, N. V. Nucci, K. A. Sharp and J. M. Vanderkooi, J. Phys. Chem. B **110**, 13670 (2006).

38.   S. Magazù, F. Migliardo and S. F. Parker, J. Phys. Chem. B **115**, 11004 (2011).

39.   D. Averett, M. T. Cicerone, J. F. Douglas and J. J. de Pablo, Soft Matter **8**, 4936 (2012).

40.   T. E. Dirama, G. A. Carri and A. P. Sokolov, J. Chem. Phys. **122**, 114505 (2005).

41.   R. A. Riggleman and J. J. de Pablo, J. Chem. Phys. **128**, 224504 (2008).

42.   S. Magazù, F. Migliardo, F. Affouard, M. Descamps and M. T. F. Telling, J. Chem. Phys. **132**, 184512 (2010).

43.   S. Magazù, F. Migliardo and M. T. F. Telling, J. Non-Crystalline Solids **357**, 691 (2011).

44.   G. Caliskan, A. Kisliuk, A. M. Tsai, C. L. Soles and A. P. Sokolov, J. Chem. Phys. **118**, 4230 (2003).

45.   J. E. Curtis, T. E. Dirama, G. A. Carri and D. J. Tobias, j. Phys. Chem. B Lett. **110**, 22953 (2006).

46.   T. E. Honadel and G. J. Killian, Cryobiology **25**, 331 (1988).

47.   A. Einstein, in *Investigations on the Theory of the Brownian Motion*, edited by R. Fürth (Dover, New York, 1956).

48.   P. Debye, *Polar Molecules* (Dover, New York, 1929).

49.   B. Guchhait, H. A. R. Gazi, H. K. Kashyap and R. Biswas, J. Phys. Chem. B **114**, 5066 (2010).

50.   H. A. R. Gazi, B. Guchhait, S. Daschakraborty and R. Biswas, Chem. Phys. Lett. **501**, 358 (2011).

51.   M. G. Mazza, N. Giovambattista, H. E. Stanley and F. W. Starr, Physical Review E **76**, 031203 (2007).

52.   A. Das, R. Biswas and J. Chakrabarti, J. Phys. Chem. A **115**, 973 (2011).

53.   S. Daschakraborty and R. Biswas, J. Phys. Chem. B **115**, 4011 (2011).

54.   C. A. Angell, Chem. Rev. **102**, 2627 (2002).

55.   M. L. Horng, J. A. Gardecki, A. Papazyan and M. Maroncelli, J. Phys. Chem. B **99**, 17311 (1995).

56.   R. Biswas, J. E. Lewis and M. Maroncelli, Chem. Phys. Lett. **310**, 485 (1999).

57.   J. E. Lewis, R. Biswas, A. G. Robinson and M. Maroncelli, J. Phys. Chem. B **105**, 3306 (2001).

58.   T. Pradhan and R. Biswas, J. Phys. Chem. A **111**, 11514 (2007).

59.   T. Pradhan and R. Biswas, J. Phys. Chem. A **111**, 11524 (2007).

60.   C. F. Chapman and M. Maroncelli, J. Phys. Chem. **95**, 9095 (1991).

61.   K. Dahl, R. Biswas, N. Ito and M. Maroncelli, J. Phys. Chem. B **109**, 1563 (2005).

62.   T. Pradhan, P. Ghoshal and R. Biswas, J. Phys. Chem. A **112**, 915 (2008).

63. M. Maroncelli and G. R. Fleming, J. Chem. Phys. **86**, 1090 (1987).

64. M. Maroncelli, J. Mol. Liq. **57**, 1 (1993).

65. R. S. Fee and M. Maroncelli, Chem. Phys. **183**, 235 (1994).

66. M. L. Horng, J. A. Gardecki and M. Maroncelli, J. Phys. Chem. A **101**, 1030 (1997).

67. J. R. Lakowicz, *Principles of Fluorescence Spectroscopy*. (Kluwer Academic, New York, 1999).

68. J. E. Lewis and M. Maroncelli, Chem. Phys. Lett. **282**, 197 (1998).

69. K. N. Kirschner, A. B. Yongye, S. M. Tschample, J. Gonzaález- Outeiriňo, C. R. Daniels, B. L. Foley and R. J. Woods, J. Comput. Chem. **29**, 622 (2008).

70. W. L. Jorgensen, D. S. Maxwell and J. Tirado-Rives, J. Am. Chem. Soc. **118**, 11225 (1996).

71. T. Kulschewski and J. Pleiss, Mol. Sim. **39**, 754 (2013).

72. M. P. Allen and D. J. Tildesley, *Computer simulations of liquids*. (Oxford University Press, New York, 1987).

73. W. Smith, T. R. Forester and I. T. Todorov, *DL_POLY Classic*. (STFC Daresbury Laboratory, Daresbury, 2012).

74. S. Nose, J. Chem. Phys. **81**, 511 (1984).

75. W. G. Hoover, Phys. Rev. A **31**, 1695 (1985).

76. J. P. Ryckaert, G. Ciccotti and H. J. C. Berendsen, J. Comput. Phys. **23**, 327 (1977).

77. J. P. Hansen and I. R. McDonald, *Theory of simple liquids*. (Academic Press, New York, 1986).

78. A. Rahman, Phys. Rev. **136**, 405 (1964).

79. E. Flenner and G. Szamel, Phys. Rev. E **72**, 011205 (2005).

80. C. Toninelli, M. Wyart, L. Berthier, G. Biroli and J. Bouchaud, Phys. rev. E **71**, 041505 (2005).

81. C. Dasgupta, A. V. Indrani, S. Ramaswamy and M. K. Phani, Europhys. Lett. **15**, 307 (1991).

82. C. Donati, S. Franz, S. C. Glotzer and G. Parisi, cond-mat/9905433.

83. A. Luzar and D. Chandler, Nature **379**, 55 (1996).

84. A. Luzar and D. Chandler, Phys. Rev. Lett. **76**, 928 (1996).

85. A. Chandra, Phys. Rev. Lett. **85**, 768 (2000).

86. C. R. Moyland, J. Phys. Chem. **98**, 13513 (1994).

87.   W. Baumann and Z. Nagy, Pure Appl. **65**, 1729 (1993).

88.   N. Mataga, T. Okada and H. Masuhara, in *Dynamics and Mechanisms of Plzotoinduced Electron Tran.fer and Related Phenomena* (Elsevier, Amsterdam, 1992), pp. 211.

89.   J. Tomczak and K. Dobek, J. Luminescence **129**, 884 (2009).

90.   R. J. Cave and E. W. Castner, Jr. , J. Phys. Chem. A **106**, 12117 (2002).

91.   B. Guchhait, S. Daschakraborty and R. Biswas, J. Chem. Phys. **136**, 174503 (2012).

92.   J. B. Brubach, A. Mermet, A. Filabozzi, G. A. and P. Roy, J. Chem. Phys. **122**, 184509 (2005).

93.   R. Jimenez, G. R. Fleming, P. V. Kumar and M. Maroncelli, Nature **369**, 471 (1994).

94.   T. Pradhan, P. Ghoshal and R. Biswas, J. Chem. Sci. **120**, 275 (2008).

95.   H. A. R. Gazi and R. Biswas, J. Phys. Chem. A **115**, 2447 (2011).

96.   S. Indra and R. Biswas, J. Chem. Phys. **142**, 204501 (2015).

97.   R. Chelli, P. Procacci, G. Cardini and S. Califano, Phys. Chem. Chem. Phys. **1**, 879 (1999).

98.   J. A. Padro, L. Saiz and E. Guardia, J. Mol. Str. **416**, 243 (1997).

99.   L. J. Root and B. J. Berne, J. Chem. Phys. **107**, 4350 (1997).

100.   A. Patist and H. Zoerb, Colloids and Surfaces B: Biointerfaces **40**, 107 (2005).

101.   M. Sakurai, in *Water and Biomolecules* (2009), pp. 219.

102.   A. M. Funston, T. A. Fadeeva, J. F. Wishart and E. W. Castner, Jr. , J. Phys. Chem. B **111**, 4963 (2007).

103.   J. A. Ingram, R. S. Moog, N. Ito, R. Biswas and M. Maroncelli, J. Phys. Chem. B **107**, 5926 (2003).

104.   S. Arzhantsev, N. Ito, M. Heitz and M. Maroncelli, Chem. Phys. Lett. **381**, 278 (2003).

105.   S. Arzhantsev, H. Jin, G. A. Baker and M. Maroncelli, J. Phys. Chem. B **111**, 4978 (2007).

106.   M. D. Ediger, Ann. Rev. Phys. Chem. **51**, 99 (2000).

107.   H. Sillescu, J. Non-Cryst. Solids **243**, 81 (1999).

108.   G. D'Errico, O. Ortona, F. Capuano and V. Vitagliano, J. Chem. Eng. Data **49**, 1665 (2004).

109.   F. Faupel, W. Frank, M. Macht, H. Mehrer, V. Naundorf, K. Ratzke and H. R. Schober et al, Rev. Mod. Phys. **75**, 237 (2003).

110.   J. Habasaki and K. L. Ngai, J. Non-Cryst. Solids **352**, 5170 (2006).

111.   T. Pal and R. Biswas, Theor. Chem. Acc. **132**, 1348 (2013).

112.   K. Kim and S. Saito, J. Chem. Phys. **133**, 044511 (2010).

113.   N. Lačević, F. W. Starr, T. B. Schrøder, V. N. Novikov and S. C. Glotzer, Phys. Rev. E **66**, 030101 (2002).

114.   T. Pal and R. Biswas, J. Chem. Phys. **141**, 104501 (2014).

115.   T. Pal and R. Biswas, J. Phys. Chem. B (2015) DOI: 10.1021/acs.jpcb.5b08763.

116.   T. Abete, A. de Candia, E. Del Gado, A. Fierro and A. Coniglio, Phys. Rev. Lett. **98**, 088301 (2007).

117.   S. E. Abraham and B. Bagchi, Phys. Rev. E **78**, 051501 (2008).

118.   T. Kawasaki and H. Tanaka, J. Phys.: Condens. Matter **23**, 194121 (2011).

119.   D. Laage and J. T. Hynes, Chem. Phys. Lett. **433**, 80 (2006).

120.   S. Indra and R. Biswas, Mol. Sim. **41**, 471 (2015).

121.   S. Indra and R. Biswas, Chem. Phys. Lett. (2015) (submitted).

Chapter 6

Hydrogen-bond Dynamics of Water in Presence of An Amphiphile, Tetramethylurea: Signature of Confinement-induced Effects

6.1 Introduction

Study of confined water is an important area of research because water shows significant changes[1-15] in both structural and dynamical properties upon encapsulation. Fluorescence spectroscopic measurements and simulation studies seem to suggest drastic decrease of static dielectric constant (ε_0) of bulk water upon confinement.[16-19] Confined water is found in biology such as in lipid bilayers, ion channels and protein cavities[20-23]; 'biological water' at protein surfaces[24]; in chemistry such as in fuel cells,[25] gels and reverse micelles[13,26-30]; in technology such as in carbon nanotubes,[31-33] granular and porous materials,[34] etc. Computer simulations on the effects of confinement on structure and dynamics of binary liquid mixtures composed of asymmetric particles[35] have attempted to provide answers to some basic questions of this area.

Behaviour of water molecules in the vicinity of hydrophobic solute molecules is an issue of intense research. It has been found from both experimental and theoretical studies that reorientation dynamics of water molecules in the hydration shell of hydrophobes exhibits substantial retardation.[36-43] Dynamic anisotropy measurements of water around a hydrophobic molecule[32] reveal that water molecules become immobilized in the hydration shell of hydrophobic solute, supporting the controversial iceberg model.[44] Interestingly, a combined computer simulation and theoretical study[38] has suggested no immobilization of water molecules in the hydrophobic hydration layer and thus debated the validity of the iceberg model. Solute-excluded volume effects at the transition state are found to be responsible for the slowing down

of water reorientation. Concentrated aqueous solutions are found to behave like confining environments due to the steric effects rendered by the solute molecules.[45,46] Hydrophobic molecules tend to aggregate in solution. At higher solute concentrations, these aggregates distribute throughout the solution. Consequently, water molecules are forced to reside by the side of the surfaces created by these aggregated moieties. This results in significant retardation of reorientational and translational dynamics of interfacial water molecules residing at the surface of the solute aggregates.[47] By this way, water shows similar behaviour in concentrated aqueous solutions as found in explicit confinements.

The extensive hydrogen-bond (H-bond) network of water plays a key role in determining the structure and dynamics of aqueous systems. Therefore, experiments,[48-52] theory and simulations[53-60] have been employed to gain insight into the mechanism of both H-bond kinetics and dynamics in water and aqueous solutions. Computer simulation study[53] first showed the non-exponential behaviour of the dynamics of forming and breaking H-bonds in liquid water due to the coupling between H-bond population and diffusion. Later, the jump reorientation mechanism[56] showed that water reorientation mechanism involves large amplitude angular jumps, rather than the commonly accepted sequence of small diffusive steps. Determination of H-bond lifetime is also a very important tool to examine the strength of H-bonds. This is largely affected by the structure of the local environment. It is important to mention here that very few attempts[61,62] have been made to calculate H-bond fluctuation dynamics for binary aqueous mixtures. Tetramethylurea (TMU) (shown in Scheme 6.1) is an amphiphilic molecule possessing both hydrophobic methyl groups and hydrophilic carbonyl group. TMU is easily soluble in water via H-bond interactions. TMU is an important biologically relevant molecule because it is a stronger denaturing agent than urea itself.[63,64]

In this chapter, we show, through molecular dynamics simulations of TMU in water at various composition mixtures, that the confining effects of TMU are transduced on H-bond fluctuation dynamics of water. We have found that the longer lived water–water and water–TMU H-bonds

exist in higher TMU concentrations. We have also observed that TMU induces significant influence on local environments that regulate the H-bond dynamics.
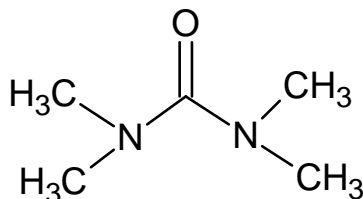
Scheme 6.1: Chemical Structure of Tetramethylurea (TMU)

6.2 Model and Force Field

Here we have considered the SPC/E model of water[65] and AMBER-type force field for TMU. The form of the force field is as follows:

$$U = \sum_{b_{ij}} K_{b_{ij}} \left(b_{ij} - b_{ij}^0 \right)^2 + \sum_{\theta_{ijk}} K_{\theta_{ijk}} \left(\theta_{ijk} - \theta_{ijk}^0 \right)^2 + \sum_{\phi_{ijkl}} \frac{K_{\phi_{ijkl}}}{fsc} \left[1 + \cos\left(n\phi_{ijkl} - \gamma \right) \right]$$

$$+ \sum_{i<j}^{N} \left\{ 4\varepsilon_{ij} \left[\left(\frac{\sigma_{ij}}{r_{ij}} \right)^{12} - \left(\frac{\sigma_{ij}}{r_{ij}} \right)^{6} \right] + \frac{q_i q_j}{r_{ij}} \right\} \quad (6.1)$$

Here, U is the total potential energy of the system. The parameters $b, b^0, \theta, \theta^0, \phi$ are actual bond length, equilibrium bond length, actual bond angle, equilibrium bond angle and dihedral angle, respectively. K_b, K_θ, K_ϕ are the force constants for bond, angle and dihedral angle, respectively. *fsc* denotes the factor by which torsional barrier is divided. γ is the phase shift angle and n the periodicity. The non-bonded interactions are included by the Lennard-Jones (LJ) potential.[66] The LJ parameters ε, σ, r are the potential well depth, van der Waals radius and distance between

atoms, respectively. The parameter q which represents the partial charge of the atom is taken to account for the Coulomb interaction. LJ interactions between unlike atoms are calculated by Lorentz–Berthelot combining rule,[66] where $\varepsilon_{ij} = \sqrt{\varepsilon_i \varepsilon_j}$ and $\sigma_{ij} = \dfrac{\sigma_i + \sigma_j}{2}$.

6.3 Simulation Details

Molecular dynamics simulations were performed using DL_POLY_Classic[67] package. We have used DL_FIELD[68] to make the input files in DL_POLY format. In this study, the methyl groups of TMU are treated by the united atom approach to avoid the complication of the simulation. All the force field parameters for TMU are taken from the literature.[69-71] A total of 512 molecules in a cubic box with periodic boundary condition have been considered. To obtain a reasonable initial configuration, we have run all the simulations in NPT ensemble at 1 atm pressure and 300K using Hoover thermostat and barostat with relaxation times of 2 and 0.5 ps, respectively. We have run a total of 2 ns simulation in NPT ensemble to attain the experimental density of each system. Then, we have used the final configuration of NPT ensemble as the initial configuration for running simulations in NVT ensemble at 300K using the Nosé–Hoover[72,73] thermostat with relaxation time of 0.5 ps. We have further equilibrated the system for a nanosecond to allow complete equilibration and then collected a 4 ns production run. Equations of motion were subsequently solved by leapfrog–Verlet algorithm[66] with time step of 1 fs. Verlet neighbour list shell width was set to 1.2 Å. Trajectories were saved after each 10 fs. Cut-off radius was set nearly to half of the box length. The Shake algorithm[74] was used to constrain all bonds involving hydrogen atoms. Electrostatic interactions were treated via the conventional Ewald summation technique.[66] In addition, we have used the TRANAL utility of MDynaMix program[75] to calculate the static dielectric constant of the SPC/E water and TMU.

6.4 Results and Discussion

6.4.1 Validity Check of the Force Field

Simulated densities at various compositions of the (water + TMU) mixtures at 1 atm pressure and 300 K temperature are compared with those from experiments[76,77] in Figure 6.1. Good agreement between composition-dependent simulated and experimental densities indicates the validity of the force field employed here.
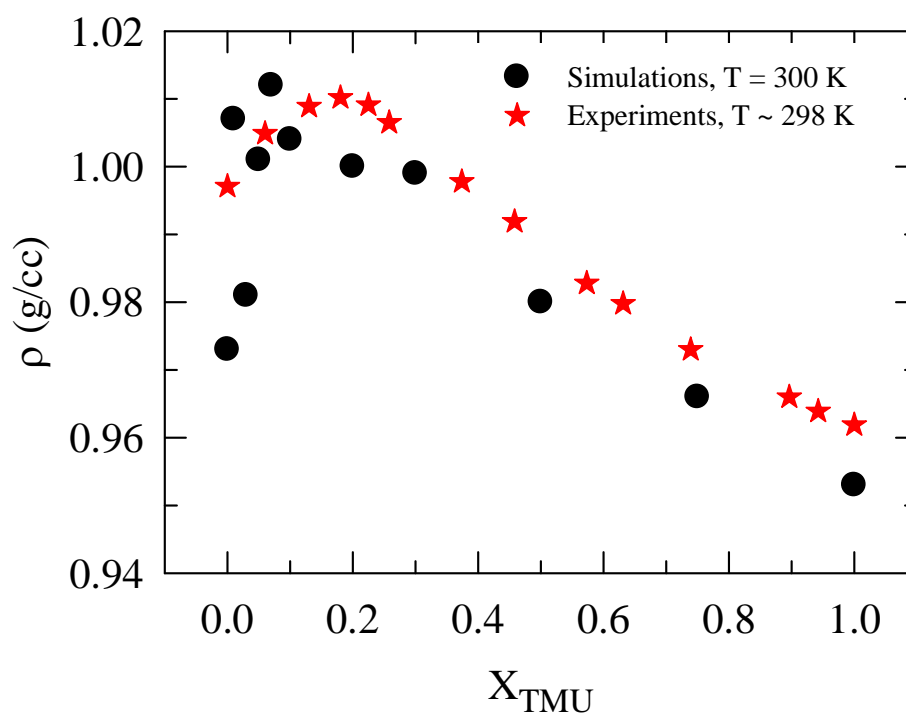
Figure 6.1: A comparison between simulated and experimental TMU mole fraction (X_{TMU})-dependent density of (water + TMU) binary mixture at 300 K and 1 atm pressure. Experimental densities are from Refs. 74 & 75.

We have also calculated ε_0 for water and TMU from simulated collective moment fluctuations and compared with the relevant experimental data. The following relation[78] has been employed to calculate ε_0:

$$\varepsilon_0 = 1 + \frac{4\pi}{3k_B TV}\left[\left\langle \mathbf{M}^2 \right\rangle - \left\langle \mathbf{M} \right\rangle^2\right], \qquad (6.2)$$

with the collective moment, $\mathbf{M} = \sum_i \boldsymbol{\mu}_i$, being the sum over individual dipole moments, $\boldsymbol{\mu}_i$, V the volume and $k_B T$ Boltzmann constant times the absolute temperature.

Our calculated ε_0 for water at 300 K temperature is ~73 and agrees well with experimental[79,80] and simulation[81] results. In contrast, the calculated ε_0 for TMU is found to be ~13 which is ~60% of the experimental value.[82] This discrepancy between simulation and experiment may arise partly from the united atom description for methyl groups in TMU and partly from system size. Note system size is an important factor in simulations for determining ε_0 as the latter is connected to the collective ($\mathbf{k} \to 0, \mathbf{k}$ being the wave vector) solvent modes. However, the H-bond dynamics that we intend to investigate is governed largely by the local environment and, therefore, consideration of 512 particles is expected to provide a semi-quantitative description of composition-dependent dynamics of this binary mixture.

6.4.2 Radial Distribution Functions

The relative structural arrangements of the atoms involved in H-bond interactions in the mixture are shown in Figure 6.2, where the simulated radial distribution functions (RDFs, $g(r)$) at several TMU mole fractions (X_{TMU}) are shown as a function of distance, r. While the upper panel depicts the simulated $g(r)$ for oxygen and hydrogen atoms of water (O(W)–H(W)), the RDFs for water hydrogen and TMU oxygen atoms (O(TMU)–H(W)) are shown in the middle

panel. At $X_{TMU} = 0$ (neat water), $g(r)$ for O(W)–H(W) exhibits its first peak at ~1.7 Å, a distance nearly the sum of the radii of the atoms involved. Expectedly, the second peak appears at a distance (~3.3 Å) approximately equal to the sum of the diameters of these atoms. Note that the O(W)–H(W) $g(r)$ peak intensity increases with the increase of X_{TMU} in the aqueous mixture, but the peak position remains nearly unaltered. This behaviour suggests that addition of TMU leads to enhanced interaction between oxygen and hydrogen atoms of water molecules. Interestingly, $g(r)$ shown in the middle panel also indicate increased interaction between water hydrogen and TMU oxygen upon addition of TMU in water. Growth of both O(W)–H(W) and O(TMU)–H(W) RDFs with increase of TMU concentration suggests that water and TMU molecules arrange themselves in the binary mixture in such a way that the H-bonding interaction between water molecules and that between water and TMU molecules are facilitated upon addition of this amphiphile. This behaviour was observed earlier also for DMSO–water binary mixtures[44] and attributed to structural percolation.

It is interesting to note in these panels that the second peak intensity of O(TMU)–H(W) $g(r)$ is much less than that of O(W)–H(W), suggesting more number of water molecules in the second solvation shell of water oxygen than that for TMU oxygen. The presence of methyl groups may be the reason for this relatively dwindled population of water molecules. This fact notwithstanding these RDFs does indicate successive enhancement of water–water and water–TMU interactions upon increase of X_{TMU} in the aqueous mixture. This means weakening of interaction among TMU molecules in the presence of water. This is indeed the scenario as evidenced in the lower panel of Figure 6.2 which depicts H_3C–CH_3 $g(r)$ for TMU molecules in this mixture. Note in this panel the $g(r)$ peak intensity decreases steadily and exhibits a trend opposite to that observed in the other two panels above. Importantly, this also indicates no aggregation among TMU molecules via methyl–methyl interaction even at large X_{TMU}. However, the enhanced interactions between water–water and water–TMU suggest decrease of
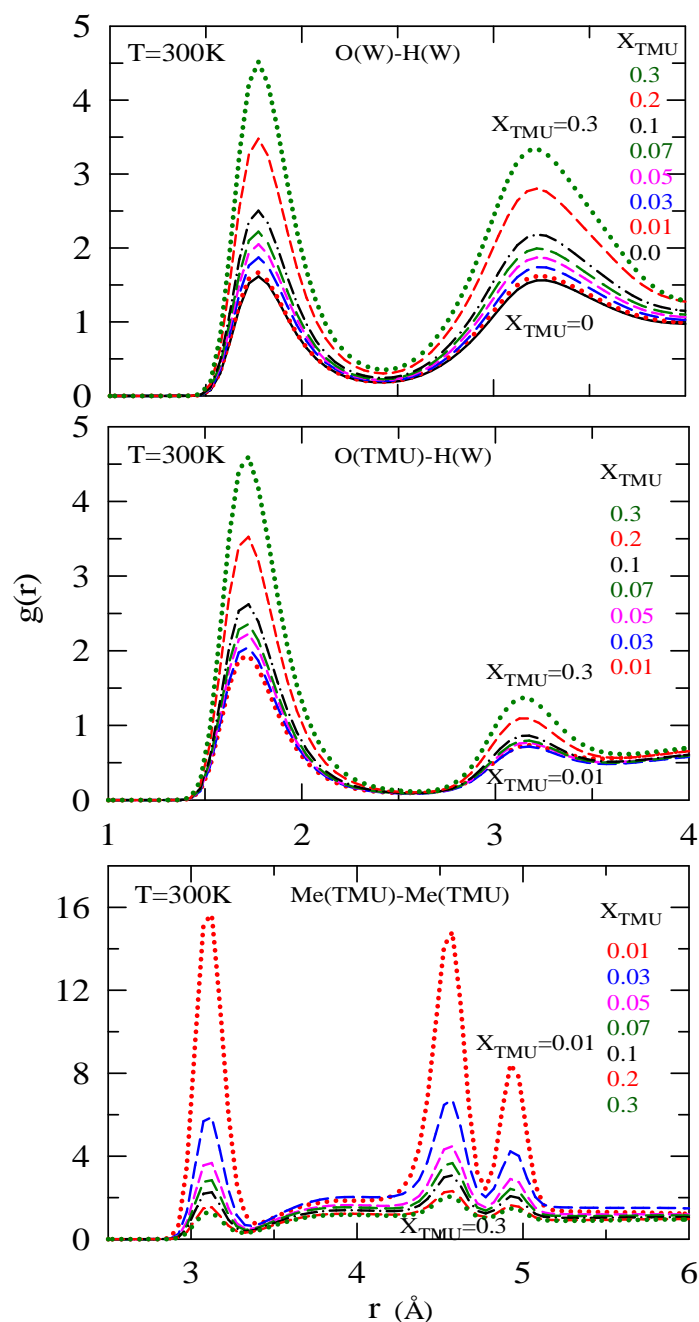
Figure 6.2: X_{TMU}-dependent representative site-site RDFs, $g(r)$, for various atomic pairs as a function of distance, r. Relevant atomic sites are indicated in each of the panels. Inset of each plot shows the atomic sites. Colour code for $g(r)$ shown in these panels is as follows: neat water: solid black; 0.01, red dot; 0.03, blue long dash; 0.05, pink short dash; 0.07, dark green long dash; 0.1, black dash-dot; 0.2, red short dash; 0.3, dark green dot.

translational diffusion coefficients of these molecules with X_{TMU}. This is what we have investigated next.

6.4.3 Mean Squared Displacements

The translational self-diffusion coefficient (D) of a particle moving in a fluid can be calculated from the mean squared displacements (MSDs) of centre-of-mass position vectors $\mathbf{r}_i(t)$ as follows:

$$\left\langle \left| \Delta \mathbf{r}(t) \right|^2 \right\rangle = \frac{1}{N} \left\langle \sum \left| \mathbf{r}_i(t) - \mathbf{r}_i(0) \right|^2 \right\rangle, \qquad (6.3)$$

with $\left\langle \left| \Delta \mathbf{r}(t) \right|^2 \right\rangle$ denoting the MSD. Subsequently, D has been calculated from the simulated $\left\langle \left| \Delta \mathbf{r}(t) \right|^2 \right\rangle$ at long time as follows[83,84]:

$$D = \left[\frac{1}{6t} \left(\left\langle \left| \Delta \mathbf{r}(t) \right|^2 \right\rangle \right) \right]_{t \to \infty}. \qquad (6.4)$$

Simulated MSDs at various X_{TMU} are presented in Figure 6.3 with upper panel depicting $\left\langle \left| \Delta \mathbf{r}(t) \right|^2 \right\rangle$ for oxygen atom of water (upper panel) and lower panel for oxygen atom of TMU. Here we have presented MSD as a function of time in double logarithmic scale in order to show the t^2 and t^1 dependencies of $\left\langle \left| \Delta \mathbf{r}(t) \right|^2 \right\rangle$ at short and long times, respectively. These dependencies are indicated in these plots by 'Slope I' and 'Slope II'. Note that there is no evidence of 'rattling in a cage' motion[85-87] although simulated $g(r)$ suggested stronger interactions between water and TMU molecules through H-bonding. Therefore, caging of TMU, even at low concentrations, by water molecules is probably non-existent in these aqueous binary mixtures.
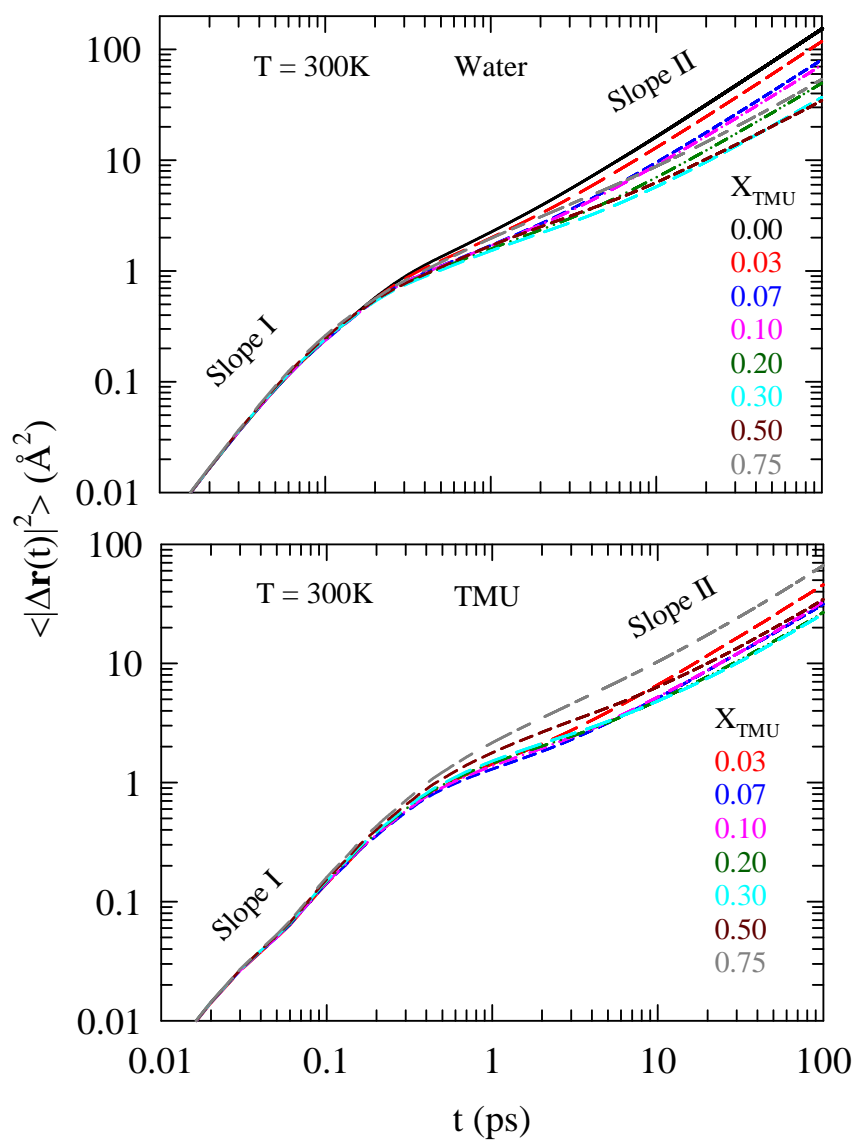
Figure 6.3: X_{TMU}-dependent simulated MSDs for water (upper panel) and TMU (lower panel) in (water + TMU) binary mixture. Colour code denotes the following: neat water, solid black; 0.03, red long dash; 0.07, blue short dash; 0.1, pink dash-dot; 0.2, dark green dash-dot-dot; 0.3, cyan long dash; 0.5, dark red short dash; 0.75, grey long dash.

Mixture composition dependence of viscosity (η) and translational diffusion (D) coefficients for water and TMU are investigated next. In simulations, η has been obtained by using the Green–Kubo relation,[83,84]

$$\eta = \frac{V}{k_B T} \int_0^\infty \langle P_{\alpha\beta}(t) \cdot P_{\alpha\beta}(0) \rangle dt, \qquad (6.5)$$

where $\alpha, \beta = x, y, z$. $P_{\alpha\beta}$ denotes the off-diagonal terms $(\alpha \neq \beta)$ of the pressure tensor. Figure 6.4 presents a comparison between the simulated and experimental[76] η for this mixture at ~300 K. Clearly, the agreement is semi-quantitative, indicating insufficiency of the model interaction potentials to represent quantitatively the interactions present in such aqueous binary mixtures,[81,88] and formation of aqueous complex through H-bond interaction.[89]

The lower panel of Figure 6.4 shows the composition dependence of the simulated D for water and TMU for this mixture at 300 K. Simulated D for SPC/E water at ~300 K by other authors[81,88] is also shown to ensure fidelity of the present simulations. Note that D for both the specie first decreases with X_{TMU} and then increases after a shallow minimum. Interestingly, one expects, from X_{TMU} dependencies of medium density (see Figure 6.1) and viscosity,[76,89] a much sharper inverted parabolic dependence for D on composition for this mixture. Slip hydrodynamic predictions for D using both simulated (broken lines) and experimental (solid lines) viscosities are also shown in the same figure to highlight the difference between the simulations and hydrodynamic predictions. The difference between the simulated and predicted values may appear from the non-hydrodynamic character of the particle movement in these binary mixtures. Measurements of D for these mixtures are, therefore, necessary to ascertain whether the X_{TMU} dependence of simulated D originates from partial decupling of diffusion from viscosity[90-94] in these mixtures or the observed dependence is simply a reflection of the non-quantitativeness of the model interaction potentials used for accurate representation of the complex interactions in these aqueous binary mixtures.
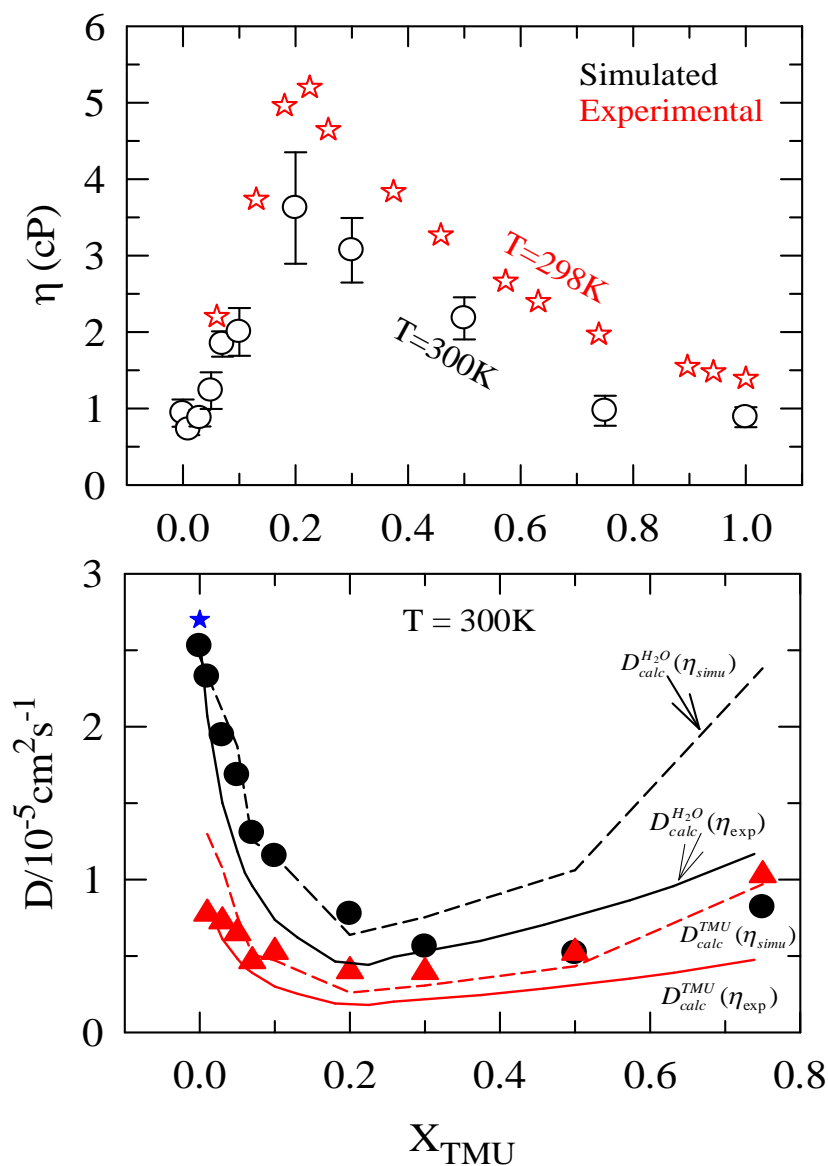
Figure 6.4: Composition dependence of viscosity (upper panel) and diffusion coefficients (lower panel) for water and TMU in (water + TMU) binary mixtures at 300 K. Simulated viscosity coefficients (η) are shown by circles with error bars. In the lower panel, filled black circles represent simulated diffusion coefficients (D) for water and filled red triangles denote the simulated D for TMU. While the solid lines represent the slip hydrodynamic predictions by using the experimental η, the dashed lines denote the same but using the simulated η. For hydrodynamic calculations, radii of water and TMU molecules used are 1.425 and 3.5 Å, respectively. Star denotes the simulated diffusion coefficient for SPC/E water at 300 K reported in Ref. 79.

6.4.4 Dynamic Heterogeneity

Dynamic heterogeneity (DH) can impart non-hydrodynamic character to the particle movements, and can be understood in terms of non-Gaussian (NG) and new non-Gaussian (NNG) parameters, and single particle displacement distributions.[95-97] The translational NG parameter $\left(\alpha_2 \right)$ can be obtained from the simulated MSD by using the following relation:

$$\alpha_2(t) = \frac{3 \left\langle \delta r^4(t) \right\rangle}{5 \left\langle \delta r^2(t) \right\rangle^2} - 1, \qquad (6.6)$$

where $\left\langle \delta r^2(t) \right\rangle = \left\langle N^{-1} \sum_{i=1}^{N} \left| \Delta \mathbf{r}(t) \right|^2 \right\rangle$ and $\left\langle \delta r^4(t) \right\rangle = \left\langle N^{-1} \sum_{i=1}^{N} \left| \Delta \mathbf{r}(t) \right|^4 \right\rangle$ with δr denoting the single particle displacement. $\Delta \mathbf{r}(t) = \mathbf{r}_i(t) - \mathbf{r}_i(0)$. Note that for homogeneous systems (for example, hot liquids), $\alpha_2(t) = 0$ for both at $t = 0$ and $t = \infty$ but $\alpha_2(t) = 0.2$ at intermediate times.[90] Therefore, systems possessing DH would be characterized by a non-monotonic time dependence of $\alpha_2(t)$ with peak higher than 0.2. This peak signifies a DH timescale which is designated as τ_{NG}. Interestingly, another much slower DH timescale may also exist in the system which can be accessed via calculating the NNG parameter $\left(\gamma(t) \right)$ as follows[95]:

$$\gamma(t) = \frac{1}{3} \left\langle \delta r^2(t) \right\rangle \left\langle \frac{1}{\delta r^2(t)} \right\rangle - 1, \qquad (6.7)$$

with $\left\langle 1/\delta r^2(t) \right\rangle = \left\langle 1/N \sum_{i=1}^{N} 1 / \left| \Delta \mathbf{r}(t) \right|^2 \right\rangle$. Clearly, $\gamma(t)$ is dominated by those particles which execute smaller displacements and contribute to a DH timescale $\left(\tau_{NNG} \right)$ slower than that reflected by τ_{NG}. For systems possessing no spatially varying relaxation rates (that is, DH) $\tau_{NG} = \tau_{NNG}$, and $\alpha_2(t)$ and $\gamma(t)$ curves would overlap.

The DH signature can also be revealed by studying the single-particle displacement distribution as follows[95-97]:

$$P[\log_{10}(\delta r);t] = \ln(10)4\pi\delta r^3 G_s(\delta r,t), \qquad (6.8)$$

where $G_s(\delta r,t)$ denotes the self-part of the van Hove correlation function.[83,84] Note for a Gaussian $G_s(\delta r,t)$, $P[\log_{10}(\delta r);t]$ becomes independent of time with a peak height of 2.13. Any deviation from the Gaussian shape and peak height would therefore indicate presence of DH in the system and may be interpreted as the origin for the partial decoupling of diffusion from solution viscosity.

Figure 6.5 shows $\alpha_2(t)$ and $\gamma(t)$ simulated for water at four different mixture compositions at 300 K. Note that these compositions (that is X_{TMU} = 0.01, 0.2, 0.3 and 0.5) are chosen to represent dilute and concentrated aqueous solutions of TMU, including the composition that corresponds to the maximum in experimental and simulated η. Simulated $\alpha_2(t)$ and $\gamma(t)$ for neat water at 300 K, shown in Figure 6.A.1 of Appendix 6.A, depict a non-monotonic dependence with a peak value of ~0.2 at intermediate times, and the peak times (τ_{NG} and τ_{NNG}) nearly overlap on each other. However, as X_{TMU} increases, the peak value increases and τ_{NG} deviates from τ_{NNG}. The appearance of these two 'slow' timescales clearly demonstrates the presence of DH in the system. Therefore, partial decoupling between D and η for water noted in Figure 6.4 at higher TMU concentration may be attributed to the DH of these aqueous binary mixtures.
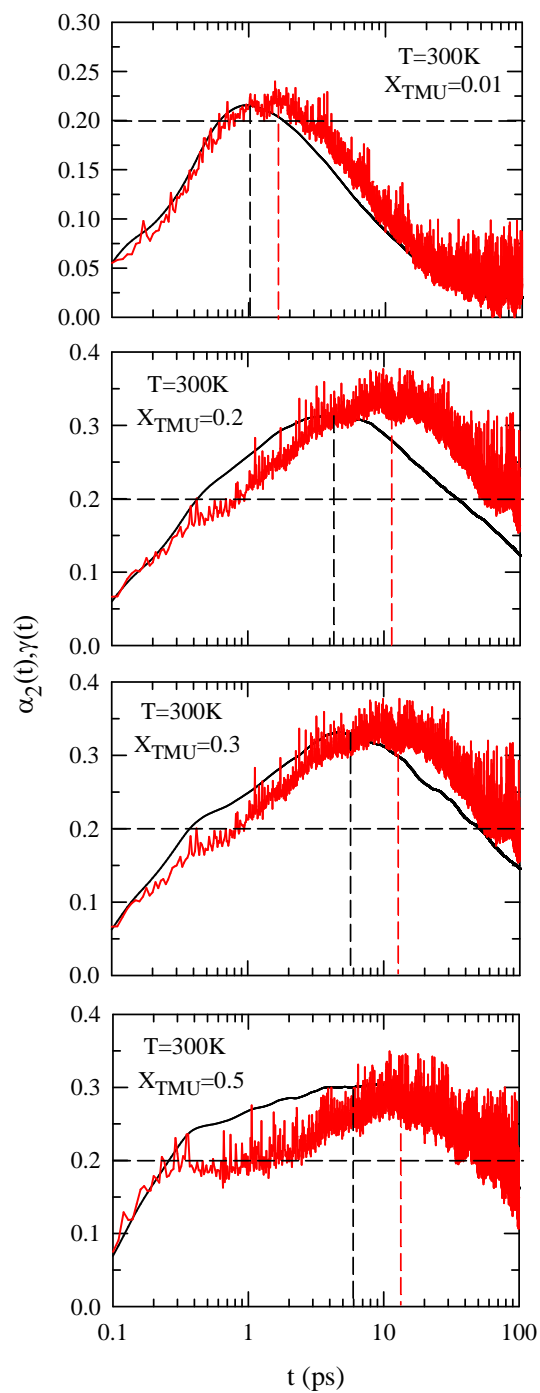
Figure 6.5: Simulated $\alpha_2(t)$ and $\gamma(t)$ for water in (water + TMU) binary mixtures at a few representative mixture compositions at 300 K. Black curve denotes $\alpha_2(t)$ and the red curve denotes $\gamma(t)$. Vertical broken lines indicate the peak times, τ_{NG} and τ_{NNG}, for $\alpha_2(t)$ and $\gamma(t)$, respectively. Horizontal line indicates the value of 0.2.
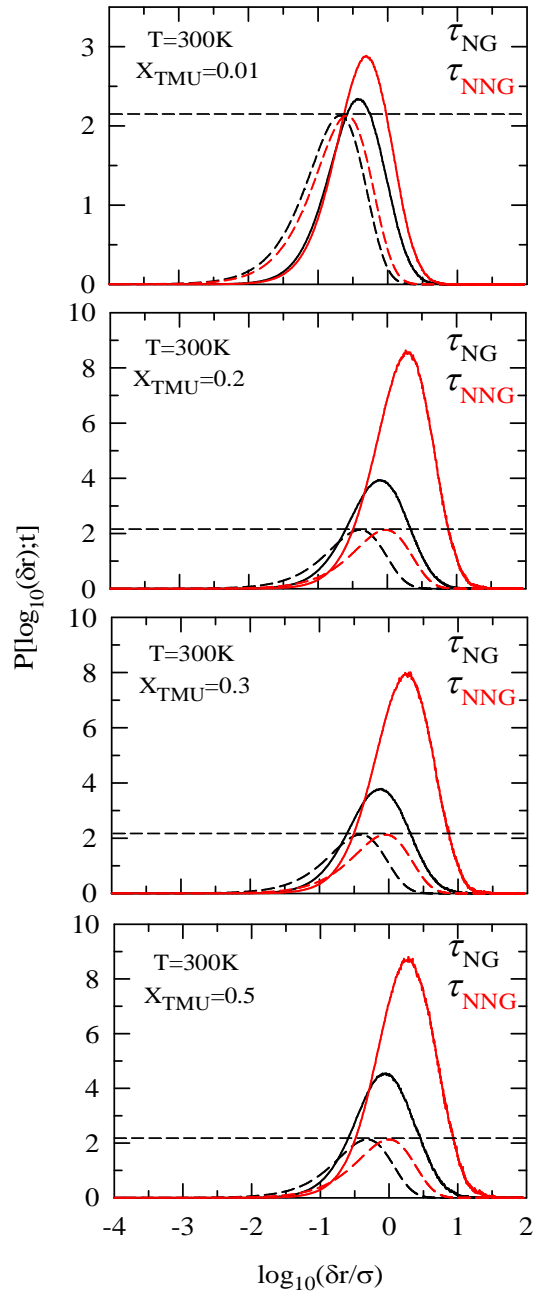
Figure 6.6: Simulated single particle displacement distributions, $P\left[\log_{10}(\delta r);t\right]$, for water at a few representative mixture compositions at 300 K. Distributions both at τ_{NG} and τ_{NNG} are shown. $P\left[\log_{10}(\delta r);t\right]$ corresponding to a Gaussian $G_s(\delta r,t)$ at these times is also shown for comparison. Horizontal broken lines in these panels indicate a value of 2.13 expected for $P\left[\log_{10}(\delta r);t\right]$ possessing a Gaussian $G_s(\delta r,t)$.

Figure 6.6 depicts the simulated $P\left[\log_{10}(\delta r);t\right]$ for water at these representative mixture compositions at τ_{NG} and τ_{NNG}. Corresponding distributions for a Gaussian $G_s(\delta r,t)$ are also shown for comparison. $P\left[\log_{10}(\delta r);t\right]$ at these DH timescales for ambient water is provided in Figure 6.A.2 (Appendix 6.A). Simulated distributions shown in these panels clearly demonstrate enhancement of DH for water upon increasing TMU concentration in these mixtures. This explains the partial decoupling of solution viscosity from water diffusion observed in Figure 6.4. Interestingly, the simulated $P\left[\log_{10}(\delta r);t\right]$ at τ_{NG} and τ_{NNG} for ambient water shows a slight deviation from the Gaussian character, which probably explains our simulated diffusion coefficient for neat water being ~10% larger than that reported in experiments $\left(\sim 2.3\times10^{-5}\ \mathrm{cm^2 s^{-1}}\right)$.

6.4.5 H-bond Dynamics

Simulated $g(r)$ presented in Figure 6.2 has already revealed pronounced interaction between water and TMU in aqueous mixture, and this is expected to deeply impact the H-bond dynamics of water in solution. We have employed the following geometric definition of H-bonding between a pair of molecules[57-60]:

1. Distance between two oxygen atoms must be less than 3.5 Å.

2. Angle between O–O bond vector and O–H bond vector must be less than 30^0.

3. Distance between O and H must be less than 2.45 Å.

How long a pair of molecules remains H-bonded can be calculated by two different time-correlation functions.[23-26] The relaxation of H-bond lifetime is calculated by the time-correlation function, $S_{HB}(t)$,

$$S_{HB}(t) = \frac{\langle h(0)H(t)\rangle}{\langle h\rangle}, \tag{6.9}$$

where $H(t)=1$ if the tagged pair of molecules, for which $h(0)$ is calculated, remains continuously H-bonded till time t, else zero. $S_{HB}(t)$ describes the probability that a tagged pair of molecules remains continuously H-bonded up to time t, and approaches to zero when H-bonding between them breaks down for the first time. The time profile of $S_{HB}(t)$ therefore represents relaxation of H-bond lifetime, and hence, the average H-bond lifetime, $\langle \tau_S^{HB} \rangle$, can be obtained via time integration of this normalised time correlation function.

The structural relaxation time of H-bond is calculated by the time-correlation function, $C_{HB}(t)$, defined as[23-26]

$$C_{HB}(t) = \frac{\langle h(0)h(t) \rangle}{\langle h \rangle},$$ (6.10)

where $C_{HB}(t)$ exhibits a much slower decay than $S_{HB}(t)$, as the former is independent of possible breaking of H-bonds between the tagged pair of molecules in the intermediate time and considers the reformation of bond after breakage. $C_{HB}(t)$ is, therefore, associated with H-bond structural relaxation, and thus the time integration of this normalised correlation function provides the average structural relaxation time, $\langle \tau_C^{HB} \rangle$.

Figure 6.7 shows the decay of $S_{HB}(t)$ and $C_{HB}(t)$ as a function of time simulated at $X_{TMU}=0$ and T = 300 K. Bi-exponential fit to $S_{HB}(t)$ and tri-exponential fit to $C_{HB}(t)$ are also shown in these figures. Note simulated $S_{HB}(t)$ and $C_{HB}(t)$ at other mixture compositions can also be similarly described via bi- and tri-exponentials, respectively. Fit parameters required for these correlation functions at all X_{TMU} values are summarised in Tables 6.B.1–6.B.4 of the Appendix 6.B. Note that multi-exponential nature of $S_{HB}(t)$ and $C_{HB}(t)$ has been found earlier also for a variety of systems, ranging from aqueous micellar solutions[60,98,99] and cyclodextrins[100] to
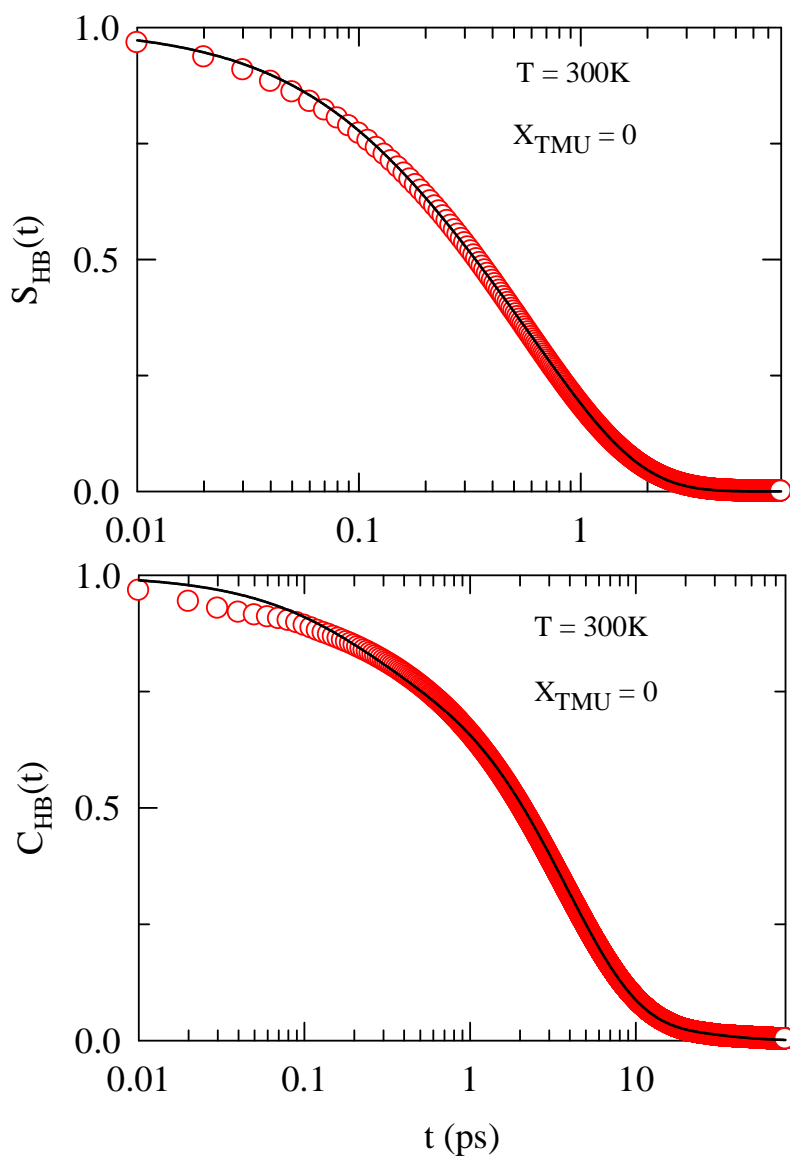
Figure 6.7: Relaxation profiles of $S_{HB}(t)$ and $C_{HB}(t)$ for neat water along with multi-exponential fits. Simulations are represented by the circles, and solid lines going through them are fits. Average relaxation times for these correlation functions at various X_{TMU} have been obtained from fit parameters as follows: $\left\langle \tau_S^{HB} \right\rangle_x = \sum_i a_i \tau_i$, a_i and τ_i are the normalised amplitudes and time constants obtained via fits to simulated $S_{HB}(t)$ and $C_{HB}(t)$.

moisturised proteins and DNA.[101,102] Note $\left\langle \tau_S^{HB} \right\rangle$ and $\left\langle \tau_C^{HB} \right\rangle$ for pure water are, respectively, ~ 0.5 and ~4 ps, which are in good agreement with earlier findings.[59-61,98-102] The multi-exponential character of the relaxations may have origin in the two different density regions that exist in liquid water – one is low density four-coordinated tetrahedral H-bonding region and the other is two or threecoordinated high density region.[103,104] However, further study is required to determine whether density fluctuations in these differently populated regions are indeed responsible for the multi-exponential relaxations of $S_{HB}(t)$ and $C_{HB}(t)$ in neat water and in water-rich solutions.

Figure 6.8 presents the X_{TMU}-dependent relaxations of $S_{HB}(t)$ for water–water and water–TMU H-bond lifetimes. Note $S_{HB}(t)$ for both cases slows down with each successive addition of TMU in the mixture, resulting in longer H-bond lifetimes in the presence of TMU. Interestingly, the enhancement of water–water H-bond lifetime upon gradual addition of TMU in aqueous solution resembles the slowing down of water confined in carbon nanotube[105] and water at the surface of an antifreeze protein.[106] Therefore, it may be stated that the presence of TMU slows down the H-bond dynamics in some ways similar to those operative inside the confinement and at the micelle and protein surfaces. One of the frames from the simulation trajectory at $X_{TMU} = 0.2$ is shown in Figure 6.9 which depicts the alignment of water and TMU molecules in the binary mixture. Figure 6.9 indeed suggests that water molecules near the TMU surface can mimic the effects observed either under confinement or near a micellar surface. It is to be mentioned here that longer H-bond lifetime does not necessarily indicate stronger H-bonds.[107] The average lifetime of H-bonds largely depends on local environments. From the simulated $g(r)$ we have noticed growth of O–H interactions between water–water and water–TMU molecules. This structural compactness probably forces the water and TMU molecules to remain H-bonded for longer times. Quantum mechanical calculations of H-bond energies may provide further information on this aspect.
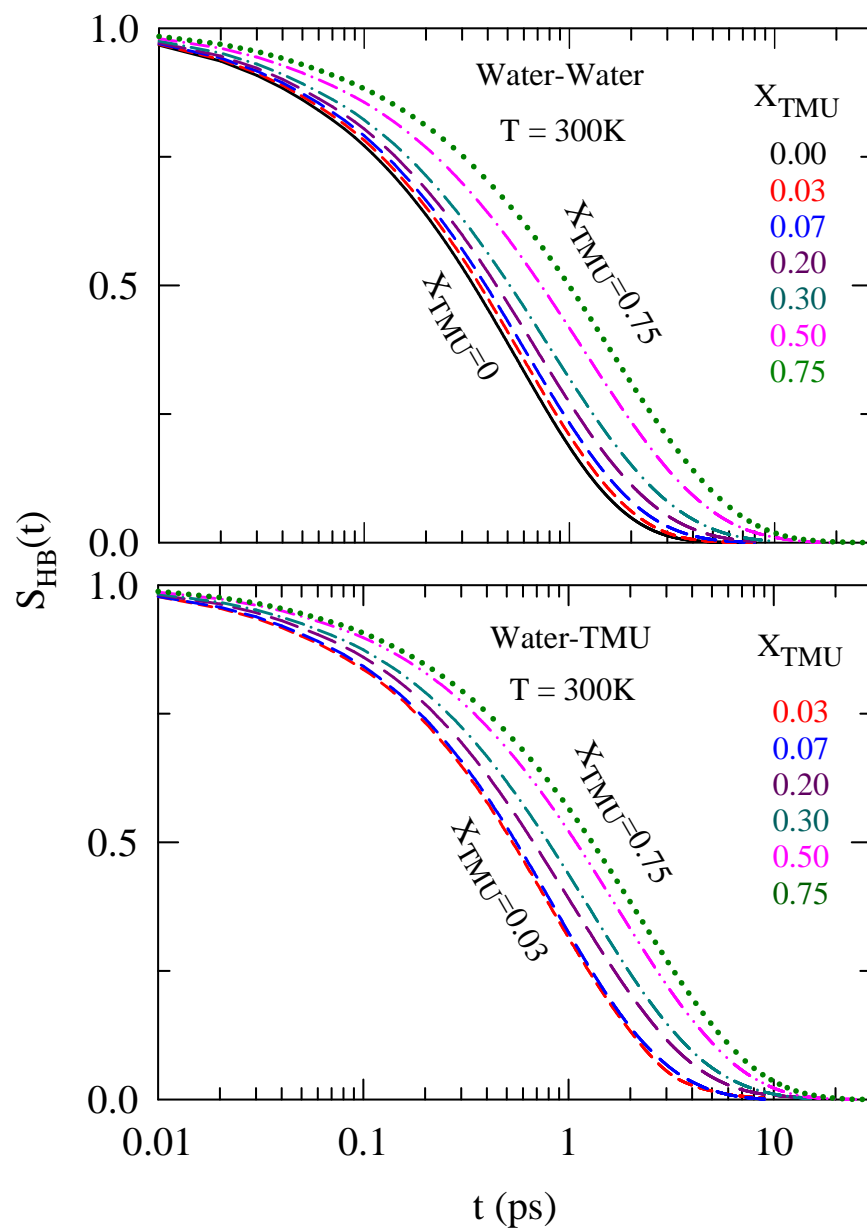
Figure 6.8: X_{TMU}-dependent relaxations of $S_{HB}(t)$ for water–water hydrogen bonding (upper panel) and water–TMU hydrogen bonding (lower panel). X_{TMU} are colour-coded as follows: neat water, solid black; 0.03, red short dash; 0.07, blue long dash; 0.2, dark pink long dash; 0.3, dark green dash-dot; 0.5, pink dash-dot-dot; 0.75, dark green dot.
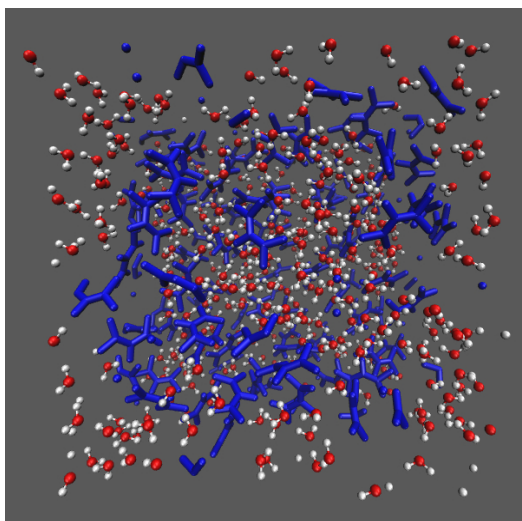
Figure 6.9: Snapshot of relative spatial arrangements of water and TMU molecules in (water + TMU) binary mixture at $X_{TMU} = 0.2$. TMU molecules are represented by blue colour, whereas water molecules are denoted by using ball and stick. Water oxygen and hydrogen atoms are shown by red and white colours, respectively.

H-bond structural relaxation functions, $C_{HB}(t)$, are shown in Figure 6.10 for water–water (upper panel) and water–TMU (lower panel) specie. As found for $S_{HB}(t)$ in Figure 6.8, $C_{HB}(t)$ also slows down upon addition of TMU in the aqueous solution, producing longer average structural relaxation times, $\langle \tau_C^{HB} \rangle$. This can also be linked to the changes in $g(r)$ upon addition of TMU in the mixture. The X_{TMU}-induced slowing down of $S_{HB}(t)$ and $C_{HB}(t)$ relaxations is summarised in Figure 6.11 where average relaxation times, $\langle \tau_S^{HB} \rangle$ and $\langle \tau_C^{HB} \rangle$, are shown as a function of TMU mole fraction in the mixture. Note that both these relaxation times increase linearly with X_{TMU}, and do not show any non-monotonic composition dependence. This clearly indicates that none of these relaxation processes are governed by medium viscosity. Moreover, $\langle \tau_S^{HB} \rangle$ and $\langle \tau_C^{HB} \rangle$ for water–TMU are longer at all X_{TMU} than those for water–water. Relatively lower diffusion of TMU may not be the reason for this as these relaxation times do not couple to
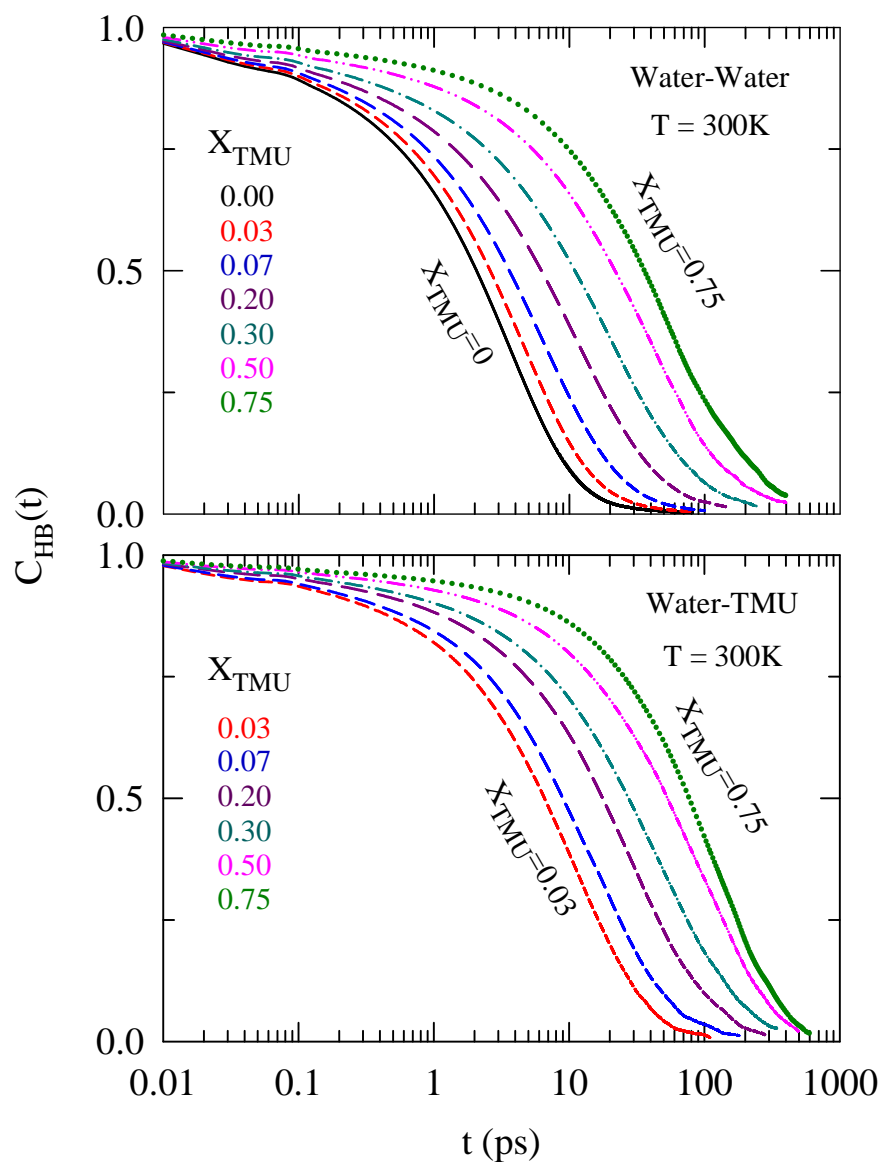
Figure 6.10: X_{TMU}-dependent relaxations of $C_{HB}(t)$ for water–water hydrogen bonding (upper panel) and water–TMU hydrogen bonding (lower panel). Representations of X_{TMU} are colour-coded and follow the sequence shown in Figure 6.8.

solution viscosity. Data in Figure 6.11 also indicate that $\left\langle \tau_S^{HB} \right\rangle$ and $\left\langle \tau_C^{HB} \right\rangle$ slow down by a factor of ~3–10 upon changing the medium from neat water to aqueous TMU solution with

$X_{TMU} = 0.75$. Interestingly, this extent of slowing down is comparable to lengthening of these quantities for water encapsulated in cyclodextrin cavities.[100]
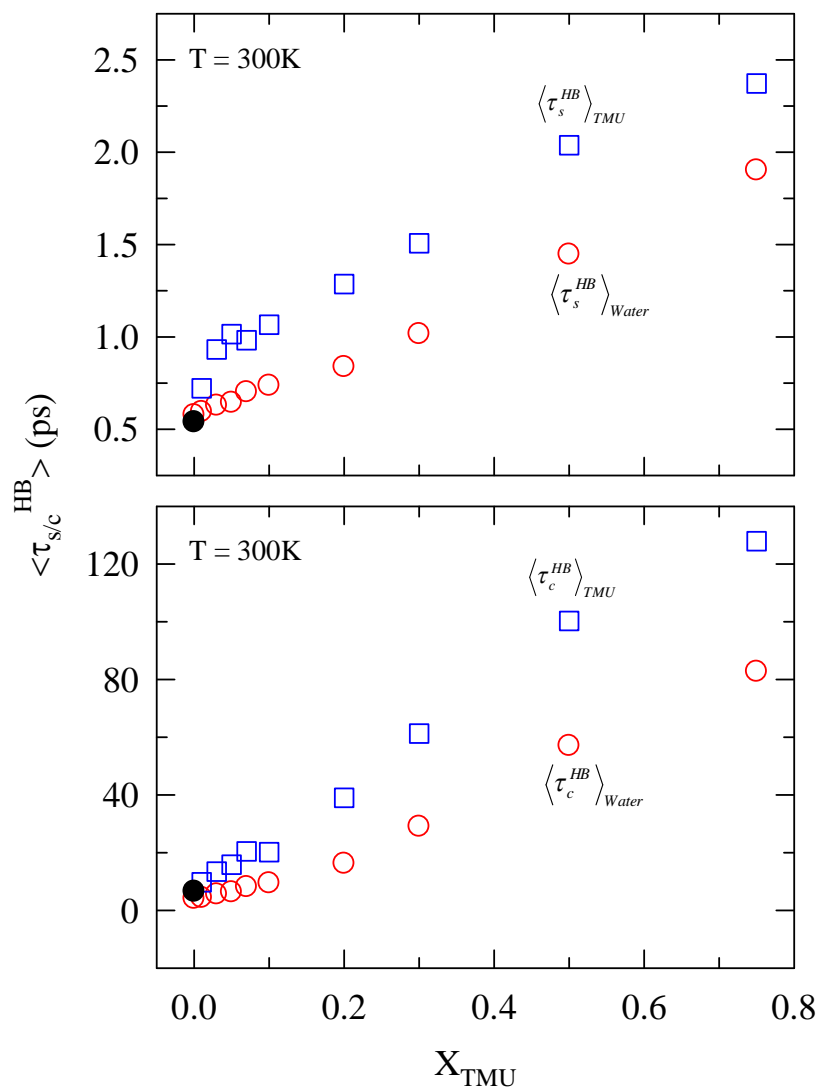
Figure 6.11: Plot of average relaxation times for X_{TMU}-dependent H-bond dynamics and structural dynamics. As discussed in the text, $\langle \tau_S^{HB} \rangle$ has been obtained analytically from fits of $S_{HB}(t)$ and $\langle \tau_C^{HB} \rangle$ similarly from $C_{HB}(t)$. Solid circles in both panels represent simulated data reported in Ref. 59.

6.5 Conclusion

In summary, this simulation study suggests considerable slowing down of H-bond relaxation dynamics in the presence of amphiphilic molecules in bulk binary mixtures, and the extent of slowing down mimics those found for encapsulated water molecules in cavities and those near micellar and biological surfaces. Simulated RDFs indicate increase of water–water and water–TMU interactions upon addition of TMU in the aqueous solution, but decrease of TMU–TMU interaction. Simulated MSDs do not show any signature of cagerattling and this has been interpreted as no evidence for the formation of TMU–water clathrate-type structure even at low TMU concentration. Simulated diffusion coefficients for both the specie seem to indicate partial decoupling of diffusion from medium viscosity. Simulated DH and single particle displacement distributions reflect deviations of particle movements from hydrodynamic behaviour. In addition, simulated diffusion coefficients do not show as pronounced composition dependence as that shown by viscosity coefficients. Use of polarisable potential and explicit treatment of methyl group in the force field for TMU may improve the agreement between the composition-dependent simulated and experimental viscosity coefficients. Relaxation profiles of H-bond lifetime and structure are multi-exponential in character, and we propose that density inhomogeneity inherent to liquid water may be responsible for this non-exponential behaviour. This aspect should be further investigated. In addition, DH of water molecules, particularly of those present at high TMU concentration, needs to be explored as the simulated diffusion coefficients appear to suggest decoupling from medium viscosity.

Appendix 6.A
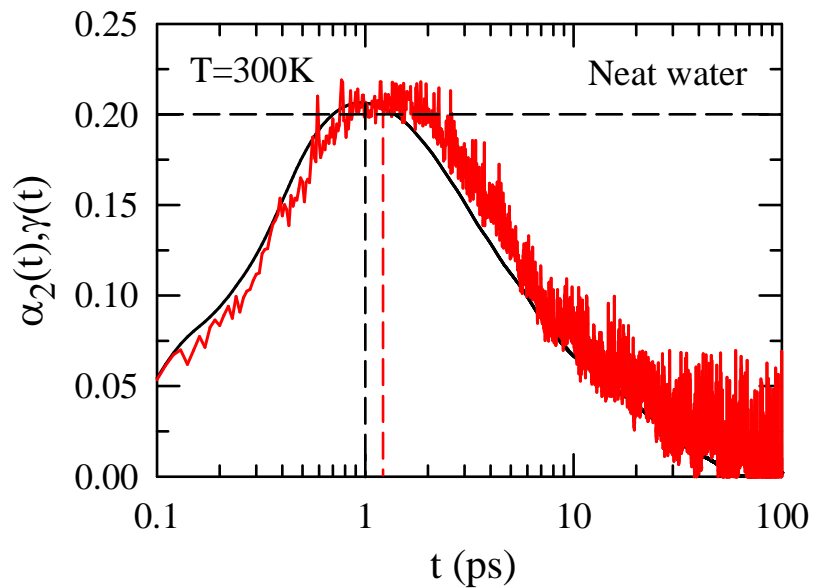
Figure 6.A.1: Simulated $\alpha_2(t)$ and $\gamma(t)$ for neat water at 300 K. Black curve denotes $\alpha_2(t)$ and the red curve $\gamma(t)$. Vertical broken lines indicate the peak-times, τ_{NG} and τ_{NNG}, for $\alpha_2(t)$ and $\gamma(t)$, respectively. Horizontal line indicates the value of 0.2.
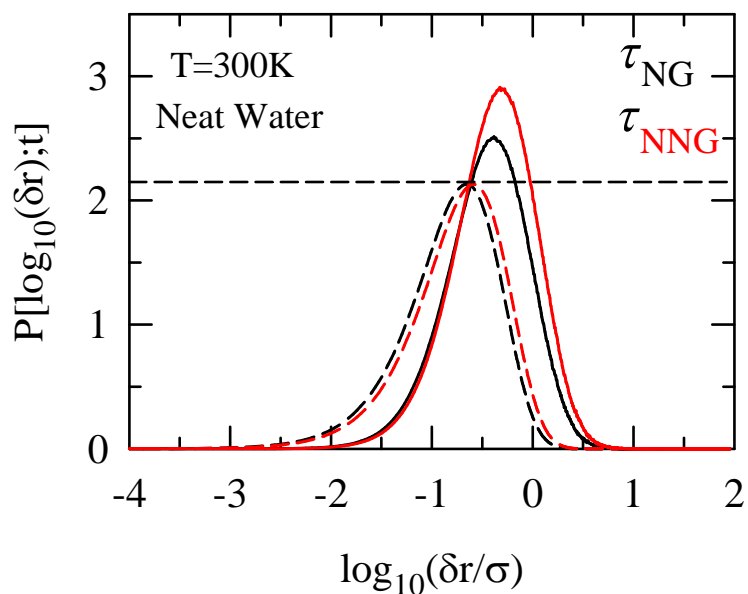
Figure 6.A.2: Simulated single particle displacement distributions, $P[\log_{10}(\delta r);t]$, for neat water at 300 K. Distributions both at τ_{NG} and τ_{NNG} are shown. $P[\log_{10}(\delta r);t]$ corresponding to a Gaussian $G_s(\delta r,t)$ at these times are also shown for a comparison. Horizontal broken lines in these panels indicate a value of 2.13 expected for $P[\log_{10}(\delta r);t]$ possessing a Gaussian $G_s(\delta r,t)$.

Appendix 6.B

Table 6.B.1: Bi-exponential fit parameters for water-water H-bond lifetime correlation $\left(S_{HB}^{w-w}(t)\right)$ decays at different TMU mole fractions and 300 K. Corresponding $\langle h \rangle$ values are listed in the last column.

X_{TMU}	a_1	τ_1/ps	a_2	τ_2/ps	τ_{av}/ps	$\langle h \rangle$
0.00	0.77	0.711	0.23	0.131	0.578	0.87
0.01	0.77	0.734	0.23	0.131	0.595	0.87
0.03	0.75	0.789	0.25	0.149	0.629	0.86
0.05	0.72	0.831	0.28	0.167	0.645	0.84
0.07	0.67	0.948	0.33	0.204	0.702	0.83
0.10	0.65	1.016	0.35	0.219	0.737	0.82
0.20	0.60	1.222	0.40	0.261	0.838	0.76
0.30	0.57	1.549	0.43	0.312	1.017	0.68
0.50	0.59	2.174	0.41	0.402	1.447	0.54
0.75	0.65	2.671	0.35	0.476	1.903	0.40

Table 6.B.2: Bi-exponential fit parameters for water-TMU H-bond lifetime correlation $\left(S_{HB}^{w-TMU}(t)\right)$ decays at different TMU mole fractions and 300 K. Corresponding $\langle h \rangle$ values are listed in the last column.

X_{TMU}	a_1	τ_1/ps	a_2	τ_2/ps	τ_{av}/ps	$\langle h \rangle$
0.01	0.65	0.969	0.35	0.264	0.722	0.13
0.03	0.72	1.194	0.28	0.260	0.932	0.14
0.05	0.65	1.399	0.35	0.301	1.015	0.14
0.07	0.66	1.320	0.34	0.325	0.982	0.17
0.10	0.64	1.466	0.36	0.355	1.066	0.18
0.20	0.58	1.912	0.42	0.421	1.286	0.27
0.30	0.59	2.218	0.41	0.485	1.507	0.36
0.50	0.65	2.840	0.35	0.548	2.038	0.54
0.75	0.67	3.264	0.33	0.562	2.372	0.73

Table 6.B.3: Tri-exponential fit parameters for water-water H-bond structural relaxations $\left(C_{HB}^{w-w}(t)\right)$ at different TMU mole fractions and 300 K. Corresponding $\langle h \rangle$ values are listed in the last column.

X_{TMU}	a_1	τ_1/ps	a_2	τ_2/ps	a_3	τ_3/ps	τ_{av}/ps	$\langle h \rangle$
0.00	0.05	22.233	0.79	3.766	0.16	0.173	4.114	0.87
0.01	0.08	19.036	0.76	3.784	0.16	0.173	4.426	0.87
0.03	0.10	21.853	0.74	4.608	0.16	0.217	5.630	0.86
0.05	0.11	23.790	0.71	5.188	0.18	0.269	6.349	0.84
0.07	0.14	27.318	0.67	6.398	0.19	0.348	8.177	0.83
0.10	0.15	31.730	0.66	7.025	0.19	0.368	9.466	0.82
0.20	0.16	55.025	0.63	11.603	0.21	0.675	16.256	0.76
0.30	0.20	88.626	0.59	18.829	0.21	1.015	29.047	0.68
0.50	0.18	184.439	0.64	36.734	0.18	1.967	57.063	0.54
0.75	0.37	170.567	0.54	36.240	0.09	0.650	82.738	0.40

Table 6.B.4: Tri-exponential fitting parameters for wat-TMU H-bond structural relaxations $\left(C_{HB}^{w-TMU}(t)\right)$ at different TMU mole fractions and 300 K. Corresponding $\langle h \rangle$ values are listed in the last column.

X_{TMU}	a_1	τ_1/ps	a_2	τ_2/ps	a_3	τ_3/ps	τ_{av}/ps	$\langle h \rangle$
0.01	0.27	20.611	0.63	6.576	0.10	0.141	9.722	0.13
0.03	0.18	34.700	0.68	10.435	0.14	0.550	13.419	0.14
0.05	0.19	43.383	0.67	11.226	0.14	0.535	15.839	0.14
0.07	0.15	66.284	0.68	15.150	0.17	1.064	20.425	0.17
0.10	0.31	41.225	0.57	12.858	0.12	0.463	20.164	0.18
0.20	0.30	87.040	0.58	22.048	0.12	0.714	38.985	0.27
0.30	0.38	121.042	0.49	30.768	0.13	1.332	61.245	0.36
0.50	0.62	143.735	0.28	39.289	0.10	1.748	100.291	0.54
0.75	0.66	166.667	0.28	63.878	0.06	0.784	127.933	0.73

References

1.   J. Swenson, R. Bergman and S. Longeville, J. Chem. Phys. **115**, 11299 (2001).

2.   M. Antognozzi, A. D. L. Humphris and M. J. Miles, Appl. Phys. Lett. **78**, 300 (2001).

3.   P. Gallo, M. Rovere and E. Spohr, J. Chem. Phys. **113**, 11324 (2000).

4.   M. Bellissent-Funel, J. Lal and L. Bosio, J. Chem. Phys. **98**, 4246 (1993).

5.   M. Meyer and H. E. Stanley, J. Phys. Chem. B **103**, 9728 (1999).

6.   F. Bruni, M. A. Ricci and A. K. Soper, J. Chem. Phys. **109**, 1478 (1998).

7.   A. Faraone, L. Liu, C. Mou, C. Yen and S. Chen, J. Chem. Phys. **121**, 10843 (2004).

8.   E. Mamontov, J. Chem. Phys. **121**, 9193 (2004).

9.   E. Tajkhorshid, P. Nollert, M. O. Jensen, L. Miercke, J. O'Connell, R. M. Stroud and K. Schulten, Science **296**, 525 (2002).

10.   K. Bhattacharyya, Chem. Commun., 2848 (2008).

11.   K. Bhattacharyya, Acc. Chem. Res. **36**, 95 (2003).

12.   B. Bagchi and B. Jana, Chem. Soc. Rev. **39**, 1936 (2010).

13.   B. Guchhait, R. Biswas and P. K. Ghorai, J. Phys. Chem. B **117**, 3345 (2013).

14.   N. E. Levinger, Science **298**, 1722 (2002).

15.   R. H. Coridan, N. W. Schmidt, G. H. Lai, P. Abbamonte and G. C. L. Wong, Phys. Rev. E **85**, 031501 (2012).

16.   R. Biswas, N. Rohman, T. Pradhan and R. Buchner, J. Phys. Chem. B **112**, 9379 (2008).

17.   N. Sarma, J. M. Borah, S. Mahiuddin, H. A. R. Gazi, B. Guchhait and R. Biswas, J. Phys. Chem. B **115**, 9040 (2011).

18.   R. Biswas, A. R. Das, T. Pradhan, D. Tauraud, W. Kunz and S. Mahiuddin, J. Phys. Chem. B **112**, 6620 (2008).

19.   S. Senapati and A. Chandra, J. Phys. Chem. B **105**, 5106 (2001).

20.   A. A. Rashin, M. Iofin and B. Honig, Biochemistry **25**, 3619 (1986).

21.   S. Bernèche and B. Roux, Nature **414**, 73 (2001).

22.   P. Ball, Chem. Rev. **108**, 74 (2008).

23.   E. Persson and B. Halle, J. Am. Chem. Soc. **130**, 1174 (2008).

24.   B. Bagchi, Chem. Rev. **105**, 3197 (2005).

25.   D. E. Moilanen, I. R. Piletic and M. D. Fayer, J. Phys. Chem. C **111**, 8884 (2007).

26.   J. Faeder and B. M. Ladanyi, J. Phys. Chem. B **104**, 1033 (2000).

27.   S. Abel, F. Sterpone, S. Badyopadhyay and M. Marchi, J. Phys. Chem. B **108**, 19458 (2004).

28.   A. Dokter, S. Wourtersen and H. Bakker, J. Proc. Natl. Acad. Sci. USA **103**, 15355 (2006).

29.   D. E. Moilanen, E. E. Fenn, D. Wong and M. D. Fayer, J. Chem. Phys. **131**, 014704 (2009).

30.   N. E. Levinger and L. A. Swafford, Annu. Rev. Phys. Chem. **60**, 385 (2009).

31.   F. Caillez, G. Stirnemann, A. Boutin, I. Demachy and A. H. Fuchs, J. Phys. Chem. C **112**, 10435 (2008).

32.   J. H. Walther, R. Jaffe, T. Halicioglu and P. Koumoutsakos, J. Phys. Chem. B **105**, 9980 (2001).

33.   S. Javadian, F. Taghavi, F. Yari and S. M. Hashemianzadeh, J. Mol. Graph Model **38**, 40 (2012).

34.   D. A. Lockington and J. Parlange, J. Phys. D: Appl. Phys. **36**, 760 (2003).

35.   S. Daschakraborty and R. Biswas, ISRAPS Bull. **25**, 84 (2013).

36.   N. Galamba, J. Phys. Chem. B **118**, 4169 (2014).

37.   Y. L. A. Rezus and H. J. Bakker, Phys. Rev. Lett. **99**, 148301 (2007).

38.   D. Laage, G. Stirnemann and J. T. Hynes, J. Phys. Chem. B **113**, 2428 (2009).

39.   H. Wei, Y. Fan and Y. Q. Gao, J. Phys. Chem. B **114**, 557 (2010).

40.   K. Tielrooij, J. Hunger, R. Buchner, M. Bonn and H. J. Bakker, J. Am. Chem. Soc. **132**, 15671 (2010).

41.   T. Pradhan, P. Ghoshal and R. Biswas, J. Phys. Chem. A **112**, 915 (2008).

42.   T. Pradhan, P. Ghoshal and R. Biswas, J. Chem. Sci. **120**, 275 (2008).

43.   H. A. R. Gazi and R. Biswas, J. Phys. Chem. A **115**, 2447 (2011).

44.   S. Roy, S. Banerjee, N. Biyani, B. Jana and B. Bagchi, J. Phys. Chem. B **115**, 685 (2011).

45.   H. S. Frank and M. W. Evans, J. Chem. Phys. **13**, 507 (1945).

46.   M. H. H. Pomata, M. T. Sonoda, M. S. Skaf and M. D. Elola, J. Phys. Chem. B **113**, 12999 (2009).

47.   G. Stirnemann, F. Sterpone and D. Laage, J. Phys. Chem. B **115**, 3254 (2011).

48.   H. J. Bakker and J. L. Skinner, Chem. Rev. **110**, 1498 (2010).

49.   Y. L. A. Rezus and H. J. Bakker, J. Chem. Phys. **123**, 114502 (2005).

50.   J. D. Eaves, J. J. Loparo, C. J. Fecko, S. T. Roberts, A. Tokmakoff and P. L. Geissler, Proc. Natl. Acad. Sci. USA **102**, 13019 (2005).

51.   M. D. Fayer, Ann. Rev. Phys. Chem. **60**, 21 (2008).

52.   M. D. Fayer and N. E. Levinger, Ann. Rev. Anal. Chem. **3**, 89 (2010).

53.   A. Luzar and D. Chandler, Nature **379**, 55 (1996).

54.   A. Luzar and D. Chandler, Phys. Rev. Lett. **76**, 928 (1996).

55.   F. Sciortino, A. Geiger and H. E. Stanley, Nature **354**, 218 (1991).

56.   D. Laage and J. T. Hynes, Science **311**, 832 (2006).

57.   A. Luzar, Faraday Discuss. **103**, 29 (1996).

58.   T. C. Berkelbach, H. S. Lee and M. E. Tuckerman, Phys. Rev. Lett. **103**, 238302 (2009).

59.   A. Chandra, Phys. Rev. Lett. **85**, 768 (2000).

60.   S. Balasubramanian, S. Pal and B. Bagchi, Phys. Rev. Lett. **89**, 115501 (2002).

61.   A. Luzar and D. Chandler, J. Chem. Phys. **98**, 8160 (1993).

62.   Z. Xia, Z. Qiang and Z. Dong-Xia, Acta Phys. Chim. Sin. **27**, 2547 (2011).

63.   C. N. Pace and H. F. Marshall, Arch. Biochem. Biophys. **199**, 270 (1980).

64.   G. Barone, P. Del Vecchio, C. Giancola and G. G. Graziano, Thermochim. Acta **227**, 67 (1993).

65.   H. J. C. Berendsen, J. R. Grigera and T. P. Straatsma, J. Phys. Chem. **91**, 6269 (1987).

66.   M. P. Allen and D. J. Tildesley, *Computer simulations of liquids*. (Oxford University Press, New York, 1987).

67.   W. Smith, T. R. Forester and I. T. Todorov, *DL_POLY Classic*. (STFC Daresbury Laboratory, Daresbury, 2012).

68.   C. W. Yong, *DL_FIELD – a force field and model development tool for DL_POLY*. (STFC Daresbury Laboratory, Daresbury, 2010).

69.   A. Kuffel and J. Zielkiewicz, J. Chem. Phys. **133**, 035102 (2010).

70.   L. J. Smith, H. J. C. Berendsen and W. F. van Gunsteren, J. Phys. Chem. B **108**, 1065 (2004).

71. P. Belletato, L. C. G. Freitas, E. P. G. Arêas and P. S. Santos, Phys. Chem. Chem. Phys. **1**, 4769 (1999).

72. S. Nose, J. Chem. Phys. **81**, 511 (1984).

73. W. G. Hoover, Phys. Rev. A **31**, 1695 (1985).

74. J. P. Ryckaert, G. Ciccotti and H. J. C. Berendsen, J. Comput. Phys. **23**, 327 (1977).

75. A. P. Lyubartsev and A. Laaksonen, Comput. Phys. Commun. **128**, 565 (2000).

76. C. Okpala, A. Guiseppi-Elie and D. M. Maharajh, J. Chem. Eng. Data **25**, 384 (1960).

77. K. Sasaki and K. Arakawa, Bull. Chem. Soc. Jpn. **46**, 2738 (1973).

78. S. W. de Leeuw, J. W. Perram and E. R. Smith, Ann. Rev. Phys. Chem. **37**, 245 (1986).

79. G. A. Vidulich, D. F. Evans and R. L. Kay, J Phys Chem. **71**, 656 (1967).

80. Fernández DP, Mulev Y, Goodwin ARH and L. S. JMH., J. Phys. Chem. Ref. Data **24**, 33 (1995).

81. D. van der Spoel, P. J. van Maaren and H. J. C. Berendsen, J. Chem. Phys. **108**, 10220 (1998).

82. A. Fratiello, R. E. Lee, D. P. Miller and V. M. Nishida, Mol. Phys. **13**, 349 (1967).

83. J. P. Hansen and I. R. McDonald, *Theory of simple liquids*. (Academic Press, New York, 1986).

84. S. Daschakraborty and R. Biswas, J. Chem. Sci. **124**, 763 (2012).

85. D. Roy, N. Patel, S. Conte and M. Maroncelli, J. Phys. Chem. B **114**, 8410 (2010).

86. T. Pal and R. Biswas, Theor. Chem. Acc. **132**, 1348 (2013).

87. J. Habasaki and K. L. Ngai, J. Non-Cryst. Solids **352**, 5170 (2006).

88. P. Mark and L. Nilsson, J. Phys. Chem. A **105**, 9954 (2001).

89. E. P. G. Arêas, J. A. G. Arêas, J. Hamburger, W. L. Peticolas and P. S. Santos, J. Colloid Interface Sci. **180**, 578 (1996).

90. T. Pal and R. Biswas, Chem. Phys. Lett. **517**, 180 (2011).

91. B. Guchhait, S. Das, S. Daschakraborty and R. Biswas, J. Chem. Phys. **140**, 104514 (2014).

92. B. Guchhait, S. Daschakraborty and R. Biswas, The Journal of chemical physics **136**, 174503 (2012).

93. A. Das, S. Das and R. Biswas, Chem. Phys. Lett. **581**, 47 (2013).

94.   B. Guchhait, H. A. R. Gazi, H. K. Kashyap and R. Biswas, J. Phys. Chem. B **114**, 5066 (2010).

95.   E. Flenner and G. Szamel, Phys. Rev. E **72**, 011205 (2005).

96.   K. Kim and S. Saito, J. Chem. Phys. **133**, 044511 (2010).

97.   T. Pal and R. Biswas, J. Chem. Phys. **141**, 104501 (2014).

98.   S. Pal, S. Balasubramanian and B. Bagchi, Phys. Rev. E **67**, 061502 (2003).

99.   S. Pal, B. Bagchi and S. Balasubramanian, J. Phys. Chem. B **109**, 12879 (2005).

100.   M. Jana and S. Bandyapadhyay, J. Phys. Chem. B **115**, 6347 (2011).

101.   S. Pal and S. Bandyapadhyay, Langmuir **29**, 1162 (2013).

102.   S. K. Sinha and S. Bandyapadhyay, J. Chem. Phys. **135**, 135101 (2011).

103.   T. Strässle, A. M. Saitta, Y. Le Godec, G. Hamel, S. Klotz, J. S. Loveday and R. J. Nelmes, Phys. Rev. Lett. **96**, 067801 (2006).

104.   A. K. Soper and M. A. Ricci, Phys. Rev. Lett. **84**, 2881 (2000).

105.   G. Hummer, J. C. Rasaiah and J. P. Noworyta, Nature **414**, 188 (2001).

106.   Y. Xu, R. Gnanasekaran and D. M. Leitner, J. Atom. Mol. Opt. Phys., 125071 (2012).

107.   D. Laage and J. T. Hynes, Chem. Phys. Lett. **433**, 80 (2006).

Chapter 7

Is Dynamic Heterogeneity of Water in Presence of A Protein Denaturing Agent Different from that in Presence of A Protein Stabilizer? A Molecular Dynamics Simulation Study

7.1 Introduction

Trimethylamine-N-oxide (TMAO) is an amphiphile that can protect the volume of a living cell by preventing damage from external osmotic or hydrostatic pressure.[1,2] It has been found that TMAO is a better protein stabilizer than other osmolytes such as betaine, methylamine etc.[3,4] However, whether TMAO affects protein stability by directly interacting with protein[5,6] or via modification of water interaction and dynamics[7,8] is still under debate. Tetramethylurea (TMU), another amphiphilic molecule, acts as a protein destabilizer, and is a stronger denaturant than urea.[5,6] Interestingly, these two molecules are of similar size (r_{TMAO} ~3 Å and r_{TMU} ~3.5 Å, r being van der Waals radius)[9,10] although TMAO possesses a zwitterion structure while TMU is a dipolar amphiphile. Because of this difference in chemical nature, TMAO is a solid at room temperature whereas TMU is a liquid. TMAO contains three hydrophobic methyl groups, and a negatively charged oxygen atom which can accept more than two hydrogen bonds (H-bonds). TMU consists of four methyl groups, and a carbonyl oxygen which can form, on an average, H-bonds with two water molecules.[11] These contrasting scenarios have motivated, like in several previous works,[11-25] the present study where immobilization or extreme slowing down of water molecules at the interfaces of these two chemically different amphiphiles has been investigated and compared via molecular dynamics simulations.

A resurgence in this area has been created in the last several years by a series of femtosecond mid-infrared measurements[12-17] which investigated the reorientational dynamics of interfacial water molecules in aqueous solutions of TMAO and TMU and revisited the celebrated iceberg model[26]. These measurements indicated extreme slowing down of water molecules

that surround these solutes and this effective immobilization is independent of amphiphile concentration. These experiments reported, depending on the identity of the amphiphile, a slowing down of ~3–8 times for the interfacial water molecules over those in the bulk. However, the effects of solute clustering on the water dynamics were not examined in these studies although TMU is known to aggregate at very low concentrations[27] whereas TMAO remains unaggregated even at large concentrations[28]. Interestingly, subsequent ultrafast optical Kerr Effect measurements[11] indicated a much weaker slowing down (approximately a factor of 2) of the interfacial water molecules with no appreciable changes in the water structure. These Kerr effect spectroscopic results were supported by previous nuclear magnetic resonance (NMR) studies[29] and molecular dynamics simulations of jump reorientations of interfacial water molecules[19,20]. These simulation studies[19,20] also reported no significant decoupling between water translation and reorientation dynamics and suggested that the slow-down of water dynamics in such solutions occur primarily due to the confining effects at large amphiphile density. Among some very recent studies,[23,30-32] slowing down of dynamics of the hydrating water molecules has been explained in terms of reduced rate of switching of H-bond partners near hydrophobic groups[31], while another group has indicated that the slow-down in water/TMAO solutions arises from a strong H-bonding between water hydroxyl group and the oxygen atom of TMAO,[23] and argued that proper modelling of the negatively charged oxygen atom is very critical for such an observation. Respective roles of energetic and topological disorders for sub-diffusive translational water dynamics were investigated but dynamical heterogeneity aspect was not studied.

In this work, we have investigated and compared the interactions of TMAO and TMU with water molecules and the subsequent water dynamics in solutions of these chemically different solutes at various mole fractions (X_{Solute}) and at 298K. More specifically, dynamical heterogeneity (DH) in terms of non-Gaussian (NG) and new non-Gaussian (NNG) parameters[33,34] have been calculated both for the interfacial and bulk water molecules at different X_{Solute}, and compared. Simulated concentration dependent rotational and translational NG parameters[35,36] reveal concentration and solute dependences, indicating effects of these solutes on water structure. Computed particle displacement distributions for water molecules are strongly non-Gaussian for both the solutes at all concentrations. The ratio between the simulated rotational and translational diffusion coefficients of water

$\left(D_R / D_T\right)$ at various concentrations deviates strongly from the hydrodynamic predictions[37] for both TMAO and TMU. A weak slow-down of diffusive dynamics of interfacial water has been observed. The H-bond fluctuating timescales,[38-40] lengthen with solute concentration, also show strong solute dependence.

7.2 Computational Details

7.2.1 Force Field Description

We used SPC/E model of water[41] and specific force fields for TMAO[18,28] and TMU[24]. Detailed description of force field and model for TMU molecule has been provided in reference 24. In the rigid model of TMAO, interaction of different atomic sites of two different molecules is given by

$$U_{ij}\left(r_{ij}\right)=\sum_{i<j}\left\{4\varepsilon_{ij}\left[\left(\frac{\sigma_{ij}}{r_{ij}}\right)^{12}-\left(\frac{\sigma_{ij}}{r_{ij}}\right)^{6}\right]+\frac{q_i q_j}{4\pi\varepsilon_0 r_{ij}}\right\}. \qquad (7.1)$$

Here, the nonbonded interactions are included by Lennard–Jones potential and Coulomb interaction. ε, σ, r are the potential well depth, van der Waals radius, and distance between atoms respectively. The parameter q represents the partial charge of the atom and ε_0 the static dielectric constant. Lennard–Jones interactions between unlike atoms are calculated by the Lorentz–Berthelot combining rules[42] where

$$\varepsilon_{ij}=\sqrt{\varepsilon_i \varepsilon_j} \ , \quad \sigma_{ij}=\frac{\sigma_i+\sigma_j}{2}. \qquad (7.2)$$

7.2.2 Simulation Procedures

A total of 512 (solute+solvent) molecules in a cubic box with periodic boundary condition were simulated first using the NPT ensemble at ambient condition and employing the DL_POLY_Classic[43] with the Hoover thermostat and barostat relaxation times of 2 ps and 0.5 ps respectively. A 2 ns simulation in this ensemble was necessary to produce the experimental density. The final configuration simulated via this NPT ensemble was then used as the initial

configuration for NVT ensemble at the ambient condition using the Nose–Hoover[44,45] thermostat with relaxation time of 0.5 ps. Then a 5 ns simulation run was completed in which first 1 ns run was considered for further equilibration in the NVT ensemble, and the last 4 ns run was analyzed for results. Equations of motion were solved by Leapfrog–Verlet algorithm[42] with time step of 1 fs. Verlet neighbour list shell width was set to 1.2 Å. Trajectories were saved after each 10 fs. Cut off radius was set nearly to the half of the box length. Statistics data were saved after each 5 time steps. The SHAKE algorithm[46] was employed to constrain all the bonds involving hydrogen atoms. Ewald summation technique[42] was used for treating the electrostatic interactions.

7.3 Results and Discussion

7.3.1 Solvation Structure in the Binary Mixture

In both the (TMAO+Water) and (TMU+Water) systems, water hydrogen atoms, H(W) can form H-bonds with the oxygen atoms of TMAO and TMU, O(TMAO) and O(TMU) respectively. Figure 7.1 represents the effect of gradual increase of TMAO mole fraction, X_{TMAO}, into water on the radial distribution functions (RDFs) involving O(W)–H(W) (upper panel) and O(TMAO)–H(W) (lower panel) pairs as a function of distance, r. Clearly, addition of TMAO increases g(r) peak intensities for both the O(W)–H(W) and O(TMAO)–H(W) distributions, keeping the peak positions unchanged. This suggests that the H-bonding interactions between water–water and water–TMAO increases upon addition of TMAO into water. Similar behaviour was also observed earlier for g(r) describing O(W)–H(W) and O(TMU)–H(W) RDFs in TMU–Water mixtures.[24] Note also that the g(r) peak intensity of O(TMAO)–H(W) is uniformly higher (~80%) at each X_{TMAO} than the corresponding O(W)–H(W) RDF. This is probably due to the enhanced electrostatic interaction because of the negative charge on the oxygen atom in TMAO. This was not found for TMU–Water systems.[24] Figure 7.A.1 (Appendix 7.A) presents the RDFs corresponding to the interaction between oxygen atoms of water–water, water–solute and solute–solute for both the (TMAO+Water) and (TMU+Water) systems. We found that for the same concentration, O(W)–O(W) g(r) peak intensity is slightly lower in the binary mixture of TMAO+Water than that of TMU+Water. This effect is opposite for O(W)–O(Solute) interaction for both the systems. As we previously mentioned that enhanced electrostatic property of TMAO

molecules drives them to interact more strongly with water.
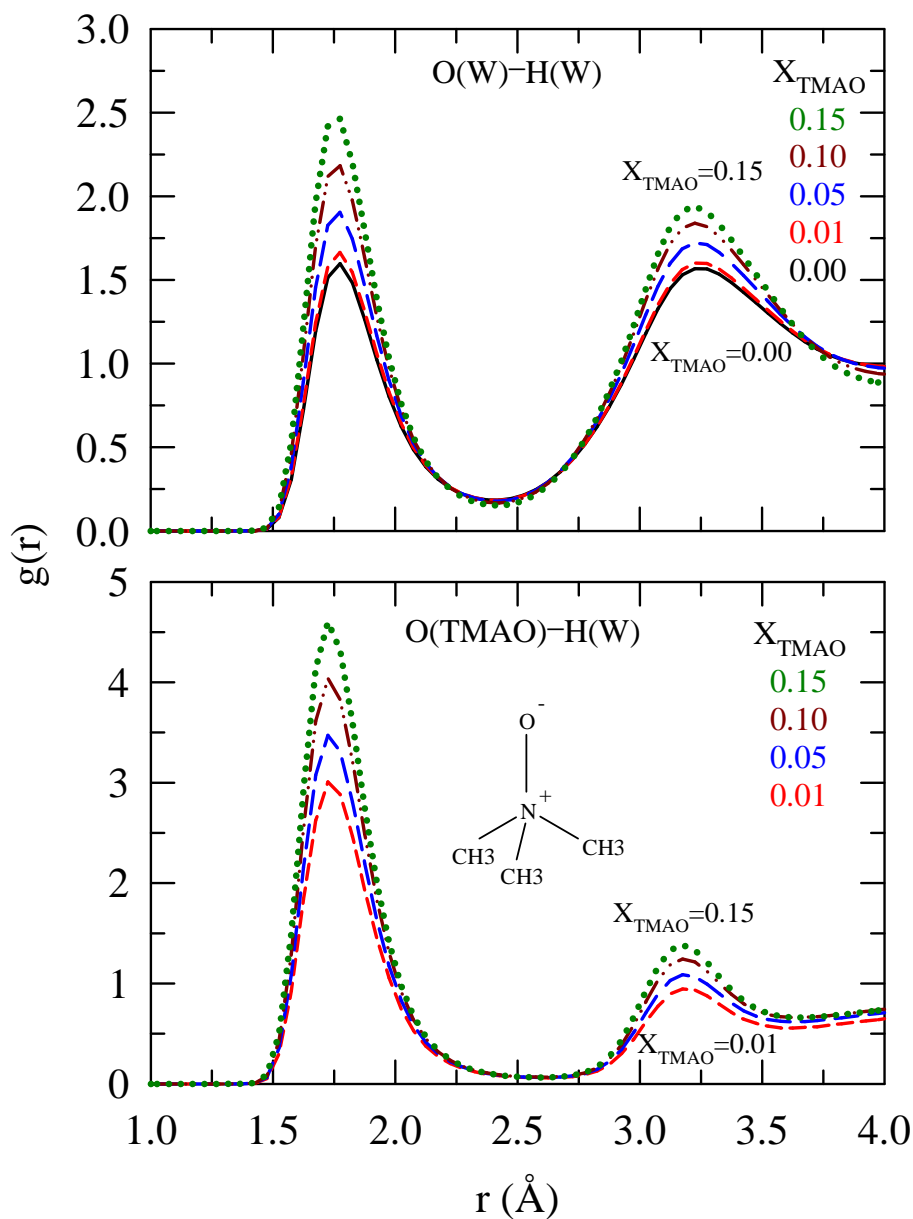
Figure 7.1: Site–site radial distribution functions, g(r), between different atomic pairs as a function of distance, r, at various TMAO mole fractions, X_{TMAO}. Color codes and line styles are as follows: black solid: pure water, red short-dash: 0.01, blue medium-dash: 0.05, dark red dash-dot-dot: 0.10, dark green dot: 0.15. Chemical structure of TMAO is also shown as inset of the lower panel.

Figure 7.2 shows the first peak intensities of O(W)–H(W) and O(Solute)–H(W) RDFs as a function of X_{Solute} for both the (TMAO+Water) and (TMU+Water) systems. Clearly, water–water H-bond interaction is stronger in TMU+Water systems than that in TMAO+Water system and the latter shows relatively greater water–solute H-bond interaction. This is again a reflection of relatively stronger interaction of TMAO with water than TMU for their different charge distributions.
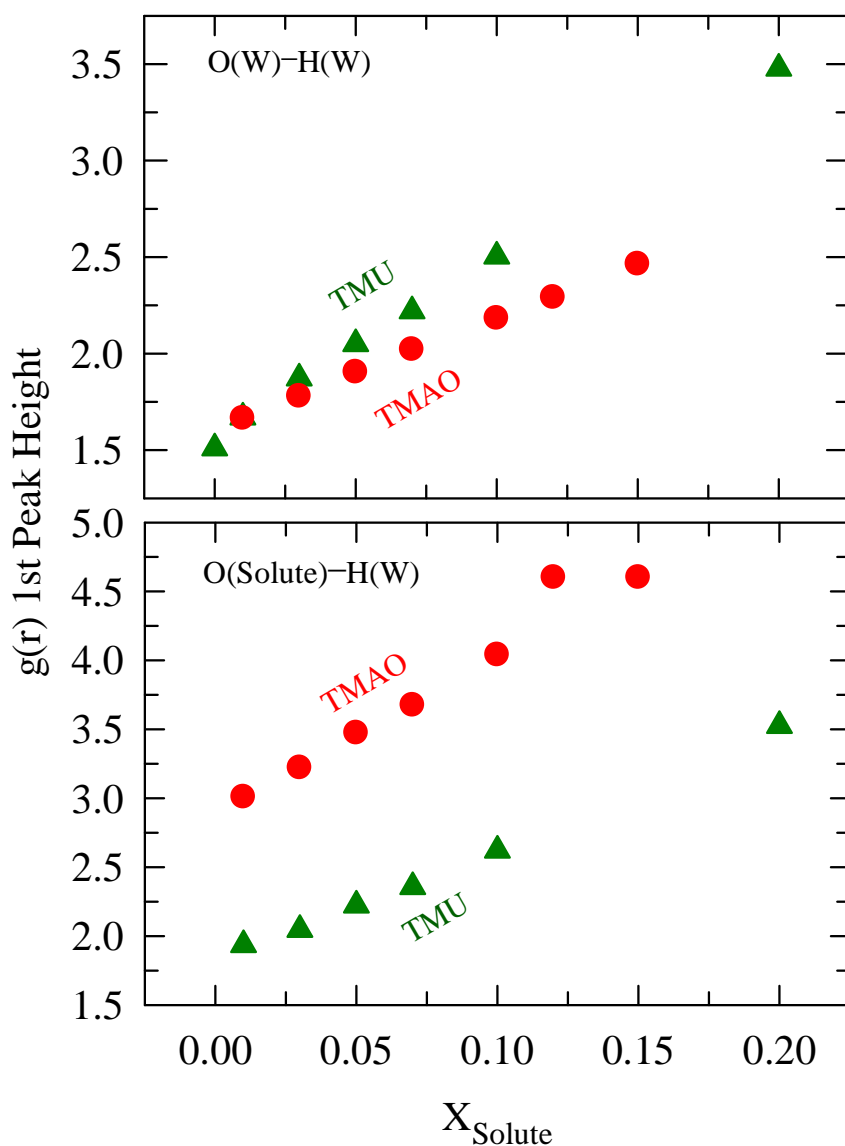
Figure 7.2: Height of the first peak of simulated g(r) as a function of X_{Solute}. Red solid circles and dark green solid triangles represent (TMAO+Water) and (TMU+Water) mixtures, respectively.

RDFs describing interaction among methyl groups of solute molecules in these aqueous solutions are shown in Figure 7.A.2 (Appendix 7.A). Note that for aqueous solutions of TMAO, Me–Me g(r) grows slowly with X_{TMAO} which is probably due to the gradual rise in solute density with increase of X_{TMAO} in the solution (higher g(r) peak intensity at $X_{TMAO} = 0.01$ indicates nothing but poor averaging). For TMU solutions, in contrast, the corresponding RDF shows intense peak at $X_{TMU} = 0.01$ and then falls of abruptly upon increasing X_{TMU}. This is a reflection of TMU aggregation at very low concentration.[27] All these suggest that TMAO molecules possess higher propensity to interact with water than among themselves. This is further confirmed from N(TMAO)–O(TMAO) RDF shown in Figure 7.A.3 (Appendix 7.A). TMU molecules also prefer to interact with water than among themselves but to a lesser extent compared to what TMAO does with water.

7.3.2 Rotational and Translational Diffusions of Water

Rotational diffusion coefficient, D_R, and translational diffusion coefficient, D_T, for water molecules in these aqueous binary mixtures have been calculated by using the following equations.[35-37,47]

$$D_R = \left[\frac{1}{4t} \left(\left\langle \left| \Delta \vec{\phi}_i(t) \right|^2 \right\rangle \right) \right]_{t\to\infty} = \left[\frac{1}{4t} \left\{ \frac{1}{N} \left\langle \sum_{i=1}^{N} \left| \vec{\phi}_i(t) - \vec{\phi}_i(0) \right|^2 \right\rangle \right\} \right]_{t\to\infty} , \qquad (7.3)$$

$$D_T = \left[\frac{1}{6t} \left(\left\langle \left| \Delta \vec{r}(t) \right|^2 \right\rangle \right) \right]_{t\to\infty} = \left[\frac{1}{6t} \left\{ \frac{1}{N} \left\langle \sum_{i=1}^{N} \left| \vec{r}_i(t) - \vec{r}_i(0) \right|^2 \right\rangle \right\} \right]_{t\to\infty} . \qquad (7.4)$$

Here, $\left\langle \left| \Delta \vec{\phi}_i(t) \right|^2 \right\rangle$ is the rotational mean squared displacement (RMSD) of –OH bond vector and $\left\langle \left| \Delta \vec{r}(t) \right|^2 \right\rangle$ is the translational mean squared displacement (MSD) of oxygen atom of water.
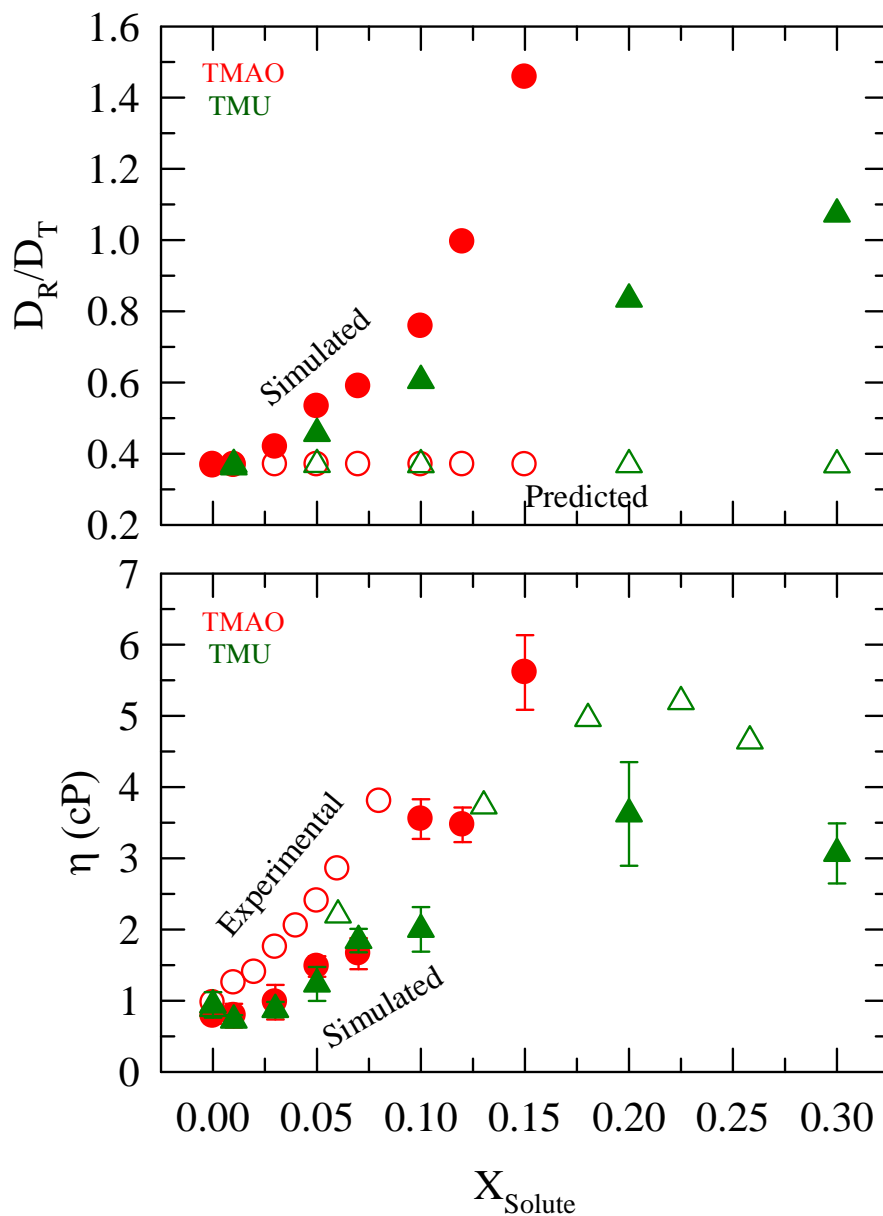
Figure 7.3: X_{Solute} dependence of the ratio between the rotational and translational diffusion coefficients, D_R / D_T (upper panel) , and viscosity coefficients, η (lower panel), for aqueous solutions of TMAO and TMU. Predictions from stick hydrodynamics (upper panel), and experimental η for these solutions (lower panel) are also shown. Experimental[24,48] and simulated η are represented by the open and solid symbols, respectively. Red represents TMAO and dark green TMU. Note the ratio, D_R / D_T, is scaled by $(\text{Å}^{-1})^2$.

Simulated X_{Solute} dependent RMSDs and MSDs are shown in Figure 7.A.4 (Appendix 7.A) in log–log scale for an expanded view of the short time dynamical behaviour. The ratio between D_R and D_T of water molecules, D_R/D_T, calculated from the slopes of these simulated RMSDs and MSDs, respectively, are presented in the upper panel of Figure 7.3. Hydrodynamic predictions[37] for the ratio, D_R/D_T, using the simulated viscosity coefficients (η) and stick boundary condition (assuming water being spherical, $D_R/D_T = 3/4\,r^2$, r being the diffuser radius) are also shown in the same panel for a comparison. Note the deviation from hydrodynamics is quite strong, particularly at large X_{Solute}. This insufficiency of hydrodynamics may imply aqueous dynamics being heterogeneous for these amphiphile solutions. Larger deviation from hydrodynamics at higher TMAO concentrations in binary mixture of TMAO+Water as compared to TMU+Water indicates that TMAO perturbs the water dynamics to a greater extent than TMU. Simulated η using the method described earlier[24] is compared to the experimental data[48] in the lower panel which shows that the present simulations can reproduce only qualitatively the experimental X_{Solute} dependence of η for these solutions. This, however, does not affect the hydrodynamic predictions for the X_{Solute} dependent D_R/D_T as η cancels out.

Next we simulate RMSDs and MSDs for those water molecules which reside within 5 Å radius of a solute (TMAO or TMU) at initial time in these solutions at different concentrations in order to explore the extent of slowing down for interfacial water molecules. Various RDFs simulated for these water molecules indicate ~20–25 water molecules within such a shell which agrees well with the experimentally estimated[11] total number of water molecules in the first solvation shells of these solutes. Figure 7.4 shows the X_{Solute} dependent RMSDs for interfacial and bulk water molecules. As rotation is faster than translation, D_R for interfacial water has been calculated within 10 ps time window, whereas D_T for the same has been calculated within 20 ps time window. The translational MSDs are presented in Figure 7.A.5 (Appendix 7.A). Table 7.B.1 (Appendix 7.B) compares the interfacial and bulk diffusion coefficients for these solutes which suggest the interfacial effects being stronger for rotation than translation. These data therefore clearly indicate that water molecules which are at the interfaces of these solutes diffuse at a slower rate than those in the bulk. This is in

general agreement with earlier experimental[11-17] and simulation[19,20] findings. However, the extent of slowing down found here is much less, the interfacial diffusion coefficients being always within ~20-30% of those simulated for the bulk. As pointed out in a very recent work,[23] inadequate representation of charge distributions in the water model used here may be responsible for such a small interfacial effects.
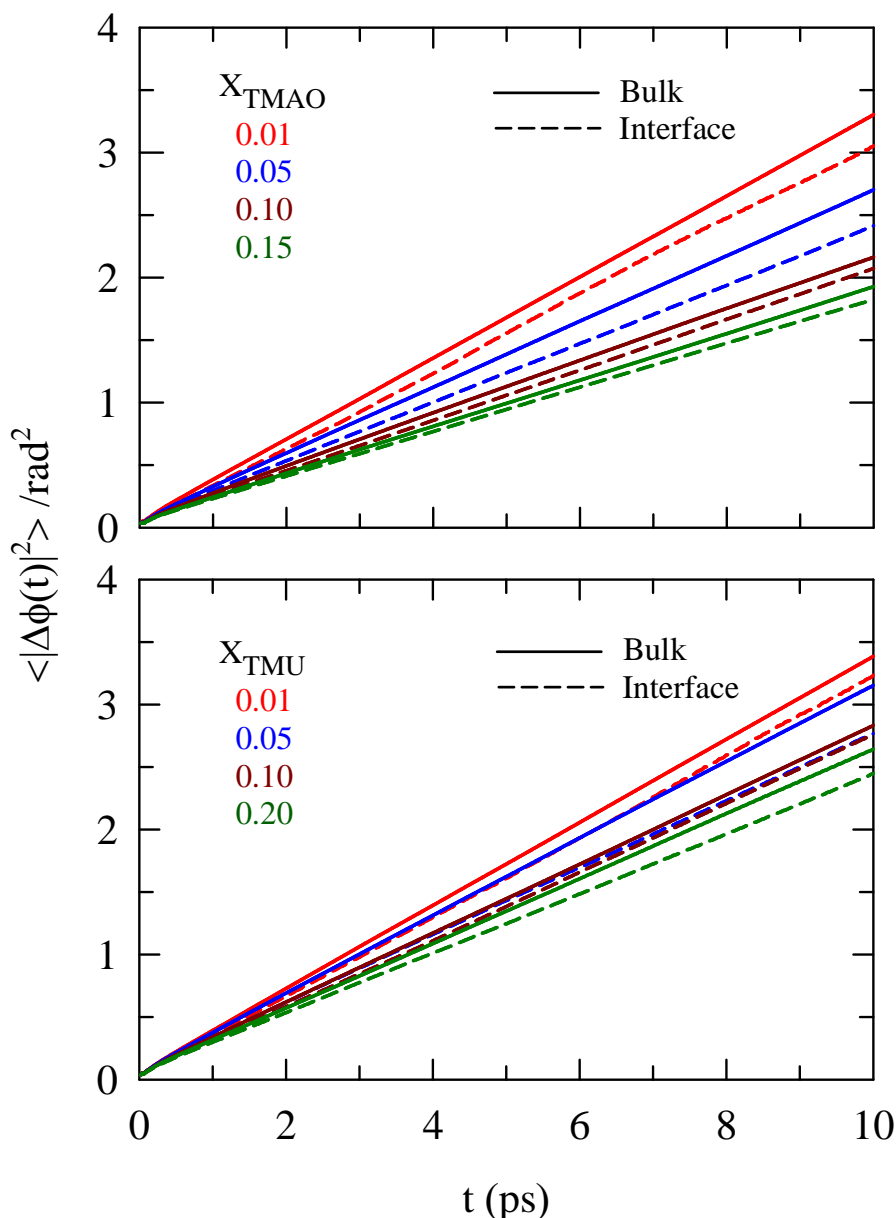
Figure 7.4: Plot of rotational mean squared displacement (RMSD), $\left\langle |\Delta\phi(t)|^2 \right\rangle$ with time, t for bulk solution (solid lines) and interfacial (dashed lines) water –OH bond at four different X_{Solute}. Representations are colour coded.

7.3.3 Rotational and Translational Dynamic Heterogeneity

The time-dependent self part of the rotational van Hove correlation function $[G_s(\theta,t)]$ for angular displacements of –OH bond of water is shown in Figure 7.5 for solutions of both the solutes at several different X_{Solute}. Corresponding calculated Gaussian distributions are also shown in both the panels. $G_s(\theta,t)$ has been calculated at times $[\tau^r_{NG}]$ when rotational NG parameter $[\alpha^r_2(t)]$ reaches the maximum. A comparison between the simulated and calculated distributions reflects deviations from the Gaussian behaviour, suggesting heterogeneous distributions of angular displacements of water molecules in solutions of both TMAO and TMU. The peak of $G_s(\theta,t)$ for pure water appears at an angle 30^0 which hardly changes (maximum 4^0) with X_{Solute}. This indicates that solute molecules do not have significant effect on the orientation angle of water.

A closer view of the dynamic heterogeneity (DH) of these solutions can be accessed by computing the NG and NNG parameter from these angular and centre-of-mass displacements. For example, the rotational NG parameter, $\alpha^r_2(t)$, obtained via the expression

$$\alpha^r_2(t) = \frac{3}{5}\frac{\langle \Delta\phi^4(t)\rangle}{\langle \Delta\phi^2(t)\rangle^2} - 1, \qquad (7.5)$$

with $\langle \Delta\phi^2(t)\rangle = \langle |\Delta\vec{\phi}_i(t)|^2\rangle$, and $\langle \Delta\phi^4(t)\rangle = \langle |\Delta\vec{\phi}_i(t)|^4\rangle$, is presented in Figure 7.6 for interfacial (dash-dot-dot lines) and bulk (solid lines) water molecules in aqueous solutions at various X_{Solute}. The non-monotonic time dependence with a large non-zero peak value of $\alpha^r_2(t)$ suggests presence of strong DH in both the systems. A closer inspection of these curves reveals that the peak beyond 100 fs of $\alpha^r_2(t)$ at different X_{Solute} is occurring at a relatively longer time for TMAO than TMU. In addition, $\alpha^r_2(t)$ peak heights for concentrated TMAO solutions are larger than for concentrated TMU solutions, suggesting stronger DH for concentrated TMAO solutions. This is due to stronger water–TMAO interaction. Figure 7.7 depicts the corresponding translational NG parameter, $\alpha^t_2(t)$, which have been obtained by
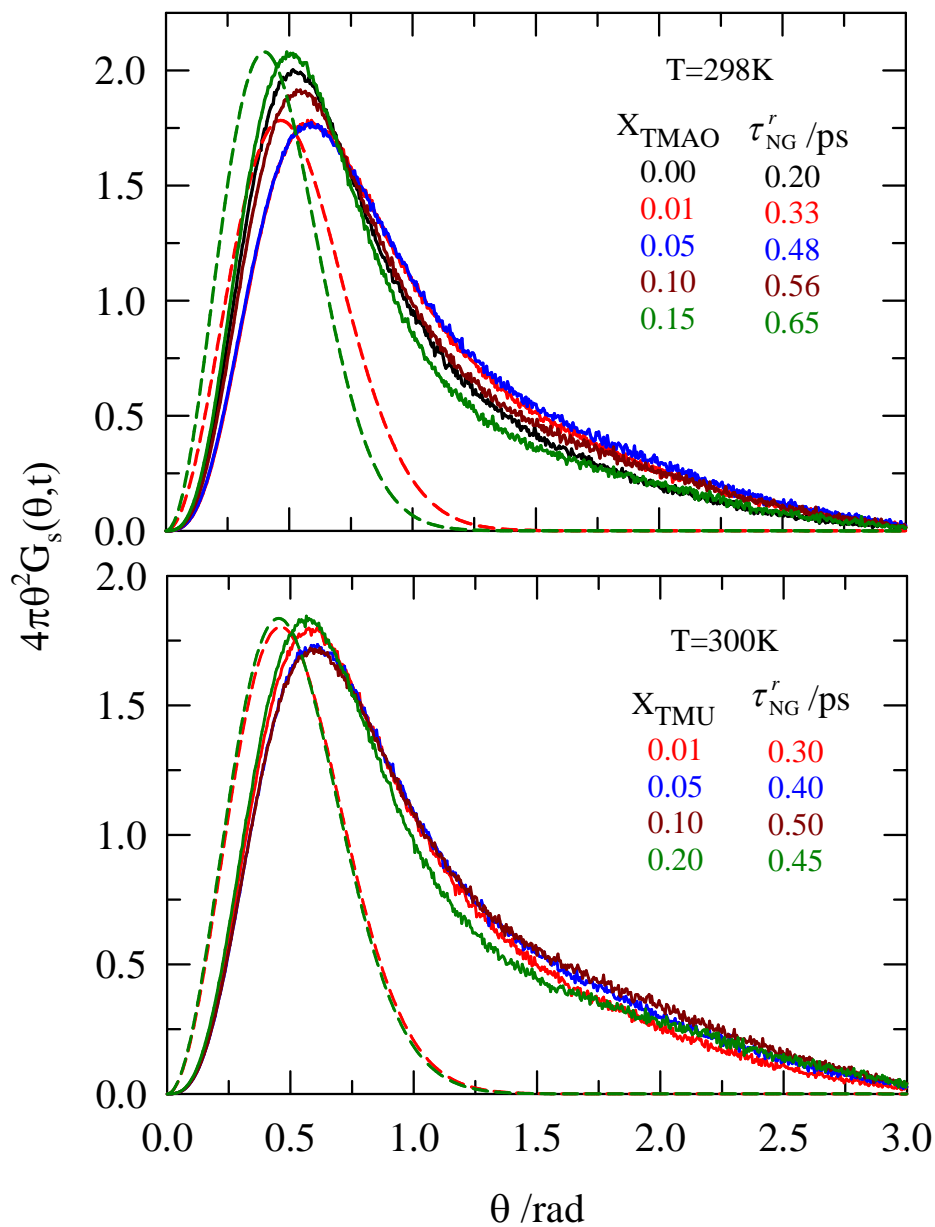
Figure 7.5: Angular distribution of time-dependent rotational van Hove self correlation function, $G_s(\theta,t)$ for water –OH bond. Dashed lines represent simulated distributions and the solid lines depict the corresponding Gaussian distribution. The times at which these distributions were determined are shown in both the panels. Representations are colour-coded.
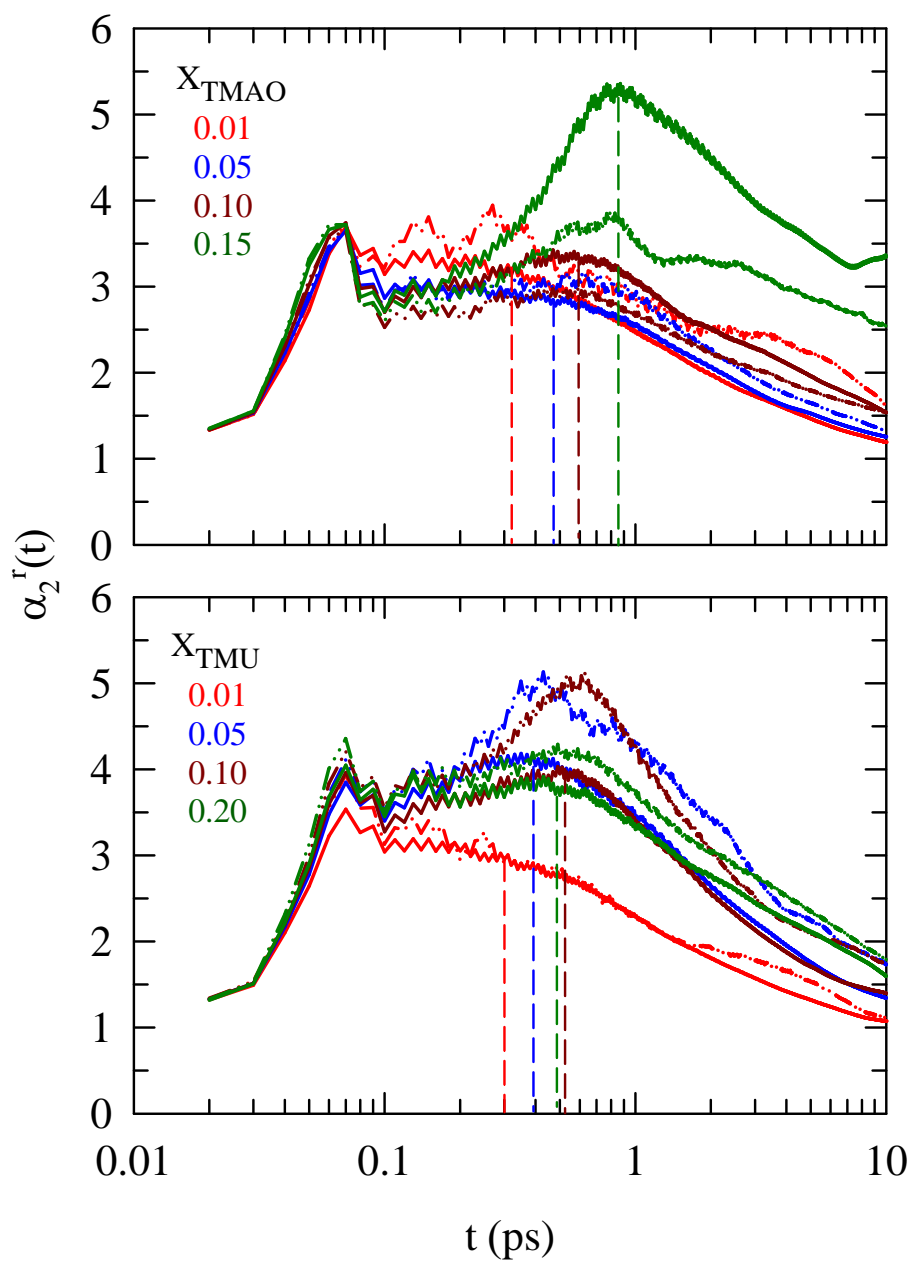
Figure 7.6: Time-dependent rotational non-Gaussian parameter, $\alpha_2^r(t)$, for bulk solution (solid lines) and interfacial (dash-dot-dot lines) water –OH bond at different concentrations of TMAO (upper panel) and TMU (lower panel) in water. Vertical dashed lines indicate peak positions of $\alpha_2^r(t)$ on time axis for bulk solutions. Representations are colour-coded.
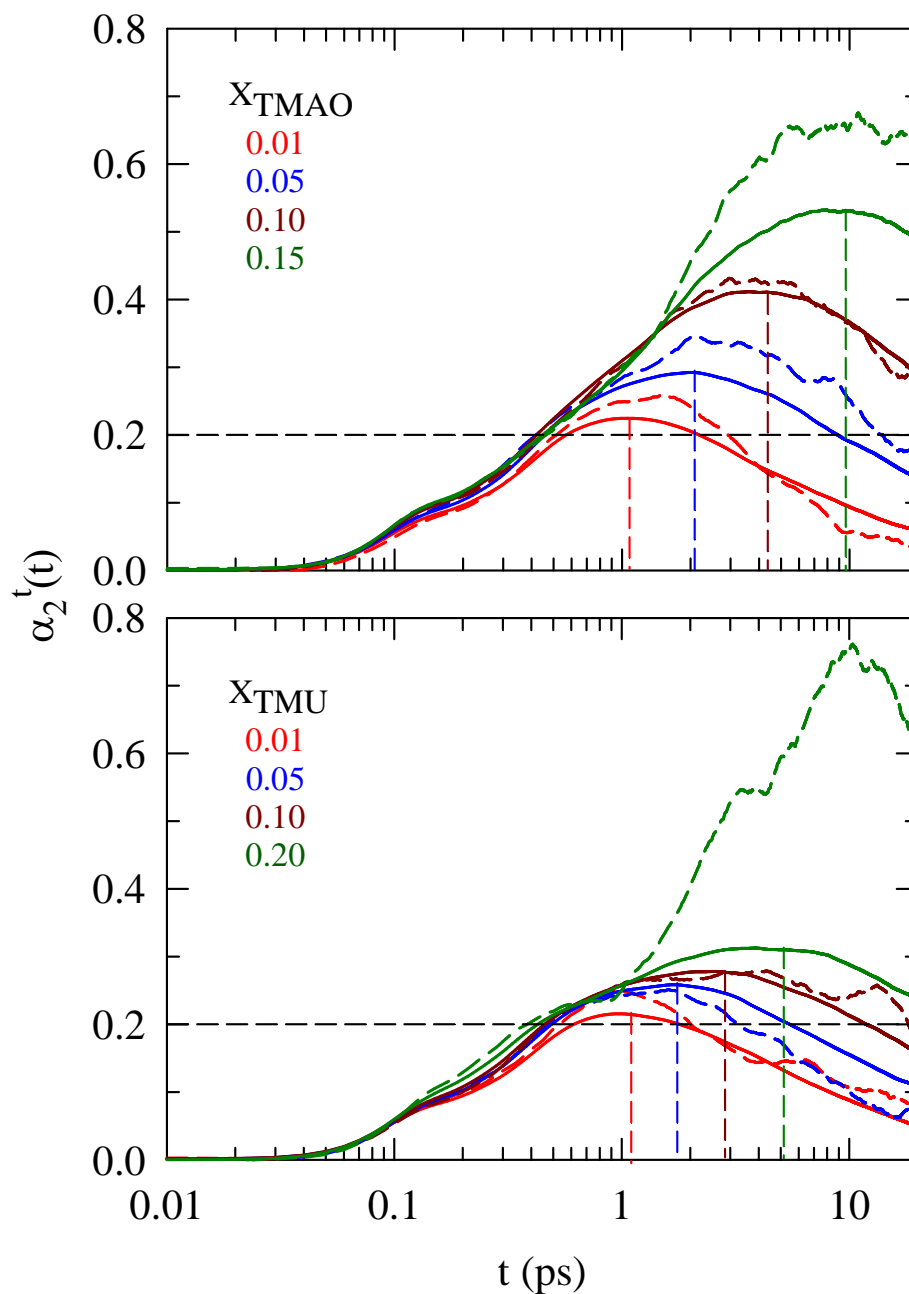
Figure 7.7: Distribution of translational non-Gaussian parameter, $\alpha_2(t)$ of bulk (solid lines) and interfacial (dash-dot-dot lines) water with time, t for different concentrations of TMAO (upper panel) and TMU (lower panel). Vertical dashed lines are drawn for each solute concentration to show the corresponding peak positions of $\alpha_2(t)$ for bulk water.

using equation 7.5 after replacing $\left\langle \Delta\phi^2(t) \right\rangle$ and $\left\langle \Delta\phi^4(t) \right\rangle$ by $\left\langle \Delta r^2(t) \right\rangle$ and $\left\langle \Delta r^4(t) \right\rangle$, respectively. Similar non-monotonic dependence has been observed at all the X_{Solute}, with peak times $\left(\tau_{NG}^t \right)$ occurring at longer times for TMAO than TMU. τ_{NG}^t also shifts to longer timescale with X_{Solute}. This suggests that the X_{Solute} dependent DH timescales in TMAO solutions are longer than those in TMU solutions. Also, $\alpha_2^t(t)$ peak heights for TMAO solutions are uniformly larger at all these X_{Solute} than for TMU solutions, revealing more heterogeneous water dynamics in presence of TMAO than TMU.

For further characterization of DH, we have calculated the translational NNG parameter,[34] $\gamma(t)$, for these solutions at various X_{Solute} by equation 6.7 of chapter 6 and shown in Figure 7.A.6 and 7.A.7 (Appendix 7.A). As observed for $\alpha_2^t(t)$, here also the peak-time $\left(\tau_{NNG}^t \right)$ shifts to longer time with X_{Solute}, and also for changing the TMU solutions to TMAO solutions. Peak-times slower than those in $\alpha_2^t(t)$ appears, suggesting that the DH can persist over a timescale longer than those reflected by τ_{NG}^t. Figure 7.8 presents a comparison between the X_{Solute} dependent τ_{NG}^t and τ_{NNG}^t which indicate presence of similar DH timescales for both the systems at low solute concentrations. But there are significantly longer peak-times for TMAO solutions at higher concentrations. Interestingly, these solution DH timescales increase with increase of X_{Solute}, and can even become approximately an order of magnitude longer than those obtained for neat ambient water[24].
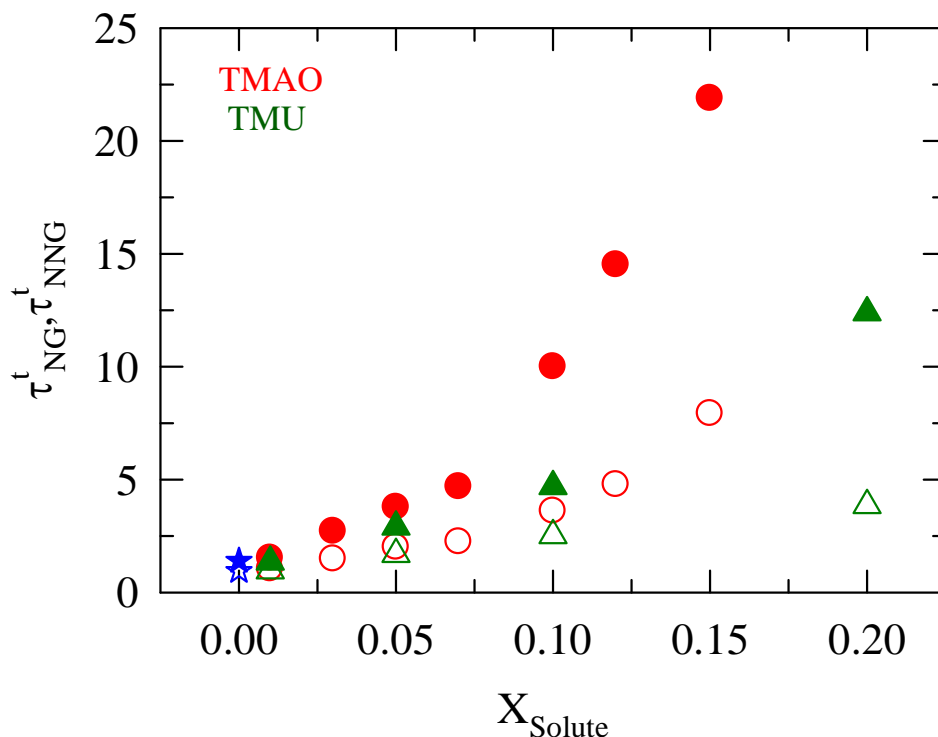
Figure 7.8: X_{Solute} dependence for the peak-times of the translational non-Gaussian parameter (τ_{NG}^{T}) and the new non-Gaussian parameter (τ_{NNG}^{T}) for (water + TMAO) and (water + TMU) systems. Filled symbols represent τ_{NNG}^{T} and open symbols τ_{NG}^{T}. Representations are colour-coded. τ_{NG}^{T} and τ_{NNG}^{T} for ambient water are also shown by stars (blue).

DH signatures for water molecules in these solutions can be further examined by investigating the probability distributions of logarithm of the single particle displacements at any given time, $P[\log_{10}(\delta r); t]$, which can be readily obtained from the self part of the van Hove correlation function, $G_s(\delta r, t)$ (see equation 6.8 of chapter 6). For a Gaussian $G_s(\delta r, t)$, $P[\log_{10}(\delta r); t]$ becomes independent of time and attains a peak height of ~2.13.[34] Figure 7.9 depicts the X_{Solute} dependent $P[\log_{10}(\delta r); t]$ obtained from the corresponding simulated $G_s(\delta r, t)$ for water molecules in TMAO and TMU containing solutions. The deviation from Gaussian behaviour is quite evident for both the solutions and the extent of deviation increases upon increasing the solute concentration in the solution.
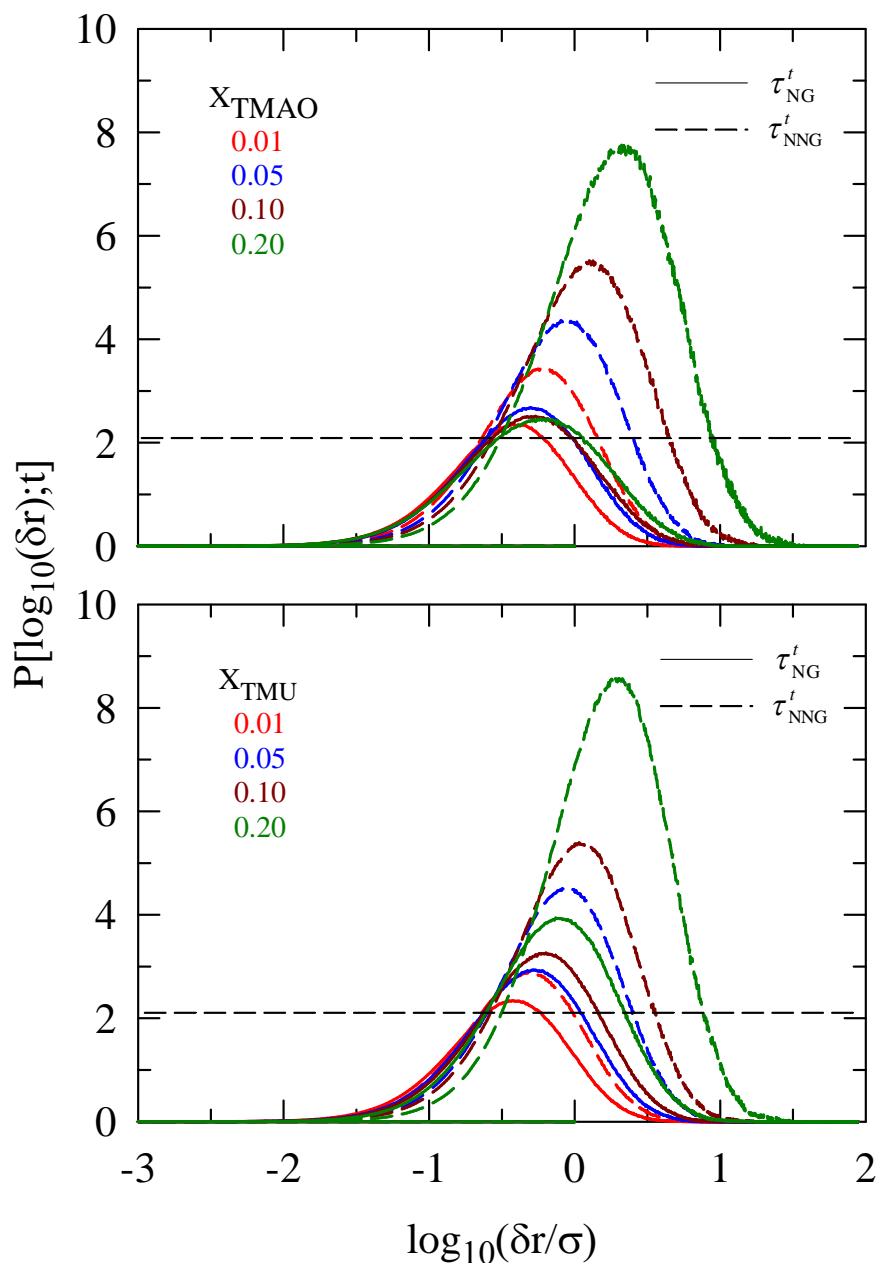
Figure 7.9: X_{Solute} dependence of the simulated single particle displacement distributions, $P[\log_{10}(\delta r);t]$ for water in TMAO (upper panel) and TMU (lower panel) solutions at the peak-times of NG (solid line) and NNG (dashed lines) parameters. Representations are, as before, colour-coded. The height of the $P[\log_{10}(\delta r);t]$ corresponding to a Gaussian $G_s(\delta r,t)$ at these times is shown by horizontal broken lines.

7.3.4 Hydrogen Bond Relaxation Dynamics

It would be interesting to investigate the H-bond relaxation timescales in such dynamically heterogeneous environments where one of the specie (TMAO here) interacts more strongly than the other (TMU). The H-bond relaxation time has been calculated by two different correlation functions: H-bond lifetime relaxation $S_{HB}(t)$ and H-bond structural relaxation $C_{HB}(t)$.[38-40] Here, we have applied the same geometric criteria as used before.[24] Figure 7.A.8 (Appendix 7.A) shows the decay of $S_{HB}(t)$ and $C_{HB}(t)$ for water–water and water–TMAO H-bonding at various TMAO mole fractions along with the fitting. Bi-exponential and tri-exponential functions were required to fit these $S_{HB}(t)$ and $C_{HB}(t)$ decays respectively. Similar multi-exponential behaviour for these relaxation functions were also observed earlier for aqueous TMU solutions.[24] Fitting parameters are summarized in Table 7.B.2–7.B.5 (Appendix 7.B). In Figure 7.10, average relaxation times $\left\langle \tau_{S/C}^{HB} \right\rangle$ for water–water and water–TMAO H-bonds at different X_{TMAO} are shown and compared the ratio between the average H-bond relaxation timescales at a given concentration for TMAO and TMU solutions, $\left\langle \tau_{S/C}^{HB} \right\rangle^{TMAO} \Big/ \left\langle \tau_{S/C}^{HB} \right\rangle^{TMU}$, for the common concentration range. As observed before in (TMU+Water) system,[24] there is a slowing down of $\left\langle \tau_{S/C}^{HB} \right\rangle$ for water–TMAO H-bonding as compared to water–water H-bonding and with increase of X_{TMAO}. The X_{Solute} dependent ratio of average times shown in this figure is always greater than unity. This clearly indicates that H-bonds in TMAO+Water system are longer-lived than in TMU+Water system. Increase of this ratio with X_{TMAO} also suggests that TMAO has larger confining ability for water than TMU. More than two-times of maximum lengthening of H-bond fluctuation timescales have been observed on moving from TMU to TMAO solutions. Here, H-bond relaxation dynamics nicely correlates with what we found from solvation structure that hydrophilic group of TMAO (the oxygen) interacts, on an average, more strongly with water than the corresponding group (the oxygen) of TMU. This has also been the observation for various DH parameters investigated in this work.
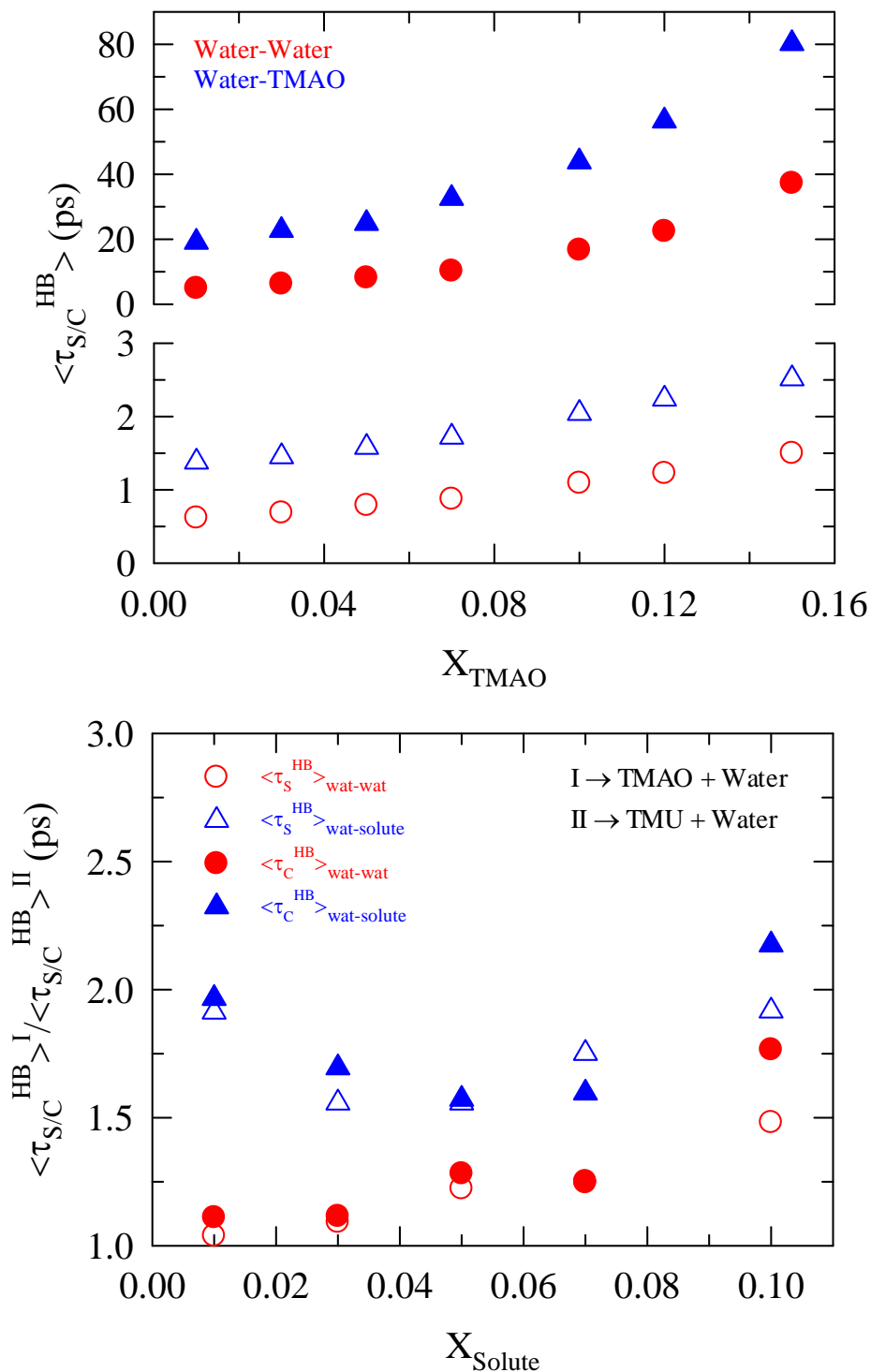
Figure 7.10: Plot of average times for H-bond lifetime and structural relaxation at different X_{TMAO} (upper panel) and the ratio of average times obtained from $S_{HB}(t)$ and $C_{HB}(t)$ decay in both TMAO–Water and TMU–Water binary mixtures (lower panel). Average timescales from $S_{HB}(t)$ and $C_{HB}(t)$ decay are shown by open and filled symbols respectively. Red circles and blue triangles represent water–water and water–solute H-bonding respectively.

7.4 Conclusion

In conclusion, DH in (Water + TMAO) and (Water + TMU) solutions are found to be moderately different although these two solutes are entirely different in their chemical nature and biological actions. The zwitterionic property of TMAO does induce enhanced interaction with water molecules compared to that observed for TMU but this has no bearing on the simulated DH timescales and single particle distributions at low solute concentrations. But in concentrated solutions, these two solutes show markedly different DH timescales. Interfacial diffusion coefficients have been found to be somewhat smaller than those for bulk solutions, agreeing qualitatively with the existing experimental and simulation results. The extent of slowing down is, however, small (~20-30% at the most) which may be due either to the insufficient modelling of charge distributions for the SPC/E water and solutes employed in the present study or to the choice of the interfacial region (~5 Å) implemented here. A closer inspection of simulated DH parameters appears to reveal that aqueous TMAO solutions are more dynamically heterogeneous than the TMU counter-part. This may be due to enhanced water–TMAO interaction for the different charge distribution of TMAO, affecting the water dynamics more strongly. Simulated H-bond relaxation timescales have also been found to be longer-lived in all the TMAO solutions. Similar investigation on (water + alcohol) system[49] would be useful to understand the impact of alcohol aggregation on water dynamics. But one must be very cautious about the choice of TMAO model since flexible model of TMAO[50] provided comparatively fast dynamics which has been shown and compared with the present results in Appendix 7.C.

Appendix 7.A
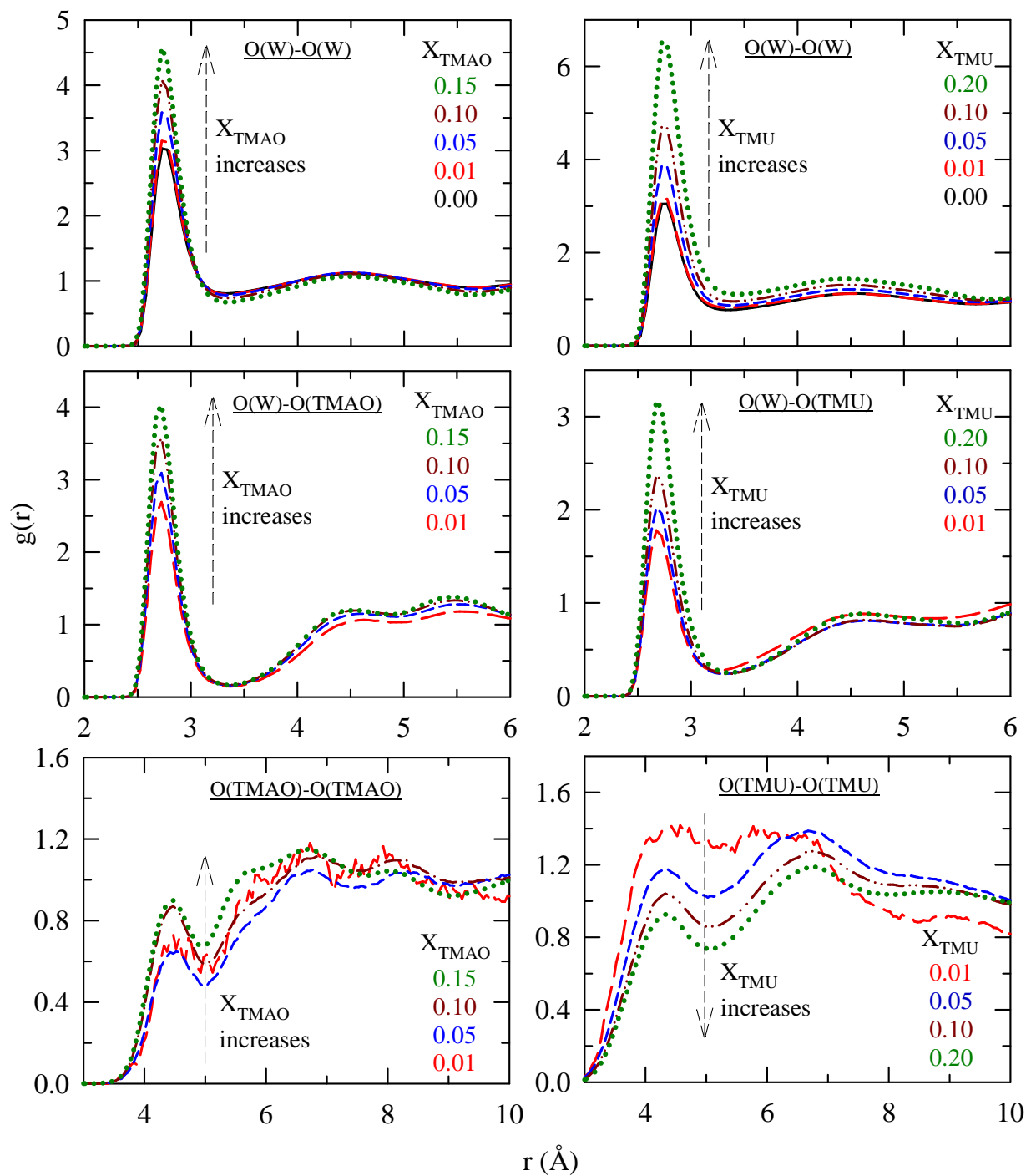
Figure 7.A.1: Site–site radial distribution functions (RDFs), g(r), between different atomic pairs at various concentrations of TMAO and TMU in water as a function of distance, r. Atomic sites are shown at the top of the each panel. Representations are colour-coded.
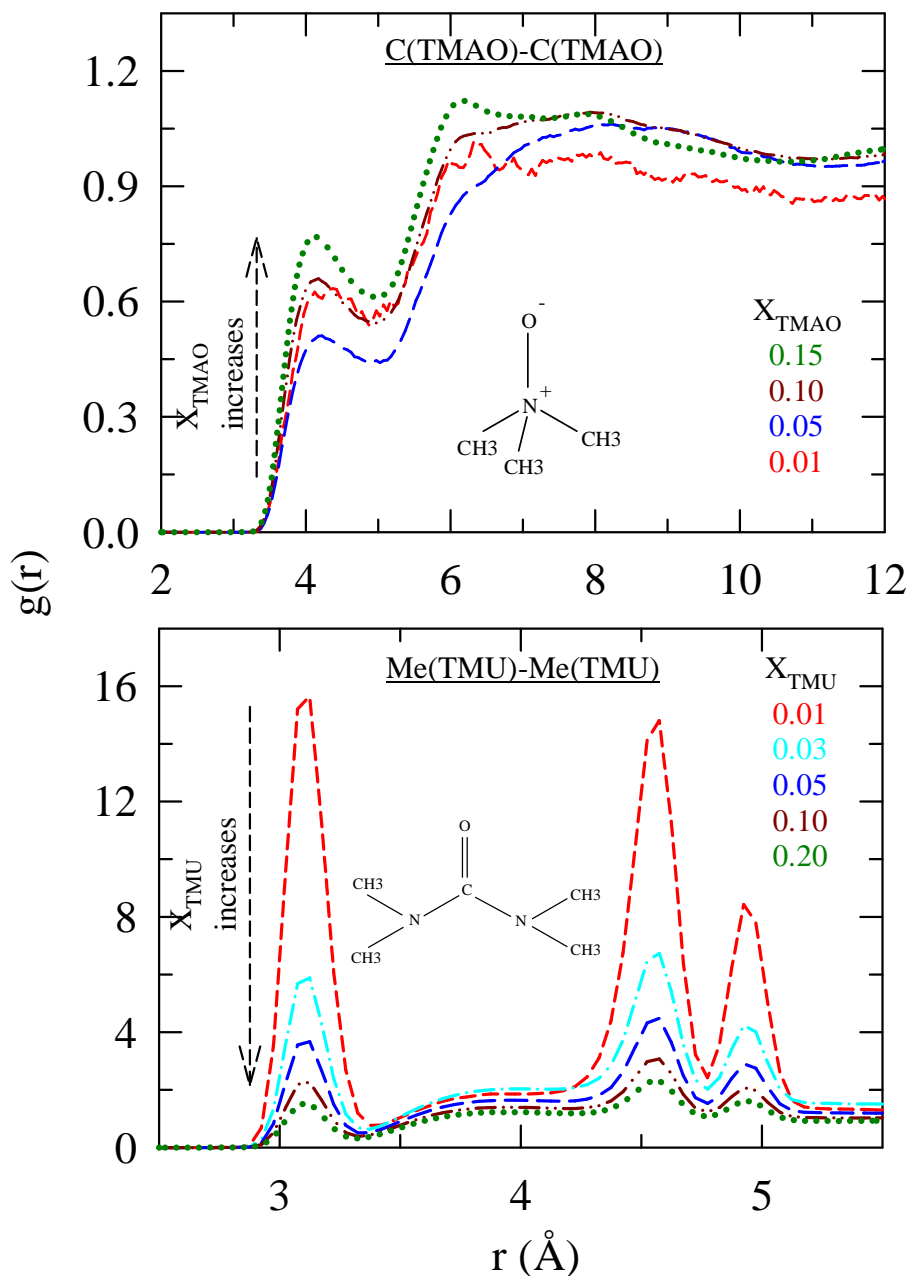
Figure 7.A.2: Site–site RDFs between atomic pairs involved in hydrophobic interaction at various concentrations of TMAO and TMU into water as a function of distance, r. Representations are colour-coded.
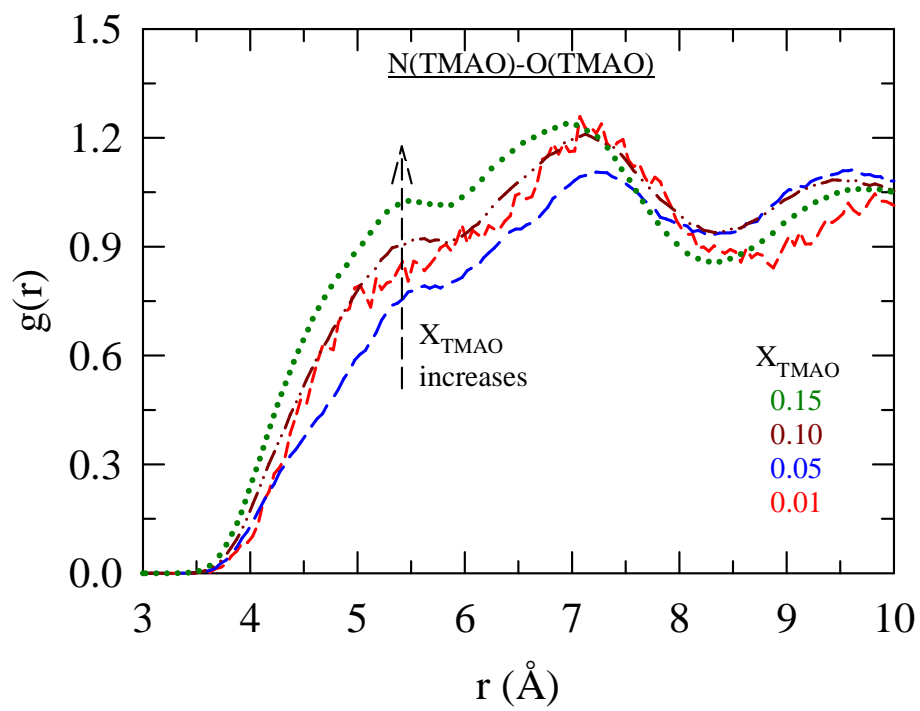
Figure 7.A.3: Plot of X_{TMAO} –dependent g(r) between N(TMAO)–O(TMAO) as a function of r.
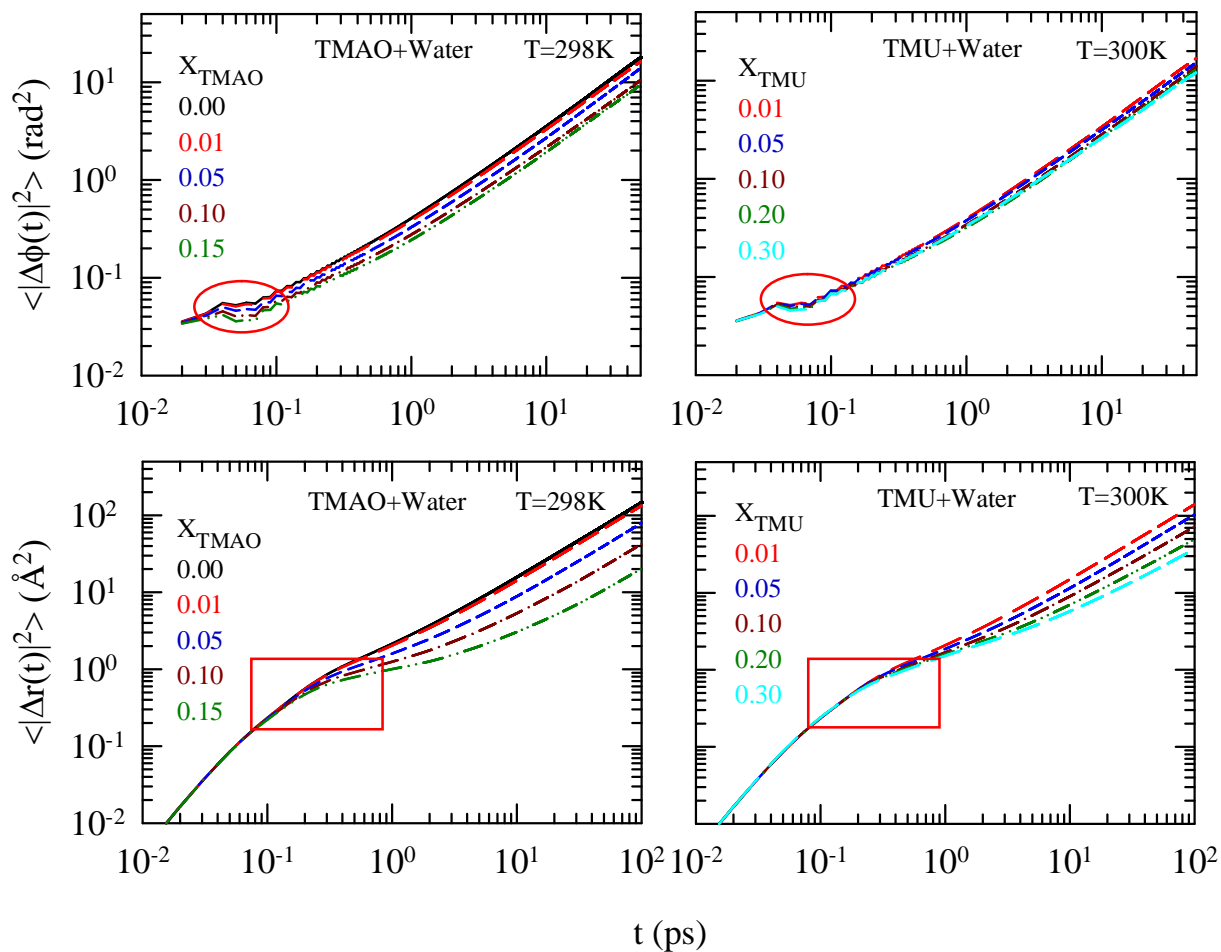
Figure 7.A.4: Plot of rotational mean squared displacement (RMSD), $\left\langle \left| \Delta \vec{\phi}_i(t) \right|^2 \right\rangle$ of water –

OH bond and translational mean squared displacement (MSD), $\left\langle \left| \Delta \vec{r}(t) \right|^2 \right\rangle$ of water at different

concentrations of TMAO (left panels) and TMU (right panels) with time, t. Circles in

$\left\langle \left| \Delta \vec{\phi}_i(t) \right|^2 \right\rangle$ plots and rectangles in $\left\langle \left| \Delta \vec{r}(t) \right|^2 \right\rangle$ plots are drawn to highlight the different

behaviours of RMSD and MSD at the time of transition from inertial to diffusive regimes. Representations are colour-coded.
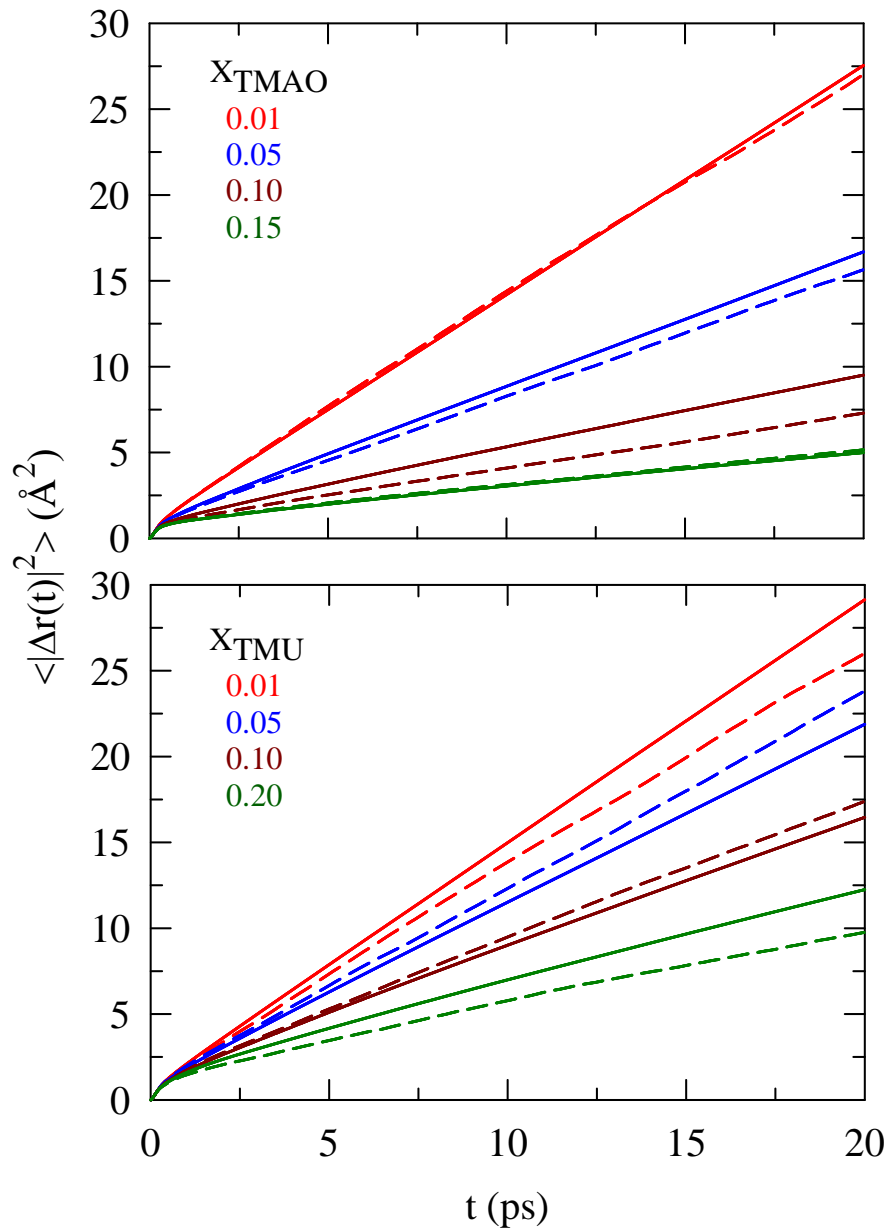
Figure 7.A.5: Plot of MSD, $\left\langle \left| \Delta \vec{r}(t) \right|^2 \right\rangle$ with time, t for bulk (solid lines) and interfacial (dashed lines) water at four different X_{Solute}.
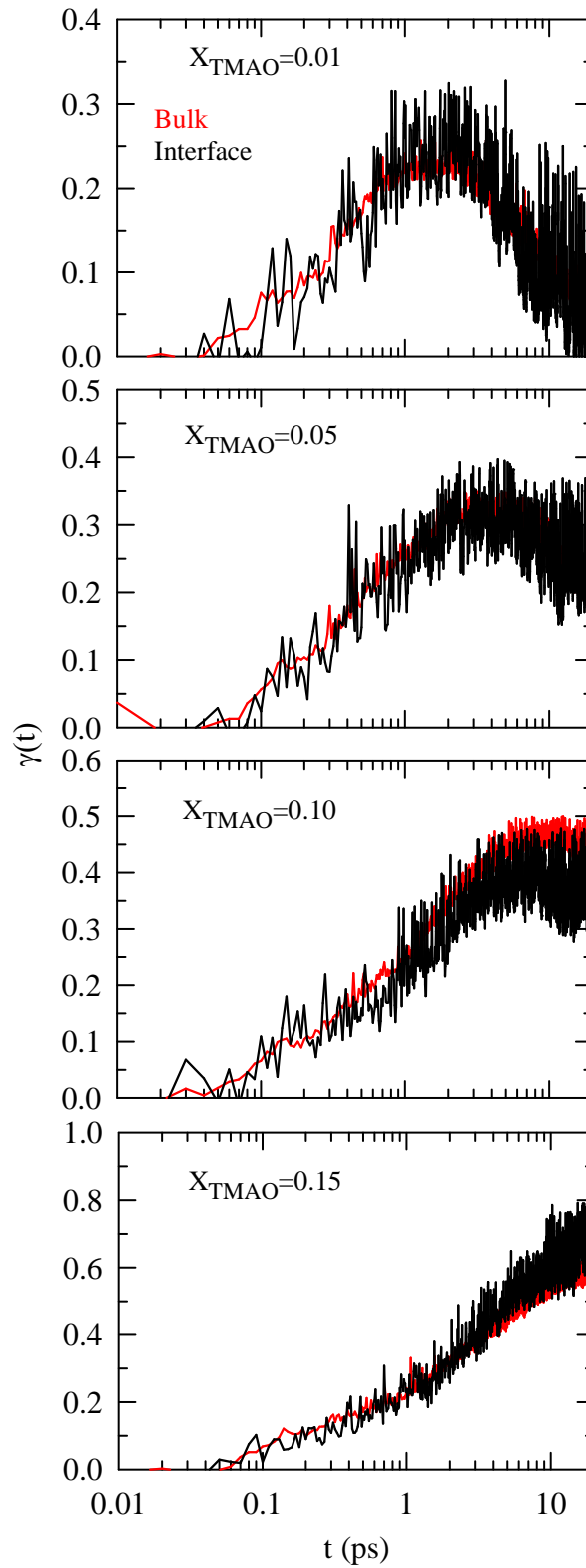
Figure 7.A.6: Distribution of translational new non-Gaussian parameter, $\gamma(t)$ with time, t at four different TMAO concentrations. $\gamma(t)$ for both the bulk and interfacial water are shown here by red and black lines respectively.
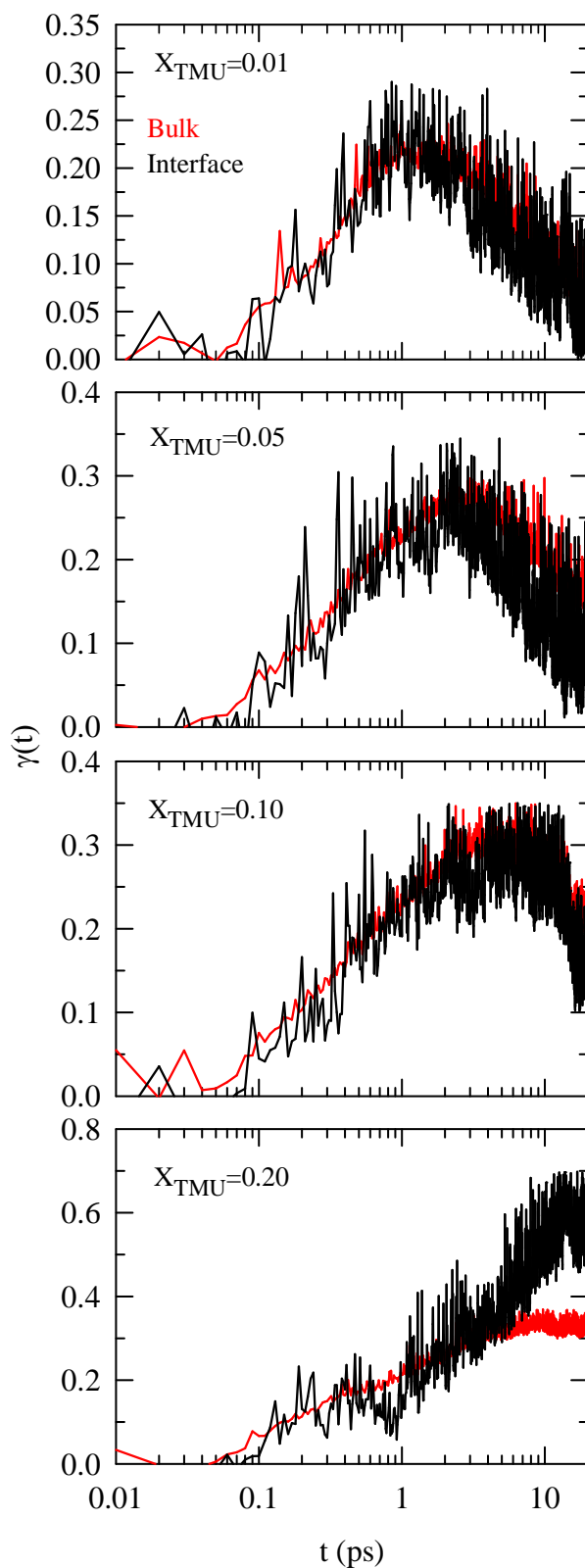
Figure 7.A.7: Distribution of translational new non-Gaussian parameter, $\gamma(t)$ with time, t at four different TMU concentrations. $\gamma(t)$ for both the bulk and interfacial water are shown here by red and black lines respectively.
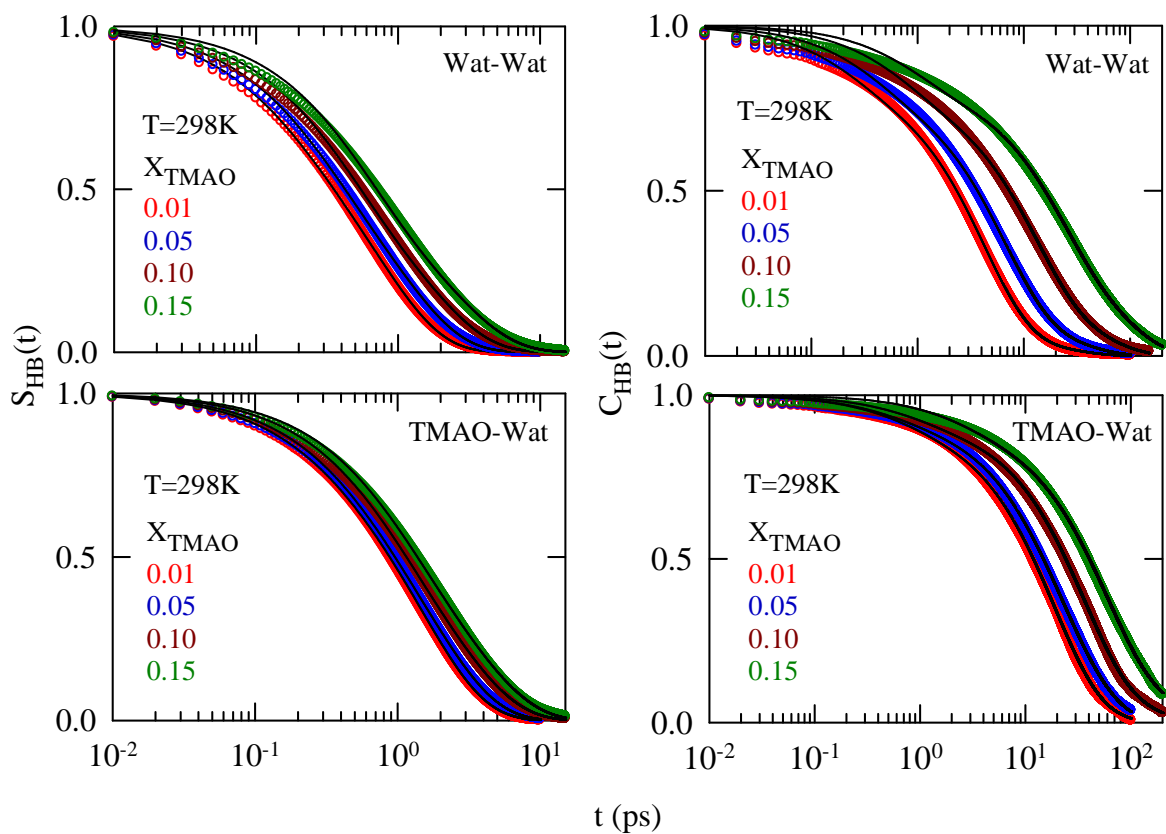
Figure 7.A.8: X_{TMAO}-dependent relaxations of $S_{HB}(t)$ and $C_{HB}(t)$ for water–water hydrogen bonding (upper panel) and water–TMAO hydrogen bonding (lower panel). Simulated data are shown by the circles. Multi-exponential fits of the simulated data are shown by solid lines. X_{TMAO} are colour-coded as follows: 0.01: red, 0.05: blue, 0.10: dark red, 0.15: dark green.

Appendix 7.B

Table 7.B.1: Rotational and translational diffusion coefficients (D_R and D_T) for bulk and interfacial water at different solute concentrations.

Rotational Diffusion						
X_{TMAO}	$D_R \left(10^{-2} / ps\right)$		X_{TMU}	$D_R \left(10^{-2} / ps\right)$		
	Bulk	Interface		Bulk	Interface	
0.01	8.11	7.53	0.01	8.44	7.95	
0.05	6.95	5.90	0.05	7.69	6.76	
0.10	5.24	5.05	0.10	6.99	6.77	
0.15	4.69	4.43	0.20	6.47	5.97	
Translational Diffusion						
X_{TMAO}	$D_T \left(10^{-5} cm^2 / s\right)$		X_{TMU}	$D_T \left(10^{-5} cm^2 / s\right)$		
	Bulk	Interface		Bulk	Interface	
0.01	2.21	2.18	0.01	2.33	2.05	
0.05	1.30	1.23	0.05	1.68	1.91	
0.10	0.69	0.54	0.10	1.15	1.35	
0.15	0.32	0.36	0.20	0.77	0.71	

Table 7.B.2: Bi-exponential fit parameters for water–water H-bond lifetime correlation $\left(S_{HB}^{w-w}(t)\right)$ decays at different TMAO mole fractions and 298K. Corresponding $\langle h \rangle$ values are listed in the last column. [All the fit parameters of H-bond relaxation decays for (TMU+Water) binary mixtures are provided in Appendix 6.B]

X_{TMAO}	a_1	τ_1/ps	a_2	τ_2/ps	τ_{av}/ps	$\langle h \rangle$
0.01	0.24	0.145	0.76	0.767	0.618	0.88
0.03	0.29	0.183	0.71	0.893	0.687	0.88
0.05	0.33	0.228	0.67	1.066	0.789	0.89
0.07	0.37	0.266	0.63	1.233	0.875	0.88
0.10	0.43	0.354	0.57	1.649	1.092	0.89
0.12	0.44	0.391	0.56	1.880	1.225	0.89
0.15	0.48	0.487	0.52	2.435	1.500	0.89

Table 7.B.3: Bi-exponential fit parameters for water–TMAO H-bond lifetime correlation $\left(S_{HB}^{w-TMAO}(t)\right)$ decays at different TMAO mole fractions and 298K. Corresponding $\langle h \rangle$ values are listed in the last column.

X_{TMAO}	a_1	τ_1/ps	a_2	τ_2/ps	τ_{av}/ps	$\langle h \rangle$
0.01	0.13	0.274	0.87	1.546	1.381	0.72
0.03	0.17	0.352	0.83	1.677	1.452	0.73
0.05	0.22	0.469	0.78	1.895	1.581	0.76
0.07	0.23	0.516	0.77	2.080	1.720	0.74
0.10	0.34	0.731	0.66	2.719	2.043	0.77
0.12	0.40	0.848	0.60	3.165	2.238	0.79
0.15	0.37	0.883	0.63	3.474	2.515	0.81

Table 7.B.4: Tri-exponential fit parameters for water-water H-bond structural relaxations $\left(C_{HB}^{w-w}(t)\right)$ at different TMAO mole fractions and 298K. Corresponding $\langle h \rangle$ values are listed in the last column.

X_{TMAO}	a_1	τ_1/ps	a_2	τ_2/ps	a_3	τ_3/ps	τ_{av}/ps	$\langle h \rangle$
0.01	0.16	0.216	0.76	4.173	0.08	21.366	4.915	0.87
0.03	0.17	0.274	0.72	4.977	0.11	24.070	6.278	0.86
0.05	0.18	0.359	0.69	6.329	0.13	28.515	8.138	0.85
0.07	0.19	0.460	0.66	7.742	0.15	33.571	10.233	0.83
0.10	0.19	0.667	0.62	11.916	0.19	48.408	16.712	0.81
0.12	0.19	0.831	0.55	14.589	0.26	54.921	22.461	0.70
0.15	0.18	0.887	0.48	19.926	0.34	80.991	37.261	0.78

Table 7.B.5: Tri-exponential fit parameters for water-TMAO H-bond structural relaxations $\left(C_{HB}^{w-TMAO}(t)\right)$ at different TMAO mole fractions and 298K. Corresponding $\langle h \rangle$ values are listed in the last column.

X_{TMAO}	a_1	τ_1/ps	a_2	τ_2/ps	a_3	τ_3/ps	τ_{av}/ps	$\langle h \rangle$
0.01	0.08	0.637	0.81	17.844	0.11	41.852	19.108	0.19
0.03	0.06	0.375	0.84	17.145	0.10	83.221	22.746	0.22
0.05	0.07	0.545	0.42	15.170	0.51	36.258	24.901	0.27
0.07	0.07	0.493	0.41	16.799	0.52	49.390	32.605	0.28
0.10	0.08	0.882	0.77	33.522	0.15	119.77	43.848	0.33
0.12	0.13	3.300	0.65	42.972	0.22	127.56	56.424	0.37
0.15	0.09	2.414	0.75	55.210	0.16	241.51	80.266	0.42

Appendix 7.C

Simulation results obtained from two different models of TMAO [rigid[18] and flexible[50]] are shown here to compare the difference between the two models. Results of (TMU+Water) binary mixtures are also included in some cases.

The total potential energy expression for the flexible model of TMAO:[50]

$$
U = \left[\sum_{bonds} k_r^{ab} \left(r_{ij} - r_0^{ab} \right)^2 \right] + \left[\sum_{angles} \left\{ k_\alpha^{abc} \left(\alpha_{ijk} - \alpha_0^{abc} \right)^2 - k_r^{ac} \left(r_{ik} - r_0^{ac} \right)^2 \right\} \right]
$$
$$
+ \left[\sum_{torsions} \sum_n k_{\tau,n}^{abcd} \left[1 + \cos\left(n\tau_{ijkl} - \tau_0^{abcd} \right) \right] \right] + \left[\sum_{i<j} \left\{ 4\varepsilon^{ab} \left[\left(\frac{\sigma^{ab}}{r_{ij}} \right)^{12} - \left(\frac{\sigma^{ab}}{r_{ij}} \right)^6 \right] + \frac{q^a q^b}{4\pi\varepsilon_0 r_{ij}} \right\} \right] \quad (7.C.1)
$$

Here, the intramolecular bonded interactions consist of harmonic terms for bond stretching (bond length, r_{ij} ; equilibrium bond length, r_0 and bond force constant, k_r), angle bending (bond angle, α ; equilibrium bond angle, α_0 and angle force constant, k_α) and torsional potential defined over cosines of the dihedral angle τ (multiplicity, n ; phase, τ_0 and torsional parameter, $k_{\tau,n}$). The two-body Urey-Bradley 1–3 interaction term is also included here which comprises a harmonic potential along the distance between first and third atoms of a bond angle. The nonbonded interactions are included by Lennard-Jones potential and Coulomb interaction. ε, σ, r are the potential well depth, van der Waals radius, and distance between atoms respectively. The parameter q represents the partial charge of the atom and ε_0 the static dielectric constant.

Figure 7.C.1: Height of the first peak of simulated g(r) as a function of X_{Solute}. Red circles and green triangles represent (TMAO+Water) and (TMU+Water) mixtures, respectively. Results obtained from rigid and flexible models of TMAO are shown by filled and open symbols respectively.
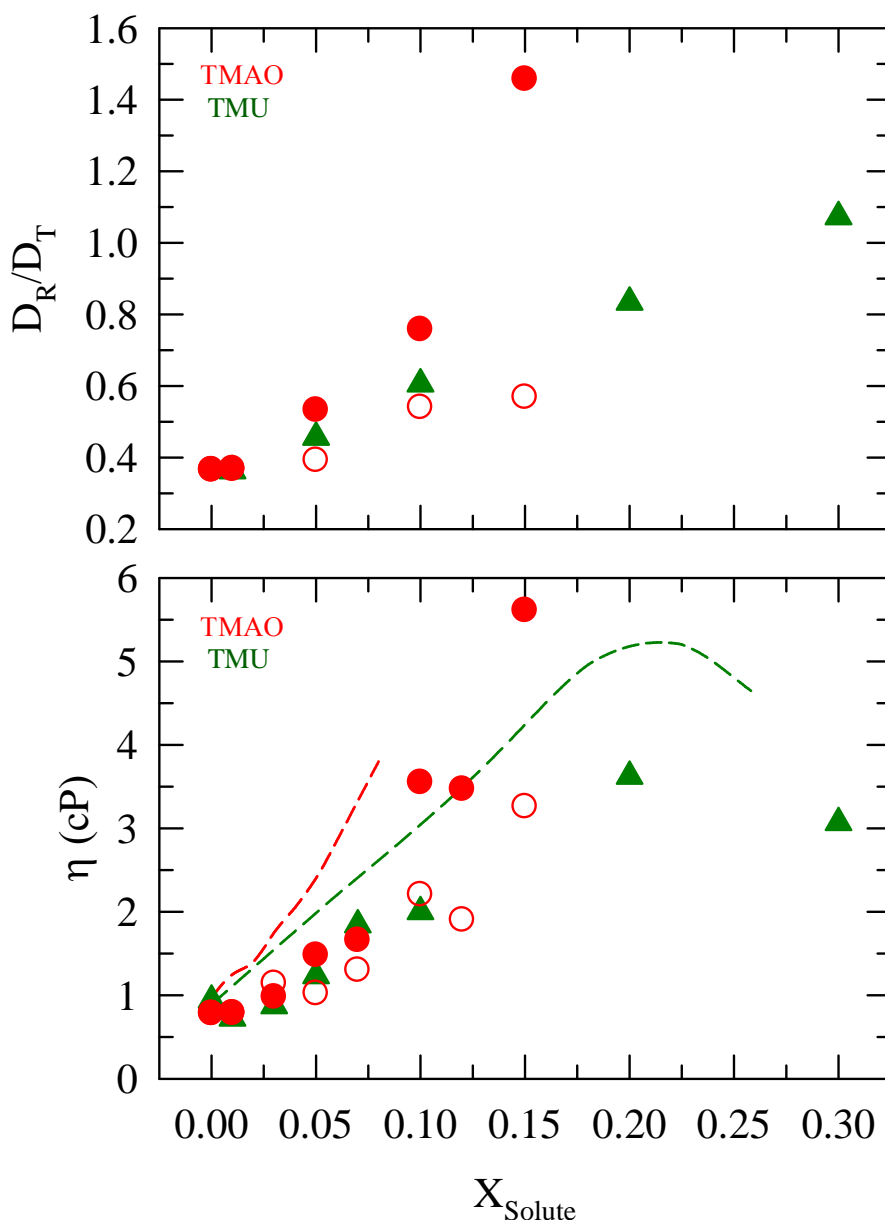
Figure 7.C.2: X_{Solute} dependence of the ratio between the rotational and translational diffusion coefficients, D_R/D_T (upper panel), and viscosity coefficients, η (lower panel), for aqueous solutions of TMAO and TMU. Experimental η for these solutions (lower panel) are also shown. Experimental and simulated η are depicted by the lines and symbols respectively. Red represents TMAO and green TMU. Filled and open symbols represent results from rigid and flexible TMAO models respectively. Note the ratio, D_R/D_T, is scaled by $(\text{Å}^{-1})^2$.
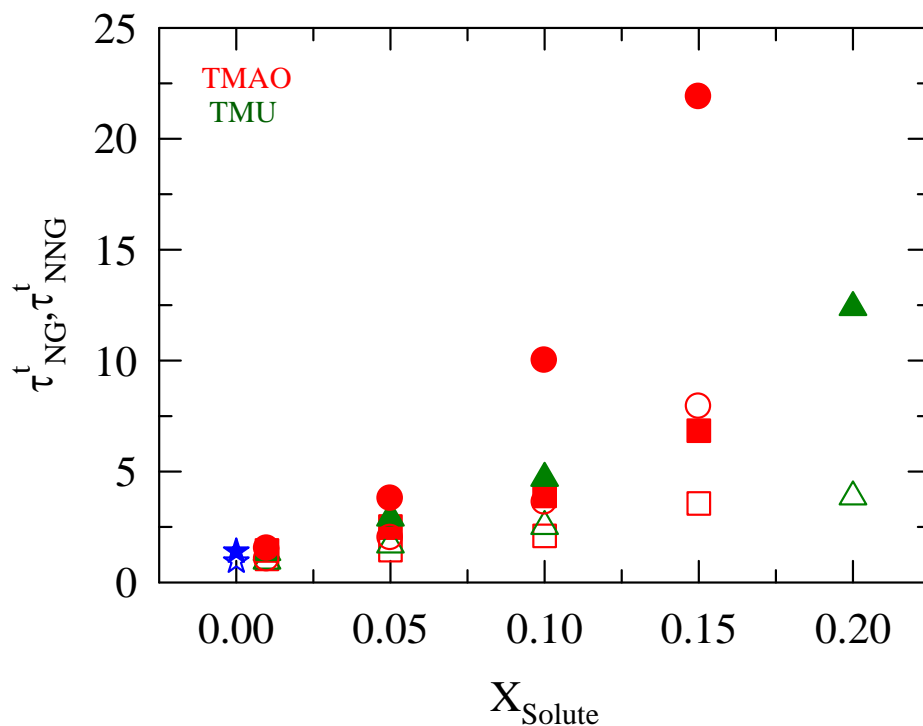
Figure 7.C.3: X_{Solute} dependence for the peak-times of the translational non-Gaussian parameter $\left(\tau_{NG}^{t}\right)$ and the new non-Gaussian parameter $\left(\tau_{NNG}^{t}\right)$ for (water + TMAO) and (water + TMU) systems. Filled symbols represent τ_{NNG}^{t} and open symbols τ_{NG}^{t}. Circles depict rigid TMAO and squares flexible TMAO. Representations are colour-coded. τ_{NG}^{t} and τ_{NNG}^{t} for ambient water are also shown by stars (blue).
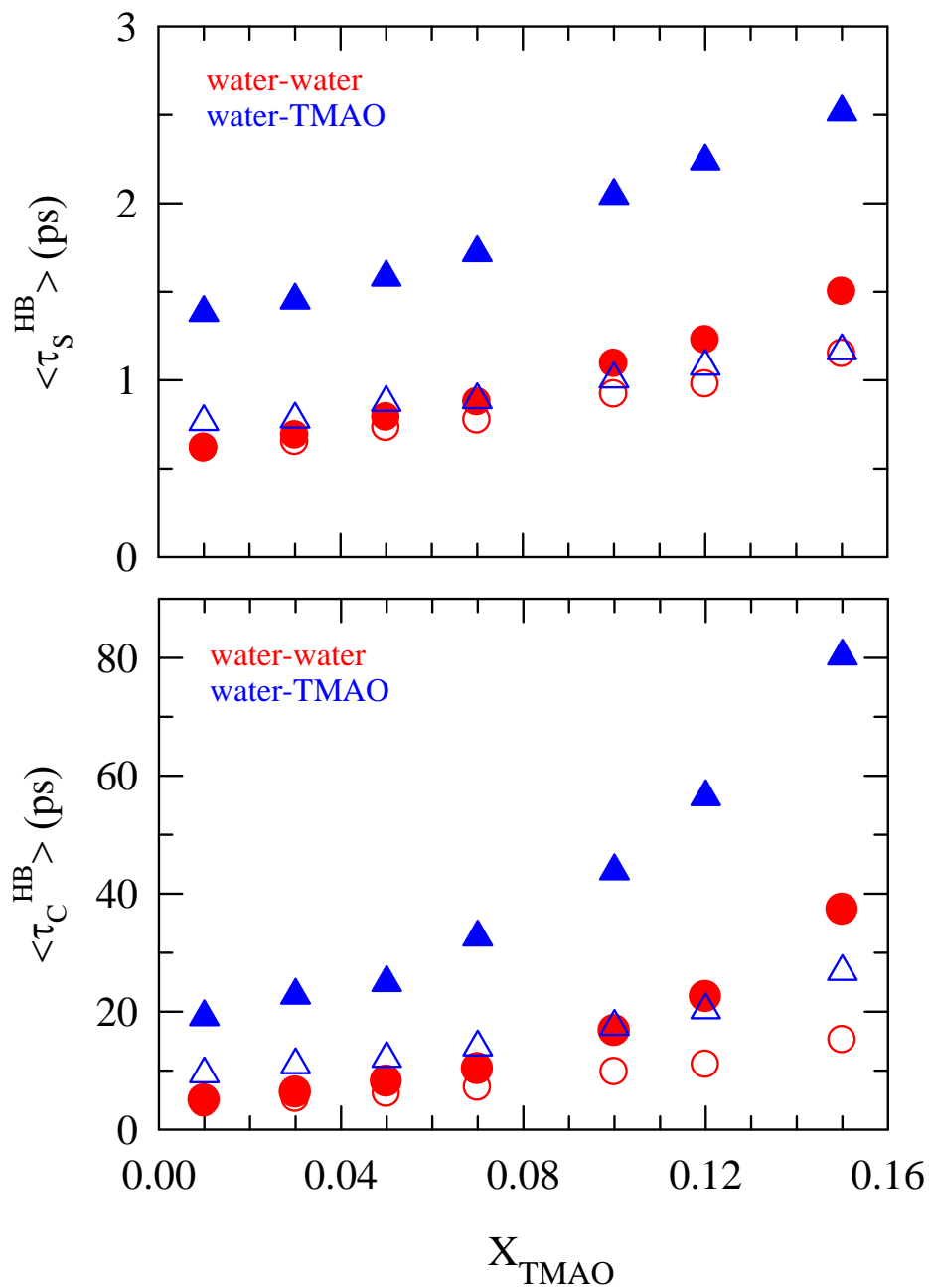
Figure 7.C.4: Plot of average times for H-bond lifetime, $S_{HB}(t)$ (upper panel) and structural relaxation time, $C_{HB}(t)$ (lower panel) at different X_{TMAO}. Filled and open symbols represent rigid and flexible TMAO models respectively. Red circles and blue triangles represent water–water and water–TMAO H-bonding respectively.

References

1.   M. B. Burg and J. D. Ferraris, J. Biol. Chem. **283**, 7309 (2008).

2.   B. Kempf and E. Bremer, Arch. Microbiol. **170**, 319 (1998).

3.   P. H. Yancey, Am. Zool. **41**, 699 (2001).

4.   V. Daggett, Chem. Rev. **106**, 1898 (2006).

5.   C. N. Pace and H. F. Marshall, Arch. Biochem. Biophys. **199**, 270 (1980).

6.   G. Barone, P. del Vecchio, C. Giancola and G. G. Graziano, Thermochim. Acta, **227**, 67 (1993).

7.   D. K. Klimov, J. E. Straub and D. Thirumalai, Proc. Natl. Acad. Sci. U.S.A. **101**, 14760 (2004).

8.   R. D. Mountain and D. Thirumalai, J. Am. Chem. Soc. **125**, 1950 (2003).

9.   L. Cser, G. Jancsó, R. Papoular and T. Grósz, Physica B **156 & 157**, 145 (1989).

10.   H. Doi, Y. Watanabe and M. Aida, Chem. Lett. **43**, 865 (2014).

11.   K. Mazur, I. A. Heisler and S. R. Meech, J. Phys. Chem. B **115**, 2563 (2011).

12.   J. Hunger, K. Tielrooij, R. Buchner, M. Bonn and H. J. Bakker, J. Phys. Chem. B **116**, 4783 (2012).

13.   K. Tielrooij, J. Hunger, R. Buchner, M. Bonn and H. J. Bakker, J. Am. Chem. Soc. **132**, 15671 (2010).

14.   Y. L. A. Rezus and H. J. Bakker, Phys. Rev. Lett. **99**, 148301 (2007).

15.   Y. L. A. Rezus and H. J. Bakker, J. Phys. Chem. B **113**, 4038 (2009).

16.   Y. L. A. Rezus and H. J. Bakker, J. Phys. Chem. A **112**, 2355 (2008).

17.   C. Petersen, A. A. Bakulin, V. G. Pavelyev, M. S. Pshenichnikov and H. J. Bakker, J. Chem. Phys. **133**, 164514 (2010).

18.   S. Paul and G. N. Patey, J. Phys. Chem. B **110**, 10514 (2006).

19.   D. Laage, G. Stirnemann and J. T. Hynes, J. Phys. Chem. B **113**, 2428 (2009).

20.   G. Stirnemann, F. Sterpone and D. Laage, J. Phys. Chem. B **115**, 3254 (2011).

21.   L. Almásy, A. Len, N. K. Székely and J. Pleštil, Fluid Phase Equilib. **257**, 114 (2007).

22.   T. Shikata and S. Itatani, J. Solution Chem. **31**, 823 (2002).

23.   K. Usui, J. Hunger, M. Sulpizi, T. Ohto, M. Bonn and Y. Nagata, J. Phys. Chem. B **119**, 10597 (2015).

24.   S. Indra and R. Biswas, Mol. Sim. **41**, 471 (2015).

25.   J. T. Titantah and M. Karttunen, J. Am. Chem. Soc. **134**, 9362 (2012).

26.   H. S. Frank and M. W. Evans, J. Chem. Phys. **13**, 507 (1945).

27.   Y. Marcus, Phys. Chem. Chem. Phys. **4**, 4462 (2002).

28.   A. Fornili, M. Civera, M. Sironi and S. L. Fornili, Phys. Chem. Chem. Phys. **5**, 4905 (2003).

29.   J. Qvist and B. Halle, J. Am. Chem. Soc. **130**, 10345 (2008).

30.   S. Imoto, H. Forbert and D. Marx, Phys. Chem. Chem. Phys. **17**, 24224 (2015).

31.   W. H. Brandeburgo, S. T. van der Post, E. J. Meijerab and B. Ensing, Phys. Chem. Chem. Phys. **17**, 24968 (2015).

32.   L. Knake, G. Schwaab, K. Kartaschew and M. Havenith, J. Phys. Chem. B **119**, 13842 (2015).

33.   A. Rahman, Phys. Rev. **136**, 405 (1964).

34.   E. Flenner and G. Szamel, Phys. Rev. E **72**, 011205 (2005).

35.   M. G. Mazza, N. Giovambattista, F. W. Starr and H. E. Stanley, Phys. Rev. Lett. **96**, 057803 (2006).

36.   T. G. Lombardo, P. G. Debenedetti and F. H. Stillinger, J. Chem. Phys. **125**, 174507 (2006).

37.   J. P. Hansen and I. R. McDonald, *Theory of simple liquids*. (Academic Press, New York, 1986).

38.   A. Luzar, Faraday Discuss. **103**, 29 (1996).

39.   A. Chandra, Phys. Rev. Lett. **85**, 768 (2000).

40.   S. Balasubramanian, S. Pal and B. Bagchi, Phys. Rev. Lett. **89**, 115501 (2002).

41.   H. J. C. Berendsen, J. R. Grigera and T. P. Straatsma, J. Phys. Chem. **91**, 6269 (1987).

42.   M. P. Allen and D. J. Tildesley, *Computer simulations of liquids*. (Oxford University Press, New York, 1987).

43.   W. Smith, T. R. Forester and I. T. Todorov, *DL_POLY Classic*. (STFC Daresbury Laboratory, Daresbury, 2012).

44.   S. Nose, J. Chem. Phys. **81**, 511 (1984).

45.   W. G. Hoover, Phys. Rev. A **31**, 1695 (1985).

46.   J. P. Ryckaert, G. Ciccotti and H. J. C. Berendsen, J. Comput. Phys. **23**, 327 (1977).

47.   S. Kämmerer, W. Kob and R. Schilling, Phys. Rev. E **56**, 5450 (1997).

48.   R. Sinibaldi, C. Casieri, S. Melchionna, G. Onori, A. L. Segre, S. Viel, L. Mannina and F. De Luca, J. Phys. Chem. B **110**, 8885 (2006).

49.   S. Indra and R. Biswas, J. Chem. Phys. **142**, 204501 (2015).

50.   K. M. Kast, J. Brickmann, S. M. Kast and R. S. Berry, J. Phys. Chem. A **107**, 5342 (2003).

Chapter 8

Fluorescence Spectroscopic Study of Electrolyte Solutions of Triflate Salts in Polar Aprotic Solvents

8.1 Introduction

Formation of free ions, ion pairs (both solvent-shared and solvent-separated), triple ions and neutral triple ions are well-known for ionic solutions of solvents with differing polarities.[1-30] Eventually, the increased polarity due to the presence of various ionic species (ion pairs etc) can modify medium effects on chemical reactions. It has also been observed solvent dynamics is altered substantially in ionic solutions compared to pure solvents. In ionic solutions, solute-ion interaction, in addition to solute-solvent interaction, contributes to the Stokes shift. This is reflected in the larger magnitude of dynamic Stokes shift in ionic solutions compared to that in the parent polar solvent. Another interesting feature of ionic solutions is that the solvation time scales for ionic solutions at room temperature are in the nanosecond regime which is much slower than those in pure polar solvents (usually in few picoseconds).[31] This slow solvation time originates from the slow ion exchange between solvation shells via translational motion whereas in pure solvents, reorientation of solvent molecules primarily govern the dynamics.

The trifluoromethanesulphonate ion, $\left(CF_3SO_3^-\right.$, abbreviated as $^-OTf\left.\right)$ which is the conjugate base of superacid triflic $\left(CF_3SO_3H\right)$, is one of the most important anions in polymer electrolytes because of its high thermal and chemical stability, strong resistance to both reductive and oxidative cleavage. Polymer electrolytes are prepared by combining polymers with appropriate salts when their ionic conductivity can be put to use as an electrolyte. Lithium triflates $\left(LiCF_3SO_3\right)$ are widely used in polymer mixtures as a solid amorphous electrolyte in thin film batteries. The lithium and triflate ions in polymer electrolytes are

found to be involved in formation of complex specie such as $Li(CF_3SO_3)$ ion pairs and $Li(CF_3SO_3)_2^-$, $Li(CF_3SO_3)_3^{2-}$ and higher clusters, which would influence the conducting properties greatly. Vibrational Spectroscopy such as Raman spectroscopy and Infrared spectroscopy has been used mostly for studying $CF_3SO_3^-$ containing system as $CF_3SO_3^-$ possesses Raman active modes.[32-34] Moreover, viscosity and conductivity study[35] showed that sodium triflates $(NaCF_3SO_3)$ are more ion-paired than lithium perchlorate $(LiClO_4)$ in polymer electrolyte. Interestingly, addition of low molecular weight co-solvent or plasticizer such as dimethylformamide (DMF) increases the ionic conductivity significantly.[36,37] But there is no study that focuses on the role of the co-solvents in polymer electrolytes.

In dielectric relaxation study (DRS) of DMF containing sodium and magnesium triflates $(NaCF_3SO_3, Mg(CF_3SO_3)_2)$ and barium perchlorate $(Ba(ClO_4)_2)$,[38] one or two low frequency (< 2 GHz) processes have been observed in addition to high frequency (~15 GHz) processes. It has been suggested that the formation of ion pairs contribute in these low frequency processes. Double solvent-separated ion-pairs are formed in case of bivalent cations whereas single solvent-separated ion-pairs are observed in monovalent cation. DRS showed that the reorientational time of these ion-pairs is in several hundreds of picoseconds, although, the dispersion contribution for this ion-pair formation to the total dielectric dispersion is < 10 %.[38] We know that solvation relaxation around a photo excited probe derives contribution from both rotational (predominant) and translational diffusion of solvent molecules.[39] Therefore, monitoring of the solvation dynamics of this system around a photo excited probe may provide further information regarding the origin of such slower timescales in DRS.

Fluorescence spectroscopy has been proven to be a very efficient tool for studying electrolyte solutions.[31,40,41] Here we have studied the effect of triflate salts, $NaCF_3SO_3$ and $Mg(CF_3SO_3)_2$ on the absorption and steady-state emission spectral properties of dissolved probe coumarin 153 (C153) and compared with the spectral behaviour of C153 in electrolyte solutions containing non-triflate salt $LiClO_4$. Solvent's dynamical response has been

measured at sufficiently higher $NaCF_3SO_3$ concentration to verify the contribution of ion-pairs formed in this solution. We have also checked the effects of this electrolyte solution on the relaxation dynamics (excited-state lifetime decay and rotational anisotropy decay) of solute C153.

8.2 Experimental Section

8.2.1 Sample Preparation

Laser grade C153 was purchased from Exciton. $NaCF_3SO_3$, $Mg(CF_3SO_3)_2$, DMF and acetonitrile (AcCN) were obtained from Sigma-Aldrich. All the chemicals were used as received. The ionic solutions were prepared by dissolving a measured amount of salt in a measured amount of solvent in volumetric flask followed by shaking the solution upto complete dissolution. Subsequently, few µL freshly prepared solution of C153 in heptane was poured into a quartz cuvette of optical path length 1 cm. The nonpolar solvent was evaporated by blowing hot air around outer surface of the cuvette. Then 3–4 ml of aliquot was added to the cuvette and stirred the solution for some time to ensure complete dissolution. Note that the concentration of C153 was maintained at $\leq 10^{-5}$ M for all the compositions studied here.

8.2.2 Density and Viscosity Measurements

Densities and viscosity coefficients of the samples were measured using, respectively, density-cum-sound analyzer (Anton Paar, DSA5000) and micro viscometer (AMVn, Anton Paar) by falling ball method.

8.2.3 Data Collection and Analysis for Steady-state and Time-resolved Fluorescence Measurements

Steady-state absorption and emission spectra were recorded using UV–Visible spectrophotometer (Model UV–2450, Shimadzu) and fluorimeter (Fluorolog, Jobin–Yvon,

Horiba) respectively. For recording emission spectra, absorbance of the solution was adjusted to ~0.1. Then the spectra were processed by standard procedure[40,42-46] discussed in chapter 2. Note that, the resolution of our instrument for peak frequency determination was ~250 cm^{-1}.

Time-resolved fluorescence measurements were carried out using the time correlated single photon counting technique (TCSPC) based on a laser system (LifeSpec–ps, Edinburgh Instruments, U.K.) that provided 409 nm light as an excitation source. The full-width at half-maximum (FWHM) of the instrument response function (IRF) measured using distilled water as a scattering medium and 409 nm excitation light was found to be ~90 ps. For solvation dynamics study, typically 17–18 decays were collected at magic angle at equally spaced wavelengths across the steady-state emission spectrum of C153 dissolved in these ionic solutions. From these collected decays solvation response function, $S(t)$ was constructed after analyzing by standard protocol[31,39,42,47-51] which was discussed elaborately in chapter 5.

For solute's rotational dynamics study, the fluorescence emission decay was collected at three different positions of emission polarizer, magic angle (54.7^0), parallel $[I_{||}(t)]$ and perpendicular $[I_{\perp}(t)]$ with respect to the polarization of the excitation light. As discussed in chapter 2, the standard procedure[48,52,53] was followed to analyse fluorescence rotational anisotropy, $r(t)$.

8.3 Results and Discussion

8.3.1 Steady-state Spectral Characteristics

Different Solvents and Common Monovalent Salt: Representative normalized absorption and emission spectra of C153 at different $NaCF_3SO_3$ concentrations in DMF have been shown in Figure 8.1. It has been observed that both absorption and emission spectra shift to the lower frequency with increase of salt concentration. For better understanding absorption and emission spectral peak frequency (ν_{peak}) and width (Γ) (FWHM) of C153 have been

plotted in Figure 8.2 as a function of concentration of $NaCF_3SO_3$ in DMF, $\left(C_{NaCF_3SO_3}\right)$ and compared with electrolyte solutions of $\left(NaCF_3SO_3 + AcCN\right)$. Note that the maximum solubility of $NaCF_3SO_3$ in AcCN was achieved upto 0.50M which is much lower than the solubility of $NaCF_3SO_3$ in DMF. Some relevant physical properties of these two solvents are
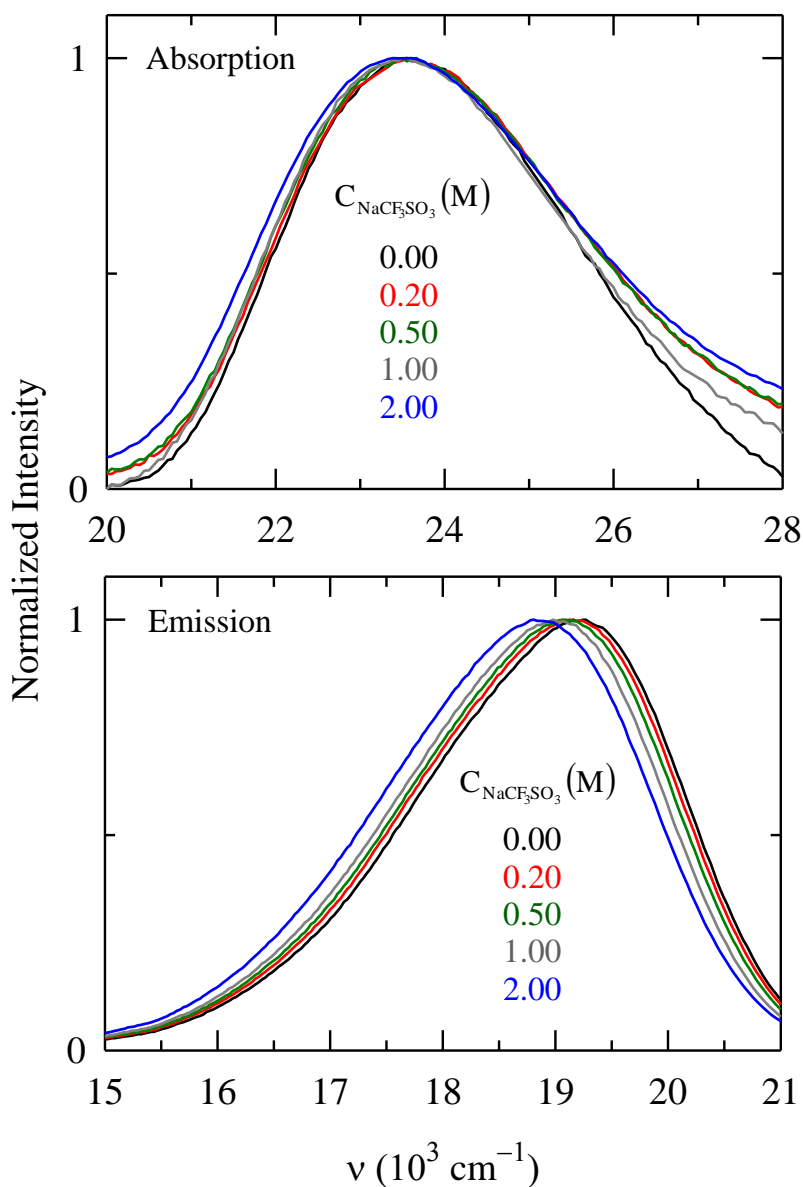
Figure 8.1: Normalized absorption (upper panel) and emission (lower panel) spectra of C153 at various concentrations of $NaCF_3SO_3$ in DMF.

summarized in Table 8.1. The figure shows that both the absorption and emission frequency of C153 undergo red-shift with increase of $NaCF_3SO_3$ concentration in the two solvents. This indicates the enhancement of polarity of the medium with addition of electrolytes into the solvent. The emission frequency exhibits comparatively larger shift than absorption frequency. As emission deals with the excited state of C153 which is more polar in nature due to larger dipole moment than that of ground state,[54] ion-induced red-shift is more pronounced in solute's emission. It is interesting to observe that the frequency lowering in emission spectra is greater in AcCN $\left(\Delta v_{em}(c_{NaCF_3SO_3}=0.0-0.50)=325\,cm^{-1}\right)$ than that of DMF $\left(\Delta v_{em}(c_{NaCF_3SO_3}=0.0-0.50)=120\,cm^{-1}\right)$, although, both the solvents have similar dielectric constants (Table 8.1). DMF has a strong ability to co-ordinate with the cations via oxygen site while two electron donating methyl groups facilitate this process. So the association of DMF with Na^+ ion reduces the possibility of formation of ion-pair in solution. As a result, triflate ions only play the role as a counter-ion. In contrast, AcCN possesses comparatively less co-ordinating ability with cations which facilitates the solute (C153)–ion interaction. Hence, ion-induced frequency decrease is more prominent in AcCN than DMF. Another important feature of this figure is the behaviour of spectral width. The Γ_{abs} increases with increasing salt concentration in DMF as well as in AcCN. This reflects the enhanced heterogeneity of the surrounding environment of C153 with increase of electrolyte concentration in solution. But Γ_{em} shows opposite behaviour of Γ_{abs}. Γ_{em} decreases with addition of electrolyte into both the solvents. This decrease of emission frequency with concomitant narrowing is reminiscent of what was observed earlier in spectral behaviour of C153 in neat polar solvents.[39]

Table 8.1: Physical Properties of Dimethylformamide (DMF) and Acetonitrile (AcCN) at 298K

Properties	DMF	AcCN
Dielectric Constant $\left(\varepsilon_0\right)$	36.71	35.94
Dipole Moment/D	3.86	3.92
Molecular Radius/Å	2.647	2.137
Density/g.cm^{-3}	0.944	0.776
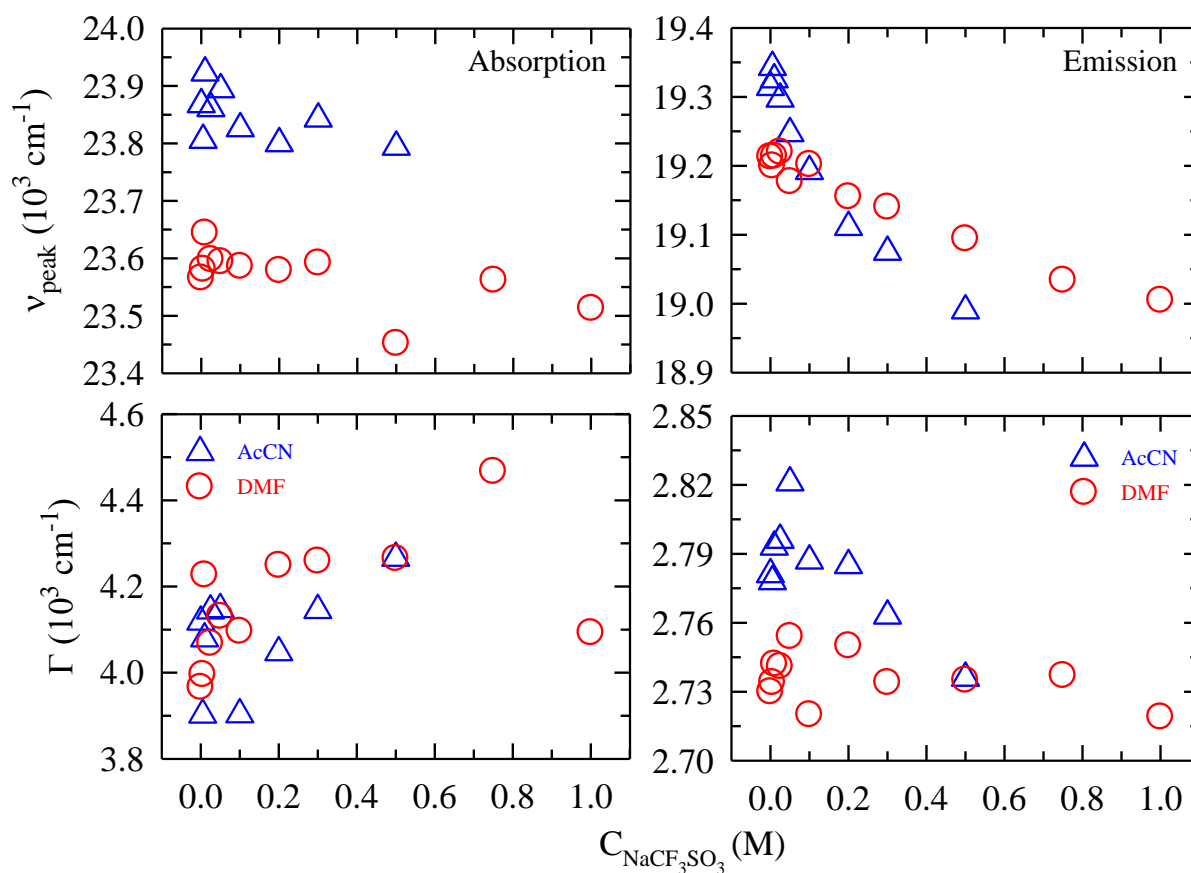
Figure 8.2: $C_{NaCF_3SO_3}$-dependent absorption (left panels) and emission (right panels) spectral peak frequency (ν_{peak}) and width (full width at half maximum, FWHM) (Γ) of C153 in DMF (red circles) and AcCN (blue triangles).

Different Monovalent Salts and Common Solvent: In Figure 8.3 we have compared the spectral properties of C153 in two different electrolyte solutions ($NaCF_3SO_3$ +AcCN) and (LiClO$_4$+AcCN) since the former is known to be more ion-paired in polymer electrolytes.[35] The data for (LiClO$_4$+AcCN) electrolyte solutions was taken from our earlier study.[40] Here, we observed that C153 shows larger spectral red-shift in presence of LiClO$_4$ $\left(\Delta\nu_{em}(LiClO_4) = 510\,cm^{-1}\right.$ and $\left.\Delta\nu_{em}(NaCF_3SO_3) = 325\,cm^{-1}\right)$. DRS study showed that an appreciable amount of triple and neutral triple ions is present in bivalent metal perchlorates–acetonitrile solutions.[55] So presence of large number of ions in the electrolyte solutions of

stronger electrolyte LiClO$_4$ may be responsible for higher polarity of the solution which results greater red-shift in the steady-state spectra of C153.

Our previous study of (LiClO$_4$ + Ethyl acetate) [40] also showed the lowering of frequency of C153 in both the absorption and emission spectra with increase of electrolyte concentration in ethyl acetate but the shifts were quite larger. In the electrolytic solutions of (LiClO$_4$ + Ethyl acetate) and (NaCF$_3$SO$_3$ + DMF), the red-shifts in ν_{abs} are ~1300 cm^{-1} and 50 cm^{-1} and the red-shifts in ν_{em} are ~1600 cm^{-1} and 360 cm^{-1} respectively upto the salt concentration of 2.0M. Polarity of DMF is much higher than ethyl acetate as the static dielectric constants of ethyl acetate and DMF are ~6 and ~37 respectively. It has been concluded from earlier fluorescence study of various electrolytic solutions[31] that the increase of solute–solvent interaction with increase of dielectric constant of the solvent reduces the ion-induced shift. Being a polar solute, C153 preferably interacts with the more polar DMF. Therefore, ions play very weak role in determining the spectral properties. As a result, the negligible ion-induced shift has been observed in (NaCF$_3$SO$_3$ + DMF) electrolytic solutions.
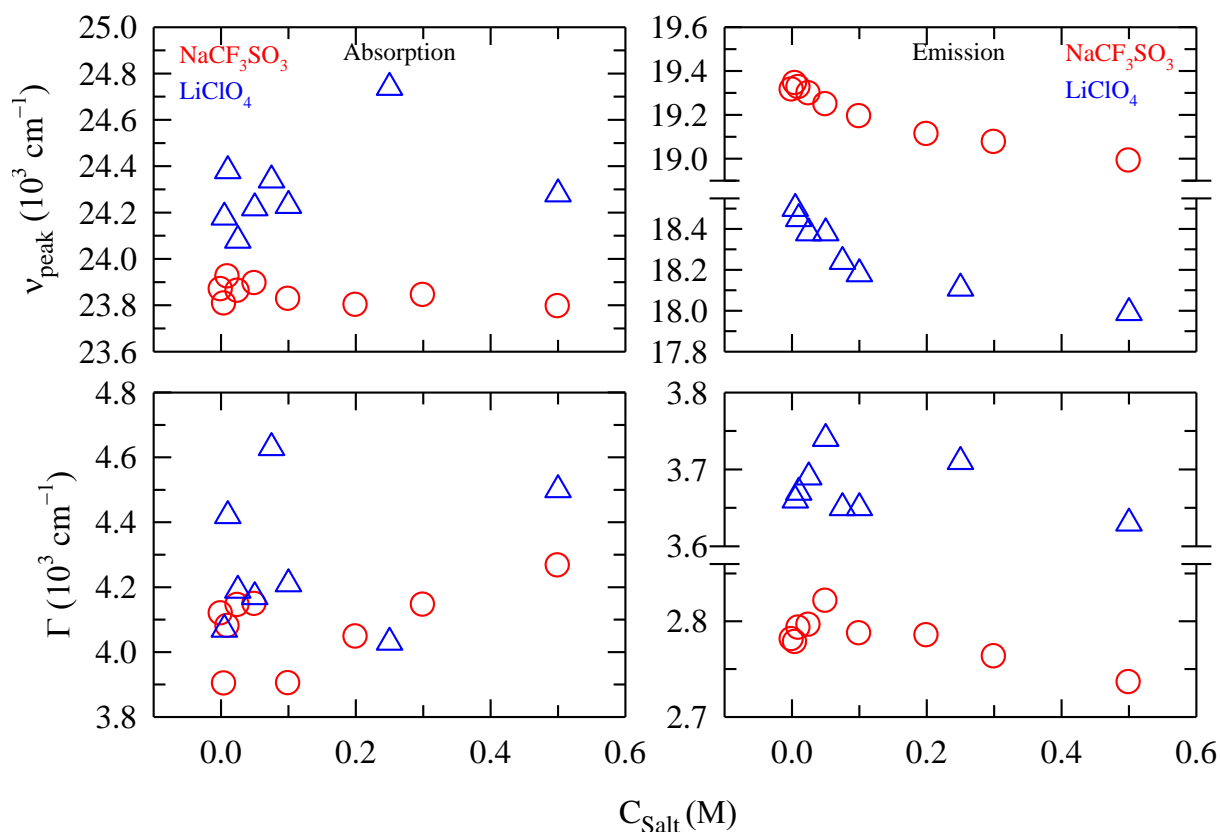
Figure 8.3: Variation of absorption (left panels) and emission (right panels) spectral peak frequency (ν_{peak}) and width (FWHM) (Γ) of C153 at different concentrations of electrolyte $NaCF_3SO_3$ (red circles) and $LiClO_4$ (blue triangles) in AcCN.

Different Bivalent Salts and Common Solvent: Next we investigated in Figure 8.4 the spectral properties of C153 in DMF solutions of monovalent $NaCF_3SO_3$ and bivalent $Mg(CF_3SO_3)_2$ respectively. Here the maximum solubility restriction for $Mg(CF_3SO_3)_2$ in DMF was 0.75 M. In case of bivalent triflate salt $Mg(CF_3SO_3)_2$, formation of double solvent separated ion-pairs has been confirmed from DRS study.[38] Solute–ion interaction has been found to increase with increase of (z/r_{ion}), where z is the charge of the ion.[31] The values of (z/r_{ion}) for Na^+ and Mg^{2+} are 0.98 and 2.78 respectively. It is interesting to observe that both the absorption and emission frequency variation with increase of C_{Salt} are almost equal in presence of these differently charged ions. This again proves that in solvents with higher

polarity, the contribution of the electrolytes gets largely reduced in determining the solute's spectral properties.
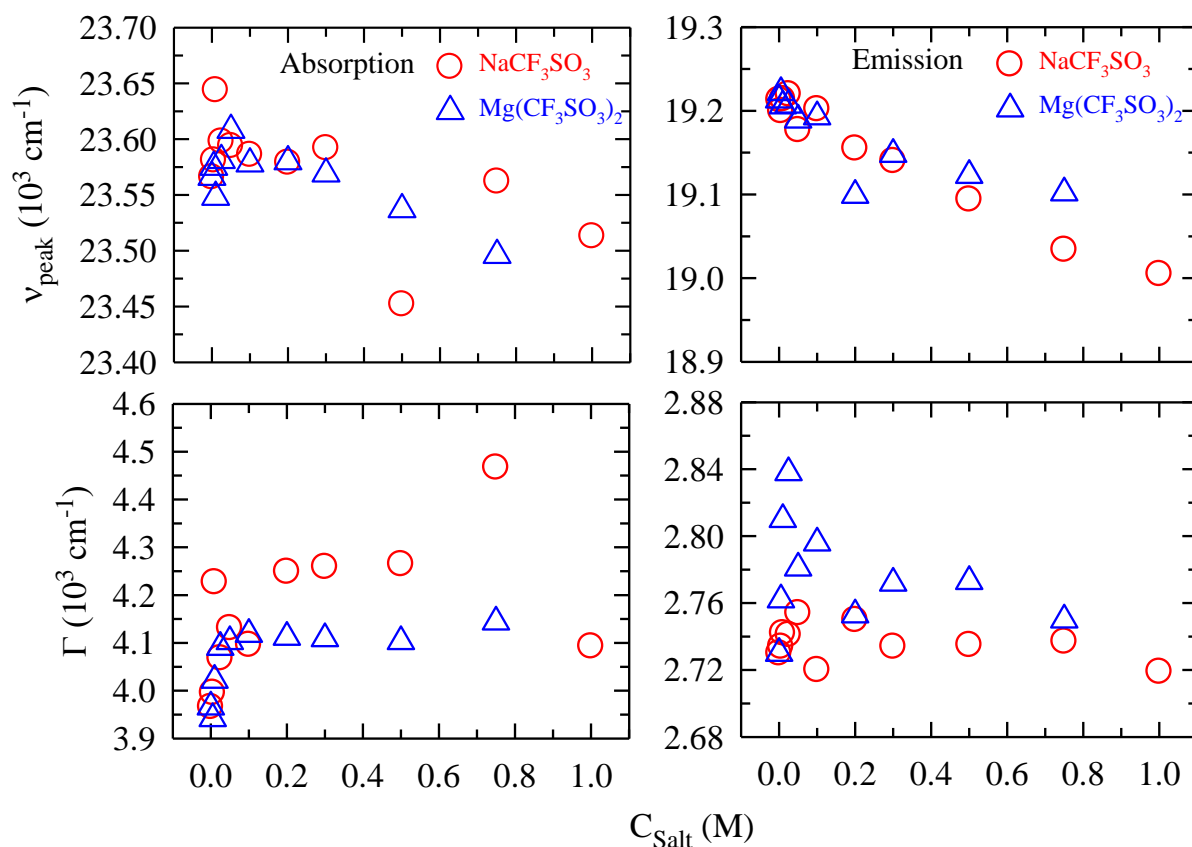
Figure 8.4: Effect of concentration of triflate salts on the absorption (left panels) and emission (right panels) spectral peak frequency $\left(\nu_{peak}\right)$ and width (FWHM) $\left(\Gamma\right)$ of C153 in DMF solutions. Red circles and blue triangles represent $NaCF_3SO_3$ and $Mg(CF_3SO_3)_2$ respectively.

Excitation Wavelength Dependent Spectral Emission

Presence of ions and dipolar solvents may create different solvation environments for the photo-excited probe and that can be well reflected monitoring the excitation wavelength dependent red-shift emission of the fluorophore.[56-58] In Figure 8.5, the average emission frequency $\langle \nu \rangle$ (upper panel) and spectral width Γ (lower panel) of C153 at three different

concentrations of $NaCF_3SO_3$ in DMF have been plotted over different excitation wavelengths λ_{ex}. Total change in both $\langle \nu \rangle$ and Γ is ~50 cm^{-1} which indicates nothing but the homogeneous environment around C153 in this electrolyte solution.
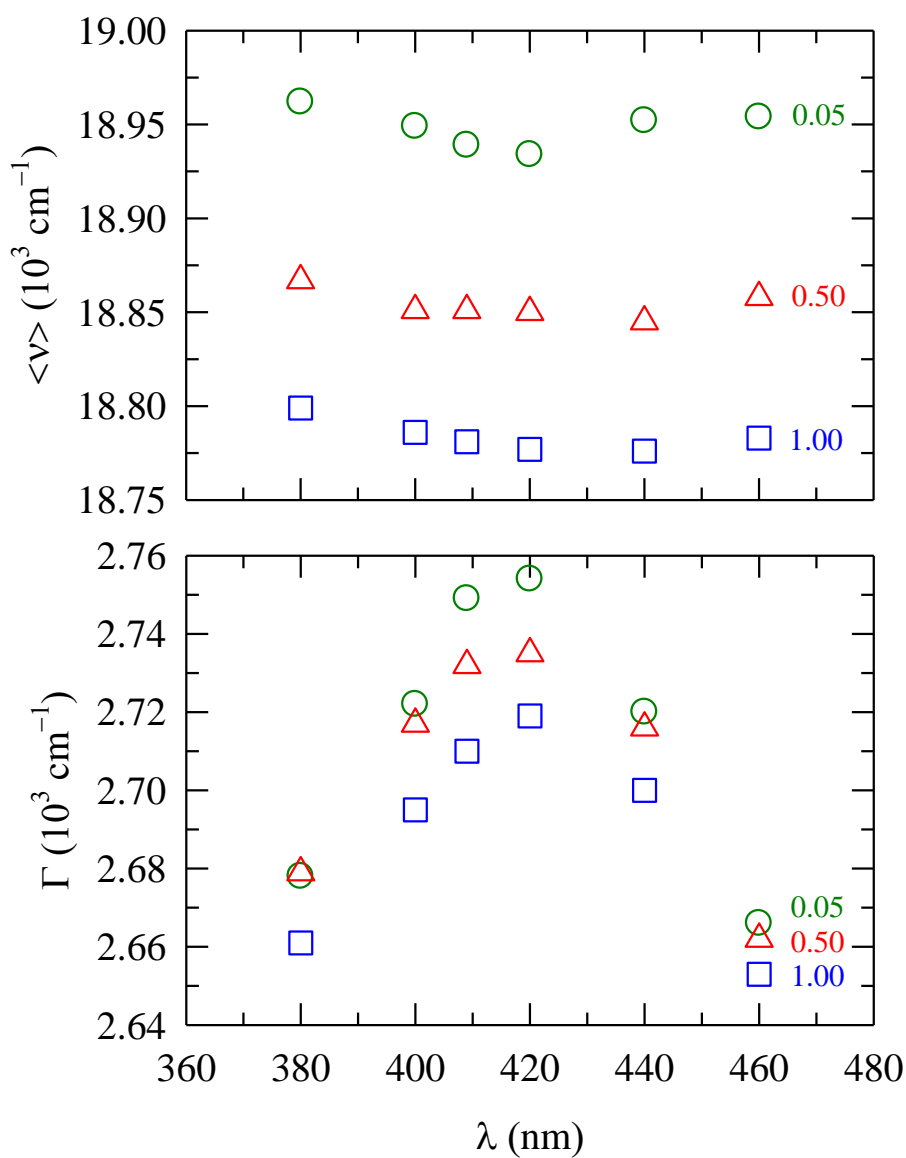
Figure 8.5: λ_{ex}-dependent emission spectral frequency (ν) and width (FWHM) (Γ) at three different concentrations of $NaCF_3SO_3$ in DMF. Here, the frequency averaging is done over first moment frequency, peak frequency and half average frequency.

8.3.2 Time-resolved Spectroscopic Studies

Solvation Response in 0.42M $\left(\text{NaCF}_3\text{SO}_3 + \text{DMF} \right)$ Solutions

As we have already discussed in the Introduction that one of our objectives of this study was to find out whether the emergence of the slower timescales (several hundred of picoseconds) in dielectric relaxation study[38] has any effect on solvation of these ionic solutions. It is well established that solvation in aprotic solvents such as AcCN, DMF is mainly governed by the fast inertial motion (100–300 fs) of the solvent molecules.[39] But addition of ions slows down the dynamics in the nanosecond regime.[1,3,31] The origin of this slow timescales was interpreted in various ways such as slow translation diffusion of the ion pairs,[1,3] ion-solute association.[31] Here, we have carried out solvation dynamics study in the highest concentrated solution of $\left(\text{NaCF}_3\text{SO}_3 + \text{DMF} \right)$ considered in DRS (~0.42M). As viscosity of the medium increases with addition of NaCF_3SO_3 into DMF (shown in Figure 8.A.1 of Appendix 8.A), this composition belongs to comparatively higher viscous region. The normalized solvation response function $S(t)$ with exponential fit has been plotted in Figure 8.6. Representative time-resolved emission spectra (TRES) and width of C153 in this ionic solution are shown in the Figure 8.A.2 of Appendix 8.A. Negligible time-dependent spectral evolution was observed. Although, the average solvation time $\langle \tau_s \rangle$ was obtained 400 ps, we found very fast solvation response of this system which could not be captured by our picoseconds instrumental resolution. The estimated and observed Stokes shifts for this system were $\nu_{est} = 1188\,cm^{-1}$ and $\nu_{obs} = 63\,cm^{-1}$ respectively. So we could get only 5% of total solvation response. It is seen from DRS[38] that ion-pair formation contributes only 8% to the total dispersion for this composition. Therefore, our result proves that the slower timescale originating from the reorientation of the ion-pairs provides insignificant contribution to the solvation response. The dominating contribution comes from the inertial motion of the solvent molecules.
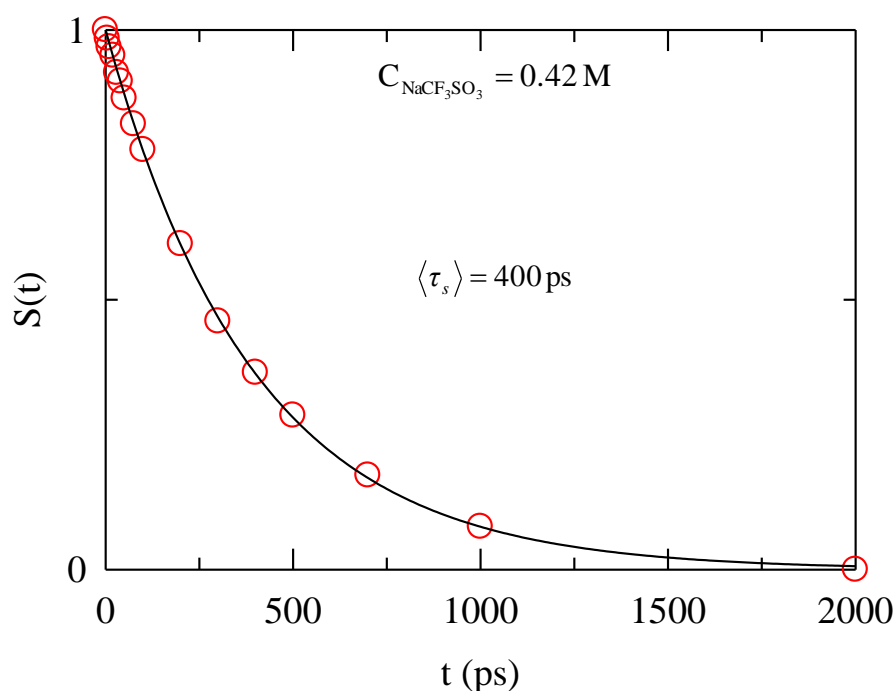
Figure 8.6: Normalized decay of solvation response function, $S(t)$ with time, t for ~0.42M $NaCF_3SO_3$ in DMF using C153. Symbols and line represent experimentally measured data and exponential fit to the data. Average solvation time, $\langle\tau_s\rangle$ obtained from fit has been shown in the inset. Here, the first moment frequency of the normalized time-resolved emission spectra (TRES) has been considered for calculation of $S(t)$.

Measurements of Relaxation Rates of C153 in $(NaCF_3SO_3 + DMF)$ Solutions

Average time constants associated with two different relaxation processes, excited-state lifetime decay and rotational anisotropy decay of C153 in $(NaCF_3SO_3 + DMF)$ electrolyte solutions are shown in Figure 8.7. Average excited-state lifetime $\langle\tau_{life}\rangle$ of C153 has been obtained from magic angle emission decay. Upper panel of Figure 8.7 shows the salt concentration dependent distribution of $\langle\tau_{life}\rangle$. Single and bi-exponential functions were required for adequate fitting of the fluorescence emission decay at low and high salt concentration regimes respectively. The fitting parameters are summarized in Table 8.2. It is

interesting to observe from the figure that $\langle \tau_{life} \rangle$ of C153 decreases with increase of concentration of $NaCF_3SO_3$ in DMF although the polarity of the medium increases. But a closer look to the fitting parameters reveals that the longer time constant τ_1, which is associated to the lifetime of the excited probe molecule, undergoes insignificant change with addition of $NaCF_3SO_3$ in DMF. This very nicely corroborates with the steady-state spectral behaviour that solute-ion interaction is highly suppressed in this electrolyte solutions. While the faster time constant τ_2, which represents the solvent reorganization time, slows down in concentrated electrolyte solutions.

Table 8.2: Single and bi-exponential fit parameters for magic angle fluorescence emission decay of C153 and average excited-state lifetime $\langle \tau_{life} \rangle$ $\left[\langle \tau_{life} \rangle = \sum_{i=1}^{n} a_i \tau_i \right]$ at different concentrations of $NaCF_3SO_3$ in DMF.

$C_{NaCF3SO3}$	a_1	τ_1/ns	a_2	τ_2/ps	$\langle \tau_{life} \rangle$/ns
0.00	1.00	5.404			
0.005	1.00	5.289			
0.01	1.00	5.309			
0.025	1.00	5.385			
0.05	1.00	5.385			
0.10	1.00	5.344			
0.20	1.00	5.236			
0.30	0.91	5.250	0.09	298.0	4.804
0.50	0.91	5.279	0.09	515.0	4.850
0.75	0.89	5.283	0.11	522.0	4.759
1.00	0.88	5.273	0.12	579.0	4.710
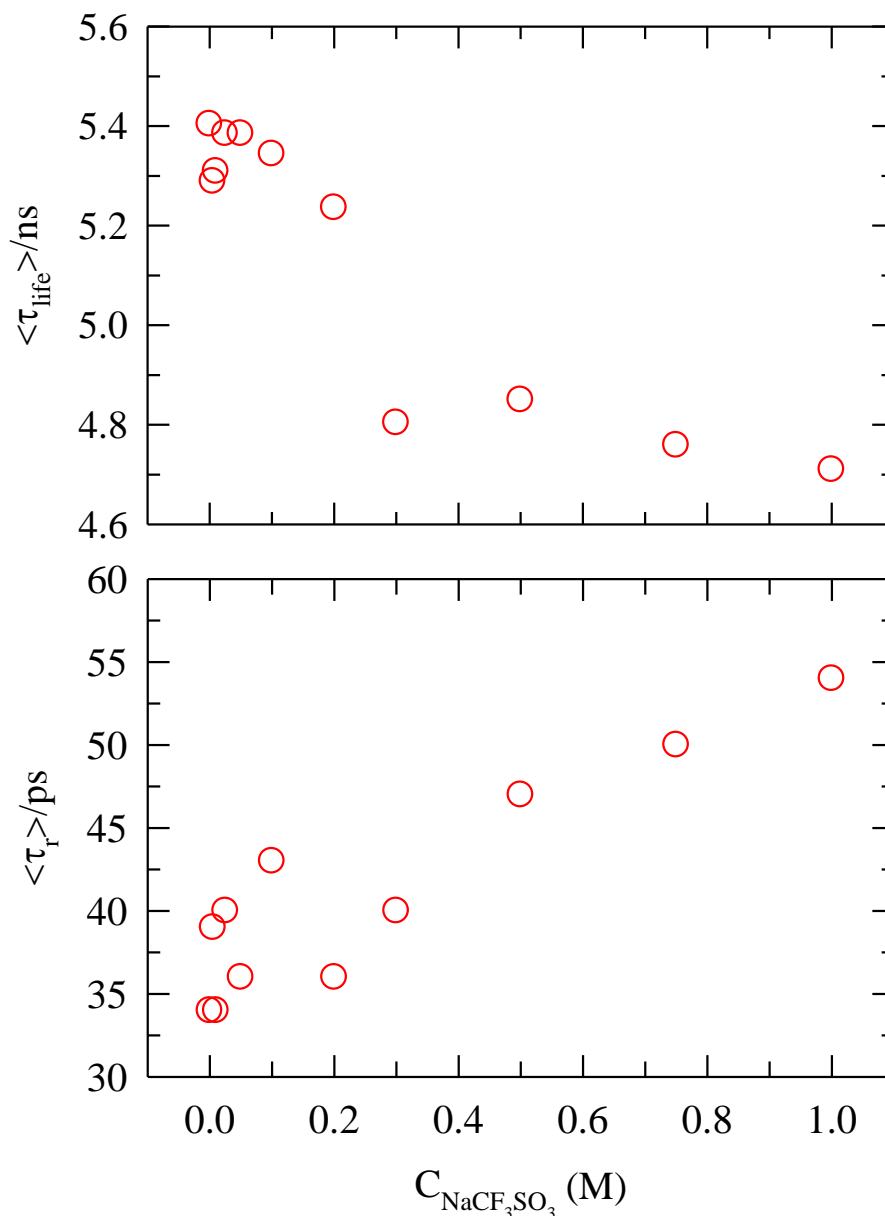
Figure 8.7: Variation of average excited-state lifetime, $\langle \tau_{life} \rangle$ (upper panel) and rotational time, $\langle \tau_r \rangle$ (lower panel) of C153 with increase of concentration of $NaCF_3SO_3$ into DMF.

Representative rotational anisotropy decay $r(t)$ of C153 in 0.20M $NaCF_3SO_3$ solution has been shown in Figure 8.A.3 of Appendix 8.A along with the exponential fit and the residual of the fitting. Here, single exponential function was sufficient to fit the anisotropy decays for

all concentrations of the electrolytes. The average rotational time $\langle \tau_r \rangle$ has been plotted as a function of $C_{NaCF_3SO_3}$ in the lower panel of Figure 8.7. $\langle \tau_r \rangle$ slows down with increase of $C_{NaCF_3SO_3}$ in DMF. This essentially maps the viscosity of the medium (Figure 8.A.1 of Appendix 8.A).

8.4 Conclusion

Addition of $NaCF_3SO_3$ into DMF does not change the polarity of the medium in significant amount due to strong ion–solvent association. As a result, very weak change has been observed in absorption and steady-state emission spectra of C153 in $\left(NaCF_3SO_3 + DMF \right)$ electrolyte solution. This strong ion–solvent interaction also prevents the formation of ion-pairs in the solution. But substantial red-shift has been observed in emission spectra of C153 in $\left(NaCF_3SO_3 + AcCN \right)$ solution. This indicates the enhanced ion–solute interaction with increase of $NaCF_3SO_3$ concentration in AcCN. Similar type of steady-state spectral behaviour has been found in case of bivalent $Mg\left(CF_3SO_3 \right)_2$ in DMF. Solvation dynamics study using instrument of picoseconds time resolution failed to capture most of the dynamics even in concentrated solution of $NaCF_3SO_3$. Rotational time of C153 in $\left(NaCF_3SO_3 + DMF \right)$ solution increases with increasing salt concentration as viscosity of the medium changes.

Appendix 8.A
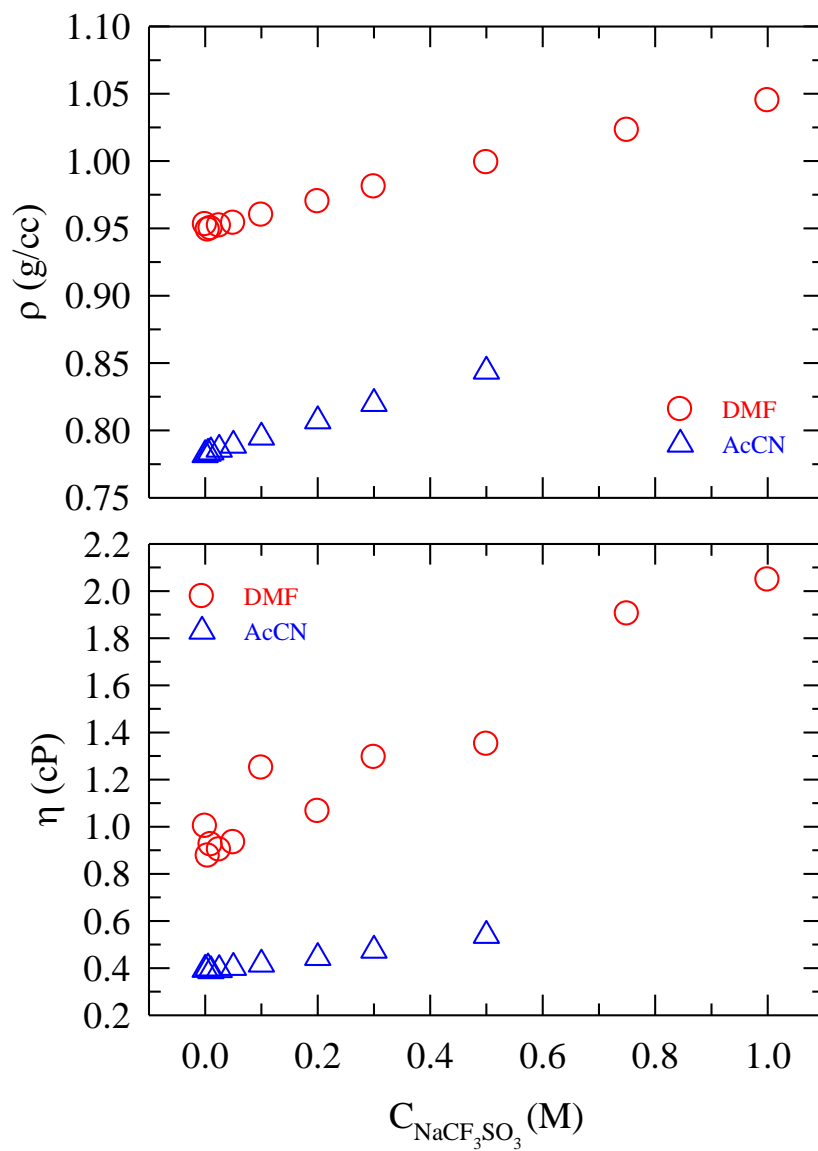
Figure 8.A.1: Density (ρ) and viscosity (η) at different concentrations of $NaCF_3SO_3$ in two different dipolar solvents DMF and AcCN at ~298K.
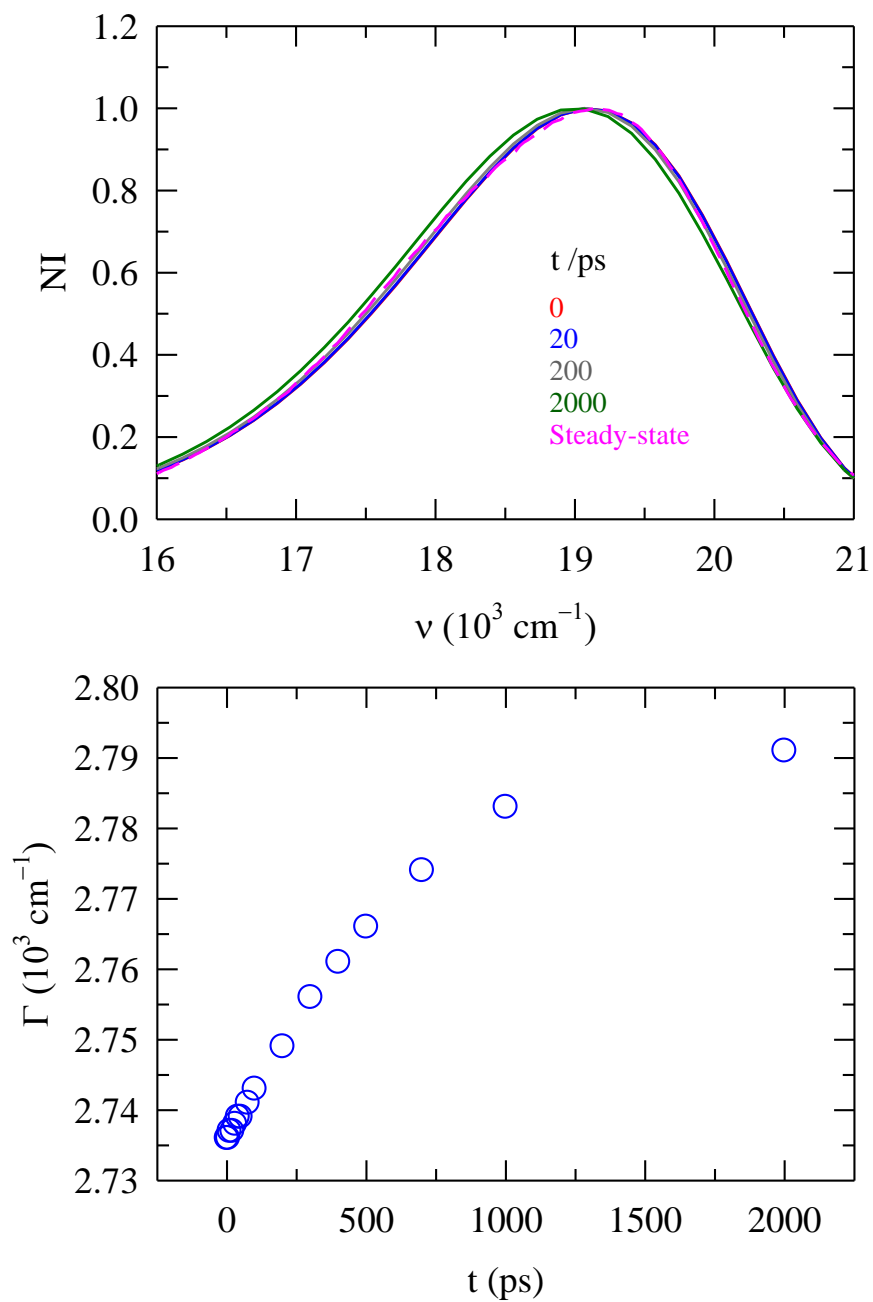
Figure 8.A.2: Synthesized time resolved emission spectra (TRES) (upper panel) of C153 at different time slices from the experimentally obtained decays in 0.42M $NaCF_3SO_3$ solution of DMF. TRES are shown at the following time intervals after solute excitation: 0 ps, 20 ps, 200 ps and 2000 ps. Steady-state emission spectrum is also shown in the panel by dashed line. Corresponding time-evolved spectral widths (FWHM) (Γ) are shown in the lower panel.
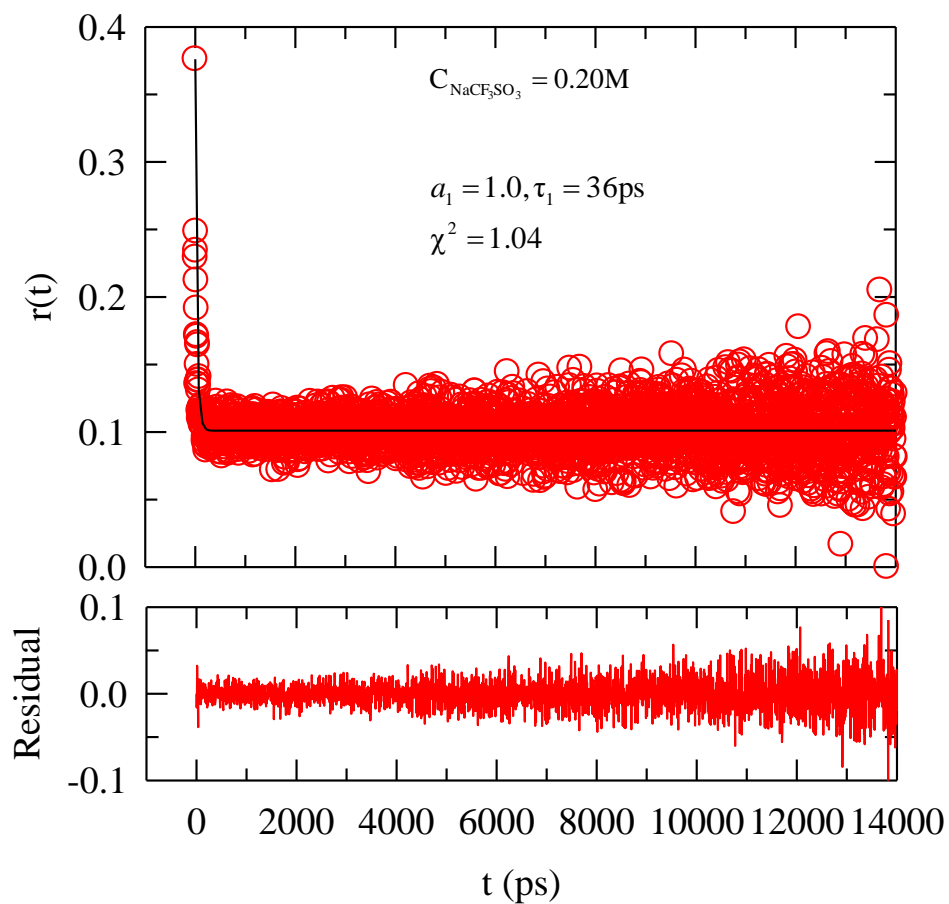
Figure 8.A.3: Representative fluorescence anisotropy decay, $r(t)$ of C153 in 0.20M NaCF$_3$SO$_3$ solution of DMF (upper panel). While open circles represent the data, the solid line shows the exponential fit through the data. Fit parameters are listed in the upper panel. The *goodness of fit parameter* (reduced χ^2) is also shown. Residual is represented in the bottom panel.

References

1.   D. Huppert, V. Ittah and M. Kosower, Chem. Phys. Lett. **159**, 267 (1989).

2.   E. Bart and D. Huppert, Chem. Phys. Lett. **195**, 37 (1992).

3.   V. Ittah and D. Huppert, Chem. Phys. Lett. **173**, 496 (1990).

4.   P. Eberspacher, E. Wismeth, R. Buchner and J. Barthel, J. Mol. Liq. **129**, 3 (2006).

5.   J. Barthel, H. Hetzenauer and R. Buchner, Ber. Bunsen-Ges. Phys. Chem. **96**, 1424 (1992).

6.   O. N. Kalugin, V. G. Panchenko and I. N. V'yunnik, Russ. J. Phys. Chem. **79**, 629 (2005).

7.   R. M. Fuoss and C. A. Kraus, J. Am. Chem. Soc. **55**, 2387 (1933).

8.   R. M. Fuoss and C. A. Kraus, J. Am. Chem. Soc. **55**, 1019 (1933).

9.   Y. Marcus and G. Hefter, Chem. Rev. **104**, 3405 (2004).

10.   J. Richardi, P. H. Fries and H. Krienke, J. Chem. Phys. **108**, 4079 (1998).

11.   D. Spanberg and K. Hermansson, Chem. Phys. **300**, 165 (2004).

12.   A. K. Mollner, P. A. Brooksby, J. S. Loring, I. Bako, G. Palinkas and W. R. Fawcett, J. Phys. Chem. A **108**, 3344 (2004).

13.   W. R. Fawcett and G. Liu, J. Phys. Chem. **96**, 4231 (1992).

14.   J. Barthel and R. Deser, J. Solution Chem. **23**, 1133 (1994).

15.   J. S. Loring and W. R. Fawcett, J. Phys. Chem. A **103**, 3608 (1999).

16.   J. N. Cha, B. S. Cheong and H. G. Cho, J. Phys. Chem. A **105**, 1789 (2001).

17.   W. W. Rudolph, G. Irmer and G. T. Hefter, Phys. Chem. Chem. Phys. **5**, 5253 (2003).

18.   J. Barthel, M. Kleebauer and R. Buchner, J. Solution Chem. **24**, 1 (1995).

19.   R. Buchner, T. Chen and G. Hefter, J. Phys. Chem. B **108**, 2365 (2004).

20.   T. Chen, G. Hefter and R. Buchner, J. Solution Chem. **34**, 1045 (2005).

21.   R. Buchner, G. T. Hefter and P. M. May, J. Phys. Chem. A **103**, 1 (1999).

22.   M. Salomon and M. C. Uchiyama, J. Solution Chem. **16**, 21 (1987).

23.   M. Salomon, S. Slane, E. Plichta and M. C. Uchiyama, J. Solution Chem. **18**, 977 (1989).

24.   M. Delsignore, H. Farber and S. Petrucci, J. Phys. Chem. **89**, 4968 (1985).

25.   M. Delsignore, H. Farber and S. Petrucci, J. Phys. Chem. **90**, 66 (1986).

26.   M. Salomon, M. Uchiyama, M. Xu and S. Petrucci, J. Phys. Chem. **93**, 4374 (1989).

27.   S. Petrucci and M. J. Eyring, Phys. Chem. **95**, 1731 (1991).

28. H. Cachet, A. Cyrot, M. Fakir and J. C. Lestrade, J. Phys. Chem. **83**, 2419 (1979).

29. Z. Chen and M. Hojo, J. Phys. Chem. A **101**, 10896 (1997).

30. W. A. Henderson, N. R. Brooks, W. W. Brennessel and V. J. Young, Jr. , J. Phys. Chem. A **108**, 225 (2004).

31. C. F. Chapman and M. Maroncelli, J. Phys. Chem. **95**, 9095 (1991).

32. B. Sandner, J. Tübke, S. Wartewig and S. Shashkov, Solid State Ionics **83**, 87 (1996).

33. J. M. Alía and H. G. M. Edwards, Vibrational Spectroscopy **24**, 185 (2000).

34. J. R. Stevens and P. Jacobsson, Can. J. Chem. **69**, 1980 (1991).

35. M. G. McLint and C. A. Angell, J. Phys. Chem. **95**, 9464 (1991).

36. A. G. Bishop, D. R. MacFarlane, D. McNaughton and M. Forsyth, Solid State Ionics **85**, 129 (1996).

37. S. F. Johnston, I. M. Ward, J. Cruickshank and G. R. Davies, Solid State Ionics **90**, 39 (1996).

38. A. Placzek, G. Hefter, H. M. A. Rahman and R. Buchner, J. Phys. Chem. B **115**, 2234 (2011).

39. M. L. Horng, J. A. Gardecki, A. Papazyan and M. Maroncelli, J. Phys. Chem. B **99**, 17311 (1995).

40. T. Pradhan and R. Biswas, J. Phys. Chem. A **111**, 11514 (2007).

41. T. Pradhan and B. R., J. Solution Chem. **38**, 517 (2009).

42. T. Pradhan, P. Ghoshal and R. Biswas, J. Phys. Chem. A **112**, 915 (2008).

43. T. Pradhan, P. Ghoshal and R. Biswas, J. Chem. Sci. **120**, 275 (2008).

44. T. Pradhan, H. A. R. Gazi and R. Biswas, J. Chem. Phys. **131**, 054507 (2009).

45. R. Biswas, J. E. Lewis and M. Maroncelli, Chem. Phys. Lett. **310**, 485 (1999).

46. J. E. Lewis, R. Biswas, A. G. Robinson and M. Maroncelli, J. Phys. Chem. B **105**, 3306 (2001).

47. T. Pradhan and R. Biswas, J. Phys. Chem. A **111**, 11524 (2007).

48. K. Dahl, R. Biswas, N. Ito and M. Maroncelli, J. Phys. Chem. B **109**, 1563 (2005).

49. M. Maroncelli and G. R. Fleming, J. Chem. Phys. **86**, 1090 (1987).

50. M. Maroncelli, J. Mol. Liq. **57**, 1 (1993).

51. R. S. Fee and M. Maroncelli, Chem. Phys. **183**, 235 (1994).

52. M. L. Horng, J. A. Gardecki and M. Maroncelli, J. Phys. Chem. A **101**, 1030 (1997).

53. J. E. Lewis and M. Maroncelli, Chem. Phys. Lett. **282**, 197 (1998).

54.   P. K. McCarthy and G. J. Blanchard, J. Phys. Chem. **97**, 12205 (1993).

55.   P. Eberspächer, E. Wismeth, R. Buchner and J. Barthel, J. Mol. Liq. **129**, 3 (2006).

56.   A. Das, S. Das and R. Biswas, Chem. Phys. Lett. **581**, 47 (2013).

57.   B. Guchhait, S. Daschakraborty and R. Biswas, J. Chem. Phys. **136**, 174503 (2012).

58.   S. Indra and R. Biswas, J. Chem. Phys. **142**, 204501 (2015).

Chapter 9

Concluding Remarks and Future Problems

9.1 Concluding Remarks

Besides the tunable properties of aqueous binary mixtures as solvents and reaction media, relevance of the aqueous solutions of amphiphiles to biological environments[1-5] motivated us to carry out extensive study in this area. For this purpose we chose amphiphilic molecules of different classes. First, we considered long chain alcohol 2-butoxyethanol (BE) which forms single phase solution with water at room temperature. However, there exists a lower critical solution temperature (LCST)[6,7] for this solution slightly above the room temperature. Therefore, this system provided a unique opportunity to investigate which of the phenomena- critical concentration fluctuation or hydrophobic aggregation – plays the determining role for the solution structure. Second, we chose tetramethylurea (TMU) as the amphiphile because researchers have been debating about the nature of the methyl groups attached to electronegative nitrogen atoms.[8] The question here is whether the methyl groups attached to the nitrogen atom is hydrophobic in character. Third, amphiphilic molecules with closed-loop structures such as cycloethers, in which orientational freedom of the hydrophobic groups is restricted, were also our interest to study. We investigated with these molecules whether deformation of water structure recognizes the chemical character – dipolar or quadrupolar – of the added cosolvent in the resulting aqueous binary mixtures. A detail study of these problems is presented in chapter 2, 3 and 4 respectively. In these three chapters, solution properties of the binary mixtures have been probed by monitoring the spectral evolution of a dissolved solute by florescence spectroscopic technique. In chapter 4, we also carried out all-atom molecular dynamics simulation for better interpretation of our experimental results. Binary mixture of cryoprotectants (trehalose and glycerol), which is biologically very important system, was investigated by combined

fluorescence and computer simulation techniques in chapter 5. For microscopic level understanding of the interactions taking place with addition of TMU into water and subsequent effects on the water dynamics, detail simulation study was performed in chapter 6. The amphiphiles-induced modification of dynamic heterogeneity of water molecules was examined in chapter 7. The amphiphiles were trimethylamine-N-oxide (TMAO) and TMU, which show completely opposite roles in biological environments.[2-5] Solute-solvent interactions were further studied in chapter 8 by fluorescence spectroscopic approach in electrolyte solutions containing triflate salts in polar solvents. Since every chapter contains concluding remarks, we refrain from providing a summary of all the conclusions. Rather, we discuss below a list of problems that may be studied in future with a statement that the central theme of the present thesis has been exploration and understanding of the structure and dynamics of multi-component mixtures via spectroscopic measurements and computer simulations.

9.2 Future Problems

9.2.1 Structural and Dynamical Change of the Surrounding Environment of Dissolved Probe C153 in BE/water Binary Mixtures by Computer Simulation Study

From the fluorescence spectroscopic study of aqueous solutions of BE,[9] we have observed anomalous behavior of a dissolved probe coumarin 153 (C153) at very low BE concentrations. Absorption spectral frequency of C153 shows a red-shift with decrease of solution polarity up to $X_{BE} = 0.02$, which has been correlated with the enhancement of local solution structure around the probe. Molecular dynamics simulation study of BE/water binary mixture[10] also reported that aggregation among the tail (hydrophobic) parts of BE reaches maximum at $X_{BE} = 0.02$. Therefore, it will be very interesting to study how such type of hydrophobic aggregation among the BE molecules affects the solvation structure of the dissolved probe C153 at low BE concentration regimes. This can be done via molecular dynamics simulations of BE/water binary mixtures by adding one or two C153 molecules into it (to maintain very dilute concentration of

C153). Determination of lifetime and size of these aggregates would be useful and can complement the experimental data. In addition, characterization of dynamic heterogeneity aspects of this binary mixture and a comparison with other alcohol/water binary mixtures would constitute a very interesting problem.

9.2.2 Characterization of Micellar Structure in Aqueous Solutions of Long Chain Alcohols and Comparison of Interfacial Dynamics of Water Molecules around the Alcohol Aggregates with the Bulk Water

Study of aqueous solutions of alcohols with long chain hydrophobic tail showed that these alcohol molecules have a high propensity to form micelle-like aggregates.[7,10,11] It has been also observed that aggregation reaches maximum at a particular alcohol concentration.[10] Therefore, characterization of the length scales of this aggregated species would provide important insight into this problem. The dynamics of water molecules at the interface of the micelles would be different from that of the bulk. It is really important to know up to what extent this aggregated species perturb the dynamics of the water molecules. How does the dynamics of the interfacial water molecules differ from that of bulk? One can check how compact the micellar structure is and how are their lifetime and size distributions. What is the timescales of temporal heterogeneity and correlation lengths in this system? Another point was raised from the simulation study[10] of BE/water binary mixture that system size should be sufficiently large for maintaining the micelle structure, specially, at relatively high amphiphile concentrations. Thus, one should check the effect of system size for this kind of system, and bring out a semi-quantitatively correct picture.

9.2.3 Determination of Tetrahedrality of Water in Aqueous Solutions of Amphiphiles

Experimental study of aqueous solutions of amphiphiles showed that the relaxation timescales of fluorophore exhibit two different slopes depending upon the amphiphile concentration.[9,12,13] We have suggested this slope change is associated with the disruption of tetrahedral H-bond network of water to zigzag chain-like structure. Therefore, calculations of tetrahedral order parameter of water at different amphiphile concentrations will provide further insight to the experimental interpretation. Several geometric order parameters have been suggested so far to characterize the local structure of liquid water and its tetrahedral arrangement. But their respective merits have remained elusive.[14] So, one needs to be careful in selection of the order parameter. Separating the individual percentage of water molecules belonging to different coordination states[15] and monitoring the variation of this percentage with the change of amphiphile concentration can be an alternative pathway to verify the critical amphiphile concentration where the solution structural transition takes place. System size would be an important factor here and should be handled with the desired dexterity.

9.2.4 Percolation in Aqueous Solutions

In aqueous solutions of DMSO, the anomalous behavior[16-18] at low solute concentrations has been demonstrated by a continuum percolation-like transition.[19] In the binary mixtures of TMU/water, simulation study showed the growth of both water-water and water-TMU H-bonding interactions with increase of TMU concentrations into water.[20] In contrast, hydrophobic interaction among the methyl groups is found to decrease with increase of TMU concentration. This type of structural arrangement is closely related to the formation of percolation network. Identification of this percolating structure and its distribution with increase of TMU concentration would be an interesting problem to study. The effect of the hydrophobic moieties on the percolation threshold can also be inspected by substituting the methyl groups of TMU with higher homologues.

The above is a representative of the relevant yet interesting problems in the area of multi-component aqueous and non-aqueous mixtures where many important basic scientific aspects have remained unexplored. Application of a variety of spectroscopic techniques, such as 2D-IR, ultrafast transient absorption, fluorescence up-conversion, and dielectric relaxation measurements extending from megahertz to terahertz in combination with neutron/X-ray scattering measurements computer simulations will surely bring out the fundamentals of these complex and rich systems. We look forward to this excitement of the new age physical chemistry where ultrafast measurements characterize the ultraslow chemical events.

References

1.   S. Roy, B. Jana and B. Bagchi, J. Chem. Phys. **136**, 115103 (2012).

2.   P. H. Yancey, Am. Zool. **41**, 699 (2001).

3.   V. Daggett, Chem. Rev. **106**, 1898 (2006).

4.   C. N. Pace and H. F. Marshall, Arch. Biochem. Biophys. **199**, 270 (1980).

5.   G. Barone, P. del Vecchio, C. Giancola and G. G. Graziano, Thermochim. Acta, **227**, 67 (1993).

6.   J. Schmitz, L. Belkoura and D. Woermann, J. Chem. Phys. **101**, 476 (1994).

7.   G. D'Arrigo, F. Mallamace, N. Micali, A. Paparelli, J. Teixeira and C. Vasi, Prog. Colloid Polym. Sci. **84**, 177 (1991).

8.   Y. Koga, P. Westh, K. Nishikawa and S. Subramanian, J. Phys. Chem. B **115**, 2995 (2011).

9.   S. Indra and R. Biswas, J. Chem. Phys. **142**, 204501 (2015).

10.   R. Gupta and G. N. Patey, J. Phys. Chem. B **115**, 15323 (2011).

11.   R. C. Castillo, H. C. Domínguez and M. Costas, J. Phys. Chem. **94**, 8731 (1990).

12.   S. Indra and R. Biswas, J. Chem. Sci. (2015) (under review).

13.   S. Indra, B. Guchhait and R. Biswas, J. Chem. Phys. (2015) (under review).

14.   E. Duboué-Dijon and D. Laage, J. Phys. Chem. B **119**, 8406 (2015).

15.   E. Guardia, I. Skarmoutsos and M. Masia, J. Phys. Chem. B **119**, 8926 (2015).

16.   J. Mazurkiewicz and P. Tomasik, J. Phys. Org. Chem. **3**, 493 (1990).

17.   U. Kaatze, M. Brai, F. Sholle and R. Pottel, J. Mol. Liq. **44**, 197 (1990).

18.   A. Luzar and D. Chandler, J. Chem. Phys. **98**, 8160 (1993).

19.   S. Roy, S. Banerjee, N. Biyani, B. Jana and B. Bagchi, J. Phys. Chem. B **115**, 685 (2011).

20.   S. Indra and R. Biswas, Mol. Sim. **41**, 471 (2015).